

**Estimation of 2D and 3D In-situ Stresses Using Back Analysis  
of Measurements of Well / Borehole Deformation**

by

Cui Lin

Submitted in partial fulfillment of the requirements  
for the degree of Doctor of Philosophy

at

Dalhousie University  
Halifax, Nova Scotia  
November 2019

© Copyright by Cui Lin, 2019

# TABLE OF CONTENTS

<b>LIST OF TABLES</b> .....	<b>vii</b>
<b>LIST OF FIGURES</b> .....	<b>x</b>
<b>ABSTRACT</b> .....	<b>xiii</b>
<b>LIST OF ABBREVIATIONS AND SYMBOLS USED</b> .....	<b>xiv</b>
<b>ACKNOWLEDGEMENTS</b> .....	<b>xviii</b>
<b>CHAPTER 1 INTRODUCTION</b> .....	<b>1</b>
1.1 IMPORTANCE OF IN-SITU STRESSES IN GEOTECHNICAL, MINING AND PETROLEUM ENGINEERING .....	1
1.2 ORIGIN OF IN-SITU STRESSES IN ROCK MASSES .....	4
1.2.1 Gravitational Stresses .....	4
1.2.2 Tectonic Stresses .....	5
1.2.3 Residual Stresses and Thermal Stresses .....	5
1.3 COMPONENTS OF IN-SITU STRESSES .....	6
1.4 CURRENT MEASUREMENT METHODS OF IN-SITU STRESSES .....	7
1.5 RESEARCH OBJECTIVES .....	11
<b>CHAPTER 2 LITERATURE REVIEW IN MEASUREMENT METHODS OF IN-SITU STRESSES</b> .....	<b>14</b>
2.1 A BRIEF REVIEW OF MEASUREMENT METHODS OF IN-SITU STRESSES .....	14
2.2 OVERCORING METHODS MEASURING THE COMPLETE 3D IN-SITU STRESSES .....	17
2.2.1 Strain Cells .....	17
2.2.2 USBM Deformation Cell .....	20
2.2.3 Summary .....	21
2.3 METHODS MEASURING STRESS COMPONENTS IN A PLANE .....	22
2.3.1 Hydraulic Fracturing .....	22
2.3.2 Hydraulic Tests on Pre-existing Fractures (HTPF) .....	26
2.3.3 Borehole Slotting .....	28
2.3.4 Flat Jack .....	30
2.3.5 Back Analysis of Excavation or Drilling .....	32

2.3.6 Strain Recovery Method .....	35
2.3.7 Geophysical Methods.....	37
2.3.8 Borehole Breakout .....	38
2.3.9 Geological Observation.....	41
2.4 COMPARISON AND SUMMARY .....	43
<b>CHAPTER 3 BASIC THEORY OF DISPLACEMENT-BASED BACK ANALYSIS FOR IN-SITU STRESS DETERMINATION .....</b>	<b>47</b>
3.1 EFFECT OF DRILLING ON FIELD STRESSES .....	47
3.2 FORMULATION OF A GENERAL EQUATION FOR DEFORMATION ANALYSIS.....	50
3.2.1 Radial Displacement in a Stress Field with Equal Horizontal Stress Components.....	51
3.2.2 Radial Displacement in a Stress Field with Differential Horizontal Stress Components.....	52
3.3 BACK ANALYSIS FOR ESTIMATING THE IN-SITU STRESSES .....	53
<b>CHAPTER 4 WELL SIZE MEASUREMENT AND FUNDAMENTALS OF RESERVOIR ROCK FORMATION .....</b>	<b>55</b>
4.1 CALIPER LOGGING.....	55
4.2 ROCK FORMATION POROSITY AND PORE PRESSURE .....	58
4.3 ROCK PERMEABILITY .....	60
4.4 EFFECTIVE STRESS LAW .....	61
<b>CHAPTER 5 TWO-DIMENSIONAL BACK ANALYSIS OF WELL DEFORMATION.....</b>	<b>62</b>
5.1 STRESSES IN THE VICINITY OF A WELL IN RESERVOIR ROCK FORMATION.....	62
5.1.1 Effect of Drilling Mud Pressure .....	64
5.1.2 Effect of Permeability of Rock Formation and Well Wall .....	64
5.2 STRESSES IN THE VICINITY OF A WELL IN DIFFERENT SCENARIOS .....	67
5.2.1 An In-situ Stress Field with Differential Horizontal Stress Components .....	67
5.2.2 An In-situ Stress Field with Equal Horizontal Stress Components .....	70
5.3 MATHEMATICAL MODELS FOR 2D BACK ANALYSIS BASED ON WELL DEFORMATION .....	71
5.3.1 Relationship between Diametrical Convergence and In-situ Stresses .....	71

5.3.2 Mathematical Models in a Stress Field with Differential Horizontal Stress Components.....	76
5.3.3 Mathematical Models in a Stress Field with Equal Horizontal Stress Components.....	80
5.3.4 Summary of Various Scenarios and Mathematical Models.....	81
5.3.5 Mathematical Models Derived from Linear Poro-thermo-elastic Theory .....	82
5.4 SOLUTIONS TO THE IN-SITU STRESSES FROM CONVERGENCE MEASUREMENTS.....	84
<b>CHAPTER 6 STATISTICAL ANALYSIS FOR DETECTING ERRONEOUS DATA AND RESULT OPTIMIZATION.....</b>	<b>86</b>
6.1 INTRODUCTION .....	86
6.2 MULTIPLE LINEAR REGRESSION ON DIAMETRICAL CONVERGENCE MEASUREMENTS.....	87
6.3 LOCATING ERRONEOUS DATA.....	89
6.3.1 Locating Outliers.....	89
6.3.2 Locating High Leverage Points.....	91
6.4 MEASURING INFLUENCE OF DATA POINTS .....	91
6.5 STATISTICAL MEASURE OF REGRESSION RESULTS.....	92
6.5.1 Standard Deviation.....	93
6.5.2 Correlation Coefficient.....	93
6.5.3 Regression Significance .....	94
6.6 SUMMARY .....	95
<b>CHAPTER 7 TEST OF 2D BACK ANALYSIS AND ASSESSMENT OF MUD-PORE PRESSURE EFFECTS.....</b>	<b>98</b>
7.1 TEST CONDITION.....	98
7.2 AUTOMATED 2D CALCULATION.....	98
7.3 INPUT PARAMETERS OF TEST EXAMPLE.....	102
7.4 ANALYSIS AND RESULTS.....	104
7.4.1 Stress Calculation.....	104
7.4.2 Result Optimization by Statistical Analysis.....	108
7.4.3 Brief Summary of Test of 2D Stress Calculation and Statistical Analysis ....	110
7.5 ASSESSMENT OF EFFECTS OF PORE AND MUD PRESSURE.....	110
7.5.1 Effects of Pore Pressure Distribution and Mud Pressure .....	110

7.5.2 Effects of Change of Mud Pressure .....	112
<b>CHAPTER 8 THREE-DIMENSIONAL STRESS BACK ANALYSIS FROM WELL/BOREHOLE DEFORMATION.....</b>	<b>115</b>
8.1 EXPLORING THEORETICAL MINIMUM REQUIREMENTS FOR DETERMINATION OF THE 3D COMPLETE STRESS TENSOR.....	115
8.1.1 Stress Tensor and Diametrical Convergence in One Single Well / Borehole .....	116
8.1.2 Stress Tensor and Diametrical Convergence in More Than One Well or Borehole .....	116
8.2 STRESS TRANSFORMATION IN 3D FROM A LOCAL COORDINATE SYSTEM TO A GLOBAL COORDINATE SYSTEM .....	119
8.3 MATHEMATICAL MODELS FOR 3D STRESS BACK ANALYSIS BASED ON DIAMETRICAL CONVERGENCE .....	122
8.3.1 Mathematical Models in a Stress Field with Differential Horizontal Stress Components.....	122
8.3.2 Mathematical Models in a Stress Field with Equal Horizontal Stress Components.....	125
8.4 COMBINING INFORMATION FROM DIFFERENT WELLS .....	126
8.4.1 Combining Information from Two Well Sections or Boreholes.....	127
8.4.2 Combining Information from Three Well Sections or Boreholes.....	127
8.5 SOLUTIONS TO THE IN-SITU STRESSES FROM COMBINED MEASUREMENTS .....	128
<b>CHAPTER 9 TEST OF 3D BACK ANALYSIS AND ASSESSMENT OF INFLUENCING FACTORS.....</b>	<b>130</b>
9.1 MODEL TEST CONDITIONS .....	130
9.2 CALCULATION OF IN-SITU STRESSES FROM 3D BACK-ANALYSIS .....	131
9.3 INPUT PARAMETERS OF TEST EXAMPLES.....	133
9.4 ANALYSIS AND RESULTS.....	133
9.4.1 Results from Two Well Sections / Boreholes .....	133
9.4.2 Results from Three Well Sections or Boreholes.....	135
9.4.3 Effect of Inclination Angle Interval between Measurement Sections/Planes.	140
9.4.4 Effects of Number of Measurement in a Section / Plane .....	144
9.5 OPTIMIZATION BY STATISTICAL ANALYSIS .....	149
9.6 DISCUSSION ON PRACTICAL APPLICATION.....	152

<b>CHAPTER 10 SOFTWARE DEVELOPMENT IN 2D ANALYSIS .....</b>	<b>155</b>
10.1 SOFTWARE STRUCTURE.....	155
10.2 PROCESS FLOW DESIGN .....	156
10.3 SOFTWARE TESTING .....	158
<b>CHAPTER 11 CONCLUSIONS AND RECOMMENDATIONS .....</b>	<b>162</b>
11.1 CONCLUSIONS.....	162
11.2 RECOMMENDATIONS.....	164
<b>REFERENCES.....</b>	<b>166</b>
APPENDIX A Governing Equations in Linear Elastic Theory .....	174
APPENDIX B Typical Values of Mechanical Properties for Some Rock Types.....	177
APPENDIX C Isotropic Linear Poroelastic and Thermoelastic Stress Strain Law .....	178
APPENDIX D Fundamentals of Multiple Linear Regression .....	180
APPENDIX E Some Tables for Statistical Analysis .....	182
APPENDIX F Stresses in 2D.....	186
APPENDIX G Principal Stresses and Orientations in 3D .....	187
APPENDIX H Analytical Solution to a Cubic Equation.....	192
APPENDIX I Results of Back-analyzed 3D In-situ Principal Stresses .....	195

## LIST OF TABLES

Table 1.1 Activities requiring information of the in-situ stresses in mining and petroleum engineering practices .....	1
Table 2.1 Available methods for measuring the in-situ stresses.....	16
Table 2.2 Comparison of in-situ stress measurement methods.....	44
Table 4.1 Porosity at different formation depth for typical rock materials .....	59
Table 4.2 Permeability ( $\times 10^{-3} \mu\text{m}^2$ , or md) at different depth for typical rock materials .....	60
Table 5.1 Various scenarios and mathematical models .....	82
Table 7.1 Measurement angles of the 9 measurement locations .....	103
Table 7.2 Input parameters for different scenarios .....	103
Table 7.3 Diametrical convergence data.....	104
Table 7.4 Applied and back-analyzed 2D in-situ principal stresses .....	105
Table 7.5 Diametrical convergence from applied and back-analyzed 2D in-situ stresses .....	107
Table 7.6 Hypothetic errors for scenario 3 with larger error at -35%.....	108
Table 7.7 $t$ and $d$ values during each iteration .....	109
Table 7.8 Results from WLS analysis for the diametrical convergence set of data with a larger error .....	109
Table 7.9 Some important statistical parameters from WLS analysis for the diametrical convergence set of data with a larger error .....	109
Table 9.1 Assumed 3D in-situ principal stresses .....	133
Table 9.2 Results of back-analyzed 3D in-situ principal stresses from two well sections or boreholes (the 1 <sup>st</sup> combination).....	135
Table 9.3 Results of back-analyzed 3D in-situ principal stresses from three well sections / boreholes .....	136
Table 9.4 Measurement angles $\theta$ [°] with different number of measurement .....	145
Table 9.5 Introduced random errors [%] for statistical analysis.....	149
Table 9.6 $t$ and $d$ values for model 3 in regression analysis in 3D in-situ stress determination .....	150
Table 9.7 Results of 3D in-situ principal stresses from WLS analysis.....	151
Table 9.8 Identified points with $t_{max}$ and $d_{max}$ and some important statistical parameters .....	151

Table 10.1 Same set of random errors set for different scenarios (up to 15%) .....	159
Table 10.2 Comparison of calculated stresses from the automated analysis sheets developed in Excel and the software developed using C++ for scenario 1 .....	159
Table 10.3 Comparison of calculated stresses from the automated analysis sheets developed in Excel and the software developed using C++ for scenario 2 .....	159
Table 10.4 Comparison of calculated stresses from the automated analysis sheets developed in Excel and the software developed using C++ for scenario 3 .....	160
Table 10.5 Comparison of calculated stresses from the automated analysis sheets developed in Excel and the software developed using C++ for scenario 4 .....	160
Table 10.6 Comparison of calculated stresses from the automated analysis sheets developed in Excel and the software developed using C++ for scenario 5 .....	160
Table B.1 Some mechanical properties for some common rock types.....	177
Table E.1 Upper bound for critical values for standardized residual .....	182
Table E.2 <i>F</i> critical values .....	184
Table I.1 Results of 3D back-analyzed in-situ principal stresses from two well sections or boreholes (the 2 <sup>nd</sup> combination).....	195
Table I.2 Results of 3D back-analyzed in-situ principal stresses from two well sections or boreholes (the 3 <sup>rd</sup> combination) .....	195
Table I.3 Results of $([M_{3Dcon}]_{com}^T [M_{3Dcon}]_{com})^{-1} ([M_{3Dcon}]_{com}^T [M_{3Dcon}]_{com})$ from two well sections or boreholes (the 1 <sup>st</sup> combination).....	196
Table I.4 Results of $([M_{3Dcon}]_{com}^T [M_{3Dcon}]_{com})^{-1} ([M_{3Dcon}]_{com}^T [M_{3Dcon}]_{com})$ from two well sections or boreholes (the 2 <sup>nd</sup> combination).....	196
Table I.5 Results of $([M_{3Dcon}]_{com}^T [M_{3Dcon}]_{com})^{-1} ([M_{3Dcon}]_{com}^T [M_{3Dcon}]_{com})$ from two well sections or boreholes (the 3 <sup>rd</sup> combination) .....	196
Table I.6 Random errors with 6 measurements for different maximum error.....	197
Table I.7 Random errors with different number of measurements (maximum error in input data 20%).....	198
Table I.8 Back-analyzed 3D in-situ principal stresses with various random errors in input data for scenario 1 .....	199
Table I.9 Back-analyzed 3D in-situ principal stresses with various random errors in input data for scenario 2.....	200
Table I.10 Back-analyzed 3D in-situ principal stresses with various random errors in input data for scenario 3.....	201
Table I.11 Back-analyzed 3D in-situ principal stresses with various random errors in input data for scenario 4.....	202



Table I.12 Back-analyzed 3D in-situ principal stresses with various random errors in input data for scenario 5.....	203
Table I.13 Back-analyzed 3D in-situ principal stresses with different inclination angle interval for scenario 1 .....	204
Table I.14 Back-analyzed 3D in-situ principal stresses with different inclination angle interval for scenario 2 .....	205
Table I.15 Back-analyzed 3D in-situ principal stresses with different inclination angle interval for scenario 3 .....	206
Table I.16 Back-analyzed 3D in-situ principal stresses with different inclination angle interval for scenario 4 .....	207
Table I.17 Back-analyzed 3D in-situ principal stresses with different inclination angle interval for scenario 5 .....	208
Table I.18 Back-analyzed 3D in-situ principal stresses using different number of measurements for scenario 1.....	209
Table I.19 Back-analyzed 3D in-situ principal stresses using different number of measurements for scenario 2.....	210
Table I.20 Back-analyzed 3D in-situ principal stresses using different number of measurements for scenario 3.....	211
Table I.21 Back-analyzed 3D in-situ principal stresses using different number of measurements for scenario 4.....	212
Table I.22 Back-analyzed 3D in-situ principal stresses using different number of measurements for scenario 5.....	213

## LIST OF FIGURES

Figure 1.1 Schematic diagram showing wellbore instability problems.....	2
Figure 1.2 In-situ stresses prior to any man-made or artificial disturbance.....	3
Figure 1.3 Induced stress contour in the vicinity of the well after drilling from Boundary Element simulation using Phase2 software.....	3
Figure 1.4 Three dimensional in-situ stresses underground .....	6
Figure 1.5 Outline of the research work .....	13
Figure 2.1 Sketch of typical steps for overcoring method.....	18
Figure 2.2 Strain gage configuration for each rosette viewed from axis of borehole.....	18
Figure 2.3 Strain gage orientations in borehole .....	19
Figure 2.4 The relationship between the measured strains and the 3D in-situ stresses ....	20
Figure 2.5 Diametrical deformation measurements at 0°, 60°, 120° from <i>x</i> -axis.....	21
Figure 2.6 Basic steps of hydraulic fracturing.....	23
Figure 2.7 Pressure vs. time record for hydraulic fracturing .....	23
Figure 2.8 Fracture induced in a vertical well by hydraulic fracturing method .....	24
Figure 2.9 Schematic diagram of HTPF .....	27
Figure 2.10 Cross-section view of borehole slotting set-up .....	28
Figure 2.11 Tangential stress relief next to a slot at a borehole surface from Finite Element simulation .....	29
Figure 2.12 Flat jack set-up .....	30
Figure 2.13 Record of distance between the pins in the flat jack test.....	31
Figure 2.14 Field measurement of stress changes by excavation .....	33
Figure 2.15 Relative movement measurement and convergence measurement and their calculations .....	34
Figure 2.16 Tangential stress on the borehole wall as a function of azimuth with respect to the maximum principal stress in a plane perpendicular to the borehole axis .....	39
Figure 2.17 Schematic cross-section of borehole breakout .....	39
Figure 2.18 Caliper logging tools .....	40
Figure 2.19 Drilling-induced fracture.....	40
Figure 2.20 Illustration of fault types and directions of the inferred stresses.....	42
Figure 3.1 Governing equations relating force, stress, strain and displacement.....	47
Figure 3.2 Stress change after drilling .....	48

Figure 3.3 A new state of stresses after drilling in cylindrical coordinates and in-situ stresses prior to drilling in Cartesian coordinates .....	48
Figure 3.4 Displacement-based back analysis .....	54
Figure 4.1 Schematic diagram of mechanical caliper measuring the diameter of a well .....	56
Figure 4.2 Schematic drawing of multi-arm caliper tools .....	56
Figure 4.3 Illustration of ultrasonic caliper measurement .....	57
Figure 4.4 Schematic showing rock formation with pore space in the vicinity of a drilled wellbore.....	58
Figure 4.5 Fluid flowing through the rock pore space under pressure .....	60
Figure 5.1 Factors affecting the near-wellbore stress distribution.....	63
Figure 5.2 Penetration effect of drilling mud for a non-sealing wellbore wall.....	65
Figure 5.3 An in-situ stress field with differential horizontal stress components .....	67
Figure 5.4 An in-situ stress field with equal horizontal stress components.....	70
Figure 5.5 Stress model surrounding a well.....	72
Figure 5.6 Convergence between two opposite points on the well wall.....	74
Figure 5.7 Convergence calculation model .....	75
Figure 7.1 2D in-situ stress automated analysis interface information for the second package .....	99
Figure 7.2 Programming source codes for matrix manipulation .....	101
Figure 7.3 Assumed in-situ stresses in two dimensions in the test example .....	102
Figure 7.4 Diameter measurements at different locations around the well .....	103
Figure 7.5 Comparison of diametrical convergence from applied and back-analyzed 2D in-situ stresses .....	106
Figure 7.6 Pore pressure distribution at the different measuring directions after drilling .....	111
Figure 7.7 Comparison of diametrical convergence for 5 scenarios .....	112
Figure 7.8 Effect of mud pressure on the diametrical convergence at different locations on the wellbore wall for different scenarios .....	113
Figure 8.1 Wells / boreholes used to determine the in-situ stresses from diametrical convergence measurements .....	115
Figure 8.2 Three mutually-perpendicular wells used to determine the in-situ stresses from diametrical convergence measurements .....	117

Figure 8.3 Two non-perpendicular wells / boreholes used to determine the in-situ stresses from diametrical convergence measurements.....	118
Figure 8.4 Illustration for 3D stress measurement in a directional well.....	126
Figure 9.1 Factors that may influence 3D back analysis of diametrical convergence.....	130
Figure 9.2 Interface information for the 3D in-situ stress automated analysis.....	131
Figure 9.3 Typical output (with up to 15% errors in input data).....	132
Figure 9.4 Magnitudes of the back-analyzed and applied principal stresses with various random errors in input data for all 5 scenarios. ....	137
Figure 9.5 Output errors of the back-analyzed principal stress magnitudes in comparison with the actual principal stresses versus the introduced maximum random input errors for all 5 scenarios.....	138
Figure 9.6 Orientations of the back-analyzed and applied principal stresses with various random errors in input data for all 5 scenarios. ....	139
Figure 9.7 Magnitudes of the back-analyzed and applied principal stresses with different inclination angle interval for all 5 scenarios. ....	141
Figure 9.8 Output errors of the back-analyzed principal stress magnitudes in comparison with the actual principal stresses versus inclination angle interval for all 5 scenarios... ..	142
Figure 9.9 Orientations of the back-analyzed principals stresses with different inclination angle intervals for all 5 scenarios.....	143
Figure 9.10 Magnitudes of the back-analyzed principal stresses using different number of measurements for all 5 scenarios. ....	146
Figure 9.11 Output errors of the principal stress magnitudes versus number of measurements for all 5 scenarios. ....	147
Figure 9.12 Orientations of the back-analyzed principal stresses using different number of measurements for all 5 scenarios. ....	148
Figure 10.1 Input data file.....	155
Figure 10.2 Output data file.....	156
Figure 10.3 Graphical interface .....	156
Figure 10.4 Screenshot of some source codes written in Dev C++ compiler.....	157
Figure 10.5 Basic flow chart in programming.....	158
Figure F.1 2D stress definition and stress in an arbitrary direction.....	186
Figure G.1 3D stress definition and stress in an arbitrary plane.....	187
Figure G.2 Principal stress orientation.....	189

## **ABSTRACT**

In-situ stress state in underground plays a significant role in planning, design, ground support, well drilling and wellbore stability control. The overcoring method with strain gauges on borehole wall is the only method for determining the complete 3D stresses. However, this method requires physical access and cannot be applied to petroleum engineering. The purpose of this research is to develop a practical back-analysis method using measured borehole deformation to determine a) the 2D in-situ stresses in the plane perpendicular to the borehole as an alternative method, and b) most importantly the complete 3D in-situ stresses for use in petroleum and other rock engineering.

The difficulty in determining the 3D stresses from 2D borehole deformation measurement is overcome with differential-direction drilling. This requires diametrical convergence measurement in three non-parallel planes as a minimum. For petroleum application, this can be achieved by measurements in three different sections of a directional well with a total inclination angle interval between the measurement planes at least  $35^\circ$ . The three sets of measured convergence are combined through comprehensive coordinate and direction relationships. Conditions in petroleum fields are also considered and a total of five comprehensive models are developed based on permeability, pore and mud pressure in both 2D and 3D analyses. In addition, statistical approaches are applied to help detect erroneous data and search for the best-fit solution.

To facilitate calculation, automated analysis packages based on excel have been developed for different scenarios in both 2D and 3D analyses. A standalone software for 2D analysis is also developed. The developed method has been verified using simulated measurement data. The results show that the back-analyzed stresses agree well with the applied stresses when input errors are small. Even with up to 30% input errors, the result converges to the real solution with smaller difference between the back-analyzed stresses and the real solution. This demonstrates the accuracy and reliability of the solutions, and confirms the validity of the developed method and the analysis procedure.

## LIST OF ABBREVIATIONS AND SYMBOLS USED

Below is the list of abbreviations and symbols used in this thesis.

### Abbreviations

HTPF	Hydraulic tests on pre-existing fractures
DIF	Drilling induced fractures
ASR	Anelastic strain recovery
DSCA	Differential strain curve analysis
USBM	US Bureau of Mine cell
Std	Standard deviation
OLS	Ordinary least square
WLS	Weighted least square

### Symbols

$\sigma$	Normal stress
$\sigma_r, \sigma_\theta, \sigma_{zz}$	Normal stress in the $r, \theta, z$ directions
$\sigma_x, \sigma_y, \sigma_z$	Normal stress in the $x, y, z$ directions
$\tau$	Shear stress
$\tau_{r\theta}$	Shear stress in the $\theta$ - $r$ plane
$\tau_{\theta z}$	Shear stress in the $\theta$ - $z$ plane
$\tau_{rz}$	Shear stress in the $r$ - $z$ plane
$\tau_{xy}$	Shear stress in the $x$ - $y$ plane
$\tau_{yz}$	Shear stress in the $y$ - $z$ plane
$\tau_{zx}$	Shear stress in the $x$ - $z$ plane
$\varepsilon$	Strain
$\varepsilon_r, \varepsilon_\theta, \varepsilon_{zz}$	Normal strain in the $r, \theta, z$ directions
$\varepsilon_{max}$	Maximum strain in a plane
$\varepsilon_{min}$	Minimum strain in a plane
$\gamma_{r\theta}, \gamma_{\theta z}, \gamma_{rz}$	Shear strains
$u$	Displacement vector

$u_r, u_\theta, u_{zz}$	Displacement in the $r, \theta, z$ directions
$u_x, u_y$	Displacement in the $x, y$ directions
$u_{con}$	Convergence displacement
$u_d$	Diametrical convergence
$\sigma_o$	In-situ stresses, field stresses
$\sigma_{Hmax}$	Maximum horizontal in-situ principal stress
$\sigma_{Hmin}$	Minimum horizontal in-situ principal stress
$\sigma_{max}$	Maximum in-situ principal stress in a plane
$\sigma_{min}$	Minimum in-situ principal stress in a plane
$\sigma_1, \sigma_2, \sigma_3$	Maximum, intermediate and minimum principal stresses in 3D, respectively
$I_1, I_2, I_3$	Stress invariants
$\lambda_p, \delta_p$	Trend and plunge of 3D principal stress
$\rho$	Density of rock mass
$\gamma$	Average volume weight
$g$	Gravity constant (9.81 N/kg)
$h$	Depth below surface
$E$	Young's modulus
$\nu$	Poisson's ratio
$\nu_u$	Undrained Poisson's ratio
$\lambda$	Lamé's elastic constant
$G$	Shear modulus, modulus of rigidity
$\varphi$	Porosity
$k$	Permeability
$\alpha$	Biot's coefficient
$s$	Skempton's coefficient
$r_o$	Radius of borehole (well)
$r$	Distance from the well axis to a point in the rock mass
$\theta$	Azimuth angle relative to the $x$ -axis in the $xy$ plane perpendicular to borehole axis $z$ , measured from the $x$ axis counter clockwise
$\theta'$	Azimuth angle relative to the maximum principal stress direction counter clockwise

$\delta_{Hmax}$	Direction of maximum horizontal principal stress with respect to $x$ axis in a plane perpendicular to the well / borehole axis
$\eta$	Angle between the measurement line and the reference direction – $x$ axis
$\xi$	Strain gage orientation
$\zeta$	Angle from slot
$[M]$	Coefficient matrix
$[M_{con}]$	Convergence coefficient matrix
$M_m$	Coefficient for mud pressure
$M_p$	Coefficient for pore pressure
$[T]$	Transformation matrix
$p_m$	Mud pressure
$p_p$	Pore pressure
$\alpha_T$	Coefficient of linear thermal expansion
$T$	Temperature in a well
$T_o$	Temperature under initial condition
$I$	Inclination angle of a well, measured from vertical direction, positive in the counter-clockwise direction
$\beta$	Bearing angle of a well, angle between $y$ axis (N) and the projection line of $oy'$ in $oxy$ plane, positive in the clockwise direction
$n$	Total measurement number
$m$	Unknown parameter number, number of freedom degree
$R$	Ordinary residual
$S_{min}$	Minimum sum of squares
$t$	Standardized residual
$t_{max}$	Maximum standardized residual value
$t_o$	Critical standardized residual at a given confidence level
$d$	Influence measure parameter
$d_{max}$	Maximum value of influence measure parameter
$h_{ii}$	The $i$ th diagonal elements of hat matrix $[H]$
$r_c$	Correlation coefficient
$F$	Regression significant quantity



$F_o$	Critical regression significant quantity at a given significance level
$T_s$	Tensile strength
$p_{c1}$	Fracture initiation pressure
$p_s$	Shut-in pressure
$p_r$	Reopening pressure

## **ACKNOWLEDGEMENTS**

I would like to express my gratitude to my supervisor Prof. Steve D.H. Zou for his continuous support, guidance and encouragement during my Ph.D. study, research and writing of this thesis. His immense knowledge and insightful ideas helped me to widen my research perspective and overcome the obstacles I have been facing through my research.

I would like to thank the rest of my supervisory committee, Prof. Dmitry Garagash and Prof. George Jarjoura, for their constructive suggestions and comments, which were very helpful for my research work. I would also like to thank the external examiner Prof. Hani Mitri for reading this thesis and giving valuable input.

I am grateful to master student Haoran Sun, undergraduate students Nikrooz Naserifard and Nazanin Omrani-Moghaddam, for providing assistance in computer programming.

Finally, I want to appreciate financial support provided by NS Graduate Scholarship and G.G. Meyerhof Graduate Fellowship, and my family for their support and encouragement to complete this research .

# CHAPTER 1 INTRODUCTION

## 1.1 IMPORTANCE OF IN-SITU STRESSES IN GEOTECHNICAL, MINING AND PETROLEUM ENGINEERING

In-situ stress state is of great interest in geotechnical, mining and petroleum engineering. It is one of the most basic parameters in underground engineering projects (Amadei and Stephansson 1997). Table 1.1 lists the activities that require the information of the in-situ stresses in mining and petroleum engineering.

**Table 1.1** Activities requiring information of the in-situ stresses in mining and petroleum engineering practices

Field	Mining engineering	Petroleum engineering
Activities	<ul style="list-style-type: none"> <li>• Stability analysis and failure prevention of underground opening</li> <li>• Design of opening shape and geometry</li> <li>• Determination of excavation methods, sequence and orientation</li> <li>• Design of mine layouts</li> <li>• Prediction and prevention of rock bursts</li> <li>• Selection of support systems</li> </ul>	<ul style="list-style-type: none"> <li>• Forecasting and control of wellbore stability</li> <li>• Well planning</li> <li>• Improvement of well drilling safety</li> <li>• Selection of casing</li> <li>• Management of reservoir production</li> </ul>

In mining engineering, the in-situ stress field is disturbed when an underground opening is created. It affects the distribution and magnitude of the induced stresses around underground openings. If the induced stresses are large enough to exceed the strength of the rock mass, this may cause rock failure. The in-situ stresses also influence the opening geometry, opening shape, excavation sequence and orientation of underground excavations. Accordingly, the in-situ stress field is vital in helping underground excavation, mine design, support system selection and rock failure prevention.

The same is in petroleum engineering. Wells drilled into the rock mass are the only accesses developed to reach an oil and gas reservoir in underground porous rock structure which oil and gas have accumulated within. Wellbore stability during drilling and production activities is of major concern to petroleum engineers. The instability issues, such as wellbore collapse, fracturing, lost circulation, stuck pipe, etc., may endanger the whole drilling process and production operations, as shown in Figure 1.1, which may result in time and economic losses (Afsari et al 2010, Aadnøy and Looyeh 2011). Therefore, maintaining a stable wellbore is of great importance during drilling and production of oil and gas wells.

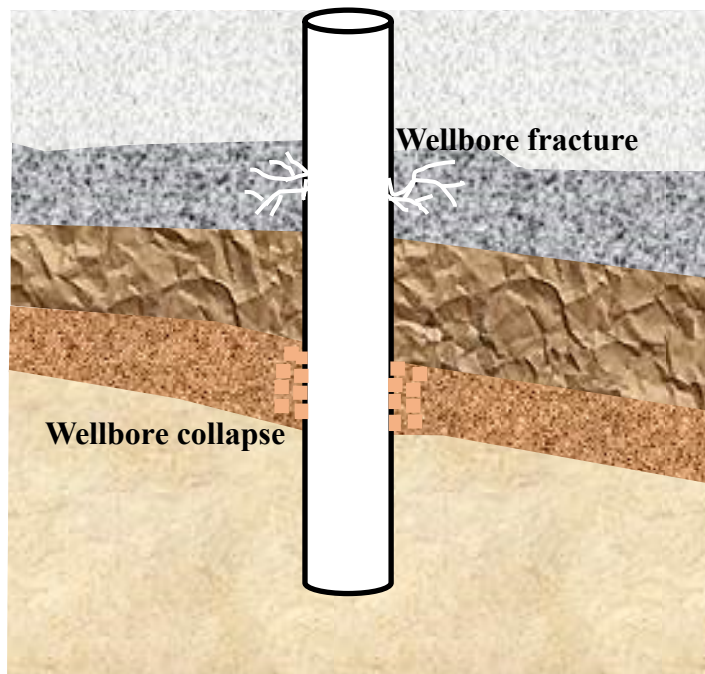


**Figure 1.1** Schematic diagram showing wellbore instability problems

Wellbore instability is primarily an indication of how rocks respond to the induced stress concentration around the wellbore. Before a well is drilled, subsurface rocks are under a balanced stress condition. Once a well is drilled into a formation, drilling disturbs the stress field in surrounding area of the well since the stressed solid material is removed. A stress redistribution will occur in the vicinity of the well. The in-situ stresses (far-field stresses, Figure 1.2) will be redistributed around the wellbore (new stress state, Figure 1.3). If this new stress state exceeds the rock strength, it may lead to well failure. Hence in-situ stresses are among the key factors that affect stress concentrations along wellbore wall. They play

significant roles in well planning, drilling and wellbore stability control. In-situ stresses are essential for the development of an oil and gas reservoir and reliable estimate of the in-situ stresses has been a dream for many people in petroleum industry.

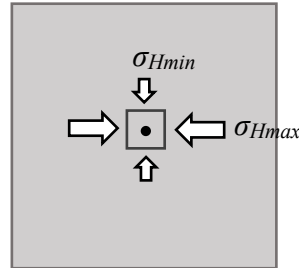
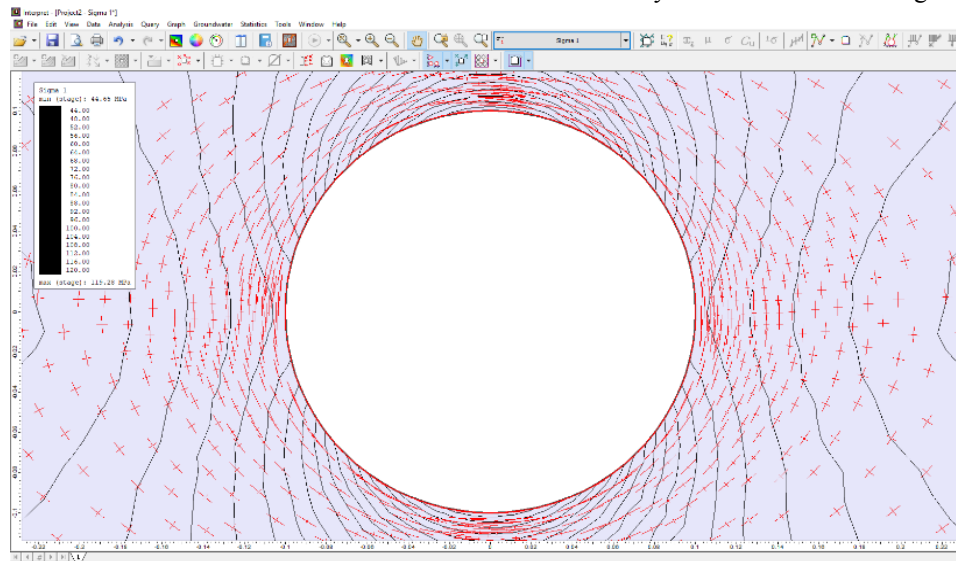
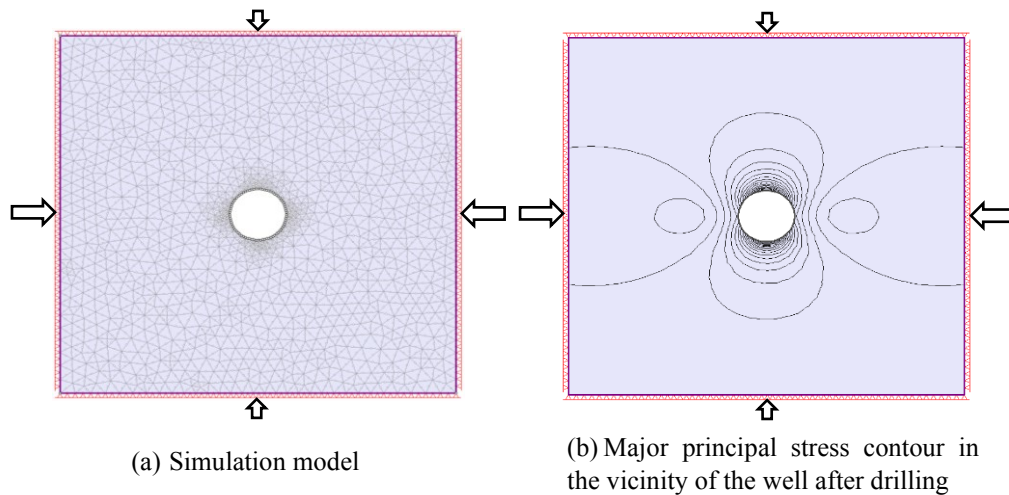


**Figure 1.2** In-situ stresses prior to any man-made or artificial disturbance



**(c)** Change of principal stress directions due to drilling (magnified image)

**Figure 1.3** Induced stress contour in the vicinity of the well after drilling from Boundary Element simulation using Phase2 software ( $\sigma_{Hmax} = 54.50$  MPa,  $\sigma_{Hmin} = 40.0$  MPa,  $E=20$  GPa,  $\nu=0.19$ )

## 1.2 ORIGIN OF IN-SITU STRESSES IN ROCK MASSES

Rock is the material in the surface layer of the Earth. Rock masses in the Earth's crust are initially stressed in their natural state. These natural stresses are “in-situ stresses” or “field stresses”. They can be understood as compressional force acting on the rock in a certain underground depth.

The in-situ stresses are related to the weight of the overlying strata and the geological history of the rock mass. They comprise gravitational stresses, tectonic stresses, residual stresses, and thermal stresses, etc. Among them, gravitational stresses and tectonic stresses are the two principal contributing sources to the in-situ stresses.

### 1.2.1 Gravitational Stresses

Gravitational stress is caused by the Earth's gravity field and governed by the weight of the overlying strata (overburden) (Zang and Stephansson 2010). It increases with depth in the earth's crust. Generally, when calculating it, the rock mass surrounding the calculating point is assumed to be a homogeneous, isotropic and continuous body. In this scenario, the vertical component of gravitational stress in the rock mass is proportional to the average rock density and the depth below the ground surface.

$$\sigma_z = \gamma h = \rho g h \quad (1.1)$$

where  $\gamma$  is the average volume weight in  $\text{kN/m}^3$ ,  $\rho$  is the average density of the rock mass in  $\text{kg/m}^3$ ,  $g$  is equal to  $9.8 \text{ N/kg}$  and  $h$  is the depth in m.

If the rock density is variable  $\rho(h)$ , the vertical component of gravitational stress is computed by

$$\sigma_z = g \int_0^h \rho(h) dh \quad (1.2)$$

### **1.2.2 Tectonic Stresses**

Tectonic stresses result from a pervasive force field imposed by movements in the earth's crust occurring continuously. Driving forces for the plate movement come from the mantle of the earth, which moves due to heat differences between the core of the earth and the cooler crust (Herget 1988). In the development history of earth, many tectonic movements have ever occurred. During the acute period of each tectonic movement, folds, faults, joints, cleavage, etc. formed, which is called mountain-making movement. During the relaxation period of each tectonic movement, some strata are ascending or descending slowly. This is epeirogeny movement.

According to the scale of tectonic stress field, it can be divided into global tectonic stress field and local tectonic stress field (Heidbach et al 2007). The global tectonic stress is induced by the relative displacement of tectonic plates. The local tectonic stress field contains isostasy and active faults.

### **1.2.3 Residual Stresses and Thermal Stresses**

Residual stresses are “locked-in” stresses associated with the previous history of the rock (Jaeger and Cook 1976, Holzhausen and Johnson 1979). They can develop in rock if there are local phase transformations, inelastic strains, or differences in thermal or elastic properties. Such stresses are self-equilibrating stresses and known to exist, both on a small and a large scale.

Thermal stresses are due to heating or cooling of rock. A typical linear coefficient of thermal expansion is given for sandstone as  $10.8 \times 10^{-8}$  m per  $1^\circ\text{C}$  change of temperature (Herget 1988). In tectonic activity area, thermal stresses exist around the area of inrush of magma.

### 1.3 COMPONENTS OF IN-SITU STRESSES

At a depth of  $h$  below the ground surface, the pre-existing stress state is in three dimensions (3D), forming a stress field (Zou 2015). The state of stress at a point within a rock mass can, in general, be represented by the nine different stress components defined in an  $x, y, z$  coordinate system, as shown in Figure 1.4. These components can be grouped into two categories: (1) normal stresses,  $\sigma_x, \sigma_y$  and  $\sigma_z$ , and (2) shear stresses,  $\tau_{xy}, \tau_{yx}, \tau_{yz}, \tau_{zy}, \tau_{xz}$  and  $\tau_{zx}$ . In this research work, compressive stresses are usually defined as positive entities and tensile stresses as negative.

The nine stress components can be assembled into a  $3 \times 3$  matrix known as the stress tensor (Fjar et al 2008). Normal stresses are on the diagonal and shear stresses are off the diagonal.

$$[\sigma_o] = \begin{bmatrix} \sigma_x & \tau_{xy} & \tau_{xz} \\ \tau_{yx} & \sigma_y & \tau_{yz} \\ \tau_{zx} & \tau_{zy} & \sigma_z \end{bmatrix} \quad (1.3)$$

where  $[\sigma_o]$  is the in-situ stress tensor.

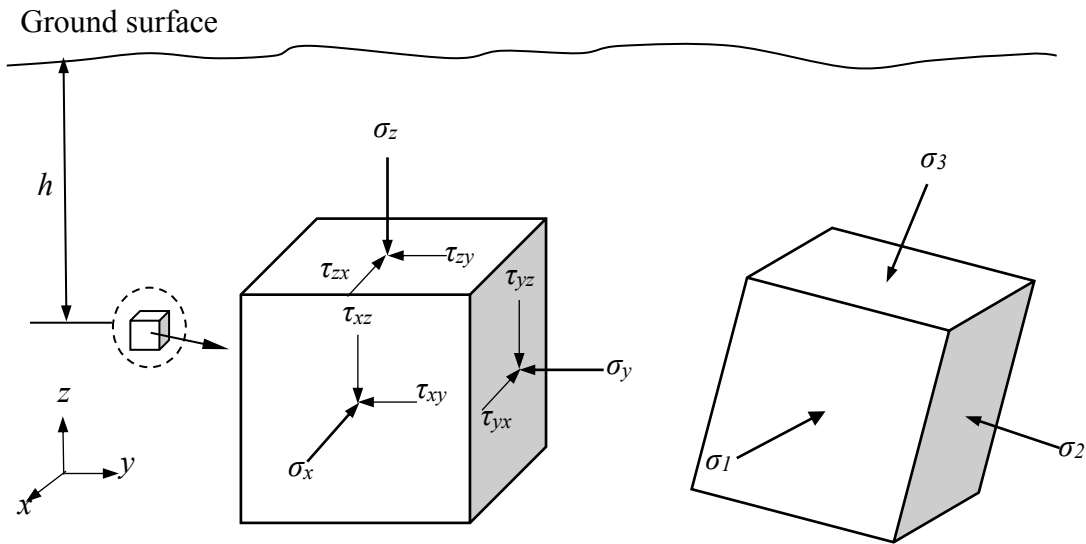


Figure 1.4 Three dimensional in-situ stresses underground

From equilibrium principles:

$$\tau_{xy} = \tau_{yx}, \tau_{yz} = \tau_{zy}, \tau_{xz} = \tau_{zx} \quad (1.4)$$



Thus this 3D stress field has six independent stress components  $\{\sigma_x, \sigma_y, \sigma_z, \tau_{xy}, \tau_{yz}, \tau_{zx}\}$  in terms of the  $x, y, z$  axes. The stress state can be completely described by these six independent components.

It is always possible to find a particular orientation of the coordinate axes for which all shear stresses are zero, the stresses are purely normal and called principal stresses. In 3D, there are three principal stresses, which are perpendicular to each other. They are customarily denoted by the symbols  $\sigma_1, \sigma_2$  and  $\sigma_3$  (Hoek and Brown 1990). By convention,  $\sigma_1$  is chosen for the major principal stress,  $\sigma_2$  is chosen for the intermediate principal stress, and  $\sigma_3$  is for minor principal stress.

$$\sigma_1 \geq \sigma_2 \geq \sigma_3 \quad (1.5)$$

The stress state at a point in the rock mass can also be presented in terms of the principal stresses, which can also be expressed in the form of matrix

$$[\sigma_o] = \begin{bmatrix} \sigma_1 & 0 & 0 \\ 0 & \sigma_2 & 0 \\ 0 & 0 & \sigma_3 \end{bmatrix} \quad (1.6)$$

and their directions, called principal directions.

#### 1.4 CURRENT MEASUREMENT METHODS OF IN-SITU STRESSES

The existing methods for measuring the in-situ stresses include overcoring, borehole slotting, hydraulic fracturing, hydraulic tests on pre-existing fractures (HTPF), flat jack, back analysis of excavation or drilling, strain recovery, borehole breakout, geological observation and geophysical methods, etc. (Amadei and Stephansson 1997, Stacey and Wesseloo 2002, Lin et al 2019).

##### a) Overcoring

The stresses around a borehole are totally relieved by overcoring. The strains or displacements created by the relief process are monitored and measured in boreholes or on the surrounding rock. Based on the elastic behavior of rock materials, the in-situ stresses

can be calculated from the measurements of strain or deformation. There are two commonly-used types of measurement devices, CSIR or CSIRO triaxial strain cells and USBM deformation cells. For the CSIR or CSIRO cells, three strain rosettes, each carrying three or four strain gauges, are used to obtain nine or twelve measurements, therefore providing nine or twelve independent equations for the solution of the in-situ stress components in 3D from a single drilled hole. USBM cells measures the deformation in one plane perpendicular to the borehole axis, by which the 2D in-situ stresses are determined.

b) Hydraulic fracturing and mini-frac test

With these methods, fractures are developed through pumping fluid (usually water) into a borehole and the fluid pressure is applied along a section of the borehole isolated by packers in a series of pressurization cycles. The pressure values which are required to generate, propagate, sustain, and reopen fractures in the test section are recorded (Goodman 1989, Fjar et al 2008, Sarwade et al 2009) and orientation of the hydraulically induced or opened fractures is observed. They can be used to determine the magnitudes and directions of the in-situ principal stresses, in two dimensions, in the plane perpendicular to the borehole. This kind of methods has been widely used in petroleum industry and it is presently the only method which allows the determination of ground stresses in deep wells.

c) Hydraulic tests on pre-existing fractures (HTPF)

HTPF makes use of pre-existing fractures surrounding a borehole and reopens them by pumping the liquid into the borehole. The average normal stress acting perpendicular to the plane of the pre-existing fracture is determined and a sufficient number of fractures with varying dip and strike are needed to estimate the in-situ stresses in the plane perpendicular to the borehole axis.

d) Borehole slotting

The stresses are relieved locally by cutting slots into the borehole wall. The strain relief adjacent to the slots is then measured. Measurements from at least three slots in one borehole are necessary to determine the 2D in-situ stresses in the plane normal to the axis of the borehole.

e) Flat jack

The equilibrium of a rock mass is disturbed by cutting slots on a rock surface, which in turn creates deformation. If a jack is inserted into the slot and pressurized until all deformation has vanished. The cancellation pressure is used as a direct estimate of the magnitude of stress normal to the plane of the slot. This test only yields one component of the 2D in situ stresses on the rock surface, that is, in the plane normal to the jack.

f) Back analysis of excavation or drilling

Back analysis of measured strain changes or displacements induced by excavation or drilling is currently applied to evaluate the 2D in-situ stresses in the plane perpendicular to borehole axis. It partially relieves the stresses around a measurement device and does not require overcoring. It is possible to assess the six components of the stress tensor. However the procedure to determine the complete 3D stresses is complex.

g) Geophysical methods, strain recovery, borehole breakout and geological observation

There are some other approaches, such as geophysical methods, strain recovery, borehole breakout and observation from geological features, etc. Geophysical methods relate some physical property parameters of rock formation obtained from well logging to magnitudes and directions of the maximum and minimum horizontal stresses. Strain recovery method is based on monitoring the response of core samples following drilling. Upon relief from an in-situ stress field, core samples tend to expand most in the direction of maximum stress relief and least in the direction of minimum stress relief. Borehole breakout is a method to identify the direction of the minimum stress in the plane perpendicular to a borehole axis by observation of stress induced failure, such as spalling or sloughing of material from the borehole wall. There is a close correlation between the geological structures and the directions of the principal in-situ stresses, which is possible to infer the directions of maximum and minimum horizontal principal stresses from geological observations. These methods typically give the indication of principal stress directions.

The detailed overview of the above methods for measurement and estimation of in-situ stresses will be presented in Chapter 2.

#### 1) Methods for estimation of the 3D in-situ stresses

Methods that measure borehole strains during overcoring appear most common and are the only methods for the complete 3D stresses. They are widely used in geotechnical and mining engineering. However they require physical access to the location where stresses are to be measured and allowance of complete stress relief by overcoring. Thus, they are not suitable for application in small deep wells, that is, in petroleum engineering field.

#### 2) Methods for estimation of the 2D in-situ stresses

Other measurement methods generally provide results of the orientations and/or magnitudes of some components of the in-situ stresses, mostly the maximum and the minimum stresses in the plane perpendicular to a borehole. In some methods the vertical stress is assumed as a principal stress.

- Borehole slotting is employed to determine the 2D stresses in the plane perpendicular to the borehole axis. Flat jack measures the average excavation-induced stress perpendicular to the jack plane within the range of the cutting depth. They also require physical access to the location where stresses are to be measured. Therefore, they are also not suitable for application in deep wells and cannot be directly applied to petroleum industry because the very limited physical access via a well does not allow overcoring, cutting the slots or completely stress relief around a device in the ground.
- Although a couple of methods are available for measuring the orientations and magnitudes of some components of the in-situ stresses in petroleum engineering, they are limited to specific directions and 2D dimensions. For example, hydraulic fracturing, HTPF, and mini-frac tests are able to evaluate the magnitudes and orientations of 2D field stresses in the plane perpendicular to a well. Strain recovery, geophysical and geological methods normally determine the orientations of the maximum and minimum horizontal stresses and assumes the vertical stress component as a principal stress. The results of stress from geological methods are historical and may not be the current state. Borehole breakout can obtain the orientations of maximum and minimum

principal stresses perpendicular to the borehole axis. Back analysis is currently used to determine the 2D in-situ stresses in the plane perpendicular to the borehole axis in mining, geotechnical and petroleum engineering. It has showed potential to determine the complete 3D stresses. Therefore, at present, no method is available to determine the complete 3D in-situ stresses around a well in petroleum industry.

## **1.5 RESEARCH OBJECTIVES**

The purpose of this research is to develop a practical method for estimation of the 2D and 3D in-situ stresses.

The idea is to use well / borehole diametrical convergence as input data and conduct comprehensive analysis of the measured data to correlate to the in-situ stresses, thereby to provide the best estimate of the in-situ stresses. This requires comprehensive mathematical formulation and detailed back-analysis.

- 1) Two-dimensional back analysis of well deformation as an alternative to existing methods
  - The effects of permeability of well wall and rock formation, mud pressure and pore pressure on the stresses in the vicinity of a well need to be analyzed.
  - With consideration of these factors, the relationship between the well deformation and the in-situ stresses needs to be established.
  - The mathematical models for 2D back analysis based on well deformation will be developed considering different well wall and rock formation conditions.
  - Statistical methods will be implemented for detecting erroneous data and results optimization, whereby to decrease the effects of errors in measurement data and improve back analysis results.
  - This 2D back analysis method will be tested using simulated measurement data.

- 2) Three-dimensional back analysis of well / borehole deformation for use in petroleum engineering as well as in mining and geotechnical engineering
- The minimum requirement for estimation of the in-situ stresses in complete three dimensions (3D) will be explored.
  - The relationship between the well / borehole deformation and the 3D stress tensor will be formulated by combining the information from all wells / boreholes required to solve for all six stress components.
  - The mathematical models for estimating the in-situ stresses in 3D in a rock mass taking into account different applications will be developed.
  - This 3D back analysis method will be tested and assessed using simulated measurement data.
  - The following influencing factors affecting the solutions of the back-analyzed 3D in-situ stresses will be discussed:
    - Number of well sections / boreholes;
    - Errors in input of diametrical convergence;
    - Inclination angle interval between measurement sections /planes;
    - Number of measurements in a section / plane.
- 3) Automated calculation & analysis
- Automated analysis packages need to be developed to integrate the back analysis and show results. It is expected to perform automatic calculation, display the measured data on screen and accurate results.

A flow chart outlining the research is shown in Figure 1.5.

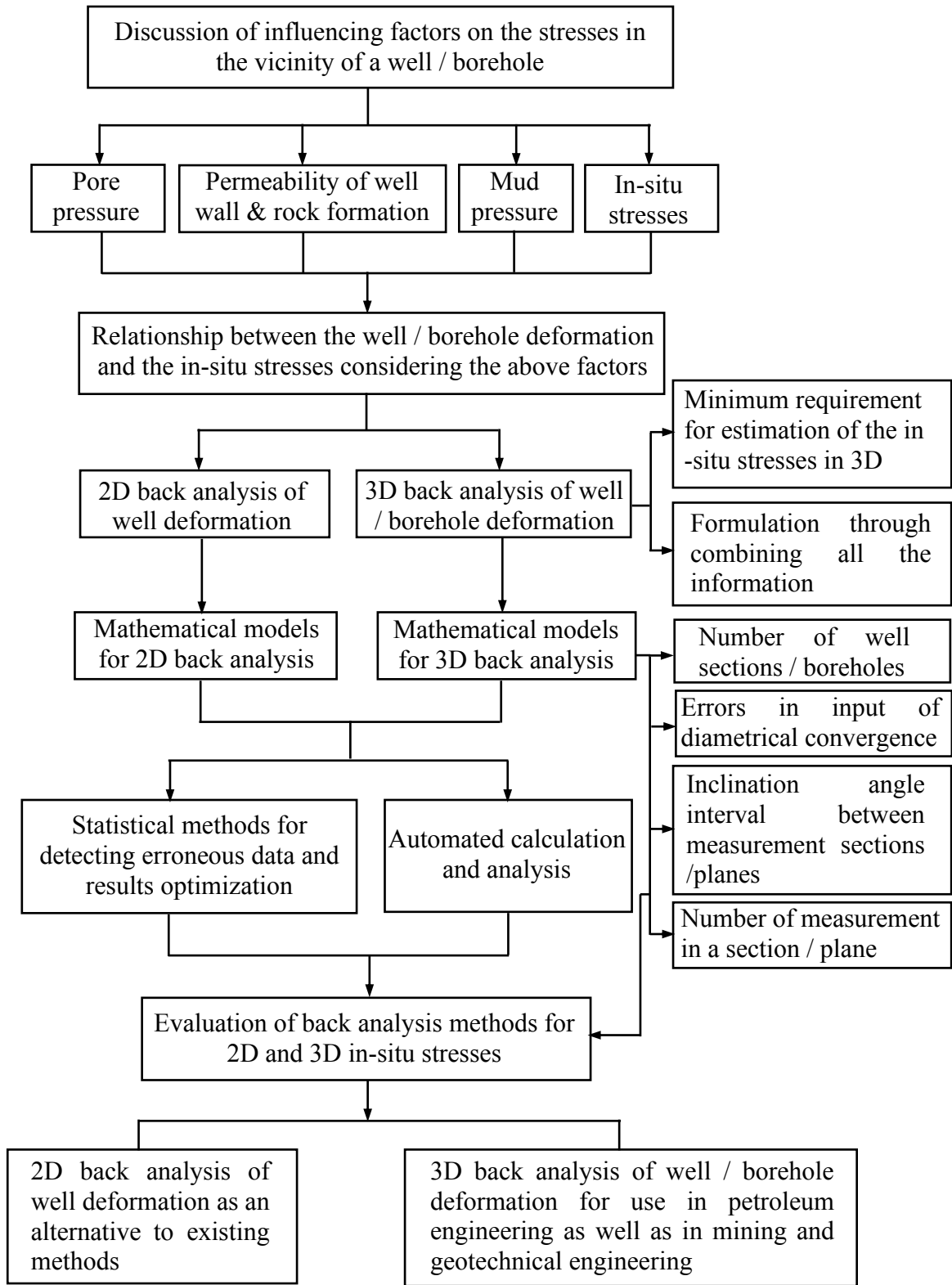


Figure 1.5 Outline of the research work

## **CHAPTER 2 LITERATURE REVIEW IN MEASUREMENT METHODS OF IN-SITU STRESSES**

### **2.1 A BRIEF REVIEW OF MEASUREMENT METHODS OF IN-SITU STRESSES**

As discussed in Chapter 1, the magnitudes and orientations of the underground in-situ stresses are of general concern in mining and petroleum industries. They are impacted by several factors including the weight of overlying materials, geologic structures (on local and regional scales), tectonic forces within the earth's crust, residual stress and thermal stress. The complexity of the relations between these factors and the in-situ stress usually affects reliable estimation of the in-situ stresses. Moreover, compared with rock mass properties, the state of in-situ stresses in a rock mass is difficult to measure. They cannot be measured directly. All stress measurement techniques need to disrupt the rock to create a response that can then be measured and analyzed (Goodman 1989). The response is in the form of strain, displacement or hydraulic pressure record and several assumptions about the rock's constitutive behavior are made. The in-situ stresses are inferred from these responses.

The methods for measuring and estimating the in-situ stresses can be divided into the following main groups (Wang 2014, Lin et al 2019):

- Borehole-based methods

A borehole is created in a rock mass and the response surrounding the borehole is measured induced by excavation or drilling itself, or by completely relieving the stresses, or by pumping the liquid.

- Drill core-based methods

Some methods are for measuring the in-situ stresses based on the rock property of stress memory. Rock, in situ, tends to develop a “memory” of the stress field under which it has been confined (Stacey and Wesseloo 2002). When a rock sample is removed from underground, namely, its confining environment, it will react to its



unloading, which is related to the original confining stress field. This type of method is to monitor the response of core samples following drilling for the interpretation of stress “memory” in the rock.

- Methods performed on rock surfaces

If there is an access to a rock face, stress can be measured using these methods. The jacking method is one of methods performed on the rock surface. A slot (planar or circular) on a rock surface is cut to disturb the equilibrium of a rock mass. Reference pins or strain gages placed in the near vicinity of the slot are employed to measure deformation as a result of slot cutting. Then a device such as a jack is inserted into the slot and pressurized until the deformation has vanished. The original stress normal to the plane of the slot is determined from this cancellation pressure required to null the deformation.

- Geophysical and geological observation methods

There are two other types of methods based on different principles (Goodman 1989).

- a) Methods depending upon the relationship between principal stress direction and different types of geological structures, such as fault, dike, folds, and earthquake focal;
- b) Methods considering correlation between stress and physical properties, including borehole acoustic logging, seismic method, etc.

The major methods in these groups are summarized in Table 2.1.

Next, the commonly used methods for the in-situ stress measurement are introduced and reviewed in detail. The basic principles, advantages and disadvantages of these methods are discussed and compared.

**Table 2.1** Available methods for measuring the in-situ stresses

Group	Basic principle	Commonly used methods
Borehole-based	Complete stress relief (linear elastic stage)	<ul style="list-style-type: none"> <li>– Overcoring with strain cells</li> <li>– Overcoring with deformation cells</li> <li>– Borehole slotting</li> </ul>
	Rock fracture (failure)	<ul style="list-style-type: none"> <li>– Hydraulic fracturing</li> <li>– Hydraulic tests on pre-existing fractures (HTPF)</li> <li>– Mini-frac</li> </ul>
	Stress induced compressive failure	<ul style="list-style-type: none"> <li>– Borehole breakout method</li> </ul>
	Stress induced tensile failure	<ul style="list-style-type: none"> <li>– Drilling induced fractures (DIF)</li> </ul>
	Back analysis of excavation or drilling (linear elastic stage)	<ul style="list-style-type: none"> <li>– Back analysis of excavation or drilling with strain cells</li> <li>– Back analysis of excavation or drilling with deformation measurement instruments</li> </ul>
Drill core-based	Strain recovery	<ul style="list-style-type: none"> <li>– Anelastic strain recovery (ASR)</li> <li>– Differential strain curve analysis (DSCA)</li> </ul>
Methods performed on rock surfaces	Partial stress relief	<ul style="list-style-type: none"> <li>– Jacking method</li> </ul>
Geophysical methods	Correlation between geophysical logging parameters of rock formation (rock properties) and the stresses	<ul style="list-style-type: none"> <li>– Borehole acoustic logging</li> <li>– Seismic survey</li> </ul>
Geological observation methods	Relationship between the principal stress directions and geological features	<ul style="list-style-type: none"> <li>– Fault slip data analysis</li> <li>– Earthquake focal mechanisms</li> </ul>

## **2.2 OVERCORING METHODS MEASURING THE COMPLETE 3D IN-SITU STRESSES**

Overcoring method is used to estimate the complete 3D stresses underground, particularly in mining and geotechnical engineering. In this case, strains around a borehole during overcoring, which provide complete stress relief, are measured and analyzed. This method requires physical access to the location where stresses are to be measured and allowance of complete stress relief by overcoring.

With the overcoring method, a larger-diameter borehole is drilled in the rock mass to the desired depth where stresses are to be determined. Then a small concentric pilot hole is advanced from the bottom of the borehole. A measurement instrument (stress cell or deformation cell) is installed in the pilot hole. Subsequently the larger borehole is extended by overcoring, completely relieving stresses around the cell within the cylinder of rock. The changes in strains around the borehole wall or diametric deformation across the borehole are simultaneously recorded. Based on the measured strains or displacements, the in-situ stress components acting on the overcored rocks can be calculated by using formula derived from the theory of linear elasticity for continuous, homogenous and isotropic rocks (Fairhurst 2003). Figure 2.1 demonstrates the typical steps of overcoring method and the cross-section view of stress measurement by overcoring.

### **2.2.1 Strain Cells**

There are typically two kinds of measuring instruments for strain changes, CSIR cell and CSIRO cell. A major advantage using these cells is that they allow the 3D state of stress to be determined from one single borehole. The CSIR triaxial strain cell contains three rosettes of strain gauges at 120° apart. In each rosette, four electric wire resistance strain gauges are glued onto the wall of the borehole in different directions (Vreede 1981), as demonstrated in Figure 2.2. The CSIRO cell has similar configuration as the CSIR cell. It also consists of three rosettes 120° apart, each of which has three- or four-component strain gauges (Sarwade et al 2009).

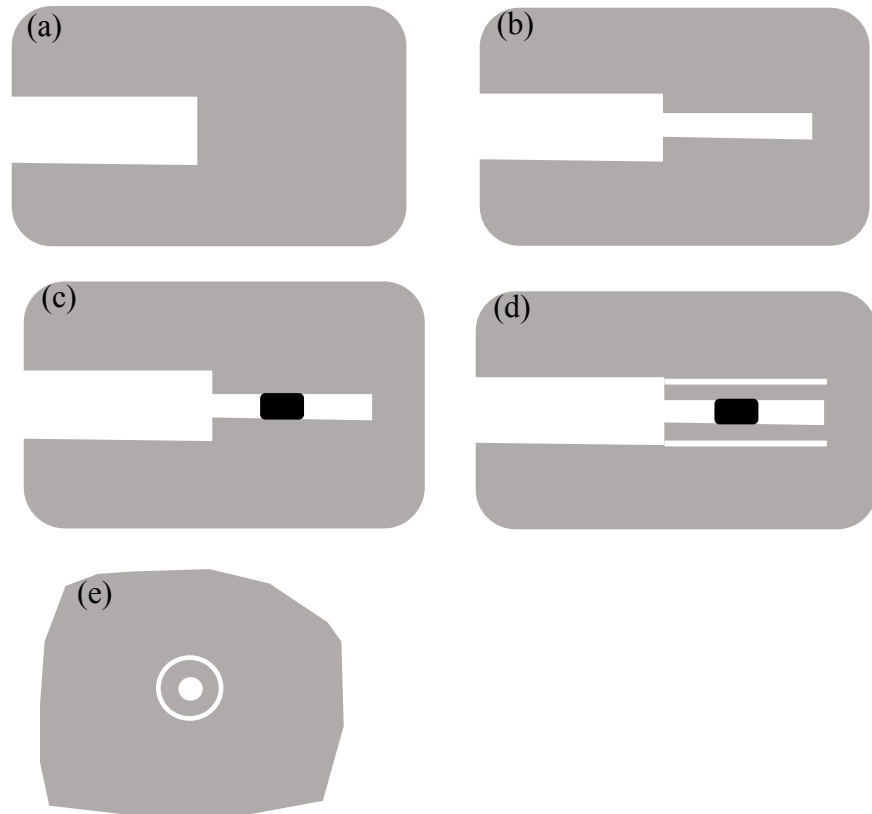


**Figure 2.1** Sketch of typical steps for overcoring method: (a) a larger-diameter borehole drilled to the desired measurement depth; (b) a small pilot hole advanced from the bottom of the borehole; (c) a measurement instrument installed in the pilot hole; (d) the larger borehole extended by overcoring to completely relieve stresses; (e) cross-section view of stress measurement by overcoring

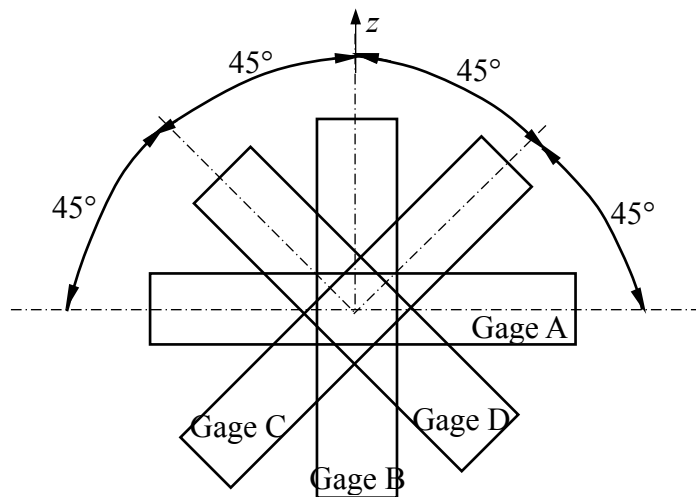


**Figure 2.2** Strain gage configuration for each rosette viewed from axis of borehole

There are six unknown components for the 3D in-situ stresses. Nine (or twelve) strain

measurements are made from different locations around the borehole wall. This makes redundant equations available. There are two angles,  $\xi$  and  $\theta$ , which are used to define the strain gauge orientations, as shown in Figure 2.3. Figure 2.4 demonstrates the procedure for establishing the relationship between the measured strains and the six components of the in-situ stresses.

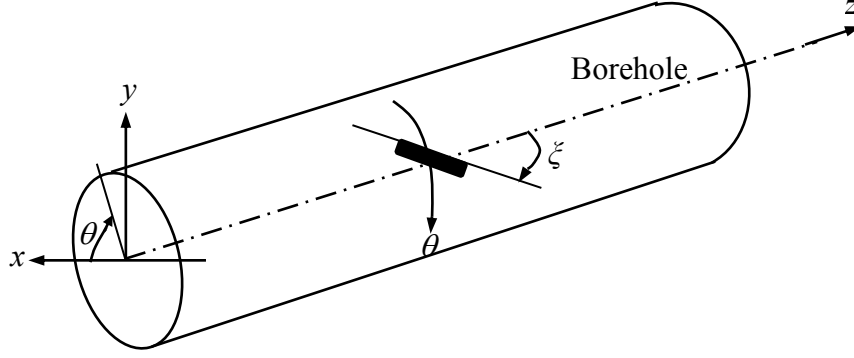


**Figure 2.3** Strain gauge orientations in borehole

The set of equations allowing the calculation of the 6 stress components from strain measurements can be written in a simplified matrix format:

$$\varepsilon_{\eta} = [c]\{\sigma_o\} = [c_1 \quad c_2 \quad c_3 \quad c_4 \quad c_5 \quad c_6]\{\sigma_o\} \quad (2.1)$$

where  $\varepsilon_{\eta}$  is a strain gauge reading,  $[c]$  is the coefficient matrix depending on the rock properties, the strain gauge orientation angles  $\theta$  and  $\xi$ , and  $\{\sigma_o\}$  is the in-situ stress tensor to be determined,

$$\{\sigma_o\} = \begin{Bmatrix} \sigma_x \\ \sigma_y \\ \sigma_z \\ \tau_{xy} \\ \tau_{yz} \\ \tau_{zx} \end{Bmatrix} \quad (2.1a)$$

The elements of  $[c]$  are defined below (Duncan-Fama and Pender 1980):

$$\begin{aligned} c_1 &= \{[k_1 - 2(1-\nu^2)k_2 \cos 2\theta] \sin^2 \xi - \nu \cos^2 \xi\} / E \\ c_2 &= \{[k_1 + 2(1-\nu^2)k_2 \cos 2\theta] \sin^2 \xi - \nu \cos^2 \xi\} / E \\ c_3 &= (\cos^2 \xi - \nu k_4 \sin^2 \xi) / E \\ c_4 &= -4(1-\nu^2)k_2 \sin 2\theta \sin^2 \xi / E \\ c_5 &= 2(1+\nu)k_3 \cos \theta \sin 2\xi / E \\ c_6 &= -2(1+\nu)k_3 \sin \theta \sin 2\xi / E \end{aligned} \quad (2.2)$$

where  $E$  and  $\nu$  are Young's modulus and Poisson's ratio, respectively. For CSIRO cell,  $k_i$  ( $i = 1, 4$ ) depends on the Poisson's ratio of the epoxy, the inner radius of the cell, the Poisson's ratio of the rock, the ratio between the inner and outer radii of the cell, and the ratio between the shear modulus of the epoxy and the shear modulus of the rock. When CSIR cell is employed, all  $k_i = 1.0$ .

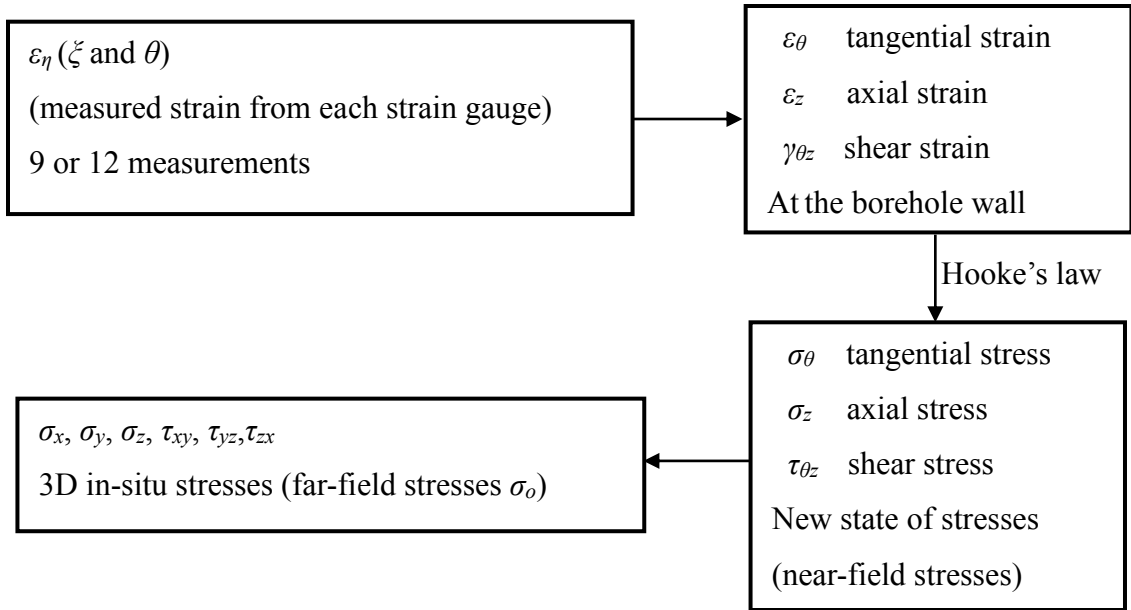


**Figure 2.4** The relationship between the measured strains and the 3D in-situ stresses

### 2.2.2 USBM Deformation Cell

Two prevalent deformation cells are the US Bureau of Mine cell (USBM) and the Sibra in-situ stress tool (IST). The principle for both cells is the same. The USBM instrument has a three-component borehole deformation gauge. The diametrical deformation is measured in three directions (60 degree apart) in the same diametral plane, as depicted in Figure 2.5.

With only one borehole, the three stress components  $\sigma_x$ ,  $\sigma_y$  and  $\tau_{xy}$  in the  $x, y$  plane normal to the borehole axis and one stress component  $\sigma_z$  parallel to the borehole axis can be expressed as Eqn. (2.3) (Amadei and Stephansson 1997) and two stress components of  $\{\sigma_o\}$  are missing.

$$u_d = \frac{2r_o}{E} \left[ \begin{matrix} 1 + 2 \cos 2\theta(1-\nu^2) & 1 - 2 \cos 2\theta(1-\nu^2) & -\nu & \theta(1-\nu^2) \end{matrix} \right] \{\sigma_o\}^* \quad (2.3)$$

where  $u_d$  is the diametrical deformation,  $r_o$  is the radius of the borehole,  $\theta$  is measured from the  $x$  axis counter clockwise, and  $\{\sigma_o\}^*$  is given as

$$\{\sigma_o\}^* = \begin{pmatrix} \sigma_x \\ \sigma_y \\ \sigma_z \\ \tau_{xy} \end{pmatrix} \quad (2.3a)$$

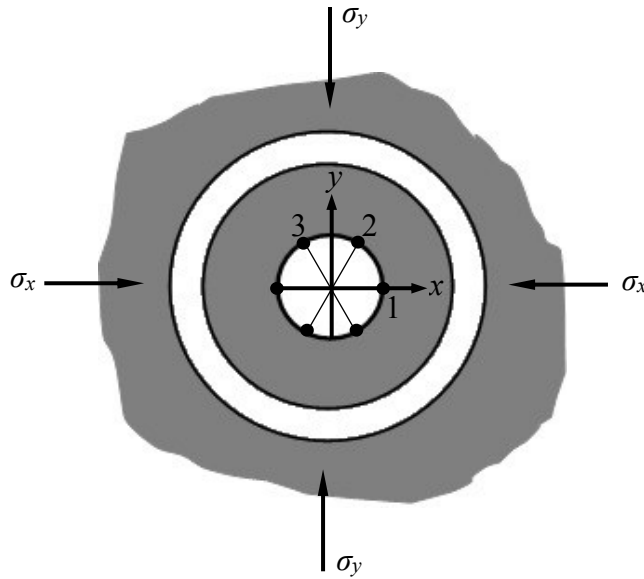


**Figure 2.5** Diametrical deformation measurements at  $0^\circ$ ,  $60^\circ$ ,  $120^\circ$  from  $x$ -axis

### 2.2.3 Summary

The overcoring method is probably the only method for measuring the complete 3D stresses (all magnitudes and orientations). It is a mature method in fundamental theory and practical use. However, there are some limitations:

- 1) It is very expensive because of the need for large overcoring equipment and labor;
- 2) It requires physical access to the measurement location, which is not applicable to small deep well in petroleum engineering;
- 3) It may give scattering results of the stress state due to small rock volume involved;
- 4) The rock mass is assumed to be homogeneous, isotropic and elastic and the results can be affected by local rock properties.

## 2.3 METHODS MEASURING STRESS COMPONENTS IN A PLANE

### 2.3.1 Hydraulic Fracturing

Hydraulic fracturing is a method originated in the oil industry from oil well stimulation (Goodman 1989, Wang 2009). The basic principle of this method is to correlate the shut-in and reopening pressures during fracturing with the maximum and minimum stresses in a plane perpendicular to the borehole axis. An isolated section of a borehole is sealed off with inflatable straddle packers on either side of the section and then is slowly pressurized with a fluid (Figure 2.6a). As the fluid pressure increases in the borehole, the initial compressive stresses on the borehole wall are reduced and at some points become tensile. Pressurization continues until the borehole wall ruptures through tensile failure (Brady and Brown 2004). At the initiation of fracturing, the stress reaches  $-T_s$  (tensile strength) and down-hole fluid pressure is  $p_{cl}$  (the fracture initiation pressure). Fractures are initiated simultaneously in diametrically opposite positions on the borehole periphery. If fluid pumping continues, the crack propagates. The fracture develops in a direction parallel to the maximum stress. The orientation of the initiated fracture thus coincides with the orientation of the maximum stress in a plane perpendicular to the borehole axis. The fluid penetrates the rock mass and the pressure acts on the walls of the fracture. The fluid pressure falls in the test section. Eventually the pressure down the hole will fall to a steady value  $p_s$ . This is called “the shut-in pressure”. After relaxation of the pressure and its subsequent repressurization, the peak borehole pressure achieved  $p_r$  is less than the initial fracturing pressure  $p_{cl}$ . This pressure is named “the reopening pressure”. Figure 2.7 demonstrates a typical recording of pressure versus time for a hydraulic fracturing operation.

After hydrofracturing, the borehole is inspected using a borehole camera, or an impression packer (Figure 2.6b), to determine the orientation of the induced fracture. This in turn gives the orientation of the maximum principal stress in the plane perpendicular to the borehole axis, as shown in Figure 2.8. An impression packer consists of an inflatable element wrapped with a replaceable soft rubber film. When the packer is inflated, the film is



extruded into the fracture, which leaves a permanent impression on the surface (Amadei and Stephansson 1997).

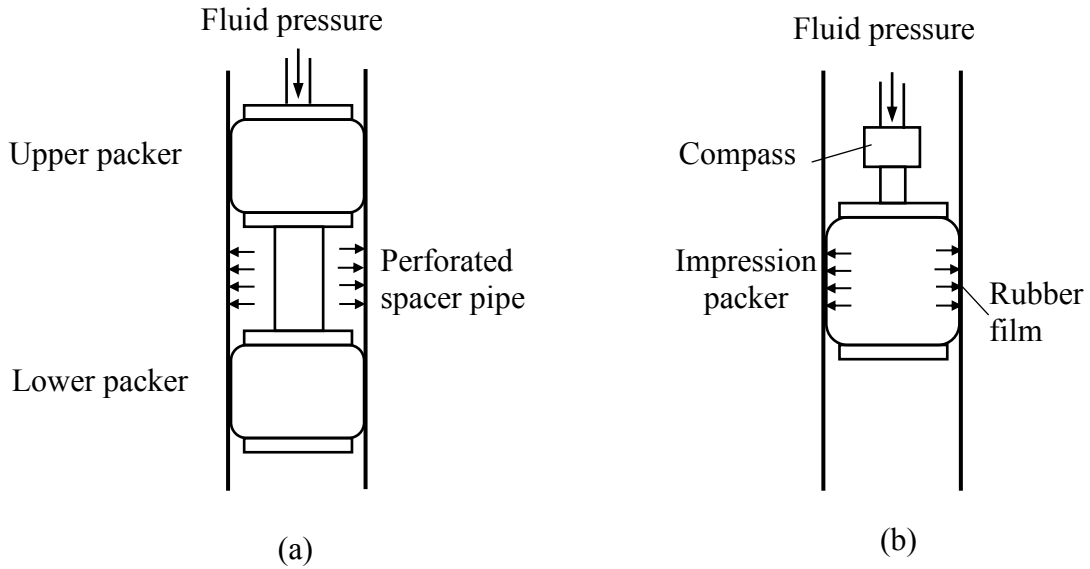


**Figure 2.6** Basic steps of hydraulic fracturing: (a) fracturing of the rock in the borehole wall by pressurization, (b) using impression packer and compass to determine fracture orientation

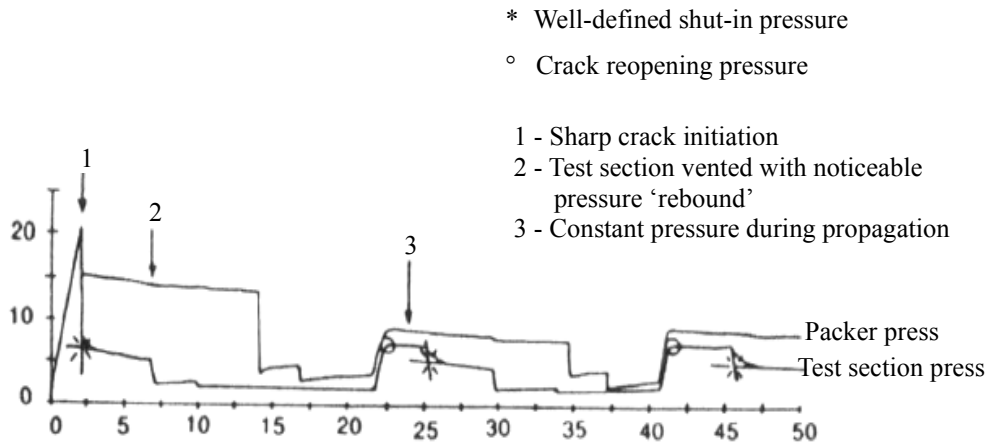


**Figure 2.7** Pressure vs. time record for hydraulic fracturing (after Brady and Brown 1993)

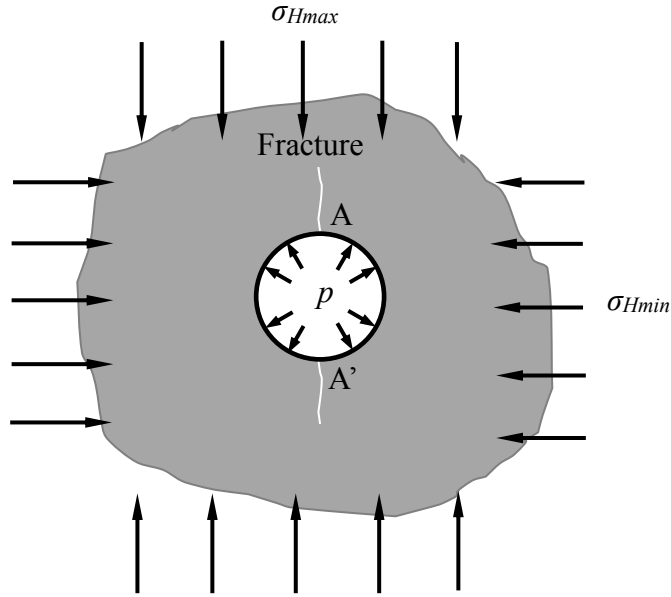


**Figure 2.8** Fracture induced in a vertical well by hydraulic fracturing method

Two key parameters defined on the borehole pressure record are the instantaneous shut-in pressure  $p_s$  and the fracture reopening pressure  $p_r$ .

The new stresses around a circular hole can be calculated from the following equations (Zou 2015).

$$\sigma_r = 0.5\sigma_{\max} \left[ (1+K)\left(1 - \frac{r_o^2}{r^2}\right) - (1-K)\left(1 - 4\frac{r_o^2}{r^2} + 3\frac{r_o^4}{r^4}\right) \cos 2\theta \right] \quad (2.4a)$$

$$\sigma_\theta = 0.5\sigma_{\max} \left[ (1+K)\left(1 + \frac{r_o^2}{r^2}\right) + (1-K)\left(1 + 3\frac{r_o^4}{r^4}\right) \cos 2\theta \right] \quad (2.4b)$$

$$\tau_{r\theta} = 0.5\sigma_{\max} \left[ -(1-K)\left(1 + 2\frac{r_o^2}{r^2} - 3\frac{r_o^4}{r^4}\right) \sin 2\theta \right] \quad (2.4c)$$

where  $r_o$  is radius of the hole,  $\theta$  is measured from the  $x$  axis counter clockwise and the field stress ratio  $K$  is defined as

$$K = \frac{\sigma_{\min}}{\sigma_{\max}} \quad (2.5)$$

At points A and A' (Figure 2.8) on the borehole wall, along the direction of the maximum field stress, the tangential stress reaches its minimum value:

$$\sigma_{\theta \min} = 3\sigma_{\min} - \sigma_{\max} \quad (2.6)$$

When a pressure  $p$  is applied to the interior of the borehole, the induced tangential stress at the wall of borehole is

$$\sigma_{\theta} = -p \quad (2.7)$$

The minimum tangential boundary stress is obtained by superimposing this stress.

$$\sigma_{\theta \min} = 3\sigma_{\min} - \sigma_{\max} - p \quad (2.8)$$

The condition for a new tensile crack is that the tensile stress at point A and A' should be become equal to the tensile strength  $-T_s$ . Applying this to the hydraulic fracturing test yields as a condition for creation of a hydraulic fracture

$$-T_s = 3\sigma_{\min} - \sigma_{\max} - p_{cl} \quad (2.9)$$

If the fluid pressure in the crack is smaller than the normal stress on this crack, the crack would close accordingly. It is the shut-in pressure when the hydrofracture closes, preventing further flow in the rock formation. The magnitude of the minimum principal stress component can be determined directly from the recorded shut-in pressure. This allows a direct measurement of the minimum principal stress.

$$p_s = \sigma_{\min} \quad (2.10)$$

Equation (2.9) and (2.10) allow the maximum and minimum normal stresses in the plane perpendicular to the borehole axis to be determined if the tensile strength of the rock is known.

If the tensile strength of the rock is unknown, the fracture reopening pressure  $p_r$  can be used to yield a formula for the calculation of the tensile strength in this test. The fracture reopening pressure corresponds to the state of borehole pressure where the minimum

boundary stress is zero.

$$0 = 3\sigma_{\min} - \sigma_{\max} - p_r \quad (2.11)$$

Thus

$$T_s = p_{cl} - p_r \quad (2.12)$$

The magnitude of the maximum principal stress component can be calculated from relationships involving the fracture initiation pressure, the fracture reopening pressure and the tensile strength of the rock.

In this method, it is assumed that the rock mass is continuous and elastic, at least in the zone of influence of the hole and the hydraulically induced fractures (Brady and Brown 1993).

In petroleum industry, min-frac test can also be applied to estimate the magnitudes and orientations of the maximum and minimum in-situ stresses in the plane perpendicular to a well. The difference is that in this test a liquid with a relatively small volume is injected. It is carried out before the major hydraulic fracturing treatment (Fjar et al 2008).

### **2.3.2 Hydraulic Tests on Pre-existing Fractures**

Hydraulic tests on pre-existing fractures (HTPF) can also be applied in a borehole (Cornet and Valette 1984). In conventional hydraulic fracturing, new fractures are created in the borehole wall by a pressurized liquid, whereas for HTPF the existing fractures in the borehole wall are re-opened by a pressurized liquid. The average normal stress acting perpendicular to the fracture plane is considered equal to the recorded shut-in pressure (Figure 2.9).

The average normal stress acting on the  $i$ th fracture plane is related to the in-situ stresses in the plane perpendicular to the borehole axis by Eqn. (2.13) (Cornet and Valette 1984, Cornet 1986):

$$\sigma_{ni} = \gamma z_i \cos^2 \theta_i - \frac{1}{2} \sin^2 \psi_i [S_1 + S_2 + (\alpha_1 + \alpha_2) z_i + (S_1 - S_2) \cos 2(\varphi_i - \chi) + (\alpha_1 - \alpha_2) z_i \cos 2(\varphi_i - (\chi + \omega))] \quad (2.13)$$

where  $\sigma_{ni}$  is the normal stress acting on the  $i$ th fracture plane,  $\psi_i$  is the angle between the normal  $n_i$  to the  $i$ th fracture plane and the vertical axis,  $\varphi_i$  is the orientation of the horizontal projection of  $n_i$  with respect to the north,  $\gamma$  is the weight of the overburden per unit length, and  $z_i$  is the depth of test location.  $S_1$ ,  $S_2$ ,  $\alpha_1$ ,  $\alpha_2$ ,  $\chi$ , and  $\omega$  are unknown parameters related to the stress tensor.

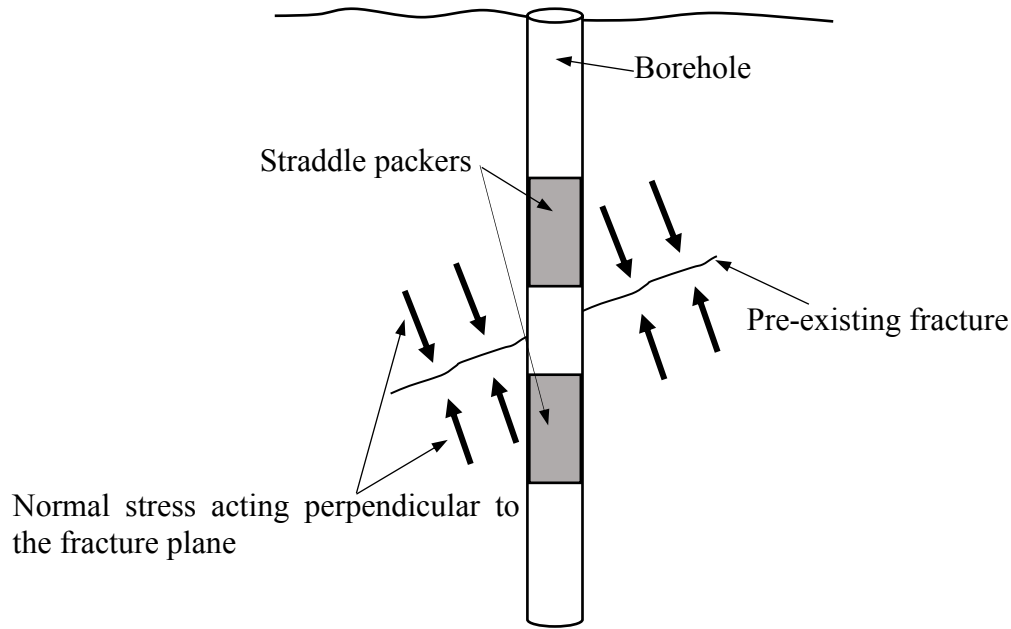


**Figure 2.9** Schematic diagram of HTPF

Since no new fractures are induced, HTPF relies on existing fractures (Lin et al 2018). The key for this method is a sufficient number of fractures with varying dip and strike. Sometimes it is not easy to find these fractures. Moreover, it is essential to know the precise locations and orientations of fractures prior to the tests. This method is time consuming (Stacey and Wesseloo 2002). Theoretically, it may be possible to estimate the 3D in-situ stresses. However, the author is not aware of any publication describing the explicit relationships between the average normal stress perpendicular to a fracture plane and all of the six independent components of the 3D in-situ stress state.

The major advantage of the above fracturing methods is that they can be applied to deep boreholes for in-situ stress estimation. They normally provide the information of the magnitudes and orientations of the maximum and the minimum stresses in the measurement plane.

In practice the vertical stress is usually assumed as a principal stress with an acceptable error and is proportional to the rock density and the depth below the surface. Thus the vertical stress and the two stresses determined from fracturing tests in a vertical borehole are sometimes used as an approximation of the three principal stresses of the in-situ stress field.

### 2.3.3 Borehole Slotting

Borehole slotting is based on the principle of local stress relief in a borehole, in which slots are cut into the borehole wall and the strain relieve adjacent to the slots is measured (Figure 2.10). In this method a properly-sized borehole (95-103 mm) is drilled first and then a half-moon shaped radial slots are sawn parallel to the borehole axis with a specially-designed device.

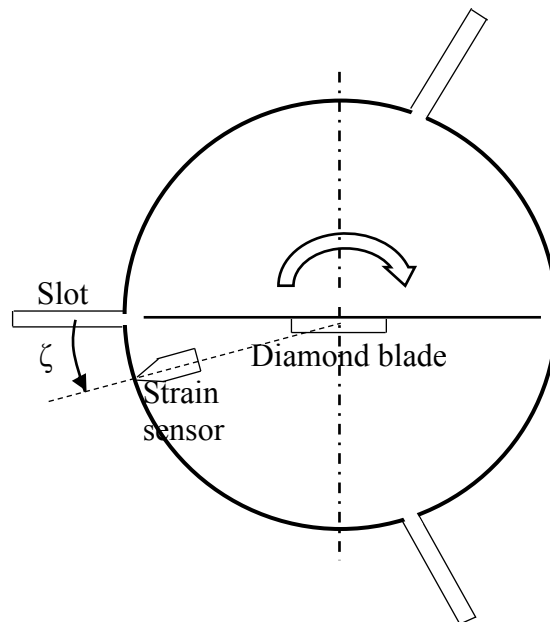


**Figure 2.10** Cross-section view of borehole slotting set-up

Directly next to the slot a specifically developed contact strain sensor that is part of the slotter is pressed with a specific force to the borehole wall during the slotting. It is used to measure the tangential strain at the borehole wall in the near vicinity (within a 15° arc) of the slot before, during and after cutting the slot. Figure 2.11 shows Finite Element simulation results of tangential stress relief at varying locations next to a slot and varying slotting depths. For points of the borehole surface close to the slot (Angle from slot < 15°), 100% stress relief occurs at slot depth of 22 mm.

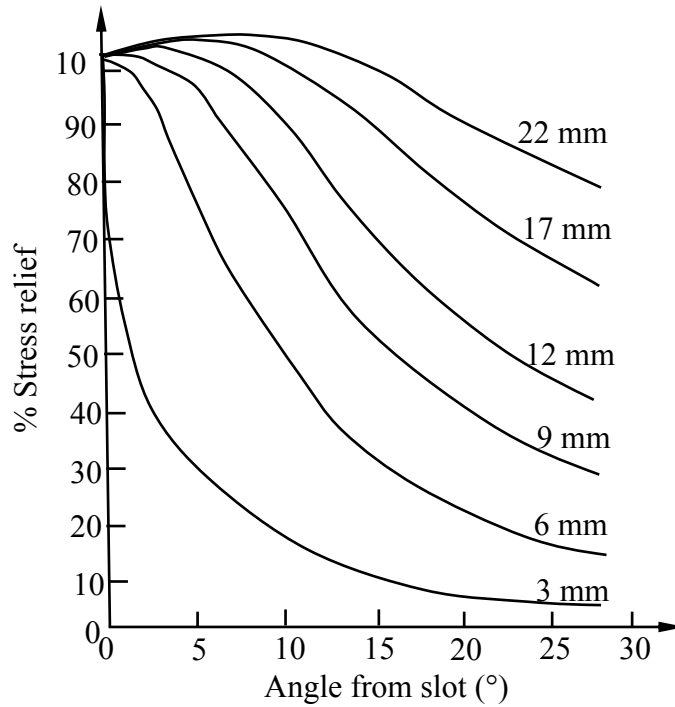


**Figure 2.11** Tangential stress relief next to a slot at a borehole surface from Finite Element simulation (after Bock and Foruria 1983)

The measured strains are converted into stresses under a plane strain condition using the theory of linear elasticity. Normally, a minimum of three longitudinal cuts (usually 120° apart) in three different directions is necessary to determine the 2D in-situ stresses in the plane perpendicular to a borehole.

$$\varepsilon_{\theta} = \frac{1-\nu^2}{E} [I - 2 \cos 2\theta \quad I + 2 \cos 2\theta \quad -4 \sin 2\theta] \{\sigma_o\}_{2D} \quad (2.14)$$

where  $\varepsilon_{\theta}$  is the tangential strain measured in different direction and  $\{\sigma_o\}_{2D}$  is the in-situ stress tensor in 2D,

$$\{\sigma_o\}_{2D} = \begin{pmatrix} \sigma_x \\ \sigma_y \\ \tau_{xy} \end{pmatrix} \quad (2.14a)$$

The significant advantage with the method is that it does not require any overcoring (Ljunggren et al 2003). However it can only estimate the three stress components in the plane perpendicular to the borehole axis.

### 2.3.4 Flat Jack

Flat jack is one of the oldest methods of stress measurement. In many aspects it can be classified as partial surface relief method.

The procedure for this method is as follows (Goodman 1989) and the flat jack test set-up is presented in Figure 2.12.

- 1) Reference pins or strain gauges are installed at suitable points on the rock face and the distance between those pins or strain gauges,  $d_l$ , is measured by extensometer.
- 2) A deep slot (planar or circular) is made perpendicular to the rock face between the reference points with overlapping holes or a rock saw to disturb the equilibrium of a rock mass.

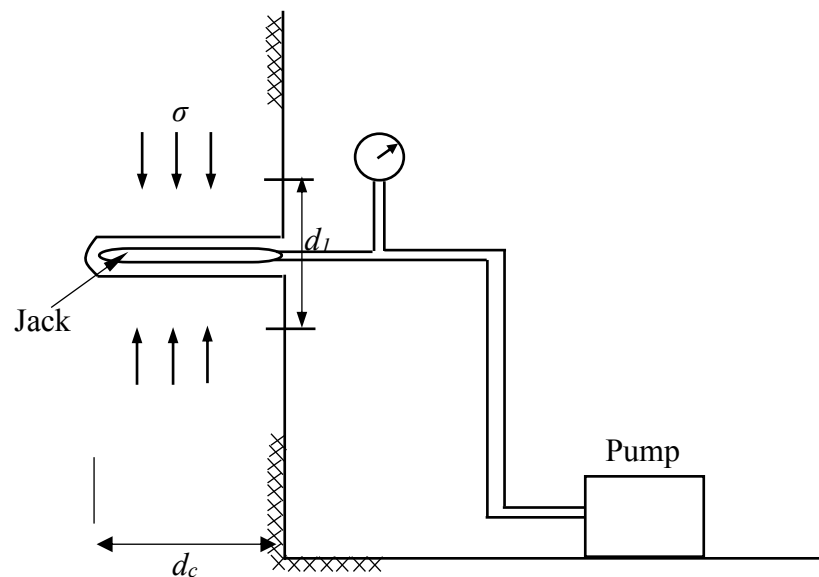
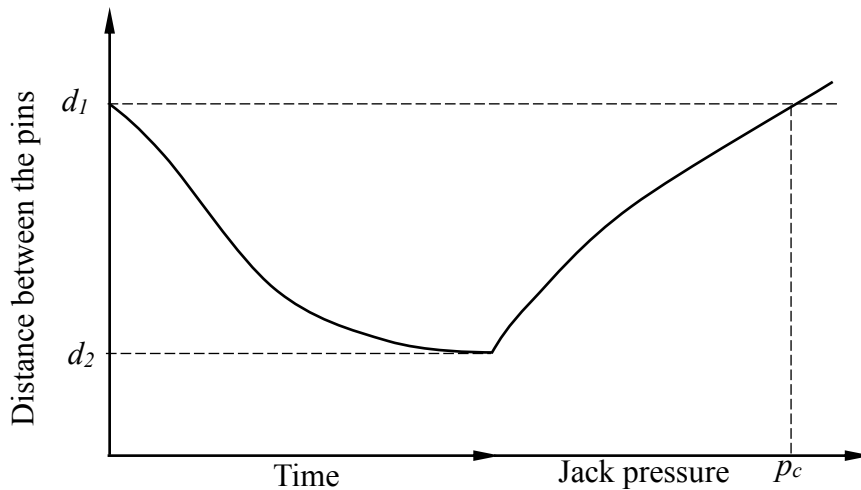


Figure 2.12 Flat jack set-up



- 3) As a result of cutting a slot, these pins converge and the distance is decreased to a smaller value  $d_2$  under an initial compression stress field normal to the plane of the slot. Their final position is measured again.
- 4) The device such as a flat jack is inserted into the slot, tightly packed with cement and pressurized.
- 5) When the pins are returned to the original position  $d_1$ , that is, deformation has vanished, the pressure in the jack is called cancellation pressure,  $p_c$ .

The cancellation pressure of the jack required to null the deformation approximates the stress normal to the plane of jack (Figure 2.13). In each flat jack test, one stress component is determined. It also should be pointed out that the measured stress is not the in-situ stress, instead, the average excavation-induced stress within the range of the cutting depth  $d_c$ .



**Figure 2.13** Record of distance between the pins in the flat jack test (after Goodman 1989)

This method can also be applied for estimation of the 2D in-situ stresses in the plane perpendicular to the borehole axis. If a borehole wall is cut with a flat jack parallel to the hole axis, the tangential stress  $\sigma_\theta$  around the hole can be measured at that location with this method. If three measurements are made in different locations around the hole, there are three tangential stresses  $\sigma_{\theta_1}$ ,  $\sigma_{\theta_2}$  and  $\sigma_{\theta_3}$ . If the borehole is perpendicular to the  $x, y$  plane, the in-situ stress components  $\sigma_x$ ,  $\sigma_y$  and  $\tau_{xy}$  in the  $x, y$  plane are related to the three measured tangential stresses by Eqn. (2.15) (Amadei and Stephansson 1997):

$$\begin{Bmatrix} \sigma_{\theta 1} \\ \sigma_{\theta 2} \\ \sigma_{\theta 3} \end{Bmatrix} = \begin{bmatrix} 1 - \cos 2\theta_1 & 1 + \cos 2\theta_1 & -4 \sin 2\theta_1 \\ 1 - \cos 2\theta_2 & 1 + \cos 2\theta_2 & -4 \sin 2\theta_2 \\ 1 - \cos 2\theta_3 & 1 + \cos 2\theta_3 & -4 \sin 2\theta_3 \end{bmatrix} \begin{Bmatrix} \sigma_x \\ \sigma_y \\ \tau_{xy} \end{Bmatrix} \quad (2.15)$$

where  $\theta$  is measured from the  $x$  axis counter clockwise.

Several major assumptions are made in the analysis of this method:

- 1) The rock mass is uniform and isotropic;
- 2) The stress relief process is assumed to be completely reversible;
- 3) Flat jacks are assumed to be aligned with the stress parallel to the surface of the opening.

### 2.3.5 Back Analysis of Excavation or Drilling

Back analysis is a practical engineering tool to evaluate geo-mechanical parameters of underground structures based on field measurements of some key parameters, such as displacements, strains and stress changes and to optimize designs. This method has been applied over the last few decades to estimate the in-situ stress state and the mechanical properties of the surrounding rock masses in geotechnical and mining engineering (Ledesma et al 1996, Mello Franco et al 2002, Jeon and Yang 2004, Oreste 2005, Deng et al 2010, Sakurai 2017).

In 1966, a back-analysis method of calculating the average ground stress components from measurements of the deformation of a circular hole was presented by Panek (Panek 1966). In the same year, Suzuki developed the measuring instruments for borehole deformation considering the roundness and roughness of the inner surface of a borehole for applying in field stresses calculation (Suzuki 1966). Back analysis was used in Kirsten (1976) in determination of rock mass elastic moduli from deformation measurements and then introduced to identify elastic parameters and earth pressure in a tunnel lining by Gioda in 1980 (Gioda 1980). Back analysis of measured displacement of tunnels based on a finite element formulation was used to determine the initial stresses by Sakurai and Takeuchi in 1983 (Sakurai and Takeuchi 1983). Kaiser and Zou in 1990 developed a stress change

fitting technique for in-situ stress determination based on back-analysis principle (Kaiser et al 1990, Zou and Kaiser 1990a and 1990b). The stress changes can be measured during the excavation of a drift by installing stress cells in the undisturbed rock mass ahead of the advancing face of the drift (Figure 2.14). Wiles and Kaiser (1994a and 1994b) combined readings from both CSIRO, CSIR and other borehole strain cells with displacement measurements from convergence gauges, extensometers, inclinometers and tiltmeters to determine the in-situ stresses. Zou (1995a) proposed a back-analysis inverse method using relative and convergence displacements and boundary element method to estimate the effective field rock properties and the in-situ stresses. Sakurai (1997, 2017) did further work with this method in rock engineering with numerical modelling.

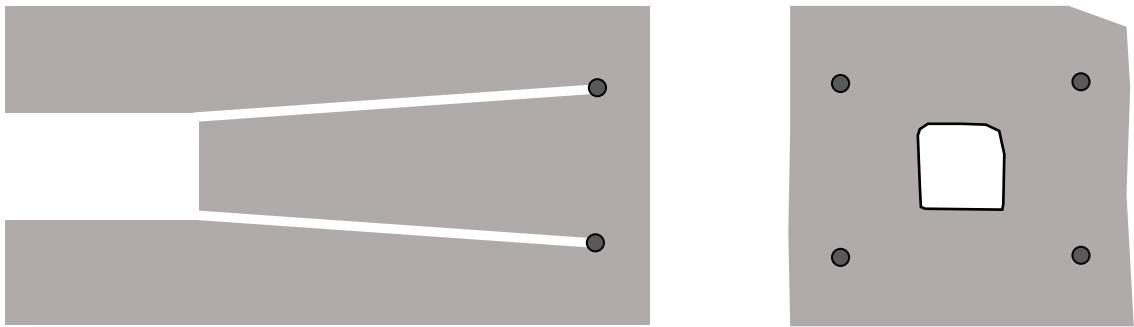


**Figure 2.14** Field measurement of stress changes by excavation

When an excavation is made, or an excavation enlarged, in a rock mass, stress changes/displacements are induced by the nearby excavation in response to the action of the in-situ stresses.

#### 1) Back analysis with strain cells

The major difference between overcoring and back analysis method is that overcoring process relieves completely the stresses around a strain cell, therefore the measured strain changes are directly from the in-situ stresses ( $\sigma_o \rightarrow 0, \Delta\sigma = \sigma_o$ ). Whereas back analysis method uses the excavation of a nearby opening to partially relieve the stress around a strain cell, accordingly the measured strain changes are not directly from the in-situ stresses but they are related indirectly ( $\sigma_o \rightarrow \sigma_n, \Delta\sigma = \sigma_n - \sigma_o$ ) and the in-situ stresses are calculated through a back analysis process.

Overcoring method is very expensive, and the measurement results often vary widely from location to location. Compared with overcoring, back analysis by excavation is relatively inexpensive when it is done during excavation and gives the stress state in a relatively large volume of rock.

## 2) Back analysis with deformation measurement instruments

The deformation of the rock mass around the opening is relatively easy to measure. It can be measured on the opening surface or inside the rock mass. Figure 2.15 shows the relative movement measurement and convergence measurement for calculation of the in-situ stresses. Lin and Zou (2016) developed a practical back analysis method for estimation of the 2D stresses in petroleum field from well deformation with consideration of different permeability of rock formation, i.e., high permeability, low permeability and non-permeability.

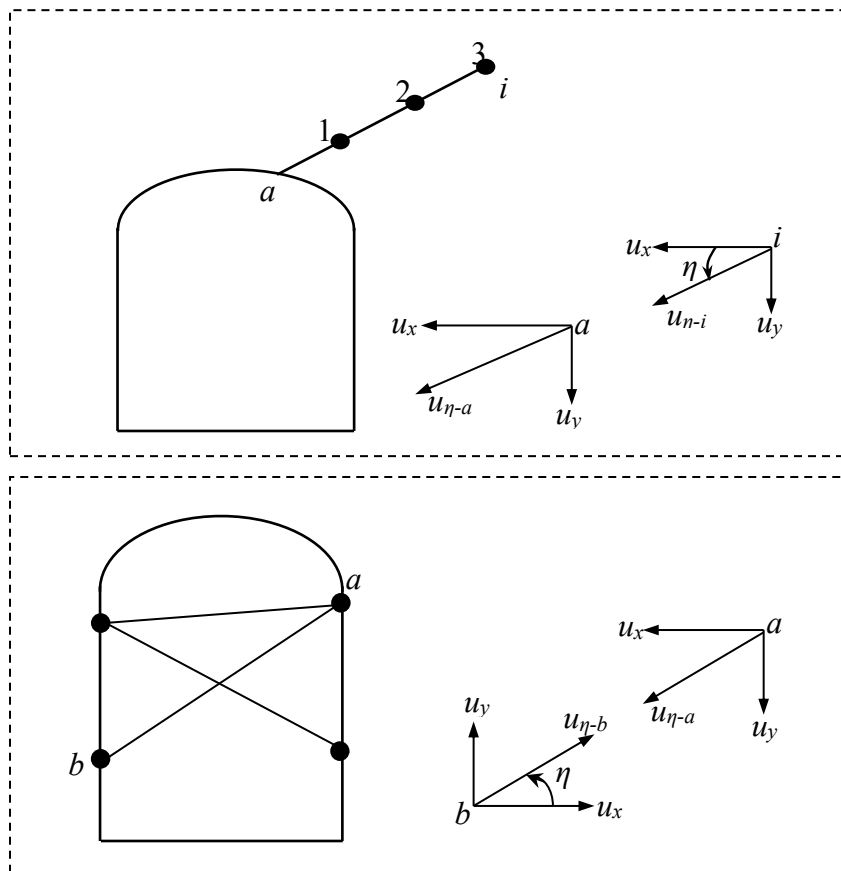


**Figure 2.15** Relative movement measurement and convergence measurement and their calculations (after Zou 1995a)

The relationship between the stress changes / displacements and the in-situ stresses can be represented by a simple equation:

$$\{\Delta\sigma\} = [M_1]\{\sigma_o\}_{2D} \quad (2.16)$$

$$\{u\} = [M_2]\{\sigma_o\}_{2D} \quad (2.17)$$

where  $\{\Delta\sigma\}$  is a matrix of stress changes,  $\{u\}$  is a matrix of displacements,  $\{\sigma_o\}$  is a matrix of the in-situ stresses, and  $[M_1]$  and  $[M_2]$  are coefficient matrices, which are functions of the geometry of the opening, location of measurement points and the rock properties.

If the stress changes or displacements induced by excavations can be measured, then the in-situ stresses can be calculated (back-analyzed) by solving the above equations:

$$\{\sigma_o\}_{2D} = ([M_1]^T [M_1])^{-1} [M_1]^T \{\Delta\sigma\} \quad (2.18)$$

$$\{\sigma_o\}_{2D} = ([M_2]^T [M_2])^{-1} [M_2]^T \{u\} \quad (2.19)$$

where superscript  $T$  and  $-1$  denote transpose and inverse of a matrix, respectively.

The method of back analysis of nearby excavation or drilling is based on the assumption of linearly elastic behaviour. If the opening / borehole is circular, analytical solution can be obtained. If the opening / borehole has an irregular shape, it is necessary to use a numerical stress simulation technique such as the Boundary Element Method (BEM) or Finite Element Method (FEM).

This back analysis method for determining the in-situ stresses from borehole / well deformation has been currently used for measuring the 2D in-situ stresses in a plane perpendicular to the borehole / well axis. It assesses average stresses over a large volume of rock mass and has showed potential to determine the complete 3D stresses.

### 2.3.6 Strain Recovery Method

There are two major methods which utilize the theory of strain recovery, anelastic strain recovery (ASR) and differential strain curve analysis (DSCA). These methods are laboratory tests which are based on core measurements. When a piece of rock is removed

from the in-situ state of stress, it tends to relax and thereby deform. The relaxation consists of an instantaneous elastic component and a time-dependent (anelastic) recovery (Amadei and Stephansson 1997).

#### 1) ASR

After unloading of a rock, the anelastic behaviour occurs. In this method, an oriented core sample is instrumented to monitor the strain changes with time, as the core relaxes or recovers from its former state of stress. Three pairs of radial inductive displacement transducers and one axial transducer are used to measure the anelastic response of the core sample.

- The extent of expansion and strain recovery provides information on the orientations of principal stresses;
- At the same time, the opening and propagation of preferential microcracks after drilling and coring are also oriented with respect to the in-situ stress field.

The directions of the most expansion and the measured maximum strain and the normals of majority cracks correspond to the orientation of the maximum principal in-situ stress. However, it is more difficult to determine the magnitude of the stresses because a constitutive viscoelastic model for strain relaxation is required.

#### 2) DSCA

In this test, the core sample is subject to hydraulic reloading in a pressure vessel after drilled out from underground. After it is brought up to the surface, the micro-cracks have had time to develop and to align themselves in the direction of the original stresses. The strain gauges are attached in the sample to record the strains in different directions as a result of the closure of the micro-cracks.

These two methods have the assumption: the principal directions of the in-situ stress field coincide with the principal directions of the strain measured. They may be used to estimate the orientation of the horizontal principal in-situ stresses in 2D at large depth as long as it is possible to recover a core. The major factors, such as temperature variations, anisotropy

of rock, non-homogeneous recovery of deformations, core recovery time, and accuracy of core orientation & small strain measurement, etc., can affect the application of these two methods (Ljunggren et al 2003).

### **2.3.7 Geophysical Methods**

Borehole acoustic logging and surface seismic survey, which are used in petroleum industry, are the possible methods to estimate the in-situ stresses (Fjar et al 2008). They are based on wave propagation in an elastic medium.

Borehole acoustic logging is a well logging tool that provides a formation's interval transit time, designated as  $\Delta t$ , which is a measure of a formation's capacity to transmit elastic waves. Seismic survey is for mapping the large subsurface structures. Elastic waves are generated by an artificial vibroseis at the surface and received by a series of sensors on the surface.

There are two approaches. The basic principle for the first approach is to measure the dynamic rock mass properties by borehole acoustic logging or surface seismic survey, correlate them to the static rock mass properties through laboratory tests on rock samples and estimate the stress magnitude based on an established relationship. In the borehole acoustic logging and surface seismic survey, the primary wave (compressional or P-wave) and secondary wave (shear or S-wave) would be received at different times after the waves propagate through the rock formation and back to the receivers. The P-waves arrive first and S-waves are the second arrival because of the higher velocity of P-wave. S-wave generally has higher energy and amplitude. These characteristics enable separation of S-wave from P-wave and allows measurement of the interval transit time for P-wave and S-wave, respectively (Serra 2004). There is a direct relationship between wave velocities or travel time and the dynamic elastic properties of rock mass (Fjar et al 2008, Hearst et al 2000).

$$E_{dyn} = \frac{\rho}{\Delta t_s^2} \left( \frac{3\Delta t_s^2 - 4\Delta t_p^2}{\Delta t_s^2 - \Delta t_p^2} \right) \times 10^9 = \frac{\rho V_s^2 (3V_p^2 - 4V_s^2)}{V_p^2 - V_s^2} \times 10^{-3} \quad (2.20)$$

$$\nu_{dyn} = \frac{\Delta t_s^2 - 2\Delta t_p^2}{2(\Delta t_s^2 - \Delta t_p^2)} = \frac{V_p^2 - 2V_s^2}{2(V_p^2 - V_s^2)} \quad (2.21)$$

where  $E_{dyn}$  is dynamic Young's modulus (MPa),  $\nu_{dyn}$  is dynamic Poisson's ratio,  $\rho$  is bulk density ( $\text{g/cm}^3$ ) (obtained through density logging),  $\Delta t_s$  is shear sonic transit time ( $\mu\text{s/m}$ ),  $\Delta t_p$  is compressional sonic transit time ( $\mu\text{s/m}$ ),  $V_s$  is shear sonic velocity (m/s), and  $V_p$  is compressional sonic velocity (m/s).

Subsequently, by laboratory tests, the quantitative correlations between dynamic and static elastic parameters can be established (Fjar et al 2008). The two horizontal principal stress components may be derived from empirical models, which relate the magnitudes of the maximum and minimum principal in-situ stresses to the static mechanical properties of the rocks,  $E$  and  $\nu$  (Yin et al 2018, Jin and Cao 2016).

In the second approach, Tang and Cheng (2004) indicated that the maximum stress orientation can be estimated using cross-dipole acoustic logging. The fast shear polarization coincides with the maximum stress axis. They also indicated that the stress magnitude may be determined in theory using the stress-induced shear-wave anisotropy effect but difficulty in practice.

### 2.3.8 Borehole Breakout

Compressive and tensile failures are two of failure modes possibly occurring in a borehole. The variation of tangential stress around the borehole is depicted in Figure 2.16.

Borehole breakout has been developed as a reliable measurement technique for principal stress orientations. It is based on the rock failure at the borehole wall. When a borehole is drilled in the ground, the material removed from the subsurface is no longer supporting the surrounding rock. As a result, the stresses become concentrated in the surrounding rock (i.e. the borehole wall). The maximum concentration is in the direction of the minimum field



stress. If the tangential stress around the borehole exceeds the compressive rock strength, borehole breakout occurs by crushing failure and thus is oriented parallel to the minimum stress ( $\sigma_{min}$ ) (Figure 2.17). Breakage of the rock results in two diametrically opposed zones of enlargement. The borehole breakout can be detected by using borehole logging tools, such as optical (borehole camera), mechanical (caliper log), acoustic (televIEWER) or electrical resistivity (formation microscanner or FMS) methods (Reinecker et al 2003, Tingay et al 2008).

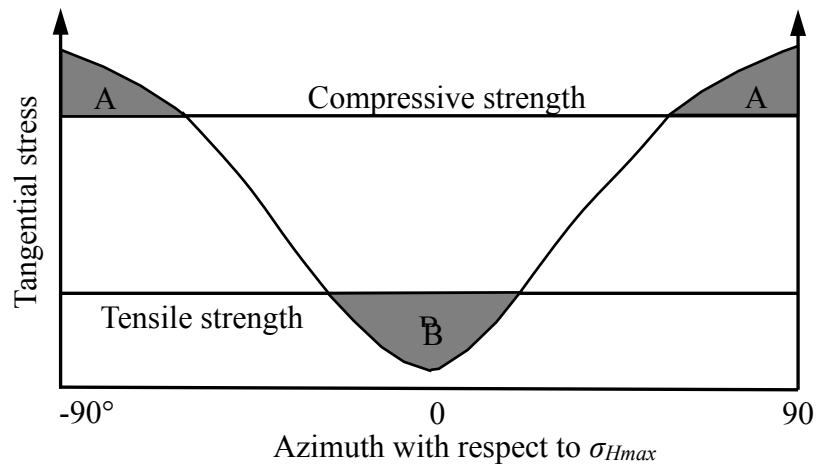


**Figure 2.16** Tangential stress on the borehole wall as a function of azimuth with respect to the maximum principal stress in a plane perpendicular to the borehole axis

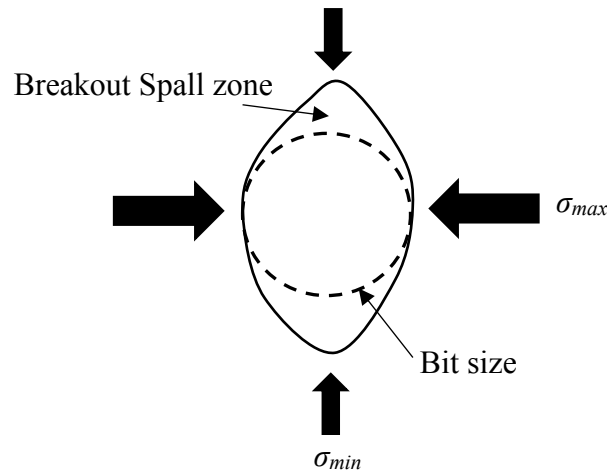


**Figure 2.17** Schematic cross-section of borehole breakout

Borehole cameras are known to provide the least reliable data for breakout analysis, as there is always a problem to center the borehole camera and to measure the depth of spalling at the borehole wall. The caliper log (four-arm and six-arm, Figure 2.18) has

commonly been used to estimate horizontal stress directions from breakout orientation (Reinecker et al 2003). The four-arm caliper measurement provides two diameters in two orthogonal directions in the borehole cross-section. Borehole image logs include both electrical (resistivity) and acoustic imaging logs (Tingay et al 2008). The FMS produces high-resolution micro-resistivity images that can be used for determining fracture and breakout orientation. Acoustic imaging tools utilize a rapidly rotating piezoelectric transducer to emit a focused high-frequency sonic pulse to the borehole wall and then records the amplitude of the return echo as well as the total travel time of the sonic pulse. This data is then processed into images of the borehole wall reflectance (based on return echo amplitude) and borehole radius (based on pulse travel time).

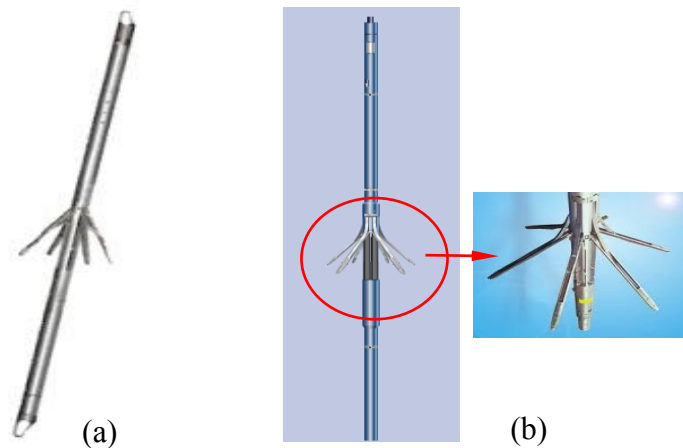


**Figure 2.18** Caliper logging tools: (a) four-arm (Landsea 2018); (b) six-arm (Schlumberger 2002)

On the other hand, when the tangential stress is reduced to tension due to borehole mud pressure and exceeds the tensile strength of the borehole wall, drilling-induced fracture forms and is oriented parallel to the maximum stress ( $\sigma_{max}$ ) (Figure 2.19).

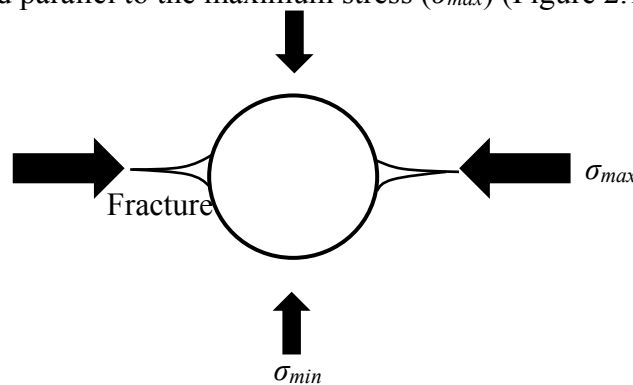


**Figure 2.19** Drilling-induced fracture

This method is quick to use and cost effective. It may be applicable for revealing the stress information at great depth which other methods may not reach. The major limitations of the method are that it only works if breakouts exist and that it applies only for obtaining the orientations of the principal stresses in a plane perpendicular to the borehole axis. This method cannot determine the magnitudes of the in-situ stresses.

### **2.3.9 Geological Observation**

Besides the borehole breakout, geological observation can also provide information for the orientation of in-situ stresses (Goodman 1989). It can be divided into two groups: methods based on the orientation, distribution, deformation and fracturing of geological features; and methods based on the first motion of earthquakes.

Geological structures have been used as indicators of paleostresses because their features have a close relationship with the in-situ state of stress in the rock mass (Wang 2014). It is also assumed that vertical stress is one of the principal stresses. Figure 2.20 shows the relationship between principal stress directions and different types of fault. In the first case of a normal fault, the minimum horizontal stress points perpendicularly to the fault trace and faulting in the rock is parallel to the maximum horizontal stress. The second case corresponds to a reverse/thrust fault. The minimum horizontal stress points horizontally to the fault trace. In the case of strike-slip fault, fracturing of the rock is parallel to the vertical stress. It was caused by a state of stress in which  $\sigma_{Hmax}$  was inclined about  $30^\circ$  with the fault trace, clockwise or counter clockwise as dictated by the sense of motion on the fault.

Sometimes dikes and flank volcanoes formed around larger craters can give indication for the direction of the minimum horizontal stress. Some dikes represent hydraulic fractures, in which case they lie perpendicular to the minimum horizontal stress.

Another analysis approach comes from the first motion interpretation of earthquake. In the case of a fault-related event it refers to the orientation of the fault plane that slipped and the slip vector is also known as a fault-plane solution. Fault plane solutions are useful for

defining the fault motion. Then this can give the information on the directions of the horizontal principal in-situ stresses.

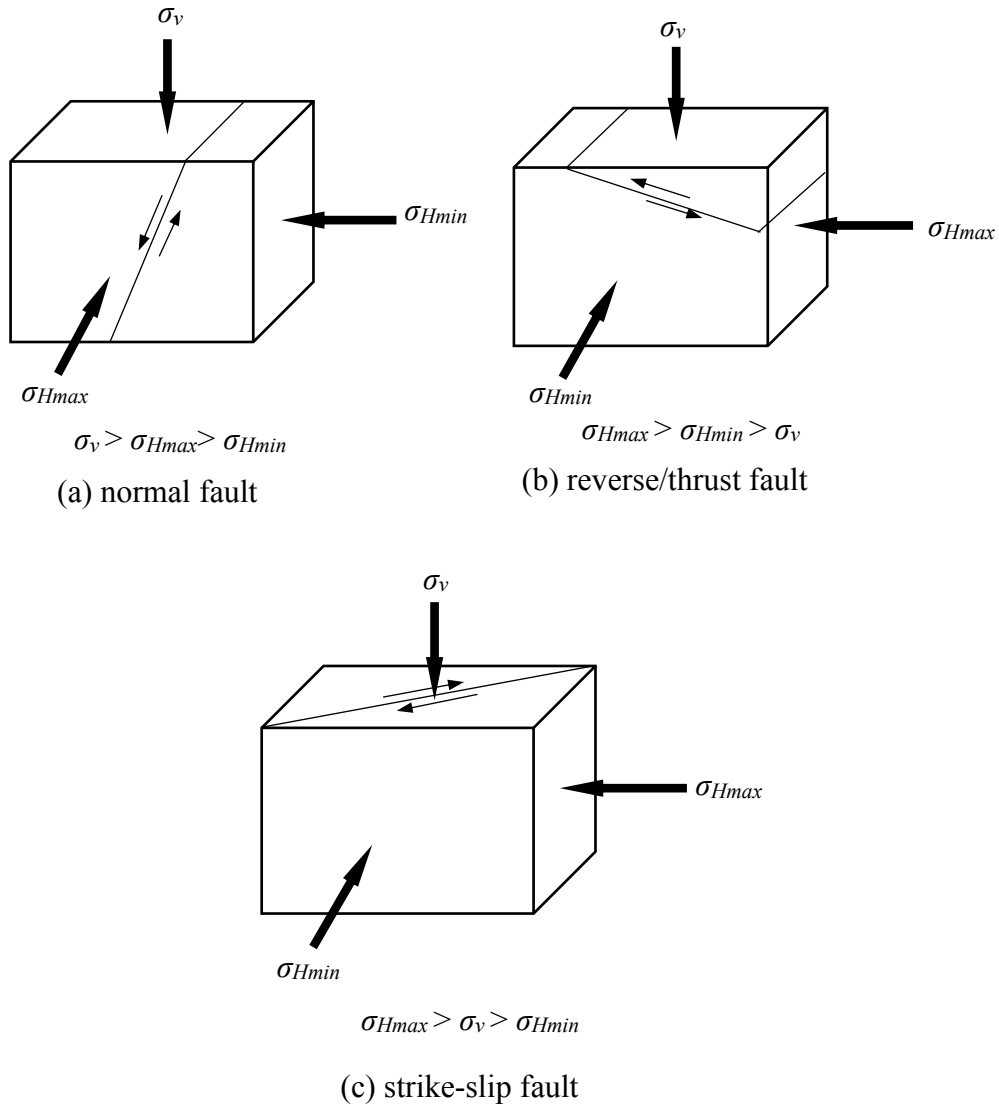


**Figure 2.20** Illustration of fault types and directions of the inferred stresses (after Amadei and Stephansson 1997)

It should be noted that most geological structures were formed a long time ago and the results of stress may not be the current state. Furthermore, the results are on a regional scale, not specific to a local area and it cannot be used to determine the in-situ stress magnitude.

## 2.4 COMPARISON AND SUMMARY

According to the above review of various methods for the in-situ stress measurement, a comparison and summary of these methods are given below and also summarized in Table 2.2.

Currently only overcoring method can be used to determine the complete 3D in-situ stresses underground. It is widely used in mining and geotechnical engineering and have been practised for many years. However it requires physical access to the location where stresses are to be measured and allowance of complete stress relief by overcoring. Thus, they are not suitable for application in small deep wells. It may give scattering results due to a small rock volume involved.

Other methods may be able to estimate the orientations and/or magnitudes of some components of the in-situ stresses. Hydraulic fracturing and mini-frac tests are widely used in petroleum engineering. They can provide the information of the magnitudes and orientations of the maximum and the minimum stresses in a plane perpendicular to the borehole axis in a large rock volume. HTPF determines the average normal stress acting perpendicular to the plane of the pre-existing fracture. A sufficient number of fractures with varying dip and strike are needed to estimate the in-situ stresses in a plane perpendicular to the borehole axis. Borehole slotting is a localized stress relief method and doesn't require overcoring. So compared with overcoring, the test procedure is simple. However it is only for estimation of the in-situ stresses in a plane perpendicular to the borehole axis in a small rock volume. Flat jack is a partial stress relief method and conducted at the surface of excavation. The average excavation-induced stress perpendicular to the jack plane is determined in each test. The 2D stresses (not necessarily the in-situ stress) in the plane normal to the jack are estimated with three tests by cutting boreholes on the surface of the opening. Back analysis utilizes the response (stress change, strain change, displacement) of a rock mass during or after excavation to calculate the in-situ stresses based on elastic theory. Numerical modeling may be adopted in the back analysis procedure for non-circular opening. It involves a large volume of rock and can be applicable in a small deep well. This

method is currently applied to evaluate the 2D in-situ stresses in a plane perpendicular to the borehole axis and possible for the complete 3D stresses. Geophysical methods relate the rock mechanical properties obtained from well logging and seismic measurement data to the in-situ stress field. They generally give the information of the maximum and minimum horizontal stresses with the assumption that the vertical stress is one of the three principal stresses. Strain recovery methods are based on monitoring the response of core samples following drilling to interpret the stress “memory” in the rock. It is typically used to estimate the orientations of the horizontal principal in-situ stresses in 2D. Borehole breakout is a stress-related phenomenon, which gives the indication of the orientations of principal stresses in a plane. With geological observation method, the vertical stress component is generally assumed to be a principal stress and the orientations of the horizontal principal in-situ stresses can be inferred. The results from this method are less accurate.

**Table 2.2** Comparison of in-situ stress measurement methods

Method	Principles and Characteristics	Advantages	Disadvantages
Overcoring	<ul style="list-style-type: none"> <li>• Complete stress relief,</li> <li>• Widely used in mining and geotechnical engineering,</li> <li>• The rock mass is assumed to be homogeneous and isotropic and linear elastic theory is applied,</li> <li>• Rock volume involved is borehole size,</li> <li>• Determine the complete 3D stresses when strain cells are used,</li> <li>• Possible to determine the complete 3D stresses by drilling at least two non-perpendicular holes when deformation cell is used.</li> </ul>	<ul style="list-style-type: none"> <li>• Determine the complete 3D stresses – magnitudes and orientations,</li> <li>• A mature method in fundamental theory and practical use.</li> </ul>	<ul style="list-style-type: none"> <li>• Requires physical access,</li> <li>• Not applicable to petroleum engineering in small wells,</li> <li>• Assess the stresses at measurement location.</li> </ul>
Hydraulic fracturing and mini-frac	<ul style="list-style-type: none"> <li>• Rock fracture induction,</li> <li>• Used in mining, geotechnical and petroleum engineering,</li> <li>• The rock mass is assumed to be continuous and elastic at least in the zone of influence of the hole,</li> <li>• Involves a fairly large rock volume,</li> <li>• Determine the magnitudes and orientations of maximum and minimum stresses in the plane perpendicular to the borehole axis.</li> </ul>	<ul style="list-style-type: none"> <li>• Give a direct estimate of the maximum and minimum stresses in a plane perpendicular to the borehole axis,</li> <li>• Relatively simple tests in comparison with overcoring method.</li> </ul>	<ul style="list-style-type: none"> <li>• Only provides the information of principal stresses in a plane.</li> </ul>

**Table 2.2** continued

Method	Principles and Characteristics	Advantages	Disadvantages
HTPF	<ul style="list-style-type: none"> <li>• Pre-existing fracture reopening.</li> <li>• Used in petroleum engineering,</li> <li>• Suitable for the rock mass containing a large number of pre-existing fractures with varying dip and strike,</li> <li>• Essential to know precise locations and orientations of fractures prior to the test,</li> <li>• Measure the average normal stress perpendicular to the fracture plane, and then determine the 2D stresses in a plane perpendicular to the borehole axis.</li> </ul>	<ul style="list-style-type: none"> <li>• Limited to existing geological fractures.</li> </ul>	<ul style="list-style-type: none"> <li>• Currently provides the information of principal stresses in a plane,</li> <li>• Time-consuming.</li> </ul>
Borehole slotting	<ul style="list-style-type: none"> <li>• Local stress relief,</li> <li>• Used in mining and geotechnical engineering,</li> <li>• The rock mass is assumed to be homogeneous and isotropic and linear elastic theory is applied,</li> <li>• Determine the 2D stresses in the plane perpendicular to the borehole axis.</li> </ul>	<ul style="list-style-type: none"> <li>• No need of overcoring.</li> </ul>	<ul style="list-style-type: none"> <li>• Only provides the information of principal stresses in a plane,</li> <li>• Assess the stresses at measurement location.</li> </ul>
Flat jack	<ul style="list-style-type: none"> <li>• Partial stress relief,</li> <li>• Used in mining and geotechnical engineering,</li> <li>• Conducted at the surface of excavation,</li> <li>• The rock mass is uniform and isotropic,</li> <li>• The stress relief process is assumed to be completely reversible,</li> <li>• Measure the average excavation-induced stress perpendicular to the jack plane within the range of the cutting depth.</li> </ul>	<ul style="list-style-type: none"> <li>• Relatively simple measurement.</li> </ul>	<ul style="list-style-type: none"> <li>• Limited to stress measurement near the surface of an opening,</li> <li>• Evaluates the 2D stresses (not necessarily the in-situ stress) in the plane normal to the jack.</li> </ul>
Strain recovery	<ul style="list-style-type: none"> <li>• Measures the in-situ stresses based on the rock property of stress memory,</li> <li>• Performs the measurement for the cored sample obtained from field,</li> <li>• Normally used in determining the orientations of maximum and minimum horizontal stresses,</li> <li>• Assumes the principal directions of the in-situ stress field coincide with the principal directions of the strain measured.</li> </ul>	<ul style="list-style-type: none"> <li>• May be used to estimate the orientation of the horizontal principal in-situ stresses in 2D at large depth.</li> </ul>	<ul style="list-style-type: none"> <li>• More difficult to determine the magnitude of the stresses,</li> <li>• The accuracy of measurement is affected by many factors.</li> </ul>

Table 2.2 continued

Method	Principles and Characteristics	Advantages	Disadvantages
Back analysis	<ul style="list-style-type: none"> <li>Relieves partially the stresses around a measurement device,</li> <li>Used in mining, geotechnical and petroleum engineering,</li> <li>The rock mass is assumed to be homogeneous and isotropic,</li> <li>Used to determine the 2D in-situ stresses in the plane perpendicular to borehole axis.</li> </ul>	<ul style="list-style-type: none"> <li>Can be used in small deep well,</li> <li>No overcoring,</li> <li>Relatively inexpensive,</li> <li>Possible to determine the complete 3D stresses.</li> </ul>	<ul style="list-style-type: none"> <li>Procedure to determine the complete 3D stresses is complex.</li> </ul>
Geophysical methods	<ul style="list-style-type: none"> <li>Correlates mechanical parameters of rock formation and the in-situ stresses,</li> <li>Normally used in petroleum industry,</li> <li>Assumes the vertical stress component as a principal stress and then determine the magnitudes and orientations of the maximum and minimum horizontal stresses.</li> </ul>	<ul style="list-style-type: none"> <li>Takes advantage of available data in well logging.</li> </ul>	<ul style="list-style-type: none"> <li>The accuracy is affected by many factors,</li> <li>Analysis is complex,</li> <li>Difficult to determine stress magnitude in practice.</li> </ul>
Borehole breakout	<ul style="list-style-type: none"> <li>Stress induced compressive failure,</li> <li>Occurs mostly in high stress deep holes,</li> <li>Estimates the orientation of the minimum stress in a plane perpendicular to the borehole axis.</li> </ul>	<ul style="list-style-type: none"> <li>Relatively quick measurement.</li> </ul>	<ul style="list-style-type: none"> <li>Only gives orientations of principal stresses in a plane,</li> <li>Cannot determine stress magnitude.</li> </ul>
Geological observation	<ul style="list-style-type: none"> <li>Correlates principal stress direction and geological features,</li> <li>Involves a very large rock volume on regional scale,</li> <li>Assumes the vertical stress component as a principal stress and then determine the orientations of maximum and minimum horizontal principal stresses.</li> </ul>	<ul style="list-style-type: none"> <li>Low cost,</li> <li>Generally applied for the estimation of the orientations of historical horizontal principal stresses.</li> </ul>	<ul style="list-style-type: none"> <li>The results of stress are historical and may not be the current state,</li> <li>No stress magnitude given,</li> <li>The results are on a regional scale.</li> </ul>



# CHAPTER 3 BASIC THEORY OF DISPLACEMENT-BASED BACK ANALYSIS FOR IN-SITU STRESS DETERMINATION

The deformation (or displacement) of the rock mass around a well is the immediate effect of drilling. Displacement-based back analysis is applied to determine the in-situ stresses using the measurements of the deformation at different locations around the well induced by drilling.

## 3.1 EFFECT OF DRILLING ON FIELD STRESSES

By the theory of linear elasticity, different types of governing equations will be used in connecting force, stress, strain and displacement, namely equilibrium equations, constitutive equations, strain-displacement equations, as depicted in Figure 3.1. The detail is given in Appendix A.

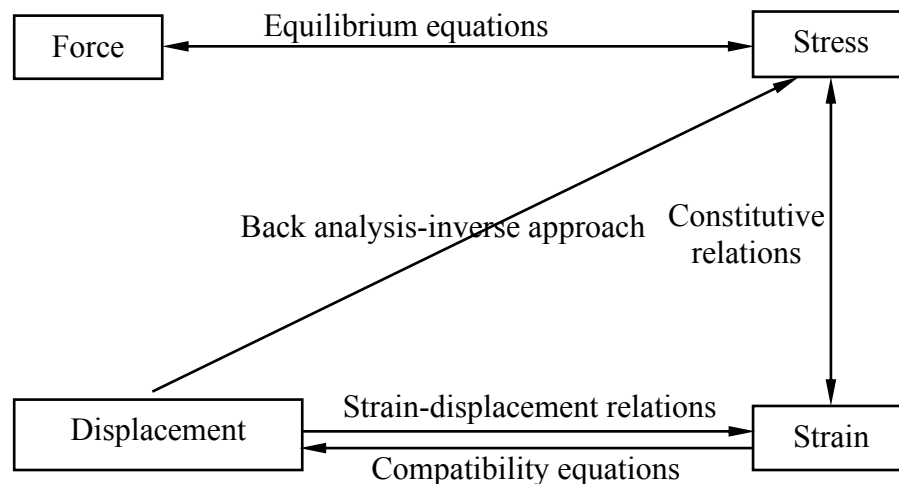


**Figure 3.1** Governing equations relating force, stress, strain and displacement

As stated in Chapter 1, the rock is subject to a three-dimensional in-situ stress field with the three components of normal stress  $\sigma_x$ ,  $\sigma_y$ , and  $\sigma_z$  and the three components of shearing stress  $\tau_{xy}$ ,  $\tau_{yz}$  and  $\tau_{zx}$ , defined in an  $x, y, z$  coordinate system (Cartesian coordinate). These are the virgin formation stresses acting in a rock mass prior to drilling.

If a circular well with the radius  $r_o$  is drilled into the rock in the direction of the  $z$  axis, there is a new state of stresses distributed in the rock surrounding the well, as demonstrated in Figures 3.2 and 3.3.

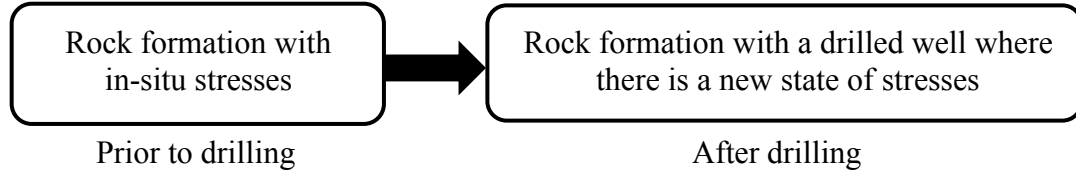


Figure 3.2 Stress change after drilling

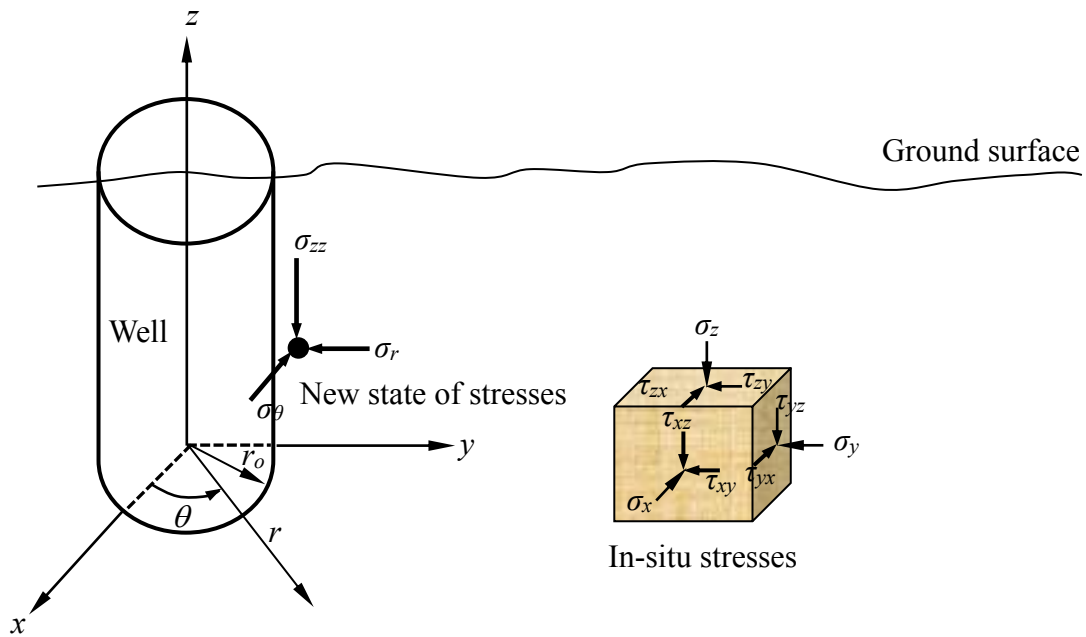


Figure 3.3 A new state of stresses after drilling in cylindrical coordinates and in-situ stresses prior to drilling in Cartesian coordinates

The new stresses after drilling of a well are (Nauroy 2011)

$$\sigma_r = \frac{1}{2}(\sigma_x + \sigma_y) \left(1 - \frac{r_o^2}{r^2}\right) + \frac{1}{2}(\sigma_x - \sigma_y) \left(1 - 4\frac{r_o^2}{r^2} + 3\frac{r_o^4}{r^4}\right) \cos 2\theta + \tau_{xy} \left(1 - 4\frac{r_o^2}{r^2} + 3\frac{r_o^4}{r^4}\right) \sin 2\theta \quad (3.1a)$$

$$\sigma_\theta = \frac{1}{2}(\sigma_x + \sigma_y) \left(1 + \frac{r_o^2}{r^2}\right) - \frac{1}{2}(\sigma_x - \sigma_y) \left(1 + 3\frac{r_o^4}{r^4}\right) \cos 2\theta - \tau_{xy} \left(1 + 3\frac{r_o^4}{r^4}\right) \sin 2\theta \quad (3.1b)$$

$$\sigma_{zz} = \sigma_z - \nu \left[ \frac{1}{2}(\sigma_x - \sigma_y) \cos 2\theta + \tau_{xy} \sin 2\theta \right] 4 \frac{r_o^2}{r^2} \quad (3.1c)$$

$$\tau_{r\theta} = \left[ -\frac{1}{2}(\sigma_x - \sigma_y) \sin 2\theta + \tau_{xy} \cos 2\theta \right] \left( 1 + 2 \frac{r_o^2}{r^2} - 3 \frac{r_o^4}{r^4} \right) \quad (3.1d)$$

$$\tau_{\theta z} = \left( -\tau_{xz} \sin \theta + \tau_{yz} \cos \theta \right) \left( 1 + \frac{r_o^2}{r^2} \right) \quad (3.1e)$$

$$\tau_{rz} = \left( \tau_{xz} \cos \theta + \tau_{yz} \sin \theta \right) \left( 1 - \frac{r_o^2}{r^2} \right) \quad (3.1f)$$

where  $r_o$  is the well radius (the geometry of the well being drilled),  $r$  is the distance from the well axis to a point in the rock mass, and  $\theta$  represents the azimuth angle relative to the  $x$ -axis in the  $xy$  plane perpendicular to the well axis  $z$ .

Eqn. (3.1) can be written in a simplified matrix form.

$$\{\sigma\} = [M_s] \{\sigma_o\} \quad (3.2)$$

where  $[M_s]$  is a coefficient matrix of size (6×6), dependent on the location and size of the well being drilled and  $\{\sigma\}$  is a stress vector given as

$$\{\sigma\} = \begin{Bmatrix} \sigma_r \\ \sigma_\theta \\ \sigma_{zz} \\ \tau_{r\theta} \\ \tau_{\theta z} \\ \tau_{rz} \end{Bmatrix} \quad (3.3)$$

is the tensor of the new state of stress surrounding the well.

In a special condition where the vertical stress is supposed to be one principal stress and in the horizontal  $xy$  plane the maximum principal stress  $\sigma_{Hmax}$  and the minimum principal stress  $\sigma_{Hmin}$  are parallel to  $x$  and  $y$  directions, respectively.  $x$  becomes the major principal direction and  $y$  the minor principal direction. In this case, the stresses at a distance  $r$  from the center of the well in cylindrical coordinates can be described as

$$\sigma_r = \frac{1}{2}(\sigma_{Hmax} + \sigma_{Hmin}) \left( 1 - \frac{r_o^2}{r^2} \right) + \frac{1}{2}(\sigma_{Hmax} - \sigma_{Hmin}) \left( 1 - 4 \frac{r_o^2}{r^2} + 3 \frac{r_o^4}{r^4} \right) \cos 2\theta \quad (3.4a)$$

$$\sigma_{\theta} = \frac{1}{2}(\sigma_{H \max} + \sigma_{H \min}) \left(1 + \frac{r_o^2}{r^2}\right) - \frac{1}{2}(\sigma_{H \max} - \sigma_{H \min}) \left(1 + 3\frac{r_o^4}{r^4}\right) \cos 2\theta \quad (3.4b)$$

$$\sigma_{zz} = \sigma_z - \nu \left[ \frac{1}{2}(\sigma_{H \max} - \sigma_{H \min}) \right] 4\frac{r_o^2}{r^2} \quad (3.4c)$$

$$\tau_{r\theta} = \left[ -\frac{1}{2}(\sigma_{H \max} - \sigma_{H \min}) \sin 2\theta \right] \left(1 + 2\frac{r_o^2}{r^2} - 3\frac{r_o^4}{r^4}\right) \quad (3.4d)$$

$$\tau_{\theta z} = 0 \quad (3.4e)$$

$$\tau_{rz} = 0 \quad (3.4f)$$

In a deep well, when a stress field with equal horizontal stress components ( $\sigma_{H \max} = \sigma_{H \min} = \sigma_h$ ) is supposed to exist, Eqn. (3.4) will reduce to

$$\sigma_r = \sigma_h \left(1 - \frac{r_o^2}{r^2}\right) \quad (3.5a)$$

$$\sigma_{\theta} = \sigma_h \left(1 + \frac{r_o^2}{r^2}\right) \quad (3.5b)$$

$$\sigma_{zz} = \sigma_z \quad (3.5c)$$

$$\tau_{r\theta} = \tau_{\theta z} = \tau_{rz} = 0 \quad (3.5d)$$

### 3.2 FORMULATION OF A GENERAL EQUATION FOR DEFORMATION ANALYSIS

The displacement-stress relationship can be derived from constitutive relations and compatibility equations.

Substituting Eqn. (A.5a) into Eqn. (A.6a) results in

$$\frac{\partial u_r}{\partial r} = \frac{1}{E} [\sigma_r - \nu(\sigma_{\theta} + \sigma_{zz})] \quad (3.6)$$

Similarly, by combining Eqns. (A.5b) and (A.6b), we have

$$\frac{\partial u_{\theta}}{\partial \theta} = \frac{r}{E} [\sigma_{\theta} - \nu(\sigma_r + \sigma_{zz})] - u_r \quad (3.7)$$

Integrating Eqn. (3.6) and Eqn. (3.7) yields

$$u_r = \int \frac{1}{E} [\sigma_r - \nu(\sigma_\theta + \sigma_{zz})] dr \quad (3.8)$$

$$u_\theta = \int \frac{r}{E} [\sigma_\theta - \nu(\sigma_r + \sigma_{zz})] d\theta - \int u_r d\theta \quad (3.9)$$

### 3.2.1 Radial Displacement in a Stress Field with Equal Horizontal Stress Components

The radial displacement around a well induced by drilling can be obtained by inserting Eqns. (3.5a), (3.5b) and (3.5c) into Eqn. (3.8) and integrating.

$$\begin{aligned} u_r &= \frac{1}{E} \int \left[ \sigma_h \left( 1 - \frac{r_o^2}{r^2} \right) - \nu \sigma_h \left( 1 + \frac{r_o^2}{r^2} \right) - \nu \sigma_z \right] dr \\ &= \frac{1}{E} \left[ \sigma_h \left( r + \frac{r_o^2}{r} \right) - \nu \sigma_h \left( r - \frac{r_o^2}{r} \right) - \nu \sigma_z r \right] + c(\theta) \\ &= \frac{r}{E} \left[ \sigma_h \left( 1 + \frac{r_o^2}{r^2} \right) - \nu \sigma_h \left( 1 - \frac{r_o^2}{r^2} \right) - \nu \sigma_z \right] + c(\theta) \end{aligned} \quad (3.10)$$

At the well wall with  $r = r_o$

$$u_r = \frac{r_o}{E} (2\sigma_h - \nu\sigma_z) + c(\theta) \quad (3.11)$$

where  $c(\theta)$  is the integration constant.

Eqns. (3.5a), (3.5b), (3.5c) and (3.10) are inserted into Eqn. (3.9).

$$\begin{aligned} u_\theta &= \int \frac{r}{E} \left[ \sigma_h \left( 1 + \frac{r_o^2}{r^2} \right) - \nu \sigma_h \left( 1 - \frac{r_o^2}{r^2} \right) - \nu \sigma_z \right] d\theta \\ &\quad - \int \left\{ \frac{r}{E} \left[ \sigma_h \left( 1 + \frac{r_o^2}{r^2} \right) - \nu \sigma_h \left( 1 - \frac{r_o^2}{r^2} \right) - \nu \sigma_z \right] + c(\theta) \right\} d\theta \\ &= - \int c(\theta) d\theta \end{aligned} \quad (3.12)$$

By Eqns. (A.5d), (A.6d) and (3.5d), we obtain

$$\gamma_{r\theta} = \frac{\partial u_\theta}{\partial r} + \frac{1}{r} \frac{\partial u_r}{\partial \theta} - \frac{u_\theta}{r} = \frac{2(1+\nu)}{E} \tau_{r\theta} = 0 \quad (3.13)$$

The results of the derivative of  $u_\theta$  with respect to  $r$  and the derivative of  $u_r$  with respect to  $\theta$  are shown in Eqn. (3.14) and Eqn. (3.15), respectively.

$$\frac{\partial u_\theta}{\partial r} = 0 \quad (3.14)$$

$$\frac{1}{r} \frac{\partial u_r}{\partial \theta} = \frac{c'(\theta)}{r} \quad (3.15)$$

After substitution of Eqns. (3.14), (3.15) and (3.12) into Eqn. (3.13), the resulting equation is

$$\frac{c'(\theta)}{r} + \frac{\int c(\theta) d\theta}{r} = 0 \quad (3.16)$$

The integration constant  $c(\theta)$  can be found from Eqn. (3.16). It is equal to 0. Accordingly, Eqn. (3.11) becomes

$$u_r = \frac{r_o}{E} (2\sigma_h - \nu\sigma_z) \quad (3.17)$$

### 3.2.2 Radial Displacement in a Stress Field with Differential Horizontal Stress Components

Following the same procedure as in the previous section, the relationship between the radial deformation and the in-situ stresses can be derived.

$$u_r = \frac{r}{E} \left\{ \begin{array}{l} \sigma_x \left\{ \frac{1}{2} \left[ ((1-\nu) + (1+\nu) \frac{r_o^2}{r^2}) + ((1+\nu) + 4(1-\nu^2) \frac{r_o^2}{r^2} - (1+\nu) \frac{r_o^4}{r^4}) \cos 2\theta \right] \right\} \\ + \sigma_y \left\{ \frac{1}{2} \left[ ((1-\nu) + (1+\nu) \frac{r_o^2}{r^2}) - ((1+\nu) + 4(1-\nu^2) \frac{r_o^2}{r^2} - (1+\nu) \frac{r_o^4}{r^4}) \cos 2\theta \right] \right\} \\ + \tau_{xy} \left\{ \left[ (1+\nu) + 4(1-\nu^2) \frac{r_o^2}{r^2} - (1+\nu) \frac{r_o^4}{r^4} \right] \sin 2\theta \right\} \\ + \sigma_z [-\nu] \\ + c(\theta) \end{array} \right\} \quad (3.18)$$

The value of integration constant  $c(\theta)$  in Eqn. (3.18) is zero, which can be found by equalling Eqn. (A.5d) to Eqn. (A.6d). In order to solving this, it is necessary to use Eqns. (A.6d), (3.1d), (3.9) and (3.18) together. The derivation for solving this constant is the same as the previous section.

$$u_r = M_1\sigma_x + M_2\sigma_y + M_3\sigma_z + M_4\tau_{xy} \quad (3.19)$$

$$\text{Where } M_1 = \frac{r_o}{E}(1 + 2\cos 2\theta - 2\nu^2 \cos 2\theta) \quad (3.20a)$$

$$M_2 = \frac{r_o}{E}(1 - 2\cos 2\theta + 2\nu^2 \cos 2\theta) \quad (3.20b)$$

$$M_3 = -\frac{r_o\nu}{E} \quad (3.20c)$$

$$M_4 = \frac{4r_o}{E}(1 - \nu^2)\sin 2\theta \quad (3.20d)$$

### 3.3 BACK ANALYSIS FOR ESTIMATING THE IN-SITU STRESSES

In comparison to direct measurement of stresses, the displacement of a well due to stress changes can be measured more easily and reliably. Measurement of displacement is also more practical in the field (Leeman 1967, Gray and Toew 1967, Zou 1995a). Results of stresses derived from field measurements are more representative in the vicinity for a planned well.

Back analysis can be basically divided into two categories: inverse and direct approaches (Zou 1995a, Feng et al 2000, Shang et al 2002, Zhang et al 2006b, Ghorbani et al 2009, Tang 2009, Dehghan et al 2012, Yazdani et al 2012, Moreira et al 2013). For the inverse approach, mathematical formulation is just the reverse of ordinary stress analysis. It is more efficient than the direct approach, but is not appropriate for non-linear problem. For the direct approach, the model does not need to be modified like the inverse approach and can be applied to non-linear problem. It however demands more iterations in analysis for a solution to converge. In this research, the inverse approach is used because it provides one step solution to a relatively small set of equations without iteration.

In the inverse approach of back analysis, the measured displacements are input data, while the in-situ stresses are output data (Figure 3.4).

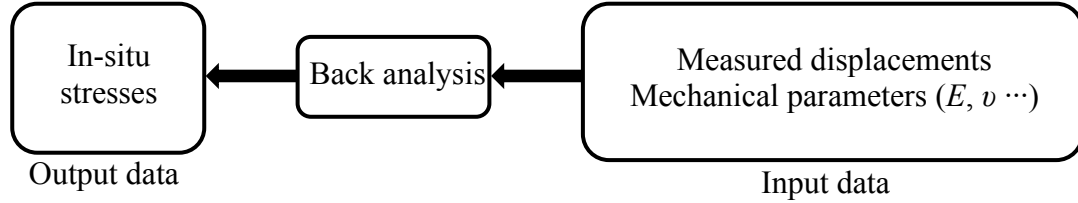


**Figure 3.4** Displacement-based back analysis

If there is a total of  $n$  measurements of displacement along different directions around a well, then Eqn. (3.19) can be expressed as a matrix form.

$$\{u_r\} = [M]\{\sigma_o\}^* \quad (3.21)$$

where  $\{u_r\}$  is the assembled displacement vector of size  $(n \times 1)$ ,  $[M]$  is the assembled displacement coefficient matrix of size  $(n \times 4)$  and  $\{\sigma_o\}^* = \{\sigma_x \ \sigma_y \ \sigma_z \ \tau_{xy}\}^T$ .

Least square method is applied to obtain the best-fit solution of the in-situ stresses  $\{\sigma_o\}^*$ . In order to provide adequate information to determine the in-situ stresses, the number of displacement measurements is usually greater than the number of unknown parameters (independent stress components in this research), and Eqn. (3.21) becomes a set of redundant equations.



# **CHAPTER 4 WELL SIZE MEASUREMENT AND FUNDAMENTALS OF RESERVOIR ROCK FORMATION**

## **4.1 CALIPER LOGGING**

Caliper logging is a practice of measuring the variations in the diameter of a well. The device used for this practice is called a caliper log (Boonen and McElhinney 2002, Special Open Hole Tools-Caliper Logs 2009, Openhole caliper logs 2015, Caliper log 2019).

It is important to accurately know the borehole diameter for

- computing wellbore volume to determine the amount of cement needed to fill up to a certain depth,
- analyzing wellbore stability,
- interpreting other logs,
- locating permeable zones as evidenced by the presence of a filter cake.

There are two major types of caliper logs: mechanical and ultrasonic caliper logs.

Most caliper tools are mechanical. They consist of two or more articulated arms, which are pushed out against the well wall by springs or hydraulic pressure (Figure 4.1). In most modern caliper tools, the arms are connected to a potentiometer circuit using transducers, which is called “contactless” linear displacement sensors. The movement of arms as a result of the variation in wellbore diameter is converted to varying electrical signal, which is measured at the surface. Eventually the change in the output signals can be converted to the change in wellbore diameter using processing software.

At present, commercial tools have from 2 to 60 fingers supplied by different manufacturers such as Gowell, Hotwell, Weatherford, Halliburton, Sondex and Spartek systems (Maxted and Hazel 1995, MSC 2014, Julian et al 2007, Warrior logging software 2014, Landsea 2018). If a multi-sensor caliper tool has 40 arms, it means that there are 20 pairs of arms to

measure the wellbore diameter in 20 different directions (Figure 4.2). The resolution and accuracy of this type of measurement tool vary in the range of 0.025 ~ 0.1 mm and 0.25~1 mm, respectively. They are affected by the number of arms and the wellbore size (MFC 2017, MSC 2014).

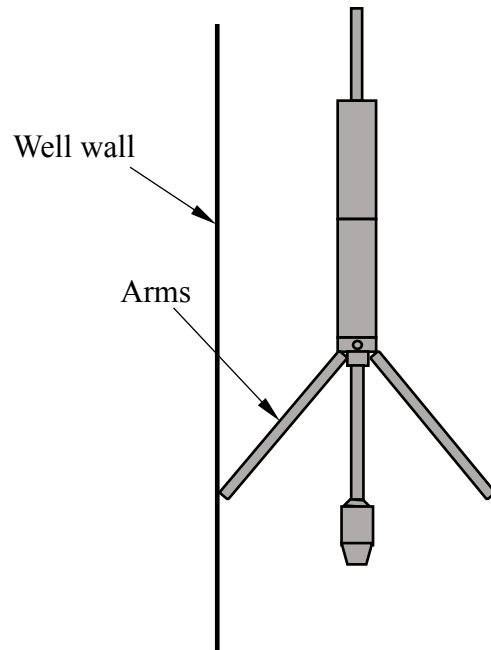


**Figure 4.1** Schematic diagram of mechanical caliper measuring the diameter of a well

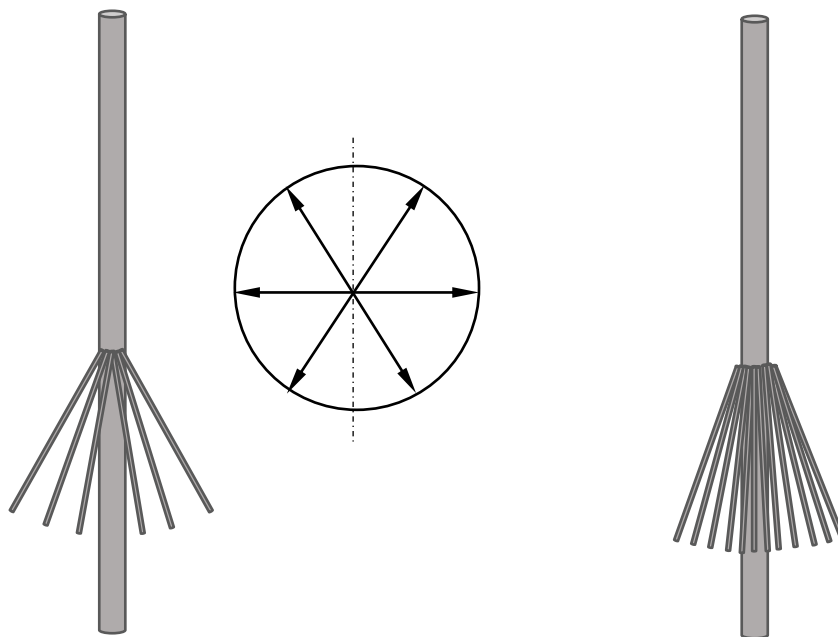


**Figure 4.2** Schematic drawing of multi-arm caliper tools

Acoustic imaging tools also act like a caliper (Borehole imaging 2015, Serra 2004). They are developed for measurement while drilling (MWD) that perform real time measurements. With this tool, a transducer (in transmit mode) emits a high-frequency pulse which is reflected by the well wall back to the transducer (in receive mode). The travel time for the acoustic pulse depends on the distance between the transducer and the well wall, as well as the velocity in the mud (Figure 4.3). The transducer is rotated to produce a cross section of the wellbore size and full-coverage images of the well wall. The resolution of measurement is 0.075 mm at 500-kHz frequency, or 0.150 mm at 250 kHz, with an accuracy of  $\pm 3$  mm.

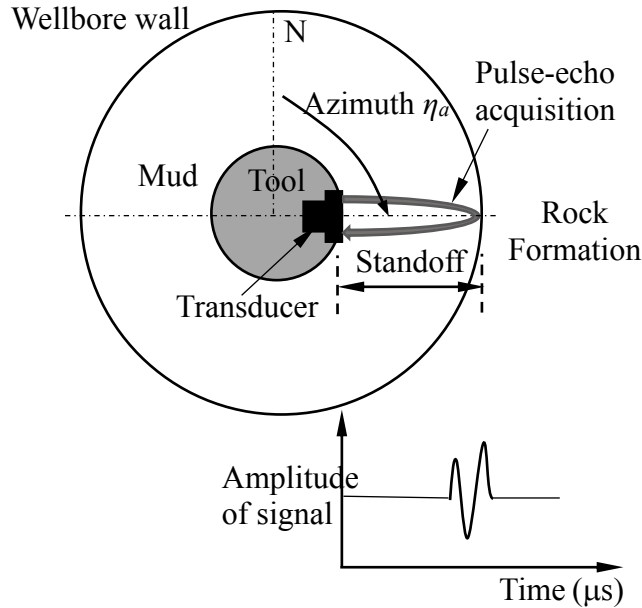


**Figure 4.3** Illustration of ultrasonic caliper measurement

Both the reflected amplitudes and the two-way travel times are recorded. By measuring the mud velocity, the travel time data can also be used to provide precise wellbore caliper information. For a given tool orientation this gives a standoff in the direction the tool is pointing. The diameter is determined by combining opposite standoff data with the diameter of the tool collar.

$$d = d_s + d_t \quad (4.1)$$

$$d_s = d_{s1} + d_{s2} = \frac{v_{mud}t_1}{2} + \frac{v_{mud}t_2}{2} \quad (4.2)$$

where  $d_s$  is the sum of opposite standoff data,  $d_t$  is the diameter of the tool collar,  $v_{mud}$  is the mud velocity,  $t_1$  is the two-way travel time in the direction  $\eta_a$ , and  $t_2$  is the two-way travel time in the direction  $\eta_a+180^\circ$ .

In this research, caliper logging data may be used to determine the diametrical convergence at different directions around a well, which are then to be related to the field stresses through the constitutional relationships between stress and deformation. This makes it possible to estimate the in-situ stresses in a rock mass around a well by displacement back analysis.

## 4.2 ROCK FORMATION POROSITY AND PORE PRESSURE

Subsurface rocks in a reservoir are porous media and often saturated with fluids (e.g., water, oil, gas, etc.). The rock actually contains two parts: rock grains and fluid-filled pores, as illustrated in Figure 4.4.

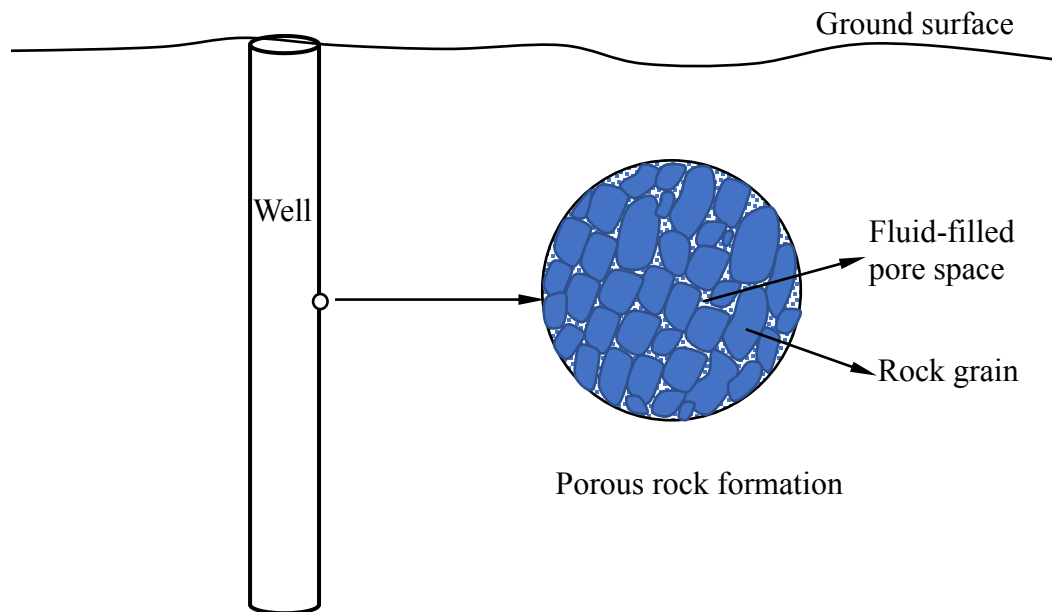


**Figure 4.4** Schematic showing rock formation with pore space in the vicinity of a drilled well

Porosity is one of the important parameters for the porous rock formation in petroleum industry. The porosity of most sedimentary rocks is generally lower than 40% and reduces

with depth. Table 4.1 lists the porosity values of some typical rocks at different depths.

**Table 4.1** Porosity at different formation depth for typical rock materials (After Aadnøy and Looyeh 2011)

Lithology	Formation depth [ft]			
	5,000	10,000	15,000	20,000
Marble	21%	10%	4%	1%
Shale	25%	15%	8%	4%
Slate	28%	19%	14%	11%
Basalt	32%	24%	19%	17%
Sandstone	36%	28%	25%	23%

The pressure of the fluid within the pore space of the formation rock is named as formation pore pressure  $p_p$ . Estimation of pore pressure is primarily based on correlation of available data from nearby wells and geophysical method (e.g., seismic data) before a well is drilled (Bourgoyne et al 1986). There are generally two kinds of formation pore pressure, which are:

a) Normal formation pore pressure (hydro-pressure)

In this situation, pore fluids are assumed to be in hydrostatic equilibrium underground. It depends on the density of the fluid in the pores, integrated from surface to the depth of interest. If the pore fluid is fresh water, the normal hydrostatic pressure gradient is usually 0.433 psi/ft, or 9.81 kPa/m. Saturated salt water generates a gradient of 0.460 psi/ft or 10.4 kPa/m.

b) Abnormal formation pore pressure (geo-pressure)

When the boundaries of some regions are impermeable, they prevent the fluid from flowing to the adjacent regions. In such case, pore pressure is abnormally high and usually ranges between 0.8 psi/ft (18.1 kPa/m) and 1 psi/ft (22.7 kPa/m).

### 4.3 ROCK PERMEABILITY

Permeability is another important parameter for the porous rock, which characterizes the ability of a fluid to flow through the rock pore space under pressure (Figure 4.5). It is controlled by the connected passages of the pore space.

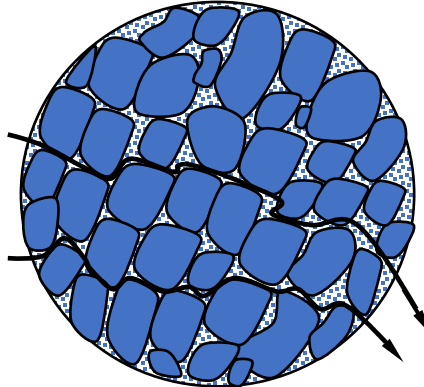


**Figure 4.5** Fluid flowing through the rock pore space under pressure

The permeability of a rock largely relies on the porosity, the rock grain size and distribution, grain shape, grain packing, and the degree of consolidation and cementation (Schön 2011). In terms of permeability, rock formations can be divided into three categories: practically impermeable dense rocks (e.g., compact magmatites, dense anhydrite, rock salt), low permeability rocks (e.g., shale to carbonates, sand/sandstone), and high permeability rocks (e.g., gravel and karstic limestone). Table 4.2 gives the permeability of some typical rock materials at different depth.

**Table 4.2** Permeability  $k$  ( $\times 10^{-3} \mu\text{m}^2$ , or md) at different depth for typical rock materials (After Aadnøy and Looyeh 2011)

Lithology	Formation depth (ft)			
	5,000	10,000	15,000	20,000
Shale	0.1	–	–	–
Granite	0.7	0.2	0.1	–
Slate	4	0.6	0.2	0.1
Sandstone	9	2	0.7	0.45
Limestone	30	5	3	1

#### 4.4 EFFECTIVE STRESS LAW

The pore fluid will carry part of the total stresses applied to the system, thus relieving the rock matrix from part of the load. This concept was defined by Terzaghi and introduced in soil mechanics in 1923 (Aadnøy and Looyeh 2011). Accordingly the deformation of the rock matrix is dominated by the effective stress, which is given as

$$\sigma' = \sigma - p_p \quad (4.3)$$

where  $\sigma$  is the normal stress,  $p_p$  is the pore pressure, and  $\sigma'$  is the effective stress.

Since a fluid at rest cannot transmit shear stresses, the effective stress is valid for normal stresses, and therefore the shear stress remains unchanged.

In a more general representation of the effective stress, a scaling factor with respect to the pore pressure is included. This is known as the Biot's coefficient  $\alpha$ .

$$\sigma' = \sigma - \alpha p_p \quad (4.4)$$

where

$$\alpha = 1 - \frac{E(1-2\nu_i)}{E_i(1-2\nu)} = 1 - \frac{K_B}{K_M} \quad (4.5)$$

where  $E$  and  $\nu$  are the modulus of elasticity and the Poisson's ratio for the bulk material, respectively. The index  $i$  refers to the inter-pore material.  $K_B$  and  $K_M$  are respectively the bulk moduli of the bulk material and of the rock matrix. The Biot's coefficient has a value in the order of 0.8-1.0 for rocks. In many applications, if no other information is available, the Biot's coefficient is usually taken as one.

# CHAPTER 5 TWO-DIMENSIONAL BACK ANALYSIS OF WELL DEFORMATION

## 5.1 STRESSES IN THE VICINITY OF A WELL IN RESERVOIR ROCK FORMATION

In petroleum engineering, in some cases porosity as well as permeability will have an impact on the near-wellbore stresses.

Apart from the in-situ stresses, some other major factors affecting the near-wellbore stress distribution include (Figure 5.1):

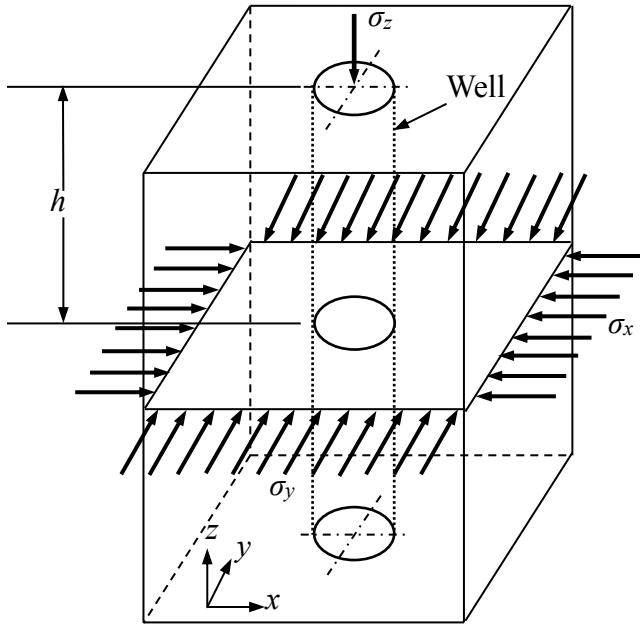
- 1) drilling fluid pressure (mud pressure)  $p_m$
- 2) pore pressure  $p_p$
- 3) permeability of rock formation and permeability of well wall

As stated in Chapter 3, once a well is drilled, the support provided by the rock is removed. This change alters the stresses. The stresses at any point on or near the well can be described in terms of:

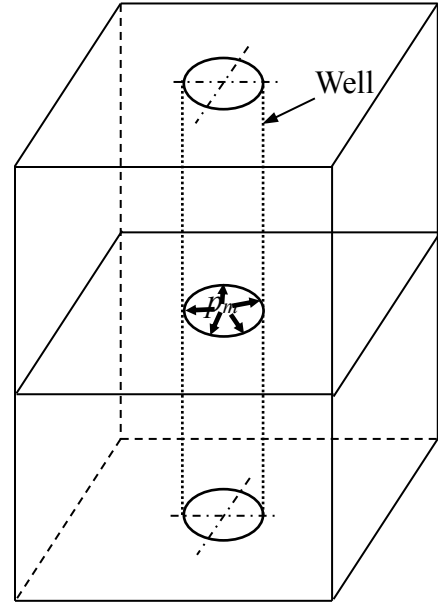
- radial stress  $\sigma_r$  acting along the radius of the wellbore
- tangential (hoop) stress  $\sigma_\theta$  acting around the circumference of the wellbore
- axial stress  $\sigma_{zz}$  acting parallel to the well path and
- shear stress components designated by  $(\tau_{r\theta}, \tau_{\theta z}, \tau_{rz})$

The relations between the new state of stresses at any point on or near the wellbore in cylindrical coordinates after drilling and the in-situ stresses in Cartesian coordinate can be expressed by Eqns. (3.1a) - (3.1f) in an elastic and isotropic medium. The detailed information can be found in Section 3.1 of Chapter 3.

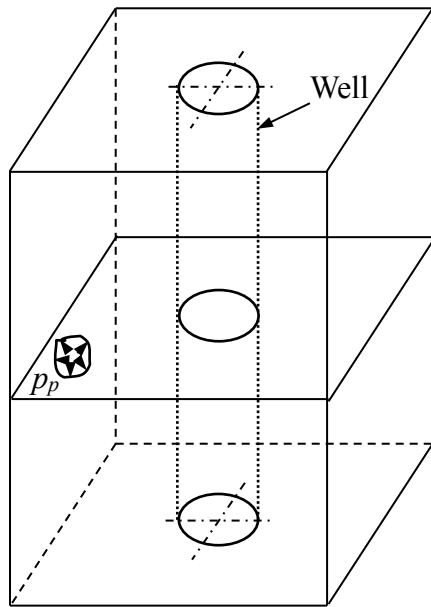




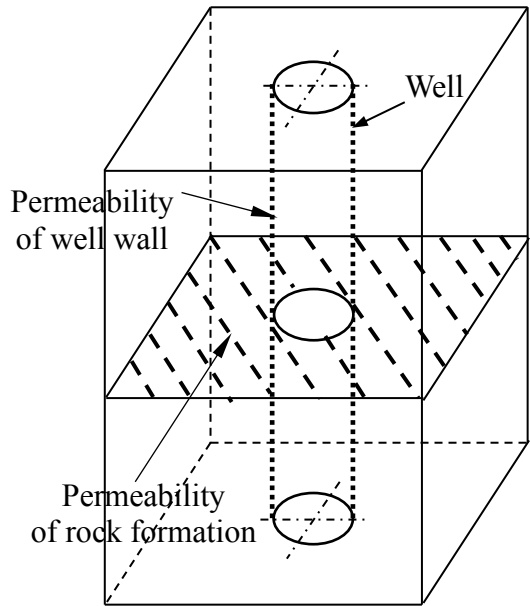
In-situ stresses  $\{\sigma_o\}$



Drilling mud pressure  $p_m$



Formation pore pressure  $p_p$



Permeability of well wall and rock formation

**Figure 5.1** Factors affecting the near-wellbore stress distribution

### 5.1.1 Effect of Drilling Mud Pressure

Drilling fluids, also referred to as drilling mud, are added to the well to facilitate the drilling process by suspending cuttings, controlling pressure, stabilizing exposed rock, providing buoyancy, cooling and lubricating.

Therefore, inside the well, there is a pressure,  $p_m$ , due to the existence of the drilling mud. This pressure also can help keep the well stable from a mechanistic point of view.

$$\begin{cases} \sigma_r = p_m \frac{r_o^2}{r^2} \\ \sigma_\theta = -p_m \frac{r_o^2}{r^2} \\ \sigma_{zz} = 0 \\ \tau_{r\theta} = 0 \\ \tau_{\theta z} = 0 \\ \tau_{rz} = 0 \end{cases} \quad (5.1)$$

There is no effect on axial stress  $\sigma_{zz}$  and the shear stresses. The drilling mud pressure  $p_m$  is proportional to well depth and mud density.

$$p_m = \rho_m g h \quad (5.2)$$

where  $\rho_m$  is the density of drilling mud used inside the well ( $\text{kg/m}^3$ ),  $h$  is the well depth (m) and  $g$  is the gravity constant (9.81 N/kg).

The mud density at different ranges of depth is designed to fit in a window between the pore pressure and formation fracture pressure (minimum principal stress). In most circumstances, the vertical stress is used as an approximation of the minimum principal stress.

### 5.1.2 Effect of Permeability of Rock Formation and Well Wall

The mud pressure in general is higher than the formation pore pressure during drilling, so that some drilling mud may penetrate into the formation under the pressure difference,

especially in high permeability rock formation. If impermeable mud cake is quickly formed on the wellbore wall, it can prevent drilling mud from flowing into the formation. In this situation, the pore pressure is not influenced by the mud pressure. If the mud cake is unable to form well on the wellbore wall, the wellbore wall is non-sealing. Accordingly part of mud in the well will penetrate into the formation, causing loss of the drilling mud (Figure 5.2). This will affect the stresses surrounding the well.

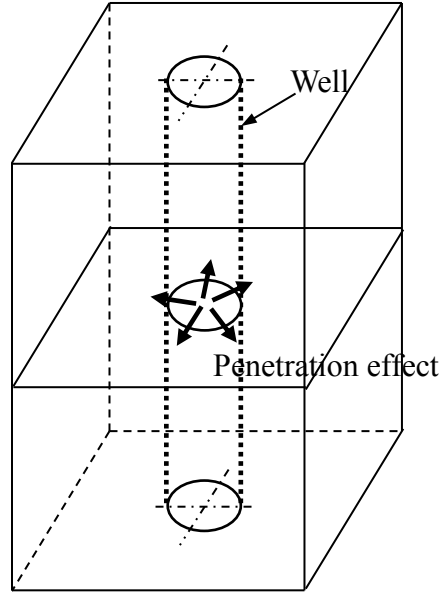


**Figure 5.2** Penetration effect of drilling mud for a non-sealing wellbore wall

The rock formation is assumed to be a porous medium and Darcy's law is applied for fluid flow in this medium. The superimposed stresses surrounding a well induced by radial flow of drilling mud into the pore space in the formation without consideration of time effect can be expressed as below (Zhao 2007):

$$\begin{cases} \sigma_r = \left[ \frac{\alpha(1-2\nu)}{2(1-\nu)} \left( 1 - \frac{r_o^2}{r^2} \right) - \phi \right] (p_m - p_p) \\ \sigma_\theta = \left[ \frac{\alpha(1-2\nu)}{2(1-\nu)} \left( 1 + \frac{r_o^2}{r^2} \right) - \phi \right] (p_m - p_p) \\ \sigma_{zz} = \left[ \frac{\alpha(1-2\nu)}{2(1-\nu)} - \phi \right] (p_m - p_p) \\ \tau_{r\theta} = \tau_{\theta z} = \tau_{rz} = 0 \end{cases} \quad (5.3)$$

For low permeability rock formation, pore fluid cannot flow out the pore space quickly enough, resulting in a pore pressure storage effect, an undrained condition. The pore pressure is instantaneously modified with respect to its original homogeneous value, which can be calculated by Skempton's equation (Charlez 1997).

$$\Delta p_p = s \Delta \sigma \quad (5.4)$$

where  $s$  is the Skempton's coefficient and  $\Delta \sigma$  is the variation in mean stress; and

$$s = \frac{1}{\alpha} \left[ 1 - \frac{K_B}{K_u} \right] \quad (5.5)$$

$$\Delta \sigma = -\frac{(1+\nu_u)}{3} \frac{4r_o^2}{r^2} \frac{(\sigma_{Hmax} - \sigma_{Hmin})}{2} \cos 2\theta' \quad (5.6)$$

$$\Delta p_p = -\frac{2s(1+\nu_u)}{3} \frac{r_o^2}{r^2} (\sigma_{Hmax} - \sigma_{Hmin}) \cos 2\theta' \quad (5.7)$$

$K_B$ ,  $K_u$  and  $\nu_u$  being respectively drained bulk modulus, undrained bulk modulus, and undrained Poisson's ratio.  $\sigma_{Hmax}$  is the maximum horizontal principal stress,  $\sigma_{Hmin}$  is the minimum horizontal principal stress, and  $\theta'$  is measured from the maximum horizontal principal stress direction counter clockwise.

In order to apply Eqn. (5.7) to the stresses in an arbitrary axis,  $\sigma_{Hmax}$  and  $\sigma_{Hmin}$  need to be resolved to  $x$  and  $y$  direction and the final expression is given as

$$\Delta p_p = -\frac{4s(1+\nu_u)}{3} \frac{r_o^2}{r^2} \left( \frac{\sigma_x - \sigma_y}{2} \cos 2\theta + \tau_{xy} \sin 2\theta \right) \quad (5.8)$$

where  $\theta$  is measured counter clockwise from the  $x$  axis.

Hence, the effects on stresses from pore pressure change  $\Delta p_p$  are

$$\begin{cases} \sigma_r = -\alpha p'_p = -\alpha \left[ p_p - \frac{4s(1+\nu_u)}{3} \frac{r_o^2}{r^2} \left( \frac{\sigma_x - \sigma_y}{2} \cos 2\theta + \tau_{xy} \sin 2\theta \right) \right] \\ \sigma_\theta = -\alpha p'_p = -\alpha \left[ p_p - \frac{4s(1+\nu_u)}{3} \frac{r_o^2}{r^2} \left( \frac{\sigma_x - \sigma_y}{2} \cos 2\theta + \tau_{xy} \sin 2\theta \right) \right] \\ \sigma_{zz} = -\alpha p'_p = -\alpha \left[ p_p - \frac{4s(1+\nu_u)}{3} \frac{r_o^2}{r^2} \left( \frac{\sigma_x - \sigma_y}{2} \cos 2\theta + \tau_{xy} \sin 2\theta \right) \right] \\ \tau_{r\theta} = \tau_{\theta z} = \tau_{rz} = 0 \end{cases} \quad (5.9)$$

## 5.2 STRESSES IN THE VICINITY OF A WELL IN DIFFERENT SCENARIOS

According to the above analysis on the effects of pore pressure, mud pressure, permeability of well wall and rock formation, the normal stresses are affected in various degrees but there are no changes on the shear stresses surrounding a well. The normal stresses surrounding a well under different scenarios can be written in the following equations.

### 5.2.1 An In-situ Stress Field with Differential Horizontal Stress Components

In general, the in-situ stress field in the plane perpendicular to the well axis has different stress components,  $\sigma_x \neq \sigma_y$ , and there are two different principal stresses in this plane (Figure 5.3).

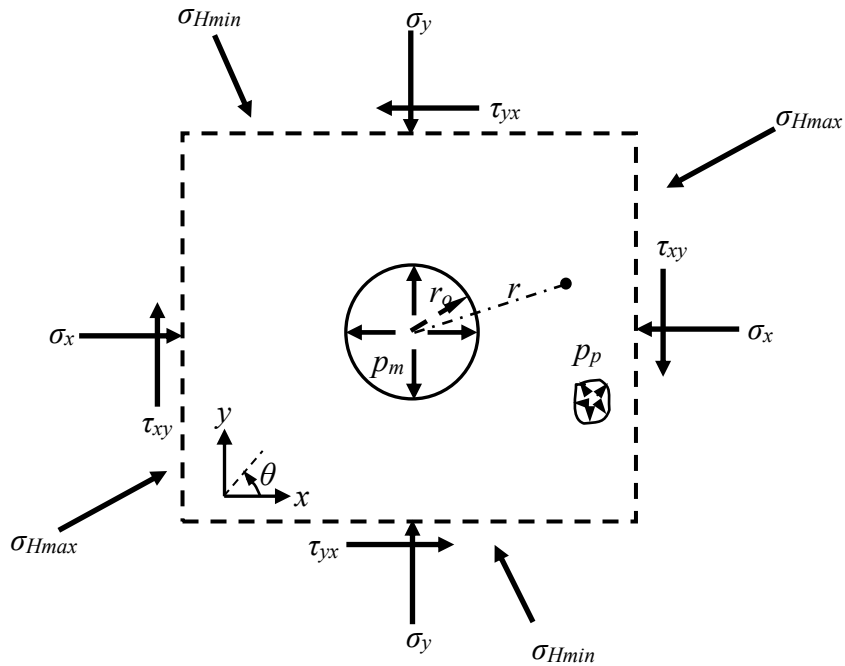


**Figure 5.3** An in-situ stress field with differential horizontal stress components

**a.** Rock formation with no pore pressure effect (NP) (scenario 1)

In this situation, no effect of pore pressure exists. The normal stresses surrounding a well after drilling are majorly affected by the in-situ stresses and drilling mud pressure, which are given as

$$\left\{ \begin{array}{l} \sigma_r = \frac{1}{2}(\sigma_x + \sigma_y) \left(1 - \frac{r_o^2}{r^2}\right) + \frac{1}{2}(\sigma_x - \sigma_y) \left(1 - 4\frac{r_o^2}{r^2} + 3\frac{r_o^4}{r^4}\right) \cos 2\theta \\ \quad + \tau_{xy} \left(1 - 4\frac{r_o^2}{r^2} + 3\frac{r_o^4}{r^4}\right) \sin 2\theta + \frac{r_o^2}{r^2} p_m \\ \sigma_\theta = \frac{1}{2}(\sigma_x + \sigma_y) \left(1 + \frac{r_o^2}{r^2}\right) - \frac{1}{2}(\sigma_x - \sigma_y) \left(1 + 3\frac{r_o^4}{r^4}\right) \cos 2\theta \\ \quad - \tau_{xy} \left(1 + 3\frac{r_o^4}{r^4}\right) \sin 2\theta - \frac{r_o^2}{r^2} p_m \\ \sigma_{zz} = \sigma_z - \nu \left[ \frac{1}{2}(\sigma_x - \sigma_y) \cos 2\theta + \tau_{xy} \sin 2\theta \right] \frac{r_o^2}{r^2} \end{array} \right. \quad (5.10)$$

This is known as Kirsh's solution (Charlez 1997).

**b.** High permeability rock formation (HPR) and permeable well wall (PW) (scenario 2)

If the rock formation is porous and highly permeable, the linear poroelastic theory will be applied instead of the linear elastic theory. When some drilling mud flows into the rock formation, this results in the superimposed stresses acting on the rock mass in the vicinity of a well. As compared with scenario 3, there is an extra term added to the formula for  $\sigma_r$ ,  $\sigma_\theta$  and  $\sigma_{zz}$ , which is given in Eqn. (5.3).

$$\left\{ \begin{array}{l} \sigma_r = \frac{1}{2}(\sigma_x + \sigma_y) \left(1 - \frac{r_o^2}{r^2}\right) + \frac{1}{2}(\sigma_x - \sigma_y) \left(1 - 4\frac{r_o^2}{r^2} + 3\frac{r_o^4}{r^4}\right) \cos 2\theta \\ \quad + \tau_{xy} \left(1 - 4\frac{r_o^2}{r^2} + 3\frac{r_o^4}{r^4}\right) \sin 2\theta + \frac{r_o^2}{r^2} p_m + \left[ \frac{\alpha(1-2\nu)}{2(1-\nu)} \left(1 - \frac{r_o^2}{r^2}\right) - \phi \right] (p_m - p_p) \\ \sigma_\theta = \frac{1}{2}(\sigma_x + \sigma_y) \left(1 + \frac{r_o^2}{r^2}\right) - \frac{1}{2}(\sigma_x - \sigma_y) \left(1 + 3\frac{r_o^4}{r^4}\right) \cos 2\theta \\ \quad - \tau_{xy} \left(1 + 3\frac{r_o^4}{r^4}\right) \sin 2\theta - \frac{r_o^2}{r^2} p_m + \left[ \frac{\alpha(1-2\nu)}{2(1-\nu)} \left(1 + \frac{r_o^2}{r^2}\right) - \phi \right] (p_m - p_p) \\ \sigma_{zz} = \sigma_z - \nu \left[ \frac{1}{2}(\sigma_x - \sigma_y) \cos 2\theta + \tau_{xy} \sin 2\theta \right] 4\frac{r_o^2}{r^2} + \left[ \frac{\alpha(1-2\nu)}{(1-\nu)} - \phi \right] (p_m - p_p) \end{array} \right. \quad (5.11)$$

**c.** High permeability rock formation (HPR) and impermeable well wall (IPW) (scenario 3)  
 In contrast to scenario 2, the wellbore wall is impermeable due to the sealing effect of the drilling mud with good performance, pore pressure maintains constant after drilling and has an impact on the stress-strain relationship. The normal stresses surrounding a well has the same expression as Eqn. (5.10).

**d.** Low permeability rock formation (LPR) and permeable well wall (PW) (scenario 4)  
 When the rock formation is porous and has low permeability, meanwhile the wellbore wall is permeable, the pore pressure after drilling is different from that before drilling. The combination effect of the change of the pore pressure and the penetration of the drilling mud into the rock formation is considered in this scenario, given as

$$\left\{ \begin{array}{l}
 \sigma_r = \frac{1}{2}(\sigma_x + \sigma_y) \left(1 - \frac{r_o^2}{r^2}\right) + \frac{1}{2}(\sigma_x - \sigma_y) \left(1 - 4\frac{r_o^2}{r^2} + 3\frac{r_o^4}{r^4}\right) \cos 2\theta \\
 \quad + \tau_{xy} \left(1 - 4\frac{r_o^2}{r^2} + 3\frac{r_o^4}{r^4}\right) \sin 2\theta + \frac{r_o^2}{r^2} p_m + \frac{4\alpha s(1+\nu)}{3} \left[\frac{1}{2}(\sigma_x - \sigma_y) \cos 2\theta + \tau_{xy} \sin 2\theta\right] \frac{r_o^2}{r^2} \\
 \quad + \left[\frac{\alpha(1-2\nu)}{2(1-\nu)} \left(1 - \frac{r_o^2}{r^2}\right) - \phi\right] (p_m - p_p) \\
 \sigma_\theta = \frac{1}{2}(\sigma_x + \sigma_y) \left(1 + \frac{r_o^2}{r^2}\right) - \frac{1}{2}(\sigma_x - \sigma_y) \left(1 + 3\frac{r_o^4}{r^4}\right) \cos 2\theta \\
 \quad - \tau_{xy} \left(1 + 3\frac{r_o^4}{r^4}\right) \sin 2\theta - \frac{r_o^2}{r^2} p_m + \frac{4\alpha s(1+\nu)}{3} \left[\frac{1}{2}(\sigma_x - \sigma_y) \cos 2\theta + \tau_{xy} \sin 2\theta\right] \frac{r_o^2}{r^2} \\
 \quad + \left[\frac{\alpha(1-2\nu)}{2(1-\nu)} \left(1 + \frac{r_o^2}{r^2}\right) - \phi\right] (p_m - p_p) \\
 \sigma_{zz} = \sigma_z - \nu \left[\frac{1}{2}(\sigma_x - \sigma_y) \cos 2\theta + \tau_{xy} \sin 2\theta\right] 4\frac{r_o^2}{r^2} \\
 \quad + \frac{4\alpha s(1+\nu)}{3} \left[\frac{1}{2}(\sigma_x - \sigma_y) \cos 2\theta + \tau_{xy} \sin 2\theta\right] \frac{r_o^2}{r^2} + \left[\frac{\alpha(1-2\nu)}{2(1-\nu)} - \phi\right] (p_m - p_p)
 \end{array} \right. \quad (5.12)$$

**e.** Low permeability rock formation (LPR) and impermeable well wall (IPW) (scenario 5)  
 This scenario has low permeability rock formation and impermeable wellbore wall. The effects of pore pressure are reflected in two aspects. One is on the stress-strain relationship (linear poroelastic theory), this is the same as scenarios 2~4, and the other is on the stresses surrounding a well due to the pore pressure change. The formulae for the normal stresses surrounding a well in this situation are

$$\left\{ \begin{aligned}
\sigma_r &= \frac{1}{2}(\sigma_x + \sigma_y) \left(1 - \frac{r_o^2}{r^2}\right) + \frac{1}{2}(\sigma_x - \sigma_y) \left(1 - 4\frac{r_o^2}{r^2} + 3\frac{r_o^4}{r^4}\right) \cos 2\theta \\
&\quad + \tau_{xy} \left(1 - 4\frac{r_o^2}{r^2} + 3\frac{r_o^4}{r^4}\right) \sin 2\theta + \frac{r_o^2}{r^2} p_m \\
&\quad + \frac{4\alpha s(1+\nu)}{3} \left[ \frac{(\sigma_x - \sigma_y)}{2} \cos 2\theta + \tau_{xy} \sin 2\theta \right] \frac{r_o^2}{r^2} \\
\sigma_\theta &= \frac{1}{2}(\sigma_x + \sigma_y) \left(1 + \frac{r_o^2}{r^2}\right) - \frac{1}{2}(\sigma_x - \sigma_y) \left(1 + 3\frac{r_o^4}{r^4}\right) \cos 2\theta - \tau_{xy} \left(1 + 3\frac{r_o^4}{r^4}\right) \sin 2\theta \\
&\quad - \frac{r_o^2}{r^2} p_m + \frac{4\alpha s(1+\nu)}{3} \left[ \frac{(\sigma_x - \sigma_y)}{2} \cos 2\theta + \tau_{xy} \sin 2\theta \right] \frac{r_o^2}{r^2} \\
\sigma_{zz} &= \sigma_z - \nu \left[ \frac{1}{2}(\sigma_x - \sigma_y) \cos 2\theta + \tau_{xy} \sin 2\theta \right] 4 \frac{r_o^2}{r^2} \\
&\quad + \frac{4\alpha s(1+\nu)}{3} \left[ \frac{(\sigma_x - \sigma_y)}{2} \cos 2\theta + \tau_{xy} \sin 2\theta \right] \frac{r_o^2}{r^2}
\end{aligned} \right. \quad (5.13)$$

### 5.2.2 An In-situ Stress Field with Equal Horizontal Stress Components

In an equal horizontal stress field, the horizontal stress is equal around a well, i.e.,  $\sigma_x = \sigma_y = \sigma_h$ , as shown in Figure 5.4. Sometimes, this is called isotropic stress field. In this case, the stresses surrounding a well are much simplified from the above equations.

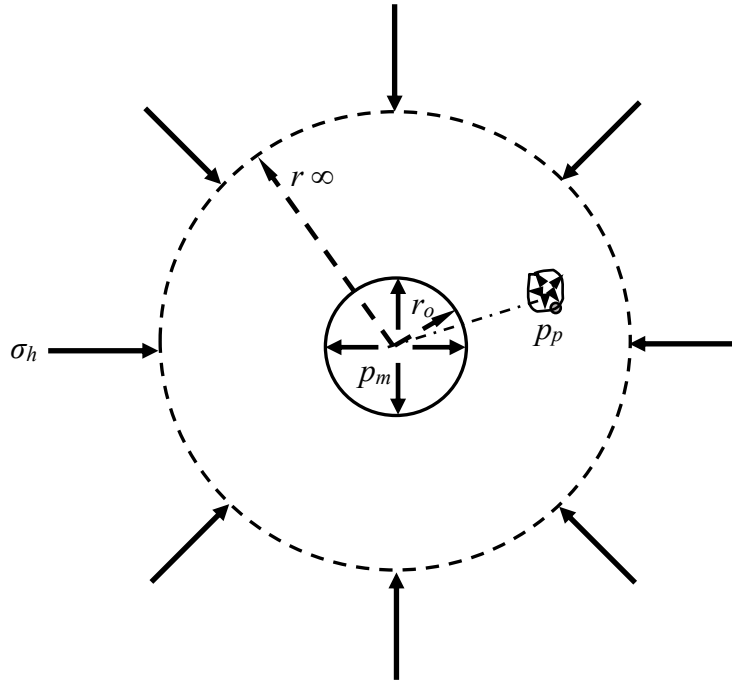


**Figure 5.4** An in-situ stress field with equal horizontal stress components



**f.** Rock formation with no pore pressure effect (scenario 6)

Since  $\sigma_x = \sigma_y = \sigma_h$  and there are no shear stresses, Eqn. (5.10) is reduced to

$$\begin{cases} \sigma_r = \sigma_h \left(1 - \frac{r_o^2}{r^2}\right) + \frac{r_o^2}{r^2} P_m \\ \sigma_\theta = \sigma_h \left(1 + \frac{r_o^2}{r^2}\right) - \frac{r_o^2}{r^2} P_m \\ \sigma_{zz} = \sigma_z \end{cases} \quad (5.14)$$

**g.** Permeable rock formation and permeable well wall (scenario 7)

In the equal horizontal stress field, both Eqns. (5.11) and (5.12) for the normal stresses surrounding a well in high and low permeability rock formations in terms of permeable wellbore wall are reduced to

$$\begin{cases} \sigma_r = \sigma_h \left(1 - \frac{r_o^2}{r^2}\right) + \frac{r_o^2}{r^2} P_m + \left[ \frac{\alpha(1-2\nu)}{2(1-\nu)} \left(1 - \frac{r_o^2}{r^2}\right) - \phi \right] (p_m - p_p) \\ \sigma_\theta = \sigma_h \left(1 + \frac{r_o^2}{r^2}\right) - \frac{r_o^2}{r^2} P_m + \left[ \frac{\alpha(1-2\nu)}{2(1-\nu)} \left(1 + \frac{r_o^2}{r^2}\right) - \phi \right] (p_m - p_p) \\ \sigma_{zz} = \sigma_z + \left[ \frac{\alpha(1-2\nu)}{(1-\nu)} - \phi \right] (p_m - p_p) \end{cases} \quad (5.15)$$

**h.** Permeable rock formation and impermeable well wall (scenario 8)

When the wellbore wall is impermeable, from Eqns. (5.10) and (5.13) with  $\sigma_x = \sigma_y = \sigma_h$  &  $\tau_{xy}=0$ , the normal stresses surrounding a well in high and low permeability rock formations have the same expression as Eqn. (5.14).

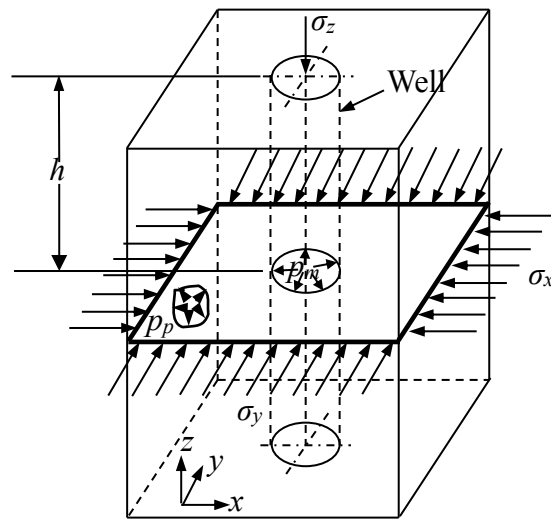
## 5.3 MATHEMATICAL MODELS FOR 2D BACK ANALYSIS BASED ON WELL DEFORMATION

### 5.3.1 Relationship between Diametrical Convergence and In-situ Stresses

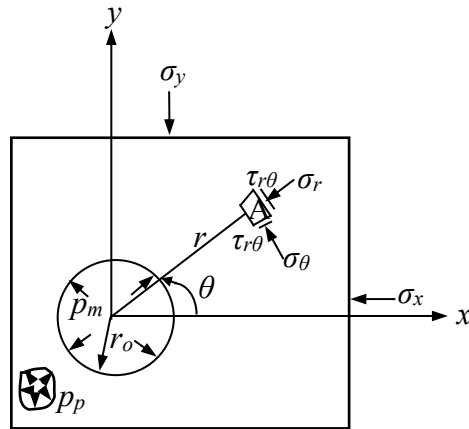
For a vertical well parallel to the  $z$  axis, the length to cross section dimension ratio is very high and deformation is limited to the  $x$ - $y$  plane except at the collar and the bottom. This

situation is considered as a plane strain problem, with  $\varepsilon_z = 0$ . In this case, the strain state can be reduced to four components corresponding to the four stress components  $\sigma_x$ ,  $\sigma_y$ ,  $\sigma_z$  and  $\tau_{xy}$ , respectively, which define completely the stress state in the plane perpendicular to the well axis. Thus, stress analysis can be conducted using a two-dimensional model.

A well is modeled as a hole in the ground formation, as shown in Figure 5.5, with an inner radius  $r_o$ . The outer boundary is considered infinite. The location of point A in a rock mass is represented by the radial distance,  $r$ , from the center of the hole and the angle  $\theta$ .



Three-dimensional model



Two-dimensional model

**Figure 5.5** Stress model surrounding a well

When a well is drilled into a formation, the stressed solid material is removed and the drilling mud provides temporary support to the well wall. As the mud pressure generally does not match the in-situ stresses, drilling induces stress redistribution around the well, causing a new set of stresses in the rock formation around the well. As a result, the deformation (or displacement) of the rock mass around the well can be observed. The displacement at point A induced by nearby drilling consists of the normal and tangential components  $u_r$  and  $u_\theta$ , which can also be expressed as the components  $u_x$  and  $u_y$  in the  $x, y$  directions, respectively. The magnitude of displacement in petroleum application is a function of the following parameters:

- the in-situ stresses  $\{\sigma_x, \sigma_y, \sigma_z, \tau_{xy}\}$  or the in-situ principal stresses  $\{\sigma_{Hmax}, \sigma_{Hmin}, \sigma_z, \theta_{Hmax}\}$  (under plane strain condition,  $\sigma_z = \nu(\sigma_x + \sigma_y)$ );
- the geometry of the well being drilled (radius  $r_o$ );
- the distance from the well ( $r$ );
- the properties of the rock mass (Young's modulus  $E$ , Poisson's ratio  $\nu$ , Biot's coefficient  $\alpha$ , porosity  $\phi$ , Skempton's coefficient  $s$ );
- the pore pressure ( $p_p$ );
- the drilling mud pressure ( $p_m$ ).

On the basis of the displacement-stress relationship, deformation of a circular hole in an isotropic linear elastic rock formation can be described in a matrix form as a function of the in-situ stress components, drilling mud pressure and pore pressure.

$$u_r = [M]\{\sigma_o\}_{2D} + M_m p_m + M_p p_p \quad (5.16)$$

where  $\{u_r\}$  is radial displacement,  $\{\sigma_o\}_{2D} = \{\sigma_x, \sigma_y, \tau_{xy}\}$  is a vector of the initial state of stress in 2D,  $[M]$  is the coefficient matrix of size  $(n \times 3)$ , depending on the location, rock properties and well size,  $M_m$  and  $M_p$  are the coefficients varying with rock properties and well size.

Eqn. (5.16) is the unified format. Under different scenarios,  $[M]$ ,  $M_m$  and  $M_p$  have different calculation equations and results.

Convergence is probably the easiest to measure. It is only necessary to measure the distance

change between any two points on the wellbore wall (e.g.,  $a$  &  $b$ ,  $a$  &  $c$ ,  $d$  &  $e$ ), as depicted in Figure 5.6. In practice in petroleum industry, the caliper logging devices measure well diameter along different directions during or after drilling. The difference between the drill bit diameter and the measured diameter represents the convergence between two opposite points on the wellbore wall induced by drilling.

The convergence reading is the sum of the displacement components at the two points along the measurement line (Zou 1995a). Diametrical convergence is the sum of the radial displacement components at the two opposite points on the wellbore wall along the measurement line.

$$u_{con-\eta\ direction} = u_{\eta-a} + u_{\eta-b} \quad (5.17)$$

where  $u_{\eta-a}$  is the radial displacement component along  $\eta$  direction at point  $a$  and  $u_{\eta-b}$  at point  $b$ .  $\eta$  is the angle between the measurement line and the reference direction –  $x$  axis.

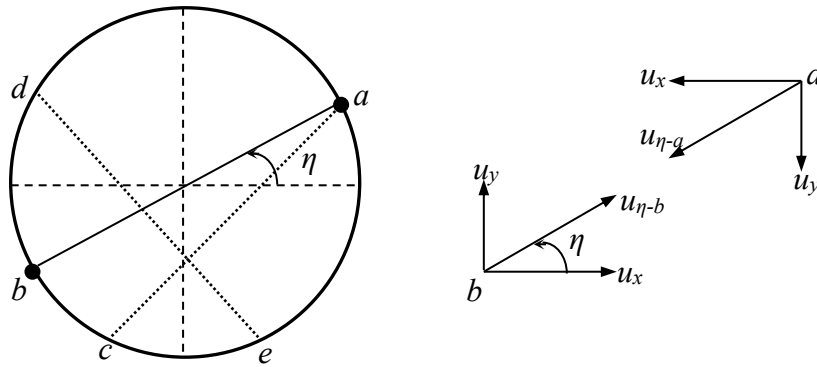


**Figure 5.6** Convergence between two opposite points on the well wall

At any point

$$u_{\eta} = [T_{\eta}] \{ u_g \} \quad (5.18)$$

where  $[T_{\eta}] = [\cos\eta \ \sin\eta]$  and  $\{ u_g \} = \{ u_x \ u_y \}^T$ .

The displacement  $u_g$  can be obtained from  $\{ u \}$  in cylindrical system by coordinate transformation.

$$\{ u_g \} = [T_g] \{ u \} \quad (5.19)$$

where  $\{ u \} = \{ u_n \ u_t \}^T$  and  $[T_g]$  is the transformation matrix. If the diametrical convergence

along different directions on the wellbore wall are measured,  $\eta = \theta$ .  $\theta$  is the angle with respect to  $x$  axis and is measured counter clockwise.  $\{u\} = \{u_r \quad u_\theta\}^T$  and

$$[T_g] = \begin{bmatrix} \cos \theta & -\sin \theta \\ \sin \theta & \cos \theta \end{bmatrix}.$$

Substituting Eqns. (5.16), (5.18) and (5.19) into Eqn. (5.17) gives

$$u_{con-\eta \text{ direction}} = [M_{con-\eta \text{ direction}}] \{\sigma_o\}_{2D} + M_{conm-\eta \text{ direction}} p_m + M_{conp-\eta \text{ direction}} p_p \quad (5.20)$$

where  $[M_{con-\eta \text{ direction}}]$  is the coefficient matrix in terms of the in-situ stresses,  $M_{conm-\eta \text{ direction}}$  and  $M_{conp-\eta \text{ direction}}$  are the coefficients of convergence in terms of mud pressure and pore pressure, respectively. They are relevant to the coordinates of two opposite points on the well wall along the measurement line or the measurement angle, well geometry and rock properties.

$$[M_{con-\eta \text{ direction}}] = ([T_\eta][T][M])_a + ([T_\eta][T][M])_b \quad (5.21)$$

$$M_{conm-\eta \text{ direction}} = ([T_\eta][T]M_m)_a + ([T_\eta][T]M_m)_b \quad (5.22)$$

$$M_{conp-\eta \text{ direction}} = ([T_\eta][T]M_p)_a + ([T_\eta][T]M_p)_b \quad (5.23)$$

The diametrical convergence in any direction on the well wall due to drilling can now be calculated from Eqn. (5.20) if the in-situ stresses are known. Figure 5.7 illustrates the convergence calculation model.  $\theta_{i_11}$  and  $\theta_{i_12}$  are the measurement angle of two opposite points  $a$  and  $b$ ;  $(x_{i_11}, y_{i_11})$  and  $(x_{i_12}, y_{i_12})$  are the coordinates of points  $a$  and  $b$ .

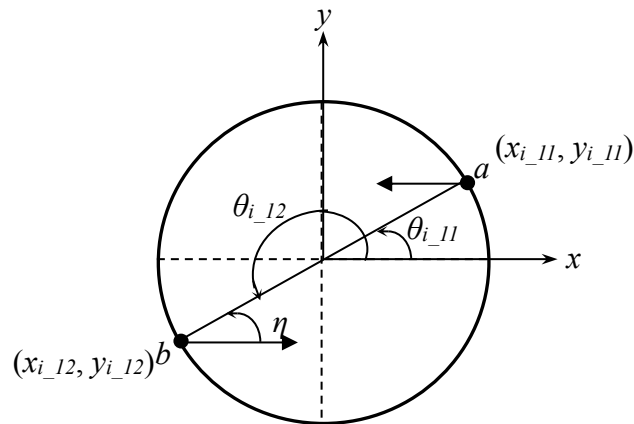


**Figure 5.7** Convergence calculation model

The convergence for points  $a$  and  $b$

$$u_{coni} = [M_{coni}] \{\sigma_o\}_{2D} + M_{conm} p_m + M_{comp} p_p \quad (5.24)$$

where  $[M_{coni}]$  is the coefficient matrix,  $M_{conm}$  and  $M_{comp}$  are the coefficients. They are associated with the measurement angle  $\theta_{i\_11}$  and  $\theta_{i\_12}$  or the coordinates of two opposite points  $(x_{i\_11}, y_{i\_11})$  and  $(x_{i\_12}, y_{i\_12})$ , well size and rock properties  $(E, \nu, \alpha, \phi, s)$ .

On the other hand, if a number of measurements are made in different directions, Eqn. (5.24) gives a set of equations. For  $n$  measured diametrical convergence, it is convenient to express Eqn. (5.24) in matrix form. Let

$$\{u_d\} = \begin{Bmatrix} u_{con1} \\ u_{con2} \\ \vdots \\ u_{conm} \end{Bmatrix}, [M_{con}] = \begin{bmatrix} M_{con11} & M_{con12} & M_{con13} \\ M_{con21} & M_{con22} & M_{con23} \\ \vdots & \vdots & \vdots \\ M_{conm1} & M_{conm2} & M_{conm3} \end{bmatrix} \quad (5.25)$$

We can rewrite Eqn. (5.24) as

$$\{u_d\} = [M_{con}] \{\sigma_o\}_{2D} + M_{conm} p_m + M_{comp} p_p \quad (5.26)$$

However the combined  $M$  matrix and coefficients will vary with the rock characteristics and field stress conditions. The detail is described in the following sections.

## 5.3.2 Mathematical Models in a Stress Field with Differential Horizontal Stress Components

### 5.3.2.1 Mathematical Model Derived from Linear Elastic Theory

If the rock formation is non-porous, the linear elastic theory is applied. The stress-strain relations and the strain-displacement relations in the linear elastic theory are described in Appendix A.

### Model 1: Rock formation with no pore pressure effect

Following the same procedure in Section 3.2 of Chapter 3, inserting Eqn. (5.10) into Eqn. (3.8) and performing integration will give the results. This time one term  $p_m$  is included. With the same method described in Section 3.2.1, the integration constant can be obtained, which is equal to 0. Consider plane strain condition

$$\varepsilon_z = 0, \gamma_{xz} = \gamma_{yz} = 0 \quad (5.27)$$

and from Eqn. (A.3c), we have

$$\sigma_z = \nu(\sigma_x + \sigma_y) \quad (5.28)$$

The diametrical convergence at the well wall ( $r = r_o$ ) in 2D can be written as

$$u_{d-1} = [M_{con1-1} \quad M_{con2-1} \quad M_{con4-1}] \{\sigma_o\}_{2D} + M_{conm-1} P_m \quad (5.29)$$

$$\text{where } M_{con1-1} = 2r_o k_1 \quad (5.30a)$$

$$M_{con2-1} = 2r_o k_2 \quad (5.30b)$$

$$M_{con4-1} = 2r_o k_3 \quad (5.30c)$$

$$M_{conm-1} = 2r_o k_4 \quad (5.30d)$$

$k_1$ ,  $k_2$  and  $k_3$  depend on the rock properties ( $E$  and  $\nu$ ) and the measurement angle ( $\theta$ ),  $k_4$  depends on the rock properties ( $E$  and  $\nu$ ).

### 5.3.2.2 Mathematical Models Derived from Linear Poroelastic Theory

Strain of the porous and permeable rocks, given by the stress-strain relationship (constitutive equation), is controlled by effective stresses rather than total stresses (Jin et al 1999, Jin and Chen 2012). The elastic theory for rock materials is not able to fully describe the behaviour of such materials, and the concept of poroelasticity has therefore to be considered (Fjaer 2008, Cheng 2016). The stress-strain relations are modified as follows.

$$\varepsilon_r = \frac{1}{E} [\sigma_r - \nu(\sigma_\theta + \sigma_{zz})] - \frac{1-2\nu}{E} \alpha p_p \quad (5.31a)$$

Similarly,

$$\varepsilon_{\theta} = \frac{1}{E} [\sigma_{\theta} - \nu(\sigma_r + \sigma_{zz})] - \frac{1-2\nu}{E} \alpha P_p \quad (5.31b)$$

$$\varepsilon_{zz} = \frac{1}{E} [\sigma_{zz} - \nu(\sigma_r + \sigma_{\theta})] - \frac{1-2\nu}{E} \alpha P_p \quad (5.31c)$$

There is no effect of pore pressure on the shear stress-strain relations.

The normal stresses can be expressed in terms of the strains and pore pressure. The detailed information can be found in Appendix C.

$$\sigma_r = \frac{E}{(1+\nu)(1-2\nu)} \left[ (1-\nu)\varepsilon_r + \nu\varepsilon_{\theta} + \nu\varepsilon_{zz} + \frac{(1+\nu)(1-2\nu)}{E} \alpha p_p \right] \quad (5.32a)$$

$$\sigma_{\theta} = \frac{E}{(1+\nu)(1-2\nu)} \left[ \nu\varepsilon_r + (1-\nu)\varepsilon_{\theta} + \nu\varepsilon_{zz} + \frac{(1+\nu)(1-2\nu)}{E} \alpha p_p \right] \quad (5.32b)$$

$$\sigma_{zz} = \frac{E}{(1+\nu)(1-2\nu)} \left[ \nu\varepsilon_r + \nu\varepsilon_{\theta} + (1-\nu)\varepsilon_{zz} + \frac{(1+\nu)(1-2\nu)}{E} \alpha p_p \right] \quad (5.32c)$$

or

$$\sigma_r = (\lambda + 2G)\varepsilon_r + \lambda\varepsilon_{\theta} + \lambda\varepsilon_{zz} + \alpha p_p \quad (5.33a)$$

$$\sigma_{\theta} = \lambda\varepsilon_r + (\lambda + 2G)\varepsilon_{\theta} + \lambda\varepsilon_{zz} + \alpha p_p \quad (5.33b)$$

$$\sigma_{zz} = \lambda\varepsilon_r + \lambda\varepsilon_{\theta} + (\lambda + 2G)\varepsilon_{zz} + \alpha p_p \quad (5.33c)$$

where  $\lambda$  is Lamé's parameter and  $G$  is shear modulus. See Appendix B for Some mechanical properties for some common rock types.

$$\lambda = \frac{E\nu}{(1+\nu)(1-2\nu)} \quad (5.34a)$$

$$G = \frac{E}{2(1+\nu)} \quad (5.34b)$$

Eqns. (5.31a) and (5.31b) are substituted into Eqn. (A.6) for integration.

$$u_r = \int \frac{1}{E} [\sigma_r - \nu(\sigma_{\theta} + \sigma_{zz})] dr - \int \frac{1-2\nu}{E} \alpha p_p dr \quad (5.35a)$$

$$u_{\theta} = \int \frac{r}{E} [\sigma_{\theta} - \nu(\sigma_r + \sigma_{zz})] d\theta - \int u_r d\theta - \int \frac{r(1-2\nu)}{E} \alpha p_p d\theta \quad (5.35b)$$



Eqns. (5.10), (5.11), (5.12) and (5.13) are substituted into Eqn. (5.35) respectively to obtain the expressions describing the relationship between the radial displacement surrounding a well and the in-situ stresses under different scenarios in porous rock formation. The resulting equations are listed as below. All integration constants are equal to zero.

**Model 2:** High permeability rock formation and permeable well wall

The diametrical convergence in this scenario can be obtained by substituting Eqn. (5.11) into Eqn. (5.35).

$$u_{d-2} = [M_{con\ 1-2} \quad M_{con\ 2-2} \quad M_{con\ 4-2}] \{\sigma_o\}_{2D} + M_{conm-2} p_m + M_{conp-2} p_p \quad (5.36)$$

where  $M_{con1-2}$ ,  $M_{con2-2}$  and  $M_{con4-2}$  are given in Eqn. (5.30a), (5.30b) and (5.30c), respectively.

$$M_{conm-2} = \frac{2r_o}{E} k_5 \quad (5.37a)$$

$$M_{conp-2} = \frac{2r_o}{E} k_6 \quad (5.37b)$$

$k_5$  and  $k_6$  are dependent on  $E$  and  $\nu$ , as well as  $\alpha$  and  $\phi$ .

**Model 3:** High permeability rock formation and impermeable well wall

In this case, Eqn. (5.10) is substituted into Eqn. (5.35). The diametrical convergence can be written as

$$u_{d-3} = [M_{con\ 1-3} \quad M_{con\ 2-3} \quad M_{con\ 4-3}] \{\sigma_o\}_{2D} + M_{conm-3} p_m + M_{conp-3} p_p \quad (5.38)$$

where  $M_{con1-3}$ ,  $M_{con2-3}$ ,  $M_{con4-3}$  and  $M_{conm-3}$  are given in Eqn. (5.30a), (5.30b), (5.30c) and (5.30d), respectively. These coefficients are the same as model 1. The only difference is that there is one more term  $M_{conp-3}$  related to pore pressure  $p_p$ , which is given in Eqn. (5.39).

$$M_{conp-3} = 2r_o k_7 \quad (5.39)$$

$k_7$  is dependent on  $E$ ,  $\nu$ , and  $\alpha$ .

**Model 4:** Low permeability rock formation and permeable well wall

The stresses surrounding the well described in Eqn. (5.12) are applied in Eqn. (5.35) to solve for the diametrical convergence.

$$u_{d-4} = [M_{con\ 1-4} \quad M_{con\ 2-4} \quad M_{con\ 4-4}] \{\sigma_o\}_{2D} + M_{conm\ -4} p_m + M_{comp\ -4} p_p \quad (5.40)$$

$$\text{where } M_{con\ 1-4} = 2r_o k_8 \quad (5.41a)$$

$$M_{con\ 2-4} = 2r_o k_9 \quad (5.41b)$$

$$M_{con\ 4-4} = 2r_o k_{10} \quad (5.41c)$$

$k_8$ ,  $k_9$  and  $k_{10}$  are determined by  $E$ ,  $\nu$ ,  $\alpha$ ,  $s$  and the measurement angle  $\theta$ .  $M_{conm-4}$  and  $M_{comp-4}$  are the same as  $M_{conm-2}$  and  $M_{comp-2}$  in model 2, respectively.

**Model 5:** Low permeability rock formation and impermeable well wall

Eqn. (5.13) is used to derive the diametrical convergence in this scenario.

$$u_{d-5} = [M_{con1-5} \quad M_{con2-5} \quad M_{con4-5}] \{\sigma_o\}_{2D} + M_{conm-5} p_m + M_{comp-5} p_p \quad (5.42)$$

where  $M_{con1-5}$ ,  $M_{con2-5}$ ,  $M_{con4-5}$ ,  $M_{conm-5}$  and  $M_{comp-5e}$  are given in Eqn. (5.41a), (5.41b), (5.41c), (5.30d) and (5.39), respectively.  $M_{con1-5}$ ,  $M_{con2-5}$  and  $M_{con4-5}$  are the same as  $M_{con1-4}$ ,  $M_{con2-4}$  and  $M_{con4-4}$  in model 4, respectively.  $M_{conm-5}$  and  $M_{comp-5}$  are the same as  $M_{conm-3}$  and  $M_{comp-3}$  in model 3, respectively.

### 5.3.3 Mathematical Models in a Stress Field with Equal Horizontal Stress Components

Following the same procedure as Section 5.3.2, the diametrical convergence under different scenarios can be derived. Horizontal stress is equal in all directions,  $\sigma_x = \sigma_y = \sigma_h$ , and  $\tau_{xy} = 0$ , accordingly the equations in Section 5.3.2 can be simplified.

**Model 6:** Rock formation with no pore pressure effect

Eqn. (5.29) can be simplified as

$$u_{d-6} = M_{con-6}\sigma_h + M_{conm-6}p_m \quad (5.43)$$

where  $M_{conm-6}$  is the same as  $M_{conm-1}$ , given in Eqn. (5.30d), and

$$M_{con-6} = 2r_o k_{11} \quad (5.44)$$

$K_{11}$  is independent of the measurement angle  $\theta$ .

**Model 7:** Porous rock formation and permeable well wall

In both scenarios, high and low permeability rock formation, the diametrical convergence has the same equations when the well wall is permeable. Eqn. (5.36) can be simplified as

$$u_{d-7} = M_{con-7}\sigma_h + M_{conm-7}p_m + M_{conp-7}p_p \quad (5.45)$$

where the coefficients  $M_{conm-7}$  and  $M_{conp-7}$  are the same as model 2, given in Eqn. (5.37a) and (5.37b), respectively.  $M_{con-7}$  is the same as model 6, given in Eqn. (5.44).

**Model 8:** Porous rock formation and impermeable well wall

Like model 7, if the well wall is impermeable, in both scenarios, high and low permeability rock formation, the diametrical convergence has the same equations.

$$u_{d-8} = M_{con-8}\sigma_h + M_{conm-8}p_m + M_{conp-8}p_p \quad (5.46)$$

where the coefficients  $M_{conm-8}$  and  $M_{conp-8}$  are the same as model 3, given in Eqn. (5.30d) and (5.39), respectively.  $M_{con-8}$  is the same as model 6, given in Eqn. (5.44).

**5.3.4 Summary of Various Scenarios and Mathematical Models**

The various scenarios and mathematical models are summarized in Table 5.1. Five mathematical models are established to take into account different well wall and rock formation conditions in a stress field with differential horizontal stress components.

- The first model is linear elastic to consider rock formation with mud pressure (without pore pressure effect), which is equivalent to the condition in mining and geotechnical engineering when mud pressure is zero.
- To consider the unique situation in a well in petroleum engineering, four poro-elastic models are also developed to consider the effects of mud pressure, pore pressure, permeability of rock formation and well wall.
- 

**Table 5.1** Various scenarios and mathematical models

Scenario	Near-wellbore stresses	Displacement-stress relations	Suitable field
NP	$f(\sigma_o, p_m)$ or $f(\sigma_o)$	Linear elastic theory Eqn. (5.29)	<ul style="list-style-type: none"> <li>• No pore pressure effect</li> <li>• Porous rock formation without mud pressure</li> </ul>
HPR and PW	$f(\sigma_o, p_m, p_m - p_p)$	Linear poroelastic theory Eqn. (5.36)	<ul style="list-style-type: none"> <li>• High permeability rock formation</li> <li>• Penetration of drilling mud into the rock formation</li> </ul>
HPR and IPW	$f(\sigma_o, p_m)$	Linear poroelastic theory Eqn. (5.38)	<ul style="list-style-type: none"> <li>• High permeability rock formation</li> <li>• Quick build-up of mud cake on the wellbore wall</li> </ul>
LPR and PW	$f(\sigma_o, p_m, \Delta p_p, p_m - p_p)$	Linear poroelastic theory Eqn. (5.40)	<ul style="list-style-type: none"> <li>• Low permeability rock formation</li> <li>• Penetration of drilling mud into the rock formation</li> </ul>
LPR and IPW	$f(\sigma_o, p_m, \Delta p_p)$	Linear poroelastic theory Eqn. (5.42)	<ul style="list-style-type: none"> <li>• Low permeability rock formation</li> <li>• No penetration of drilling mud into the rock formation</li> </ul>

### 5.3.5 Mathematical Models Derived from Linear Poro-thermo-elastic Theory

When a well is drilled, the drilling mud may alter the temperature of the surrounding formation. Temperature change will result in expansion or shrinkage of the rock formation. Consequently, the stress distribution will be influenced by the heat flow.

The thermally induced stress is given by (Fjaer 2008)

$$\sigma_T = \frac{E}{1-2\nu} \alpha_T (T - T_o) \quad (5.47)$$

The expressions for the normal stress-strain relations are modified from Eqn. (5.31a) by taking the thermal effects into consideration.

$$\varepsilon_r = \frac{1}{E} [\sigma_r - \nu(\sigma_\theta + \sigma_{zz})] - \alpha_T (T - T_o) - \frac{1-2\nu}{E} \alpha p_p \quad (5.48a)$$

Similarly,

$$\varepsilon_\theta = \frac{1}{E} [\sigma_\theta - \nu(\sigma_r + \sigma_{zz})] - \alpha_T (T - T_o) - \frac{1-2\nu}{E} \alpha p_p \quad (5.48b)$$

$$\varepsilon_{zz} = \frac{1}{E} [\sigma_{zz} - \nu(\sigma_r + \sigma_\theta)] - \alpha_T (T - T_o) - \frac{1-2\nu}{E} \alpha p_p \quad (5.48c)$$

where  $\alpha_T$  is the coefficient of linear thermal expansion ( $^{\circ}\text{C}^{-1}$ ),  $T$  is the temperature in the well, and  $T-T_o$  is the temperature change from initial condition ( $^{\circ}\text{C}$ ).

From Eqns. (5.48) and (A.6), we then find

$$u_r = \int \frac{1}{E} [\sigma_r - \nu(\sigma_\theta + \sigma_{zz})] dr - \int \frac{1-2\nu}{E} \alpha p_p dr - \int \alpha_T (T - T_o) dr \quad (5.49a)$$

$$u_\theta = \int \frac{r}{E} [\sigma_\theta - \nu(\sigma_r + \sigma_{zz})] d\theta - \int u_r d\theta - \int \frac{r(1-2\nu)}{E} \alpha p_p d\theta - \int r \alpha_T (T - T_o) d\theta \quad (5.49b)$$

The same procedure is performed as Section 5.3.2 and 5.3.3 for solving the diametrical convergence around a well under different scenarios. The formula obtained using linear poro-thermo-elastic theory can be expressed for a stress field with differential horizontal stress components and with equal horizontal stress components by Eqn. (5.50a) and (5.50b), respectively.

$$u_d = [M_{con}] \{\sigma_o\}_{2D} + M_{conm} p_m + M_{conp} p_p + M_{conT} (T - T_o) \quad (5.50a)$$

$$u_d = M_{con} \sigma_h + M_{conm} p_m + M_{conp} p_p + M_{conT} (T - T_o) \quad (5.50b)$$

where  $[M_{con}]$  is the coefficient matrix,  $M_{con}$ ,  $M_{conm}$  and  $M_{conp}$  are the coefficients. They are dependent on the different scenarios, as discussed in Section 5.3.2 and 5.3.3.  $M_{conT}$  is the same for all scenarios.

$$M_{conT} = -2 r_o \alpha_T \quad (5.51)$$

## 5.4 SOLUTIONS TO THE IN-SITU STRESSES FROM CONVERGENCE MEASUREMENTS

In a stress field with differential horizontal stress components, there are 3 unknown in-situ stress components. If the least square method is adopted, a unique best-fit solution for the unknown parameters (in-situ stress components) can be obtained.

As discussed in Section 5.3, the diametrical convergence around the well wall under different scenarios can be calculated as below:

Linear elastic theory

$$\{u_d\} = [M_{con}] \{\sigma_o\}_{2D} + M_{conm} P_m \quad (5.52a)$$

Linear poroelastic theory

$$\{u_d\} = [M_{con}] \{\sigma_o\}_{2D} + M_{conm} P_m + M_{conp} P_p \quad (5.52b)$$

Linear thermo-poro-elastic theory

$$\{u_d\} = [M_{con}] \{\sigma_o\}_{2D} + M_{conm} P_m + M_{conp} P_p + M_{conT} (T - T_o) \quad (5.52c)$$

All formulae above for the diametrical convergence analysis can be written in a general matrix form:

$$\{u_d\} = [M_{con}] \{\sigma_o\}_{2D} + C \quad (5.53)$$

where  $C$  represents all terms on the right side of Eqn. 5.60 except the term with  $\{\sigma_o\}$ .

The 1<sup>st</sup> step:

Moving  $C$  to the left side of Eqn. (5.53).

$$\{u_d\} - C = [M_{con}] \{\sigma_o\}_{2D} \quad (5.54)$$

The 2<sup>nd</sup> step:

Multiplying both sides of Eqn. (5.54) by the transpose of  $[M_{con}]$ .

$$[M_{con}]^T \cdot (\{u_d\} - C) = [M_{con}]^T [M_{con}] \{\sigma_o\}_{2D} \quad (5.55)$$

The 3<sup>rd</sup> step:

Applying the inverse of  $\{[M_{con}]^T[M_{con}]\}$  to both sides of Eqn. (5.55)

$$\begin{aligned} & ([M_{con}]^T[M_{con}])^{-1}[M_{con}]^T \cdot (\{u_d\} - C) \\ &= ([M_{con}]^T[M_{con}])^{-1} \cdot ([M_{con}]^T[M_{con}])\{\sigma_o\}_{2D} \end{aligned} \quad (5.56)$$

The final result of the matrices on the right side is a unit matrix. Therefore

$$\{\sigma_o\}_{2D} = ([M_{con}]^T[M_{con}])^{-1}[M_{con}]^T \cdot (\{u_d\} - C) \quad (5.57)$$

If the rows of  $[M_{con}]$  are linearly independent,  $[M_{con}]^T[M_{con}]$  is invertible. In this case Eqn. (5.58) has only one optimum solution for the stress from least square method and it is given by

$$\{\hat{\sigma}\}_{2D} = [M_{con}^*]^{-1}[M_{con}]^T \cdot \{u_d^*\} \quad (5.58)$$

where  $[M_{con}^*] = ([M_{con}]^T[M_{con}])^{-1}$  and  $\{u_d^*\} = \{u_d\} - C$ . The superscript “ $T$ ” and “ $-1$ ” denote matrix transpose and inversion, respectively.

Thus, in a reversed order, the in-situ stresses can be determined uniquely from the measured diametrical convergence in different directions around the wellbore wall. It is noted that the number of the measurements  $n$  should be greater than the number of unknown parameters (i.e.  $n > 3$  in two-dimensional model).

# **CHAPTER 6 STATISTICAL ANALYSIS FOR DETECTING ERRONEOUS DATA AND RESULT OPTIMIZATION**

## **6.1 INTRODUCTION**

In this method, the diametrical convergence in different locations at the well wall induced by drilling needs to be measured. The in-situ stresses are then calculated from the measured convergence based on the stress-diametrical convergence relationship at the well wall. Theoretically, the same number of measurements as the unknown parameters to be determined can be applied to obtain a solution. However, in reality, errors may occur from various sources during measurements, such as reading errors, inaccurate performance of instruments, local variations in the measurement domain in the field. Consequently, some measurement data points might be less reliable than others. Therefore, the number of the measured value is generally greater than the minimum required in order to minimize the effects of the possible occurrence of errors during measurements.

By the least square method, the best fit solution for the in-situ stresses can be calculated from Eqn. (5.58). And then the predicted corresponding diametrical convergence can be obtained from the best-fit solution. As a result, there is a residual between the measured and predicted convergence. Hence statistical regression methods need to be applied to analyze the measurement data of multiple variables (Hines and Montgomery 1990) and the main goal is to find possible measurement diametrical convergence data errors, minimize these errors and refine the results of the least square solution for the in-situ stress components.

In conventional procedure, only the ordinary residual and standard deviation are considered. The measurement data point with the maximum residual is deleted and least square method is used to obtain the estimate of the stress components. Iterations are performed to minimize the sum of squares of the residuals (standard deviation). The one producing the smallest standard deviation is unbiased minimum-variance estimates of the in-situ stresses. However, sometimes standard deviation is not enough to optimize the results. The



measurement data point with the largest residual may not be the most erroneous and may not have the most influence. In this research work, besides standard deviation, standardized residuals and influence measure will be combined to help identify the erroneous data. Moreover, the reliability of the solution and statistical significance will be assessed using correlation coefficient and  $F$ -test. It should be pointed out that if the measurement data are poor themselves, the statistic methods cannot make them better and generate a good result.

## 6.2 MULTIPLE LINEAR REGRESSION ON DIAMETRICAL CONVERGENCE MEASUREMENTS

As discussed in Section 5.4 of Chapter 5, the diametrical convergence under different scenarios can be written in a general matrix form.

$$\{u_d\} = [M_{con}] \{\sigma_o\}_{2D} + C \quad (6.1)$$

where the coefficient matrix  $[M_{con}]$  and  $C$  vary with different stress field, well wall and rock formation conditions.

In general, a measured diametrical convergence  $u_{di}$  at a measurement angle  $\theta$  can be expressed in the form of the in-situ stress component  $\sigma_j$

$$u_i = \sum_{j=1}^m M_{ij} \sigma_j + C \quad (6.2)$$

$$i = 1, \dots, n$$

$$j = 1, \dots, m$$

$C$  is constant, which is associated with pore pressure, mud pressure and temperature change depending on different scenarios.

For a specific stress field, the stress components  $\sigma_j$  are constants. They correspond to the unknown parameters. The diametrical convergence is linear in the unknown stress components  $\sigma_j$  and multiple linear regression can be applied.

There is a constant in Eqn. (6.2). Therefore, in order to perform the linear regression analysis, the expression in a matrix form describing the relationship between the

measurements of diametrical convergence along  $n$  different directions and the in-situ stress components needs to be modified as follows:

$$\{\mathbf{u}'_d\} - C = [M_{con}] \{\sigma_o\}_{2D} \quad (6.3)$$

A linear model is

$$E(\{\mathbf{u}'_d\}) = [M_{con}] \{\sigma_o\}_{2D} \quad (6.4a)$$

$n \times 1 \quad n \times m \quad m \times 1$

$$V(\{\mathbf{u}'_d\}) = [I] s_V^2 \quad (6.4b)$$

By the least square method, the best-fit solution for the in-situ stresses  $\{\sigma_o\}$  is

$$\{\hat{\sigma}_o\}_{2D} = ([M_{con}]^T [M_{con}])^{-1} \cdot [M_{con}]^T \cdot \{\mathbf{u}'_d\} \quad (6.5)$$

The predicted corresponding diametrical convergence values are

$$\{\hat{\mathbf{u}}'_d\} = [M_{con}] ([M_{con}]^T [M_{con}])^{-1} [M_{con}]^T \cdot \{\mathbf{u}'_d\} \quad (6.6a)$$

$$\text{Let's define } [H] = [M_{con}] ([M_{con}]^T [M_{con}])^{-1} [M_{con}]^T \quad (6.6b)$$

as the projection matrix, or called hat matrix.

The residuals between the measured and calculated diametrical convergence are

$$\{R\} = \{\mathbf{u}'_d\} - \{\hat{\mathbf{u}}'_d\} = ([I] - [H]) \{\mathbf{u}'_d\} \quad (6.7)$$

The covariance matrix for the estimated parameters  $\{\hat{\sigma}_o\}$  is

$$V(\{\hat{\sigma}_o\}) = ([M_{con}]^T [M_{con}])^{-1} s_V^2 \quad (6.8)$$

for the fitted response variables  $\{\hat{\mathbf{u}}'_d\}$  is

$$V(\{\hat{\mathbf{u}}'_d\}) = [H] s_V^2 \quad (6.9)$$

and for the residual  $\{R\}$  is

$$V(\{R\}) = ([I] - [H]) s_V^2 \quad (6.10)$$

This gives the minimum sum of squares

$$S_{\min} = \{R\}^T \{R\} = \sum R_i^2 \quad (6.11)$$

where  $R_i$  is the  $i$ th element of  $\{R\}$ .

The standard deviation of the residual,  $std$  is

$$std = \sqrt{\frac{S_{\min}}{n - m}} \quad (6.12)$$

where  $n$  is the diametrical convergence measurement number along different direction on the well wall, and  $m$  is the rank of  $[M_{con}]$ . In 2D and 3D stress analysis,  $m = 3$  and 6, respectively.  $std^2$  is the unbiased estimator of the variance of error  $s_V^2$ .

## 6.3 LOCATING ERRONEOUS DATA

### 6.3.1 Locating Outliers

As mentioned earlier, due to a variety of causes, for example, malfunctioning of the data acquisition system, reading errors and inaccurate performance of instruments, the data from measurements may not be very accurate and have outlying observations. An outlier refers to an observed data lying well outside of the data range. The obvious question is how to locate them and what to do with them. It should be noticed that the technique for locating outliers, as described in the following, should never be regarded as a way to reject observations. Once an outlier is found, statistical method should be used to see its discrepancy, the physical meaning should be examined carefully and the regression analysis should be carried out with and without the outlier(s) to see the effect.

The ordinary residuals are simply the difference between what is actually measured and what is predicted by the regression model. However, a data point with the largest residual may not necessarily be the most erroneous. The technique for locating outliers is based on

a test of discordancy using the standardized residuals (Zou 1995b). By Eqn. (6.7), the ordinary residuals have their covariance matrix as

$$V(R_i) = (1.0 - h_{ii}) s_V^2 \quad (6.13)$$

where  $h_{ii}$  is the  $i$ th diagonal element of the hat matrix in Eqn. (6.6b). The error variance  $s_V^2$  is unknown and the unbiased estimate of  $s_V$  is the standard deviation of residual,  $std$ , of Eqn. (6.12). Therefore the estimated variance  $s_i^2$  of  $R_i$  (the  $i$ th residual) is proportional to  $std^2$ .

$$s_i^2 = (1.0 - h_{ii}) std^2 \quad (6.14)$$

and its square root, i.e., the estimated standard error  $s_i$ , is used to weigh the ordinary residual  $R_i$ . The standardized residual is thus defined as

$$t_i = \frac{R_i}{s_i} = \frac{R_i}{std \sqrt{1 - h_{ii}}} \quad (6.15)$$

These are the weighted residuals with the weight being inversely proportional to the estimated standard error. The  $t_i$ 's are not independent but have more or less constant variance and the assumptions made for linear regression is approximately satisfied.

To detect an outlier in the data set,  $t_{\max} = \max |t_i|$  is used. If  $t_{\max} > t_o$ , a critical value, the corresponding observation is declared as an outlier.  $t_o$  is the upper bound of  $t$  at a specified confidence level  $\alpha\%$ . Some data for  $t_o$  are tabulated by Lund (1975) and Barnett and Lewis (1978) (Table for some  $t_o$  values is given in Appendix E).

In practice, the real data may contain multiple outliers. A sequential test procedure is recommended. The outliers are located one by one and the process continues until no more outliers are found. A useful rule to determine when to stop testing outliers is to look for two consecutive non-outliers (they both yield  $t_{\max}$ ). A located outlier should not have to be rejected. Instead, it should be paid more attention and be examined carefully.

### 6.3.2 Locating High Leverage Points

The hat matrix  $[H]$  projects the measured data into the predicted values. The  $i$ th diagonal elements  $h_{ii}$  of  $[H]$  represent the influence of the  $i$ th response on the  $i$ th fitted value. If an  $h_{ii}$  is unduly large, it has an undue weight in the regression. Since  $[H]$  is a function of the explanatory variables only (consisting only of the elements of matrix  $[M_{com}]$  in Eqn. (6.4a) and not including any observation), any point with a large  $h_{ii}$  is a point of high leverage.

As can be observed,

$$\frac{1}{n} \leq h_{ii} \leq 1.0 \quad (6.16)$$

the average  $h_{ii}$  must be  $\frac{m}{n}$  since the sum of the eigenvalues equals the rank  $m$  of  $[M_{com}]$  and  $[H]$ . As a rule of thumb, any point is likely a candidate of a high leverage point if

$$h_{ii} > \frac{2m}{n} \quad (6.17)$$

This is used as an approximation criterion for locating a high leverage point. Therefore the results may not be accurate. Once again a located high leverage point should not have to be rejected. Instead, it should be paid more attention and be examined carefully. The test should continue until only one non-high leverage point is found.

## 6.4 MEASURING INFLUENCE OF DATA POINTS

It is important to see how much influence the presence of the  $i$ th data point has on the regression analysis. One such influence measure is defined by  $d_i$

$$d_i = \frac{\left(\{\sigma_o\} - \{\sigma_o\}_{(i)}\right)^T \cdot [M_{con}]^T [M_{con}] \cdot \left(\{\sigma_o\} - \{\sigma_o\}_{(i)}\right)}{n \cdot std^2} \quad (6.18)$$

where  $\{\sigma_o\}$  and  $\{\sigma_o\}_{(i)}$  are the estimated parameters based on the full data and the reduced data without the  $i$ th point respectively.  $D_i$  is in fact the weighted sum of squares of deviation of the regression estimates  $\{\sigma_o\}$  from  $\{\sigma_o\}_{(i)}$ . The weights implied here are precision of the

estimate  $\{\sigma_o\}$ . The more precise the estimate, the more weights it gets in the influence measure.  $d_i$  can be equivalently written as

$$d_i = \frac{t_i^2 w_i}{m} \quad (6.19)$$

where  $w_i = h_{ii} / (1.0 - h_{ii})$  (6.20)

As can be seen,  $t_i^2$  measures the outlying role of the  $i$ th measurement and  $w_i$  measures the outlying role of the  $i$ th row of the explanatory variable matrix  $[M_{com}]$ . The influence measure is perhaps most important when the data point is a significant erroneous data point and corresponds to  $\max |d_i|$ . In this case, the  $i$ th point is most influential, contains extra information and needs careful examination.

Since outliers and high leverage points may present at the same time, they may affect each other. The test on one (eg., outlier) should be repeated after the test on another (eg., high leverage point) is finished, which declared active points. This can be carried out in two orders. Test all outliers, then all high leverage points, then all outliers again until no more unusual points are found. During the process, every detected unusual point is deleted before the next test is done. Therefore the size of the data set reduces by one after each test. This order can be reversed by testing high leverage points first. The results of tests by the two orders may differ and if possible, tests should be done in both orders to see the effect.

## 6.5 STATISTICAL MEASURE OF REGRESSION RESULTS

For a given set of data, the best-fit solution to the unknown parameters can be obtained by linear regression analysis as described earlier. The next immediate question is how good these results are and how much we can rely on them. There could be many factors affecting the result: the variability of data, the validity of the regression model, the regression assumptions, etc. Nevertheless, the following statistic parameters are helpful in making the judgement: standard deviation  $std$ , correlation coefficient  $r_c$ , regression significant  $F$ .

### 6.5.1 Standard Deviation

The standard deviation of residual is defined in Eqn. (6.12). As can be seen, the smaller the residuals, the smaller the “standard deviation”. When two sets of data in the same range are analyzed on the same regression model, smaller std means better regression results. However, as far as the same set of data is concerned, smaller std due to deleting a point does not necessarily mean a better solution since std can be demonstrated as a decreasing function of the degrees of freedom ( $n - m$ ). In fact, if  $n = m$ , there is only one solution. In this case, all residuals are zero and so is std, which means the true error variance cannot be estimated. Therefore, std cannot be completely relied on as a criterion for deleting an erroneous data point. But deleting an erroneous data point will reduce the value of std much more than deleting any other point.

### 6.5.2 Correlation Coefficient

The correlation coefficient is defined as

$$r_c = \sqrt{1 - \frac{\{R\}^T \{R\}}{\sum (u'_{di} - \overline{u'_d})^2}} \quad (6.21)$$

where  $\{R\}$  are the ordinary residuals of Eqn. (6.7),  $u'_{di}$  is the measured value of  $i$ th point and  $\overline{u'_d}$  is the mean value.

$r_c$  is a measure of the linear relationship between the response variable (diametrical convergence  $u_d$ ) and the explanatory variables  $M_j$  (which are functions of the diametrical convergence measurement locations),  $j = 1, \dots, m$ , in Eqn. (6.4a). In general, if  $n = 1$ , or one variable, Eqn. (6.3) is a model of a straight line and  $r_c$  is the slope of the line. If all data points fall on the line, the fit is perfect and  $r_c = 1.0$ . Otherwise  $r_c < 1.0$ . The smaller the value of  $r_c$ , the less linear relation.  $r_c$  appears to be a measure of regression goodness. However, there are two exceptions:

- 1)  $r_c \approx 1.0$  does not necessarily mean the regression is good because (a) when the number of measurement data equals the number of unknown parameters, a perfect fit is obtained

and  $r_c = 1.0$  no matter how bad the regression is and (b) the observations may not be representative of the true population.

- 2)  $r_c = 0$  does not necessarily mean there is no linear relation since  $r_c = 0$  can occur when (a) there is absolutely no linear relation between  $u_d$  and  $M_j$  and (b) even though the data fits a perfect linear model but the slope is nearly zero (meaning  $u_d$  is independent from  $M_j$ ).

For the case of in-situ stress analysis, the problem (a) in 1) can be solved by increasing the number of measurements and problem (b) in 1) by carrying out accurate measurements. When situation (a) of 2) occurs, the diametrical convergence shows no linear relation with the variable  $M_j$ . However, from the derivation of Eqn. (6.3), the linear relation must exist since all stress components of  $\{\sigma_o\}$  are the linear constants. The only problem source will be in  $M_j$  functions of the measurement locations, i.e., the physical model of isotropic and homogeneous media does not fit the measured data or the measurement locations are incorrect. Situation (b) of 2) will never occur in the displacement-based back analysis. As can be seen in Eqn. (6.3), the diametrical convergence is a linear function of the variable  $M_j$  with the stress components  $\{\sigma_o\}$  as the linear parameter.

### 6.5.3 Regression Significance

In a linear regression model with only one variable, the goodness of fit may be checked by the correlation coefficient  $r_c$  and the estimated parameters. However, in multiple linear regression, checking on a single parameter cannot indicate if the regression is good. A jointed test should be performed to check the regression significance. The test is based on a statistical quantity  $F$  (Pfaffenberger and Patterson 1977, Zou 1995b).

$$F = \frac{\sum (\hat{u}'_{di} - \bar{u}'_d)^2 / m}{\sum (u'_{di} - \hat{u}'_{di})^2 / (n - m - 1)} \quad (6.22)$$

which has another simple form

$$F = \frac{r_c^2 / m}{(1 - r_c^2) / (n - m - 1)} \quad (6.23)$$

where  $F$  obeys the  $F$ -distribution.



The regression significance is checked against a given significance level. If  $F > F_o$ , the regression results are meaningful. The greater the better. Otherwise, the results are meaningless at that significance level and should not be used.  $F_o$  is the critical value of  $F$  function with degree of freedom of ( $m$ ) and ( $n-m-1$ ) at the  $\alpha\%$  level and can be obtained from a statistical table. Some  $F$  critical values are listed in Appendix E.

## 6.6 SUMMARY

In order to demonstrate the statistical procedure and analysis described above, an example is given in Chapter 7.

Ordinary least square (OLS) is a conventional way with consideration of standard deviations only. During each iteration, the measured data point yielding the maximum ordinary residual  $R_{max}$  is deleted. The aim is to find the solution with the minimum standard deviation, std. However, as indicated earlier, std is not an ideal estimator of the solution quality (Zou 1995b). Weighted least square (WLS) is a modified way with consideration of standardized residuals  $t$  and influence of data points  $d$ . During each iteration, if a measured data point yielding  $t_{max}$  which is greater than  $t_o$  (outlier), or a high leverage point, is found and also produces the maximum  $d$  value, this point will be deleted before the next test is done. Two aspects need to be considered to stop iteration.

- 1) if there are two consecutive non-outliers and one non-high leverage points, test will be stopped;
- 2) If data points become less, the results will be less accurate. In this research work, there are three unknown components for 2D in-situ stresses and six unknown components for 3D in-situ stresses. There is no  $t_o$  values when the measurement number is smaller than 6 and 9 for 3 and 6 independent unknown parameters, respectively. Accordingly, from the statistical analysis point of view, the tolerance number for diametrical convergence measurements is better to be greater than 6 and 9 for 2D and 3D in-situ stress analysis, respectively.

One of the above two conditions is applicable, the iteration will be stopped.

All solutions from all iterations will be compared to find the optimum one. The procedures

of WLS is summarized as follows.

Step 1: Use least square method to obtain the best-fit solution;

The best-fit solution: 
$$\{\hat{\sigma}_o\} = ([M_{con}]^T [M_{con}])^{-1} \cdot [M_{con}]^T \cdot \{u'_d\}$$

Step 2: Calculate the ordinary residual and standard deviation;

Predicted diametrical convergence:

$$\{\hat{u}'_d\} = [M_{con}] \cdot ([M_{con}]^T [M_{con}])^{-1} [M_{con}]^T \cdot \{u'_d\}$$

Hat matrix: 
$$[H] = [M_{con}] \cdot ([M_{con}]^T [M_{con}])^{-1} [M_{con}]^T$$

Ordinary residual: 
$$\{R\} = \{u'_d\} - \{\hat{u}'_d\} = ([I] - [H])\{u'_d\}$$

Step 3: Calculate the standard deviation;

Standard deviation (std): 
$$std = \sqrt{\sum R_i^2 / (n - m)} = \sqrt{R^T R / (n - m)}$$

Step 4: Detect the erroneous data point (unusual point);

Estimated standard error:  $s_i = std \sqrt{1 - h_{ii}}$  ( $h_{ii}$ - ith diagonal element of  $[H]$ )

Standardized residual:  $t_i = R_i / s_i = R_i / std \sqrt{1 - h_{ii}}$

Outlier detection:  $t_{\max} \succ t_o$

High leverage point detection:  $h_{ii} \succ 2m/n$

Step 5: Measure the influence;

Influence measure:  $d_i = t_i^2 h_{ii} / m (1 - h_{ii})$

Step 6: Delete the outlier or high leverage point in the next iteration if the point has the most influence ( $d_{\max}$ );

Step 7: Check the regression significance;

$$\text{Correlation coefficient: } r_c = \sqrt{1 - \frac{\{R\}^T \{R\}}{\sum (u'_{di} - \bar{u}'_d)^2}}$$

$$\text{Statistical quantity } F: \quad F = \frac{r_c^2 / m}{(1 - r_c^2) / (n - m - 1)}$$

If  $F > F_o$ , the regression results are meaningful. The greater the better.

If  $F < F_o$ , the regression results are meaningless. The error sources need to be examined.

Step 8: Perform the next test and repeat step 1 to step 7;

Step 9: Stop iteration if there are two consecutive non-outlier and one non-high leverage points, or the measurement number is equal to the tolerance number;

Step 10: Compare all solutions to find the optimum one.

# **CHAPTER 7 TEST OF 2D BACK ANALYSIS AND ASSESSMENT OF MUD-PORE PRESSURE EFFECTS**

## **7.1 TEST CONDITION**

An example is introduced to demonstrate the procedure of this 2D back-analysis method and statistical analysis, as well as to test the mathematical models and the program.

In this example, analysis is performed under the assumption of linear elastic and poroelastic behaviours of rock mass in different scenarios, which have been discussed in Chapter 5 in a stress field with differential horizontal stress components. Each scenario has a mathematical model.

### 1) Linear elastic behaviour

- rock formation with no pore pressure effect (NP)

### 2) Linear poroelastic behaviour of porous rock formation

- high permeability rock formation (HPR )and permeable well wall (PW)
- high permeability rock formation (HPR) and impermeable well wall (IPW)
- low permeability rock formation (LPR) and permeable well wall (PW)
- low permeability rock formation (LPR) and impermeable well wall (IPW)

## **7.2 AUTOMATED 2D CALCULATION**

In order to facilitate the calculation, automated 2D analysis sheets have been developed based on Excel, Macro and Visual Basic programming, with three packages. These packages are designed for

Package 1: Rock formation without pore pressure effect

Package 2: High permeability rock formation (two options: permeable and impermeable well wall);

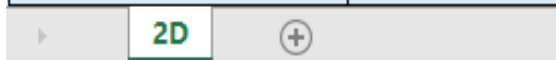
Package 3: Low permeability rock formation (two options: permeable and impermeable well wall).

The interface sheet includes Input Data, Analysis Action and Results, as shown in Figure 7.1.

DATA INPUT 2D VERTICAL WELL	
Young's modulus E [MPa]	20000
Poisson's ratio U [unitless]	0.2
Biot's coefficient $\alpha$ [unitless]	0.77
Porosity $\phi$ [ratio]	0.2
Well radius $r_w$ [m]	0.1
Mud pressure $P_m$ [MPa]	25
Pore pressure $P_p$ [MPa]	20
Radial distance $r'$ [m]	0.1
Skempton's coefficient - S [unitless]	0.92

Measurement data

Distance between the two opposite points on the wall - d [m]	Angles between measuring point from x-axis CCW $\theta$ [°]
0.199074	0.000
0.198983	30.000
0.198790	45.000
0.198977	60.000
0.199395	90.000
0.199443	120.000
0.199289	135.000
0.199132	150.000



(a) input data

## PERFORM ANALYSIS

Back Calculate in-situ Stresses for High Permeability Rock Formation with Permeable Well Wall Calculated!

Back Calculate In-situ Stresses for High Permeability Rock Formation with Impermeable Well Wall

Clear Results

(b) buttons for performing analysis

RESULTS - 2D		
Stress $\sigma_x$ [MPa]	Stress $\sigma_y$ [MPa]	Stress $T_{xy}$ [MPa]
68.41	60.23	5.35
Max principal stress $\sigma_1$ [MPa]	Min principal stress $\sigma_2$ [MPa]	Angle between $\sigma_1$ and x axis $\beta$ [°]
71.1	57.6	26.3

(c) output results

Figure 7.1 2D in-situ stress automated analysis interface information for the second package

## 1) Input Data

This section allows user to enter the data required for 2D in-situ stress analysis. It contains two tables for input data, as shown in Figure 7.1a. One table is for entering the rock properties, well geometry, mud pressure and pore pressure.

- Rock properties
  - Young's modulus  $E$
  - Poisson's ratio  $\nu$
  - Biot's coefficient  $\alpha$
  - Porosity  $\phi$
  - Skempton's coefficient  $s$
- Well geometry
  - Drill bit size (the geometry of the well being drilled)  $r_o$
  - Distance from the well axis to a point in the rock mass  $r$
- Mud pressure  $p_m$  and pore pressure  $p_p$

The other table is for entering the measurement data relevant to diametrical convergence. The Excel is programed, using VBA, to accept between 1 to 200 measurement data. The measurement data include two categories:

a) Radial or diametrical measurement

Measurement ID: 1 for radial measurement - distance between the well axis and the measurement point on the well wall; 2 for diametrical convergence measurement - distance between two opposite points on the well wall.

b) Measurement angle

$\theta$  - angle of a measured point, which is counted from  $x$ -axis counter clockwise ( $x$  axis-East,  $y$  axis-North).

All input data must meet specific requirements. If they don't meet the requirements, there will be warning messages to remind the user to check out.

## 2) Analysis

All calculation methods and analysis were programmed using Macro and VBA. The methods vary with different well wall and rock formation conditions. Rock formation conditions include highly permeable, low permeable, and non-porous rocks. For each of these conditions there is one action button. A button at the bottom in the analysis action section as seen in Figure 7.1b “Clear Results”, is for clearing previously saved data. When user clicks on this button, it runs a corresponding program written in VBA that clears results and resets all calculator sheets. Figure 7.2 gives part of the programming source codes for performing automated calculation.

```
' Matrix manipulations:
Range("AM3").Select
Range(Selection, Selection.End(xlToRight)).Select
Range(Selection, Selection.End(xlDown)).Select
Application.CutCopyMode = False
Selection.Copy
Range("AR3").Select
Selection.PasteSpecial Paste:=xlPasteValues, Operation:=xlNone, SkipBlanks _
:=False, Transpose:=True
Range("AR8:AT10").Select
Application.CutCopyMode = False
Selection.FormulaArray = "=MMULT (R[-5]C:R[-3]C[199], R[-5]C[-14]:R[194]C[-12])"
Range("AR13:AT15").Select
Selection.FormulaArray = "=MINVERSE (R[-5]C:R[-3]C[2])"
Range("AR18:II20").Select
Selection.FormulaArray = "=MMULT (R[-5]C:R[-3]C[2], R[-15]C:R[-13]C[199])"
Range("AR24:AR26").Select
Selection.FormulaArray = "=MMULT (R[-6]C:R[-4]C[199], R[-21]C[-15]:R[178]C[-15])"
Range("AR24:AR26").Select
Selection.Copy
Sheets("2D").Select
```

Figure 7.2 Programming source codes for matrix manipulation

## 3) Output results

The output data represent the results of the back-calculated in-situ 2D stresses. They are presented as 3 independent stress components  $\{\sigma_x, \sigma_y, \tau_{xy}\}$  and principal stresses  $\{\sigma_1, \sigma_2, \theta_{Hmax}\}$ .  $\sigma_1$  and  $\sigma_2$  are the maximum and minimum principal stresses in the plane perpendicular to the well axis, respectively. All stresses are shown in MPa unit consistently.  $\theta_{Hmax}$  represents the angle between the maximum principal stress and  $x$ -axis in degrees.

### 7.3 INPUT PARAMETERS OF TEST EXAMPLE

The in-situ principal stresses are assumed to be  $\sigma_{Hmax} = 54.50$  MPa and  $\sigma_{Hmin} = 40.0$  MPa at a depth of 2000 m in a two-dimensional stress field. The maximum principal stress direction is  $24^\circ$  from  $x$  direction (Figure 7.3).

The rock formation properties used in different scenarios are assumed (Chen et al 2003, Zhang et al 2006a, Ghassemi et al 2009):

- Elastic modulus  $E = 20$  GPa;
- Poisson's ratio  $\nu = 0.2$ ;
- Biot's coefficient  $\alpha = 0.77$ ;
- Porosity  $\phi = 30\%$  (for highly permeable rock, HPR) and  $15\%$  (for low permeability rock, LPR);
- Skempton's coefficient  $s = 0.92$ .

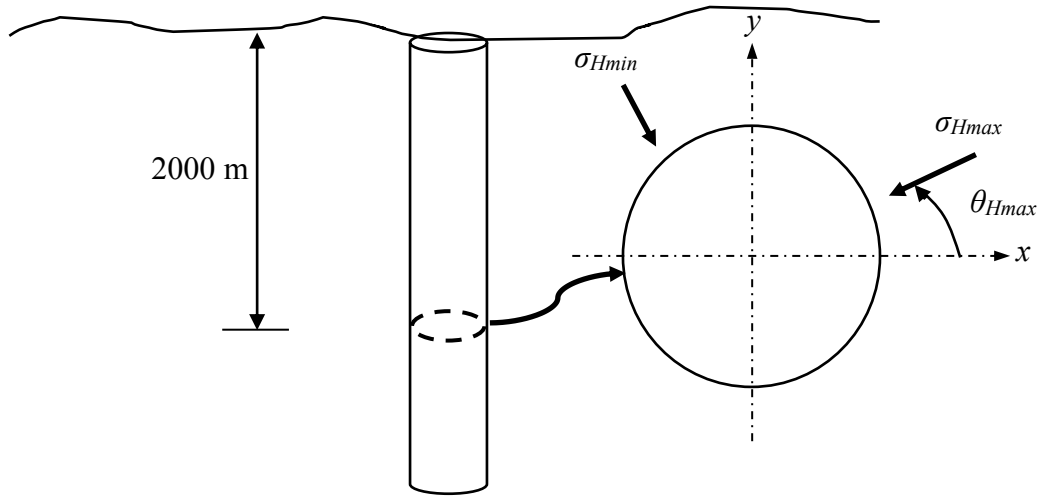


**Figure 7.3** Assumed in-situ stresses in two dimensions in the test example

The radius of the vertical well is 0.1 m. A total of 9 measurements of diameter are supposed to be made at different locations around the well (Figure 7.4). Table 7.1 lists the measurement angles of the 9 measurements.



Five scenarios are considered as stated in Section 7.1. Table 7.2 summarizes the input parameters for all scenarios.

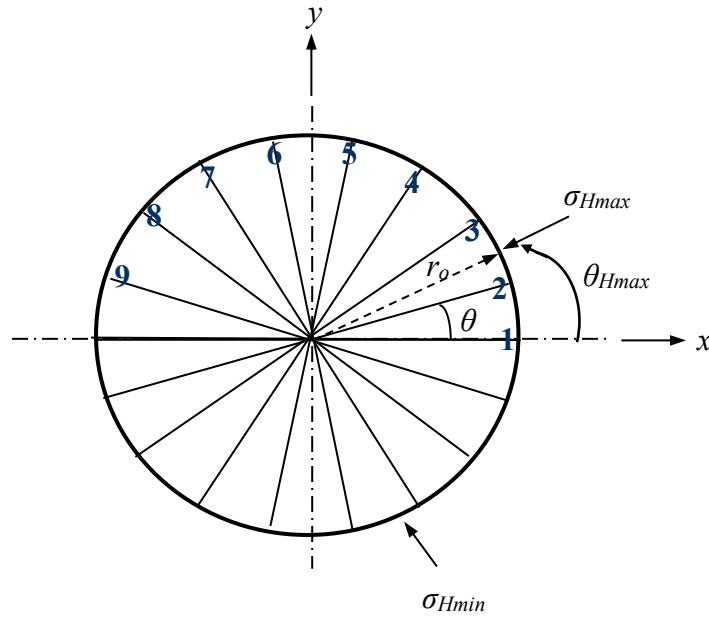


**Figure 7.4** Diameter measurements at different locations around the well

**Table 7.1** Measurement angles of the 9 measurement locations

Location	1	2	3	4	5	6	7	8	9
$\eta_i$ [°]	0	20	40	60	80	100	120	140	160
$\theta_{i_11}$ [°]	0	20	40	60	80	100	120	140	160
$\theta_{i_12}$ [°]	180	200	220	240	260	280	300	320	340

**Table 7.2** Input parameters for different scenarios

Parameters	Rock formation properties					$p_m$	$p_p$
	$E$ [GPa]	$\nu$	$s$	$\alpha$	$\phi$ [%]	[MPa]	[MPa]
Scenario 1 NP	20	0.2	—	—	—	0	0
Scenario 2 HPR and PW	20	0.2	—	0.8	30	25	20
Scenario 3 HPR and IPW	20	0.2	—	0.8	30	25	20
Scenario 4 LPR and PW	20	0.2	0.92	0.8	15	25	20
Scenario 5 LPR and IPW	20	0.2	0.92	0.8	15	25	20

Note:  $\phi$  is assumed to have different values for high permeability and low permeability rock formation, 30% for high permeability rock formation (HPR) and 15% for low permeability rock formation (LPR).

## 7.4 ANALYSIS AND RESULTS

### 7.4.1 Stress Calculation

Data of exact diametrical deformation caused by drilling at the 9 measurement locations are generated using Eqn. (5.53) with the specified in-situ stresses. These data are deemed as measured convergence and are applied to determine the in-situ stresses by the established back analysis models. In the second step, random errors of up to  $\pm 15\%$  are introduced to the exact diametrical convergence data to produce the hypothetical measurements (Table 7.3). Furthermore, the back-analyzed in-situ stresses are used to calculate the diametrical convergence at those locations for comparison. In the test, the random errors were generated by computer and statistically half positive and half negative.

**Table 7.3** Diametrical convergence data

Diametrical convergence [mm]		1	2	3	4	5	6	7	8	9
Scenario 1 NP	Exact $u_d$	1.093	1.183	1.144	0.994	0.804	0.662	0.635	0.735	0.916
	Errors [%]	-1	8	10	-14	15	-8	4	7	-11
	Hypothetic	1.083	1.273	1.259	0.855	0.924	0.611	0.659	0.788	0.819
Scenario 2 HPR and PW	Exact $u_d$	0.712	0.802	0.763	0.613	0.423	0.281	0.254	0.354	0.535
	Errors [%]	-1	8	10	-14	15	-8	4	7	-11
	Hypothetic	0.706	0.863	0.840	0.527	0.486	0.259	0.264	0.379	0.478
Scenario 3 HPR and IPW	Exact $u_d$	0.697	0.787	0.748	0.598	0.408	0.266	0.239	0.339	0.520
	Errors [%]	-1	8	10	-14	15	-8	4	7	-11
	Hypothetic	0.691	0.847	0.823	0.514	0.469	0.245	0.248	0.363	0.465
Scenario 4 LPR and PW	Exact $u_d$	0.682	0.756	0.724	0.602	0.446	0.331	0.309	0.390	0.538
	Errors [%]	-1	8	10	-14	15	-8	4	7	-11
	Hypothetic	0.676	0.813	0.797	0.517	0.513	0.305	0.320	0.418	0.481
Scenario 5 LPR and IPW	Exact $u_d$	0.663	0.736	0.704	0.582	0.427	0.311	0.289	0.371	0.519
	Errors [%]	-1	8	10	-14	15	-8	4	7	-11
	Hypothetic	0.657	0.792	0.775	0.501	0.490	0.287	0.300	0.397	0.463

The calculation procedures in different scenarios are carried out using the automated analysis sheet. The applied and back-analyzed stress results are displayed in Table 7.4.

**Table 7.4** Applied and back-analyzed 2D in-situ principal stresses

In-situ stresses $\{\sigma_o\}$		$\sigma_{Hmax}$ [MPa]	$\sigma_{Hmin}$ [MPa]	$\theta_{Hmax}$ [°]
Applied stresses		54.50	40	24
Model 1: NP	Back-analyzed stresses with exact $u_d$	54.50	40	24
	Back-analyzed stresses with hypothetical $u_d$	55.57	40.15	25.41
	Differences [%]	2.0	0.4	5.9
Model 2: HPR and PW	Back-analyzed stresses with exact $u_d$	54.50	40	24
	Back-analyzed stresses with hypothetical $u_d$	55.25	40.01	24.92
	Differences [%]	1.4	0.03	3.8
Model 3: HPR and IPW	Back-analyzed stresses with exact $u_d$	54.50	40	24
	Back-analyzed stresses with hypothetical $u_d$	55.34	40.01	24.90
	Differences [%]	1.4	0.02	3.8
Model 4: LPR and PW	Back-analyzed stresses with exact $u_d$	54.50	40	24
	Back-analyzed stresses with hypothetical $u_d$	55.27	39.97	25.08
	Differences [%]	1.4	-0.1	4.5
Model 5: LPR and IPW	Back-analyzed stresses with exact $u_d$	54.50	40	24
	Back-analyzed stresses with hypothetical $u_d$	55.25	39.97	25.05
	Differences [%]	1.4	-0.1	4.4

The solutions of the in-situ stresses are the same as the actual ones when the measured diametrical convergence is exact. There are no differences between these two sets of stress data. This is expected and it demonstrates the correct analysis process and formulations. When up to 15% errors are added to the diametrical convergence data, the solutions are slightly changed. The differences are less than the introduced errors of 15%. The corresponding diametrical convergence calculated from applied stresses and back-analyzed stresses at the 9 measurement locations are shown in Figure 7.5 and Table 7.5. By comparing these values, it is seen that the same data of diametrical convergence is obtained from the applied and the back-analyzed stresses when input data is exact. If the input data containing errors are used, the diametrical convergence at different directions on the well wall obtained from the back-analyzed stresses show errors, for most of them, less than the introduced hypothetical errors for the corresponding input diametrical convergence data.

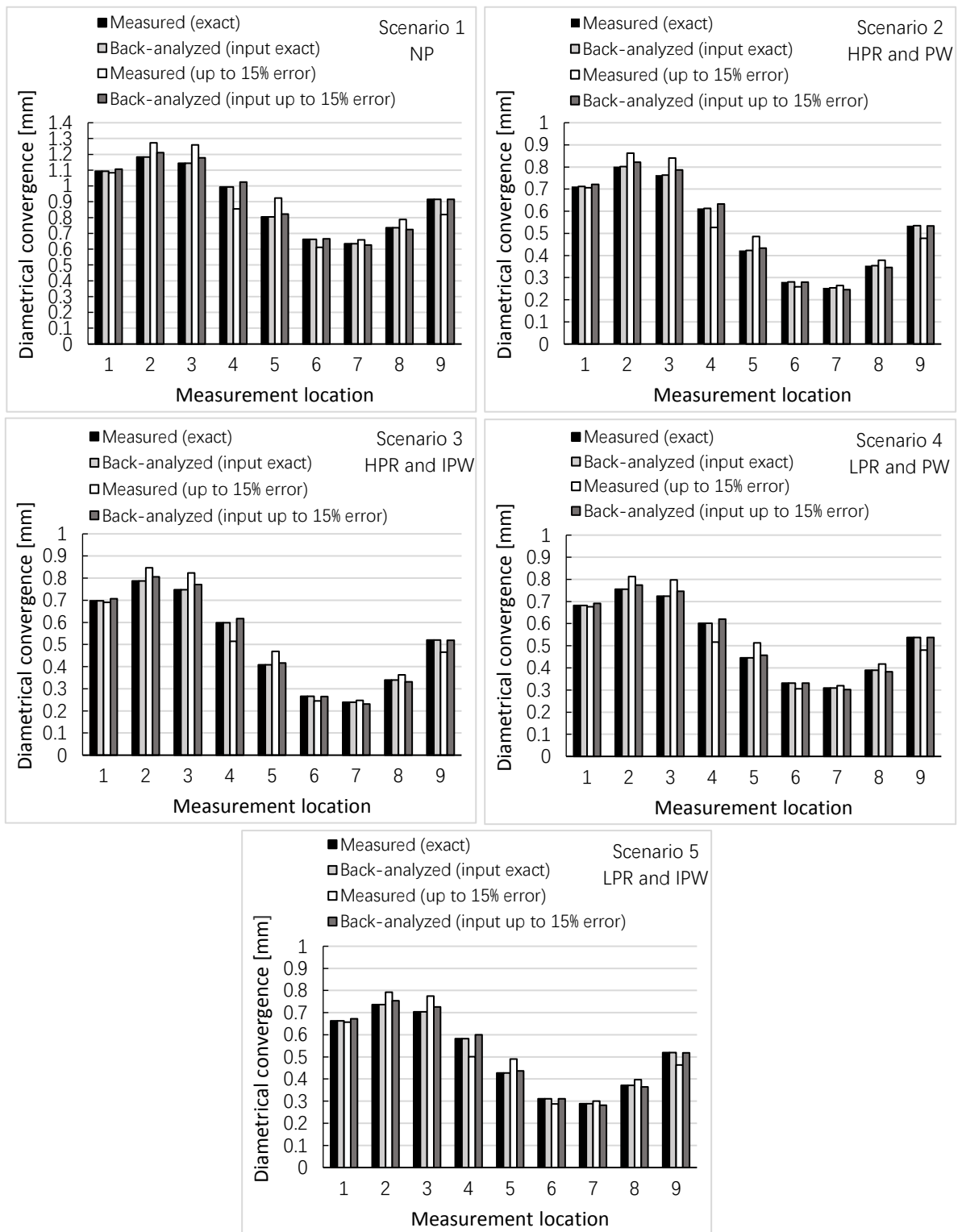


**Figure 7.5** Comparison of diametrical convergence from applied and back-analyzed 2D in-situ stresses

**Table 7.5** Diametrical convergence from applied and back-analyzed 2D in-situ stresses

Scenario	Diametrical convergence $u_d$	1	2	3	4	5	6	7	8	9
1	$u_d$ from applied stresses [mm]	1.093	1.183	1.144	0.994	0.804	0.662	0.635	0.735	0.916
	$u_d$ from back-analyzed stresses without error [mm]	1.093	1.183	1.144	0.994	0.804	0.662	0.635	0.735	0.916
	Hypothetic error [%]	-1	8	10	-14	15	-8	4	7	-11
	$u_d$ with hypothetic error [mm]	1.083	1.273	1.259	0.855	0.924	0.611	0.659	0.788	0.819
	$u_d$ from back-analyzed stresses with hypothetic error [mm]	1.106	1.210	1.178	1.024	0.822	0.665	0.627	0.725	0.915
	Produced error [%]	<b>1.2</b>	<b>2.3</b>	<b>3.0</b>	<b>3.0</b>	<b>2.2</b>	<b>0.4</b>	<b>-1.3</b>	<b>-1.4</b>	<b>-0.2</b>
2	$u_d$ from applied stresses [mm]	0.712	0.802	0.763	0.613	0.423	0.281	0.254	0.354	0.535
	$u_d$ from back-analyzed stresses without error [mm]	0.712	0.802	0.763	0.613	0.423	0.281	0.254	0.354	0.535
	Hypothetic error [%]	-1	8	10	-14	15	-8	4	7	-11
	$u_d$ with hypothetic error [mm]	0.706	0.863	0.840	0.527	0.486	0.259	0.264	0.379	0.478
	$u_d$ from back-analyzed stresses with hypothetic error [mm]	0.722	0.822	0.787	0.633	0.433	0.280	0.246	0.346	0.534
	Produced error [%]	<b>1.4</b>	<b>2.5</b>	<b>3.1</b>	<b>3.2</b>	<b>2.4</b>	<b>-0.4</b>	<b>-3.3</b>	<b>-2.3</b>	<b>-0.2</b>
3	$u_d$ from applied stresses [mm]	0.697	0.787	0.748	0.598	0.408	0.266	0.239	0.339	0.520
	$u_d$ from back-analyzed stresses without error [mm]	0.697	0.787	0.748	0.598	0.408	0.266	0.239	0.339	0.520
	Hypothetic error [%]	-1	8	10	-14	15	-8	4	7	-11
	$u_d$ with hypothetic error [mm]	0.691	0.847	0.823	0.514	0.469	0.245	0.248	0.363	0.465
	$u_d$ from back-analyzed stresses with hypothetic error [mm]	0.707	0.806	0.771	0.617	0.417	0.265	0.231	0.331	0.519
	Produced error [%]	<b>1.5</b>	<b>2.5</b>	<b>3.1</b>	<b>3.2</b>	<b>2.4</b>	<b>-0.5</b>	<b>-3.5</b>	<b>-2.4</b>	<b>-0.2</b>
4	$u_d$ from applied stresses [mm]	0.682	0.756	0.724	0.602	0.446	0.331	0.309	0.390	0.538
	$u_d$ from back-analyzed stresses without error [mm]	0.682	0.756	0.724	0.602	0.446	0.331	0.309	0.390	0.538
	Hypothetic error [%]	-1	8	10	-14	15	-8	4	7	-11
	$u_d$ with hypothetic error [mm]	0.676	0.813	0.797	0.517	0.513	0.305	0.320	0.418	0.481
	$u_d$ from back-analyzed stresses with hypothetic error [mm]	0.691	0.774	0.746	0.620	0.457	0.331	0.302	0.383	0.537
	Produced error [%]	<b>1.3</b>	<b>2.4</b>	<b>3.0</b>	<b>3.1</b>	<b>2.3</b>	<b>0</b>	<b>-2.2</b>	<b>-1.8</b>	<b>-0.2</b>
5	$u_d$ from applied stresses [mm]	0.663	0.736	0.704	0.582	0.427	0.311	0.289	0.371	0.519
	$u_d$ from back-analyzed stresses without error [mm]	0.663	0.736	0.704	0.582	0.427	0.311	0.289	0.371	0.519
	Hypothetic error [%]	-1	8	10	-14	15	-8	4	7	-11
	$u_d$ with hypothetic error [mm]	0.657	0.792	0.775	0.501	0.490	0.287	0.300	0.397	0.463
	$u_d$ from back-analyzed stresses with hypothetic error [mm]	0.672	0.754	0.726	0.600	0.437	0.311	0.282	0.364	0.518
	Produced error [%]	<b>1.3</b>	<b>2.4</b>	<b>3.1</b>	<b>3.2</b>	<b>2.3</b>	<b>0</b>	<b>-2.3</b>	<b>-1.9</b>	<b>-0.2</b>

Note: scenario 1- NP; scenario 2 – HPR and PW; scenario 3 -HPR and IPW; scenario 4 -LPR and PW; scenario 5 – LPR and IPW.

### 7.4.2 Result Optimization by Statistical Analysis

Scenario 3 is used here to demonstrate the procedure for regression analysis as described in Chapter 6. A larger error at -35% was given to the measurement points #1 (Table 7.6). It is intended to illustrate the effect of erroneous data and the process to identify erroneous point.

**Table 7.6** Hypothetic errors for scenario 3 with larger error at -35%

Measurement point	1	2	3	4	5	6	7	8	9
Hypothetic error [%]	<b>-35</b>	8	10	-14	15	-8	4	7	-11

Three iterations were performed.  $t$  and  $d$  values during each iteration are listed in Table 7.7. The results from WLS analysis are given in Tables 7.8 and 7.9.

The bold number in each column of Table 7.7 is the largest value in that column. It can be seen from the 1<sup>st</sup> iteration that the measurement data point 1 with the larger error -35% showed up with  $t_{max}$  (2.15) and  $d_{max}$  (1.11). In the meantime,  $t_{max}$  was greater than the critical value  $t_o$  at the 90% confidence level (2.13). The data point 1 was therefore identified as an outlier and to be deleted from the input data set.

In the 2<sup>nd</sup> iteration, the data point 1 was deleted and the regression analysis was repeated. The results showed that the data point 4 yielded  $t_{max}$  (1.90) and  $d_{max}$  (0.60). However,  $t_{max}$  was less than the critical value  $t_o$  at the 90% confidence level (2.03). This point was not identified as an outlier.

One more iteration was carried out for checking the possible masking effect due to multiple outliers, in which data point 4 was deleted. This iteration found that the data point 9 had  $t_{max}$  (1.66) and it was the most influential one ( $d_9 = d_{max} = 0.76$ ). However, since  $t_{max}$  is smaller than  $t_o$  (1.90) ( $t_{max} < t_o$ ), it was not considered as an outlier. There were two consecutive non-outliers. During each iteration,  $h_{i_{max}}$  was checked, and no  $h_{ii}$  value was greater than  $2m/n$ , suggesting that there was no high leverage point. Accordingly, the test was stopped.

**Table 7.7**  $t$  and  $d$  values during each iteration

Iteration	1		2		3	
	$ t $	$d$	$ t $	$d$	$ t $	$d$
1	<b>2.15</b>	<b>1.11</b>				
2	1.32	0.42	0.67	0.12	0.36	0.04
3	1.08	0.28	0.91	0.16	0.17	0.01
4	1.27	0.39	<b>1.90</b>	<b>0.60</b>		
5	0.34	0.03	1.00	0.18	0.35	0.04
6	0.52	0.07	0.31	0.02	1.29	0.34
7	0.21	0.01	0.32	0.02	0.54	0.05
8	0.84	0.17	0.54	0.06	1.41	0.41
9	0.15	0.01	1.25	0.43	<b>1.61</b>	<b>0.76</b>

**Table 7.8** Results from WLS analysis for the diametrical convergence set of data with a larger error

Iteration	2D in-situ stresses			2D in-situ principal stresses			$r_c$	Data point deleted
	$\sigma_x$	$\sigma_y$	$\tau_{xy}$	$\sigma_{Hmax}$	$\sigma_{Hmin}$	$\theta_{Hmax}$ [°]		
Applied	52.09	42.42	5.4	54.5	40	24		
1	49.79	42.71	5.82	53.05	39.44	29.34	0.905	
2	52.82	42.71	5.82	55.47	40.06	24.50	0.970	1
3	53.27	44.05	6.59	56.70	40.62	27.51	0.992	1,4

**Table 7.9** Some important statistical parameters from WLS analysis for the diametrical convergence set of data with a larger error

Iteration	$t_{max}$	$t_o$ @ 90%	Point @ $t_{max}$	$d$	$d_{max}$	$h_{iimax}$	$2m/n$	$F_o$ @90%	$F$	$F/F_o$
1	2.15	2.13	1	1.11	1.11	0.42	0.67	2.81	7.54	2.68
2	1.90	2.03	4	0.60	0.60	0.45	0.75	2.92	21.22	7.27
3	1.61	1.90	9	0.76	0.76	0.49	0.86	3.07	59.49	19.38

The reliability and quality of the regression results was also checked. It was tested on the basis of the  $F$  value assuming normal distribution of the measurement error. For a meaningful solution, the ratio  $F/F_o$  must be greater than one and the greater the better. It can be found from Table 7.9 that the results from the 2nd iteration with the data set in which the data point 1 (outlier) was deleted are meaningful and best represent the stress state at the 90% confidence level.

It is indicated from this example that this regression analysis method is useful to detect the erroneous data points and optimize the results.

### **7.4.3 Brief Summary of Test of 2D Stress Calculation and Statistical Analysis**

The stress calculation results in this example test reveal the reliability of mathematical models and the validity of program and this inverse approach of 2D back analysis taking into account pore and mud pressure. This example also demonstrates the usefulness of the statistical procedure for diametrical convergence data analysis. It can be used to locate outliers & high leverage points and test the reliability of the regression results, consequently helping to find out the solution that best represent the stress state at a certain confidence level.

It should be emphasized here that the outlier and high leverage point tests and the influence measure are the statistical techniques only, which are applied to help assess the data base and to improve the regression results statistically. If the data base is erroneous, these techniques cannot do any good to the regression results. Furthermore, although they can help verify if the regression model is valid for a given set of data, they can never themselves improve the model if the assumed physical model is invalid. Another point which should always be kept in mind is that statistics is never going to work well if the data base is small.

## **7.5 ASSESSMENT OF EFFECTS OF PORE AND MUD PRESSURE**

### **7.5.1 Effects of Pore Pressure Distribution and Mud Pressure**

Pore pressure is an important factor for wellbore stability. Pore pressure change and distribution can affect the redistribution of stresses around a well after drilling, which can be reflected by the well deformation. Figure 7.6 presents pore pressure distribution at the different measuring directions after drilling in low permeability rock formation. After introduction of a well into a stress field with differential horizontal stress components, the pore pressure at different locations depends on the azimuth. It can be seen (Figure 7.6,



generated from Eqn. 5.8) that the pore pressure is different at the different direction around the wellbore. It has a higher concentration in the direction of  $\sigma_{Hmin}$  and lower concentration in the direction of  $\sigma_{Hmax}$ .

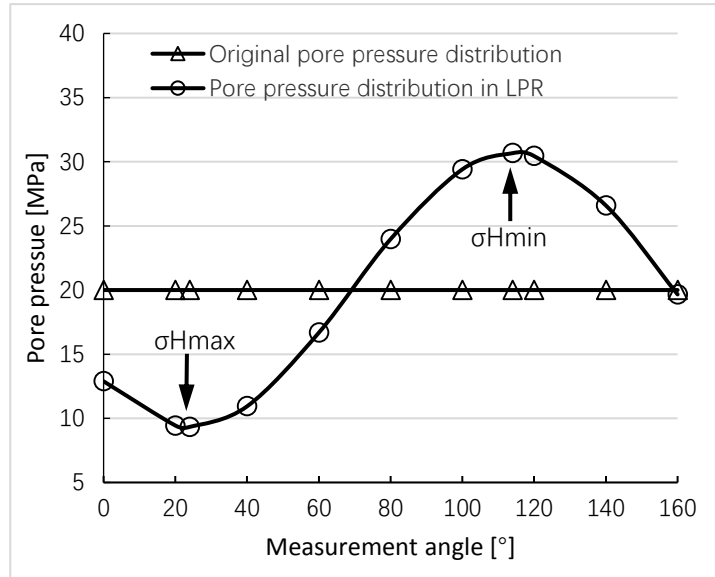


**Figure 7.6** Pore pressure distribution at the different measuring directions after drilling

In order to analyze the effects of pore pressure distribution and mud penetration from well into the rock formation on the well deformation, the diametrical convergence at different locations obtained from the back-analyzed in-situ stresses in the above example are depicted in Figure 7.7.

There is a maximum diametrical convergence in the direction of  $\sigma_{hmax}$  and a minimum diametrical convergence in the direction of  $\sigma_{hmin}$ . For scenarios 4 and 5, the rock formation has low permeability. The results show a decreased difference in diametrical convergence between the direction of  $\sigma_{Hmin}$  and  $\sigma_{Hmax}$  contrary to high permeability rock formation. This phenomenon induces different wellbore shapes after drilling in these two conditions. An oval well shape with its longer axis in the direction of  $\sigma_{Hmin}$  is a result of different diametrical convergence around the well. In low permeability rock formation, well convergence in the direction of  $\sigma_{hmax}$  and its ovalisation in the perpendicular direction can be decelerated.

Scenarios 3 and 5 have impermeable well wall, no mud will penetrate into rock formation during drilling. Whereas scenarios 2 and 4 have permeable well wall and some mud tends to penetrate into the rock formation, which decreases the mud pressure and causes the increase of diametrical convergence. Thus, for the same rock formation, the diametrical convergence with the permeable well wall is larger than that with impermeable well wall.

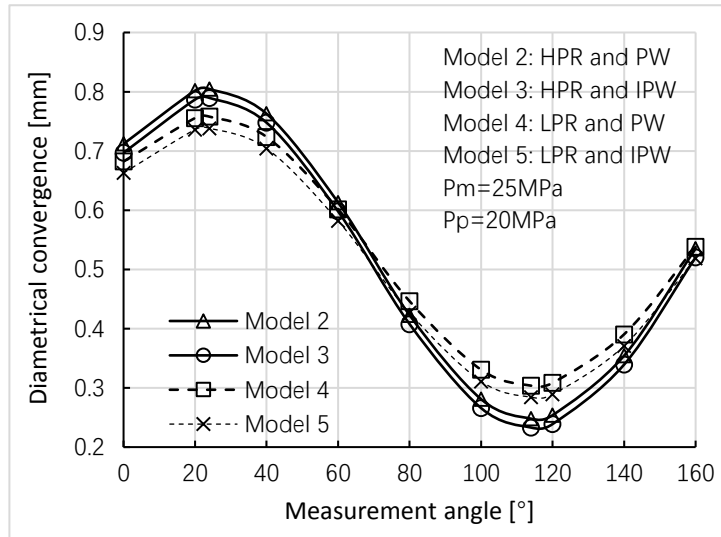


Figure 7.7 Comparison of diametrical convergence for 5 scenarios

### 7.5.2 Effects of Change of Mud Pressure

The change of mud pressure will cause deviation in diametrical convergence. Figure 7.8 depicts the diametrical convergence at different mud pressure for different scenarios. With an increase of the mud pressure, the diametrical convergence decreases. The variation in mud pressure shows a similar effect on the diametrical convergence for high and low permeability rock formations. In the same type of rock formation, as an increase in mud pressure, the mud penetration because of permeable well wall leads to the less decrement of diametrical convergence compared to impermeable well wall.

The main borehole failure mechanisms include fracturing (tensile failure) and collapse (compressive failure). Based on the “Mud weight window” – the range of mud weight which can maintain a stable wellbore, compressive failure occurs, possibly causing the well to collapse if the mud pressure is lower than  $p_{wc}$ . Mud weight can help to provide partial

support to the wellbore wall. Increasing mud pressure can resist converging and reduce the risk of wellbore collapse. At high mud pressure, expansion occurs along the axis corresponding to  $\sigma_{Hmin}$ . When the mud pressure exceeds  $p_{wf}$ , tensile failure takes place in the direction of  $\sigma_{Hmax}$ . Failure criteria can be applied to estimate the minimum mud pressure ( $p_{mc}$ ) and the maximum mud pressures ( $p_{mf}$ ) beyond which the wellbore will fail if the in-situ stress and pore pressure are known. Therefore the determination of the critical mud pressure for maintaining wellbore stability is highly dependent on the in-situ stress field, the formation pore pressure, and rock properties.

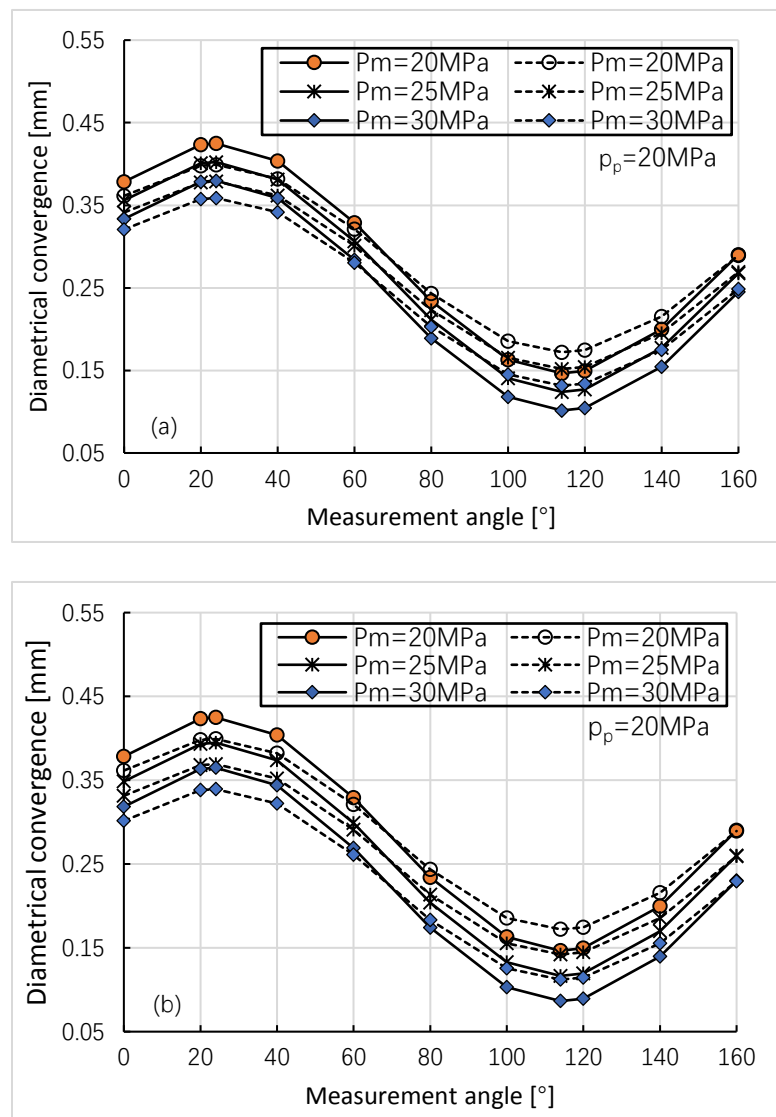


**Figure 7.8** Effect of mud pressure on the diametrical convergence at different locations on the wellbore wall for different scenarios (solid line for high permeability rock formation; dashed line for low permeability rock formation): (a) permeable well wall; (b) impermeable well wall

The above discussion of the effects of pore pressure distribution, mud penetration, change in mud pressure on wellbore deformation clearly demonstrates the importance of knowing the exact pore pressure when developing back analysis models and studying wellbore stability for different type of rock formation. For the same measurement data, the outcome of back-analyzed in-situ stresses may be different when different models are assumed. There are other factors, which may play a role in wellbore stability as well and need to be explored in future work.

# CHAPTER 8 THREE-DIMENSIONAL STRESS BACK ANALYSIS FROM WELL/BOREHOLE DEFORMATION

## 8.1 EXPLORING THEORETICAL MINIMUM REQUIREMENTS FOR DETERMINATION OF THE 3D COMPLETE STRESS TENSOR

From the discussion of Chapters 3 and 5, the diametrical convergence measurements can be made at different directions around a well in the plane perpendicular to the well axis and each  $u_{di}$  has a different set of  $M_i$ . Figure 8.1 shows three orthogonal wells (petroleum engineering / boreholes (mining and geotechnical engineering) with the same size to facilitate the following discussions.

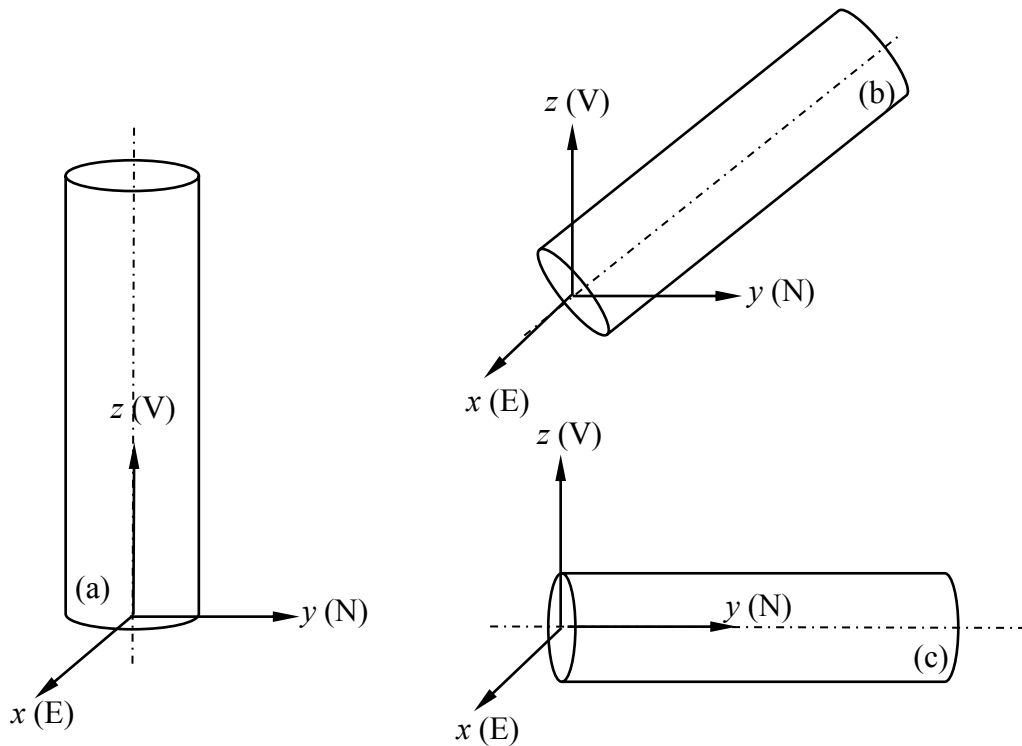


**Figure 8.1** Wells / boreholes used to determine the in-situ stresses from diametrical convergence measurements: (a) a vertical well / borehole; (b) a horizontal well / borehole (parallel to  $x$  axis); (c) a horizontal well / borehole (parallel to  $y$  axis)

### 8.1.1 Stress Tensor and Diametrical Convergence in One Single Well / Borehole

1) For a vertical well / borehole I, based on previous discussions, the well / borehole wall diametrical convergence is given as

$$\{u_d\} = [M_{con\ 1} \ M_{con\ 2} \ M_{con\ 3} \ M_{con\ 4}] \{\sigma_x \ \sigma_y \ \sigma_z \ \tau_{xy}\}^T + C \quad (8.1)$$

2) For a horizontal well / borehole II with well / borehole axis parallel to  $x$  axis

$$\{u_d\} = [M'_{con\ 1} \ M'_{con\ 2} \ M'_{con\ 3} \ M'_{con\ 5}] \{\sigma_x \ \sigma_y \ \sigma_z \ \tau_{yz}\}^T + C \quad (8.2)$$

3) For a horizontal well III with well / borehole axis parallel to  $y$  axis

$$\{u_d\} = [M''_{con\ 1} \ M''_{con\ 2} \ M''_{con\ 3} \ M''_{con\ 6}] \{\sigma_x \ \sigma_y \ \sigma_z \ \tau_{zx}\}^T + C \quad (8.3)$$

It is discovered from Eqns. (8.1), (8.2) and (8.3) that two coefficients of  $[M]$  matrix vanish and two shear stresses do not contribute to the diametrical convergence of a well / borehole. A set of diametrical convergence measured in a plane perpendicular to a well / borehole can only provide a maximum of four independent correlations between diametrical convergence and stress components. No matter how many measurements are made in the same plane or parallel planes, they are not sufficient for a complete solution of the six stress components in three dimensions. Parallel wells / boreholes have essentially the same measurement plane and make no difference.

### 8.1.2 Stress Tensor and Diametrical Convergence in More Than One Well or Borehole

1) Two perpendicular wells / boreholes

If two drilled wells / boreholes which are perpendicular to each other are considered, any two in the above three equations can be combined together based on stress directions and superposition principle as follows.

a. First well / borehole vertical, second well / borehole horizontal with well / borehole axis parallel to  $x$  axis

$$\{u_d\}_{I+II} = [M_{con1} \ M_{con2} \ M_{con3} \ M_{con4} \ M_{con5}]_{I+II} \{\sigma_x \ \sigma_y \ \sigma_z \ \tau_{xy} \ \tau_{yz}\}^T + C \quad (8.4)$$

b. First well / borehole vertical, second well / borehole horizontal with well / borehole axis parallel to y axis

$$\begin{aligned} \{u_d\}_{I+III} = & [M_{con1} \quad M_{con2} \quad M_{con3} \quad M_{con4} \quad M_{con6}]_{I+III} \{\sigma_x \quad \sigma_y \quad \sigma_z \quad \tau_{xy} \quad \tau_{zx}\}^T \\ & + C \end{aligned} \quad (8.5)$$

c. First well / borehole horizontal with well / borehole axis parallel to x axis, second well / borehole horizontal with well / borehole axis parallel to y axis

$$\begin{aligned} \{u_d\}_{II+III} = & [M_{con1} \quad M_{con2} \quad M_{con3} \quad M_{con5} \quad M_{con6}]_{II+III} \{\sigma_x \quad \sigma_y \quad \sigma_z \quad \tau_{yz} \quad \tau_{yz}\}^T \\ & + C \end{aligned} \quad (8.6)$$

As can be seen from Eqns. (8.4), (8.5) and (8.6), one shear stress of the stress tensor is still missing. Therefore diametrical convergence measurements made in two perpendicular wells / boreholes are not sufficient either.

## 2) Three perpendicular wells / boreholes

If three mutually-perpendicular wells / boreholes are used, as shown in Figure 8.2, with one being vertical and the other two horizontal, Eqns. (8.1), (8.2) and (8.3) can all be combined together.

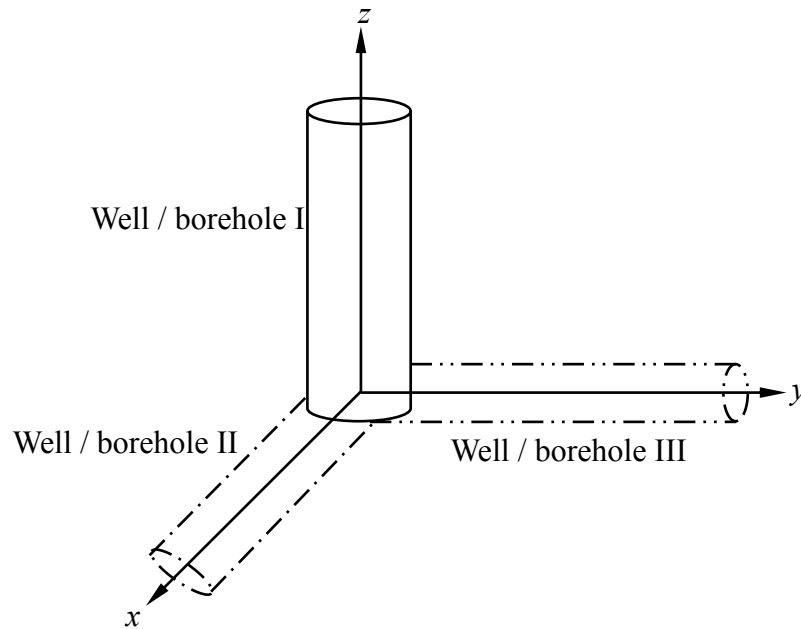


**Figure 8.2** Three mutually-perpendicular wells used to determine the in-situ stresses from diametrical convergence measurements

$$\{u_d\}_{I+II+III} = [M_{con1} \quad M_{con2} \quad M_{con3} \quad M_{con4} \quad M_{con5} \quad M_{con6}]_{I+II+III} \{ \sigma_x \quad \sigma_y \quad \sigma_z \quad \tau_{xy} \quad \tau_{yz} \quad \tau_{zx} \}^T + C \quad (8.7)$$

All six stress components in the 3D complete stress tensor are included and can be obtained from the measurements in three mutually perpendicular wells / boreholes. This method seems valid in theory. However, it does not seem practical in the field for petroleum application. Drilling three orthogonal wells like that is practically difficult and economically impossible.

### 3) Two non-perpendicular wells / boreholes

If a pair of non-perpendicular and non-parallel wells / boreholes are used, there needs to be a global coordinate system (E, N, V) and all measurements in these two wells / boreholes need to be related to the global coordinate system, as demonstrated in Figure 8.3.

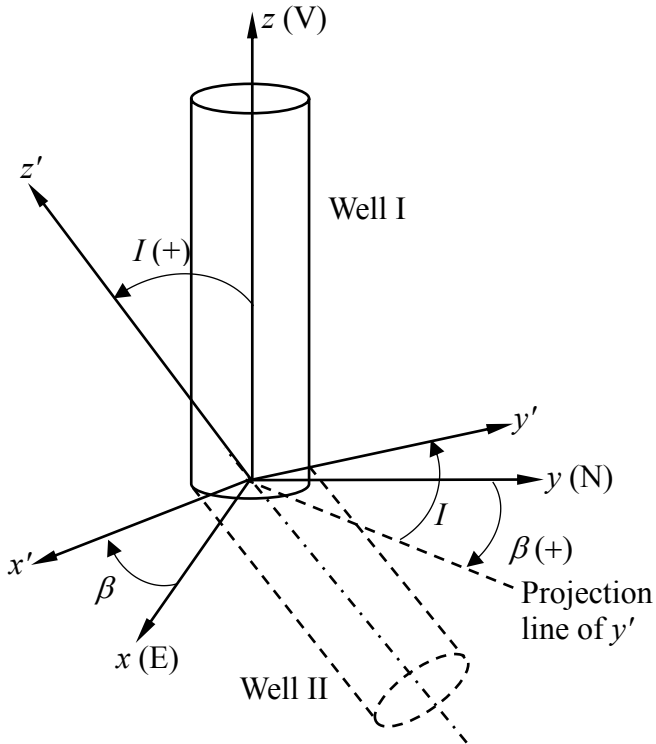


**Figure 8.3** Two non-perpendicular wells / boreholes used to determine the in-situ stresses from diametrical convergence measurements



In Figure 8.3, assume well / borehole I vertical and the other well / borehole inclined. For Well / borehole I, a coordinate system  $x, y, z$  is set to coincide with the global coordinates E, N, V. Well / borehole II is defined by rotating the  $xy$  axes clockwise from N by  $\beta$  around  $z$  and then rotating the  $y'z'$  axes by  $I$  from vertical around  $x'$ . For Well / borehole II, local coordinates  $x', y'$  and  $z'$  are used. From previous results, the diametrical convergence for the two wells / boreholes are given as

$$\{u_d\}_I = [M_{con1} \quad M_{con2} \quad M_{con3} \quad M_{con4}] \{\sigma_x \quad \sigma_y \quad \sigma_z \quad \tau_{xy}\}^T + C \quad (8.8a)$$

$$\{u_d\}_{II} = [M'_{con1} \quad M'_{con2} \quad M'_{con3} \quad M'_{con4}] \{\sigma_{x'} \quad \sigma_{y'} \quad \sigma_{z'} \quad \tau_{x'y'}\}^T + C \quad (8.8b)$$

In order to combine the above data, a transformation matrix  $[T]$  (see Eqn. 8.19c) is required to transform the stress components in  $x', y'$  and  $z'$  coordinates (local coordinate system) into components in the  $x, y$  and  $z$  coordinates (global coordinate system). After transformation, Eqn. (8.8b) becomes

$$\{u_d\}_{II} = [M''_{con1} \quad M''_{con2} \quad M''_{con3} \quad M''_{con4} \quad M''_{con5} \quad M''_{con6}] \{\sigma_x \quad \sigma_y \quad \sigma_z \quad \tau_{xy} \quad \tau_{yz} \quad \tau_{zx}\}^T + C \quad (8.9)$$

Therefore, in theory, diametrical convergence measurements from these two wells / boreholes can be combined to obtain complete solution for all six components of the three-dimensional stresses.

Through the above discussions, the complete stress components in 3D may be determined by measurements in two non-perpendicular wells / boreholes. The detail of stress transformation is discussed below.

## 8.2 STRESS TRANSFORMATION IN 3D FROM A LOCAL COORDINATE SYSTEM TO A GLOBAL COORDINATE SYSTEM

As described in the previous section, there are two coordinate systems, as shown in Figure 8.3.

- Global coordinate system:  $x, y, z$  coordinates, parallel to east-west, north-south and

vertical directions, respectively,

- Local coordinate system:  $x', y', z'$  coordinates for any well / borehole.

Each axis in the local system is defined using two angles  $\beta$  and  $I$  in the global system.

- $\beta$  – bearing angle, angle between  $y$  axis (N) and the projection line of  $oy'$  in  $oxy$  plane, positive in the clockwise direction,
- $I$  – inclination angle, measured from vertical direction, positive in the counter-clockwise direction.

The correlations between the two coordinate systems can be described by the direction cosines,  $l_{ij}$  - the cosine of the angle between the  $i$ -axis and the  $j'$ -axis. If the direction cosines of  $x', y', z'$  with respect to  $x, y, z$  are  $(l_{x'x}, l_{x'y}, l_{x'z})$ ,  $(l_{y'x}, l_{y'y}, l_{y'z})$ ,  $(l_{z'x}, l_{z'y}, l_{z'z})$  respectively, or

$$[L] = \begin{bmatrix} l_{x'x} & l_{x'y} & l_{x'z} \\ l_{y'x} & l_{y'y} & l_{y'z} \\ l_{z'x} & l_{z'y} & l_{z'z} \end{bmatrix} = \begin{bmatrix} \cos(x', x) & \cos(x', y) & \cos(x', z) \\ \cos(y', x) & \cos(y', y) & \cos(y', z) \\ \cos(z', x) & \cos(z', y) & \cos(z', z) \end{bmatrix} \quad (8.10)$$

and if stresses are in a tensor form

$$[\sigma_o]_{xyz} = \begin{bmatrix} \sigma_x & \tau_{xy} & \tau_{xz} \\ \tau_{xy} & \sigma_y & \tau_{yz} \\ \tau_{zx} & \tau_{zy} & \sigma_z \end{bmatrix} \quad (8.11)$$

and

$$[\sigma'_o]_{x'y'z'} = \begin{bmatrix} \sigma_{x'} & \tau_{x'y'} & \tau_{x'z'} \\ \tau_{x'y'} & \sigma_{y'} & \tau_{y'z'} \\ \tau_{z'x'} & \tau_{z'y'} & \sigma_{z'} \end{bmatrix} \quad (8.12)$$

$[\sigma'_o]$  in  $x', y', z'$  coordinates can be related to  $[\sigma_o]$  in  $x, y, z$  coordinates by

$$[\sigma'_o] = [L][\sigma_o][L]^T \quad (8.13)$$

or

$$[\sigma_o] = [L]^T [\sigma'_o] [L] \quad (8.14)$$

Substituting Eqn. (8.10) into Eqn. (8.13) and expanding the matrices:

$$\begin{bmatrix} \sigma_{x'} & \tau_{x'y'} & \tau_{x'z'} \\ \tau_{y'x'} & \sigma_{y'} & \tau_{y'z'} \\ \tau_{z'x'} & \tau_{z'y'} & \sigma_{z'} \end{bmatrix} = \begin{bmatrix} l_{x'x} & l_{x'y} & l_{x'z} \\ l_{y'x} & l_{y'y} & l_{y'z} \\ l_{z'x} & l_{z'y} & l_{z'z} \end{bmatrix} \begin{bmatrix} \sigma_x & \tau_{xy} & \tau_{xz} \\ \tau_{yx} & \sigma_y & \tau_{yz} \\ \tau_{zx} & \tau_{zy} & \sigma_z \end{bmatrix} \begin{bmatrix} l_{x'x} & l_{y'x} & l_{z'x} \\ l_{x'y} & l_{y'y} & l_{z'y} \\ l_{x'z} & l_{y'z} & l_{z'z} \end{bmatrix} \quad (8.15)$$

By rearranging Eqn. (8.15), a new form is given as

$$\{\sigma'_o\} = [T]\{\sigma_o\} \quad (8.16)$$

$$\text{where } \{\sigma'_o\} = [\sigma_{x'} \quad \sigma_{y'} \quad \sigma_{z'} \quad \tau_{x'y'} \quad \tau_{y'z'} \quad \tau_{z'x'}]^T \quad (8.17a)$$

$$\{\sigma_o\} = [\sigma_x \quad \sigma_y \quad \sigma_z \quad \tau_{xy} \quad \tau_{yz} \quad \tau_{zx}]^T \quad (8.17b)$$

$[T]$  is called transformation matrix.

$$[T] = \begin{bmatrix} l_{x'x}^2 & l_{x'y}^2 & l_{x'z}^2 & 2l_{x'x}l_{x'y} & 2l_{x'y}l_{x'z} & 2l_{x'z}l_{x'x} \\ l_{y'x}^2 & l_{y'y}^2 & l_{y'z}^2 & 2l_{y'x}l_{y'y} & 2l_{y'y}l_{y'z} & 2l_{y'z}l_{y'x} \\ l_{z'x}^2 & l_{z'y}^2 & l_{z'z}^2 & 2l_{z'x}l_{z'y} & 2l_{z'y}l_{z'z} & 2l_{z'z}l_{z'x} \\ l_{x'x}l_{y'x} & l_{x'y}l_{y'y} & l_{x'z}l_{y'z} & (l_{x'x}l_{y'y} + l_{y'x}l_{x'y}) & (l_{x'y}l_{y'z} + l_{y'y}l_{x'z}) & (l_{x'z}l_{y'x} + l_{y'z}l_{x'x}) \\ l_{y'x}l_{z'x} & l_{y'y}l_{z'y} & l_{y'z}l_{z'z} & (l_{y'x}l_{z'y} + l_{z'x}l_{y'y}) & (l_{y'y}l_{z'z} + l_{z'y}l_{y'z}) & (l_{y'z}l_{z'x} + l_{z'z}l_{y'x}) \\ l_{x'x}l_{z'x} & l_{x'y}l_{z'y} & l_{x'z}l_{z'z} & (l_{x'x}l_{z'y} + l_{z'x}l_{x'y}) & (l_{z'x}l_{z'y} + l_{z'y}l_{x'z}) & (l_{x'z}l_{z'x} + l_{z'z}l_{x'x}) \end{bmatrix} \quad (8.17c)$$

Similarly,

$$\{\sigma_o\} = [T]^{-1}\{\sigma'_o\} \quad (8.18)$$

The direction cosines can be expressed with bearing angle ( $\beta$ ) and inclination angle ( $I$ ) as follows:

$$\begin{bmatrix} & x & y & z \\ x' & l_{x'x} & l_{x'y} & l_{x'z} \\ y' & l_{y'x} & l_{y'y} & l_{y'z} \\ z' & l_{z'x} & l_{z'y} & l_{z'z} \end{bmatrix} = \begin{bmatrix} & x & y & z \\ x' & \cos \beta & -\sin \beta & 0 \\ y' & \cos I \sin \beta & \cos I \cos \beta & \sin I \\ z' & -\sin I \sin \beta & -\sin I \cos \beta & \cos I \end{bmatrix} \quad (8.19)$$

Substituting the direction cosines into Eqn. (8.17c) gives the transformation matrix  $[T]$  and the relationship between the stress components in the  $x', y', z'$  coordinate system and those in the  $x, y, z$  coordinate system.

## 8.3 MATHEMATICAL MODELS FOR 3D STRESS BACK ANALYSIS BASED ON DIAMETRICAL CONVERGENCE

Based on discussions in previous chapters (Chapters 3 and 5), the mathematical models under different scenarios for 3D stresses back analysis from diametrical convergence for each section are listed as follows. They are all in local coordinate system.

### 8.3.1 Mathematical Models in a Stress Field with Differential Horizontal Stress Components

**Model 1:** Rock formation with no pore pressure effect

The diametrical convergence can be written as

$$u_{3Dd-1} = \left[ M_{3Dcon1-1} \quad M_{3Dcon2-1} \quad M_{3Dcon3-1} \quad M_{3Dcon4-1} \quad M_{3Dcon5-1} \quad M_{3Dcon6-1} \right] \{ \sigma_o \} + M_{3Dconm-1} P_m \quad (8.20)$$

where

$$\begin{cases} M_{3Dcon1-1} = 2r_o f_1 \\ M_{3Dcon2-1} = 2r_o f_2 \\ M_{3Dcon3-1} = 2r_o f_3 \\ M_{3Dcon4-1} = 2r_o f_4 \\ M_{3Dconm-1} = 2r_o f_5 \\ M_{3Dcon5-1} = M_{3Dcon6-1} = 0 \end{cases} \quad (8.21)$$

$f_1, f_2$  and  $f_4$  depend on the rock properties ( $E$  and  $\nu$ ) and the measurement angle ( $\theta$ ),  $f_3$  and  $f_5$  depend on the rock properties ( $E$  and  $\nu$ ).

**Model 2:** High permeability rock formation and permeable well wall

$$u_{3Dd-2} = \left[ M_{3Dcon1-2} \quad M_{3Dcon2-2} \quad M_{3Dcon3-2} \quad M_{3Dcon4-2} \quad M_{3Dcon5-2} \quad M_{3Dcon6-2} \right] \{ \sigma_o \} + M_{3Dconm-2} P_m + M_{3Dconp-2} P_p \quad (8.22)$$

where

$$\begin{cases} M_{3Dcon1-2} = M_{3Dcon1-1} = 2r_o f_1 \\ M_{3Dcon2-2} = M_{3Dcon2-1} = 2r_o f_2 \\ M_{3Dcon3-2} = M_{3Dcon3-1} = 2r_o f_3 \\ M_{3Dcon4-2} = M_{3Dcon4-1} = 2r_o f_4 \\ M_{3Dconm-2} = 2r_o f_6 \\ M_{3Dcomp-2} = 2r_o f_7 \\ M_{3Dcon5-2} = M_{3Dcon6-2} = 0 \end{cases} \quad (8.23)$$

$f_6$  and  $f_7$  are associated with  $E$ ,  $v$ ,  $\alpha$  and  $\phi$ .

**Model 3:** High permeability rock formation and impermeable well wall

$$\begin{aligned} u_{3Dd-3} = & [M_{3Dcon1-3} \quad M_{3Dcon2-3} \quad M_{3Dcon3-3} \quad M_{3Dcon4-3} \quad M_{3Dcon5-3} \quad M_{3Dcon6-3}] \{\sigma_o\} \\ & + M_{3Dconm-3} P_m + M_{3Dcomp-3} P_p \end{aligned} \quad (8.24)$$

where

$$\begin{cases} M_{3Dcon1-3} = M_{3Dcon1-1} = 2r_o f_1 \\ M_{3Dcon2-3} = M_{3Dcon2-1} = 2r_o f_2 \\ M_{3Dcon3-3} = M_{3Dcon3-1} = 2r_o f_3 \\ M_{3Dcon4-3} = M_{3Dcon4-1} = 2r_o f_4 \\ M_{3Dconm-3} = M_{3Dconm-1} = 2r_o f_5 \\ M_{3Dcomp-3} = 2r_o f_8 \\ M_{3Dcon5-3} = M_{3Dcon6-3} = 0 \end{cases} \quad (8.25)$$

$F_8$  is related to  $E$ ,  $v$ , and  $\alpha$ .

**Model 4:** Low permeability rock formation and permeable well wall

$$\begin{aligned} u_{3Dd-4} = & [M_{3Dcon1-4} \quad M_{3Dcon2-4} \quad M_{3Dcon3-4} \quad M_{3Dcon4-4} \quad M_{3Dcon5-4} \quad M_{3Dcon6-4}] \{\sigma_o\} \\ & + M_{3Dconm-4} P_m + M_{3Dcomp-4} P_p \end{aligned} \quad (8.26)$$

where

$$\begin{cases} M_{3Dcon\ 1-4} = 2r_o f_9 \\ M_{3Dcon\ 2-4} = 2r_o f_{10} \\ M_{3Dcon\ 3-4} = M_{3Dcon\ 3-1} = 2r_o f_3 \\ M_{3Dcon\ 4-4} = 2r_o f_{11} \\ M_{3Dconm-4} = M_{3Dconm-2} = 2r_o f_6 \\ M_{3Dcomp-4} = M_{3Dcomp-2} = 2r_o f_7 \\ M_{3Dcon\ 5-4} = M_{3Dcon\ 6-4} = 0 \end{cases} \quad (8.27)$$

$f_9, f_{10}$  and  $f_{11}$  are relevant to  $E, v, \alpha, s$  and the measurement angle  $\theta$ .

**Model 5:** Low permeability rock formation and impermeable well wall

$$\begin{aligned} u_{3Dd-5} = & [M_{3Dcon1-5} \quad M_{3Dcon2-5} \quad M_{3Dcon3-5} \quad M_{3Dcon4-5} \quad M_{3Dcon5-5} \quad M_{3Dcon6-5}] \{\sigma_o\} \\ & + M_{3Dconm-5} p_m + M_{3Dcomp-5} p_p \end{aligned} \quad (8.28)$$

where

$$\begin{cases} M_{3Dcon\ 1-5} = M_{3Dcon\ 1-4} = 2r_o f_9 \\ M_{3Dcon\ 2-5} = M_{3Dcon\ 1-4} = 2r_o f_{10} \\ M_{3Dcon\ 3-5} = M_{3Dcon\ 3-1} = 2r_o f_3 \\ M_{3Dcon\ 4-5} = M_{3Dcon\ 1-4} = 2r_o f_{11} \\ M_{3Dconm-5} = M_{3Dconm-1} = 2r_o f_5 \\ M_{3Dcomp-5} = M_{3Dcomp-3} = 2r_o f_8 \\ M_{3Dcon\ 5-5} = M_{3Dcon\ 6-5} = 0 \end{cases} \quad (8.29)$$

Because measurements are made in a local coordinate system, the above equations will have the same format for different section except  $\{\sigma_o\}$  being replaced by  $\{\sigma'_o\}$  or  $\{\sigma''_o\}$  and stress transformation is required to correlate to the global stresses.

### 8.3.2 Mathematical Models in a Stress Field with Equal Horizontal Stress Components

In this stress field, the normal stress acting in the horizontal plane normal to the vertical well is equal in all directions and there are no shear stresses. The vertical stress, different from the horizontal stress, is proportional to the depth.

**Model 6:** Rock formation with no pore pressure effect

$$u_{3Dd-6} = M_{3Dcon1-6} \sigma_h + M_{3Dcon3-6} \sigma_z + M_{3Dconm-6} p_m \quad (8.30)$$

$$\text{where } M_{3Dcon1-6} = 2r_o f_{12} \quad (8.31a)$$

$$M_{3Dcon3-6} = 2r_o f_3 \quad (8.31b)$$

$$M_{3Dconm-6} = 2r_o f_5 \quad (8.31c)$$

$f_{12}$  is relevant to  $E$ .

**Model 7:** Porous rock formation and permeable well wall

$$u_{3Dd-7} = M_{3Dcon1-7} \sigma_h + M_{3Dcon3-7} \sigma_z + M_{3Dconm-7} p_m + M_{3Dcomp-7} p_p \quad (8.32)$$

where the coefficients  $M_{3Dcon1-7}$  and  $M_{3Dcon3-7}$  are the same as model 6, given in Eqn. (8.31a) and (8.31b), respectively and

$$\begin{cases} M_{3Dconm-7} = 2r_o f_6 \\ M_{3Dcomp-7} = 2r_o f_7 \end{cases} \quad (8.33)$$

**Model 8:** Porous rock formation and impermeable well wall

$$u_{3Dd-8} = M_{3Dcon1-8} \sigma_h + M_{3Dcon3-8} \sigma_z + M_{3Dconm-8} p_m + M_{3Dcomp-8} p_p \quad (8.34)$$

where the coefficients  $M_{3Dcon1-8}$ ,  $M_{3Dcon3-8}$  and  $M_{3Dconm-8}$  are the same as model 6, given in Eqn. (8.31a), (8.31b) and (8.31c), respectively and

$$M_{3Dcomp-8} = 2r_o f_8 \quad (8.35)$$

The assumption of equal horizontal stress is highly restricted to very deep well where hydrostatic stress is expected. The above Equations (8.30, 8.32 and 8.34) may provide an alternative method for estimating the in-situ stresses where applicable. However, in industrial practice this method may not have universal application. For more general purposes, the following discussions will be focused on differential horizontal stress situations where a 3D stress tensor has six independent stress components with three principle stresses.

#### 8.4 COMBINING INFORMATION FROM DIFFERENT WELLS

As discussed in Section 8.1.2, diametrical convergence measurements from at least two non-perpendicular wells / boreholes need to be used to obtain the complete solution for all six components of 3D stresses. However, in practice, in petroleum engineering, drilling two or more wells are too expensive and not practical. The concept of “multi-well” measurement can be realized in a single directionally-drilled well as shown in Figure 8.4. In this figure, I stands for the vertical section, II, III and IV stand for the three different inclined sections.

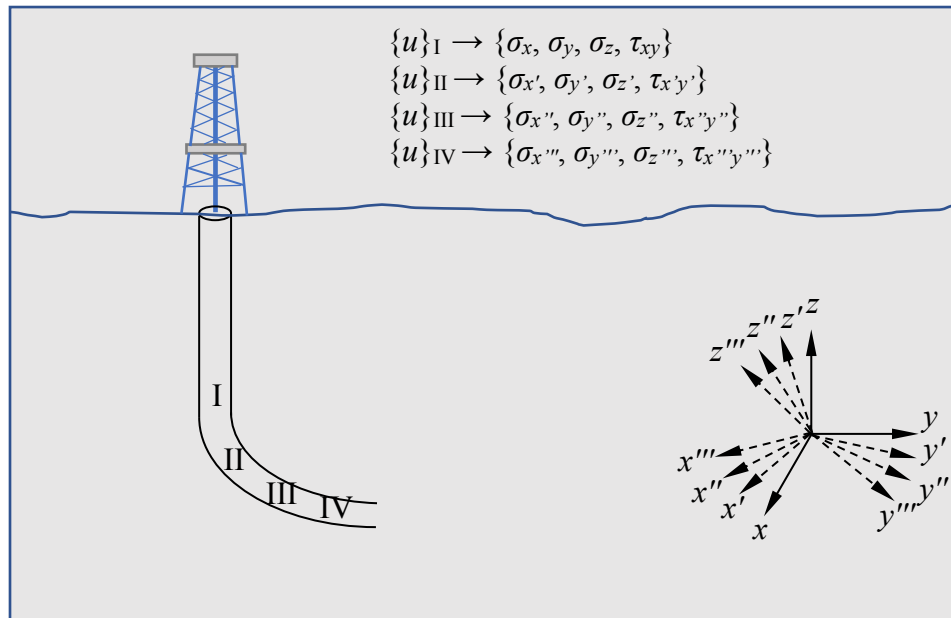


**Figure 8.4** Illustration for 3D stress measurement in a directional well



### 8.4.1 Combining Information from Two Well Sections or Boreholes

Two sets of measurements are made with one set in the vertical section I and another one set in an inclined section II, made in the two different inclined sections (e.g., II and III).

For each section:

$$\{u_{3Dd}\}_I = [M_{3Dcon}]_I [T] \{\sigma_o\} + [M_{3Dconm}] p_m + [M_{3Dconp}] p_p \quad (8.36a)$$

$$\{u'_{3Dd}\}_{II} = [M'_{3Dcon}]_{II} [T'] \{\sigma_o\} + [M_{3Dconm}] p_m + [M_{3Dconp}] p_p \quad (8.36b)$$

$$\{u''_{3Dd}\}_{III} = [M''_{3Dcon}]_{III} [T''] \{\sigma_o\} + [M_{3Dconm}] p_m + [M_{3Dconp}] p_p \quad (8.36c)$$

The mathematical model describing the relationship between the two sets of diametrical convergence measurements and the 3D stress tensor can be expressed as

$$\begin{Bmatrix} u_{3Dd} \\ u'_{3Dd} \end{Bmatrix}_{I+II} = \begin{bmatrix} M_{3Dcon\_T} \\ M'_{3Dcon\_T} \end{bmatrix}_{I+II} \{\sigma_o\} + C \quad (8.37)$$

$$\text{or } \begin{Bmatrix} u'_{3Dd} \\ u''_{3Dd} \end{Bmatrix}_{II+III} = \begin{bmatrix} M'_{3Dcon\_T} \\ M''_{3Dcon\_T} \end{bmatrix}_{II+III} \{\sigma_o\} + C \quad (8.38)$$

The above models correlate the two sets of measured data with consideration of their coordinates and direction differences.

### 8.4.2 Combining Information from Three Well Sections or Boreholes

The above proposed concept of using measurements in two sections to determine the complete 3D stresses seems to be valid in principle. However, as shown in the next chapter, there seems to be some unknown reasons in actual application for the back-analyzed solutions to  $\{\sigma_o\}$  being non-unique with large errors. Therefore, measurements in three different sections of a well are considered here. In petroleum industry, considering the practical application, three well sections will be selected in one directionally-drilled well.

Similarly to the procedure for combining information from two well sections or boreholes, if three sets of measurements are made with one set in the vertical section I and another two sets in different inclined sections II and III, or three sets in different inclined sections II, III and IV, the mathematical model can be established by combining the three sets of measured data.

- 1) One set in the vertical section I and another two sets in different inclined sections II and III

$$\begin{Bmatrix} u_{3Dd} \\ u'_{3Dd} \\ u''_{3Dd} \end{Bmatrix}_{I+II+III} = \begin{bmatrix} M_{3Dcon\_T} \\ M'_{3Dcon\_T} \\ M''_{3Dcon\_T} \end{bmatrix}_{I+II+III} \{\sigma_o\} + C \quad (8.39)$$

- 2) Three sets in different inclined sections II, III and IV

$$\begin{Bmatrix} u'_{3Dd} \\ u''_{3Dd} \\ u'''_{3Dd} \end{Bmatrix}_{II+III+IV} = \begin{bmatrix} M'_{3Dcon\_T} \\ M''_{3Dcon\_T} \\ M'''_{3Dcon\_T} \end{bmatrix}_{II+III+IV} \{\sigma_o\} + C \quad (8.40)$$

## 8.5 SOLUTIONS TO THE IN-SITU STRESSES FROM COMBINED MEASUREMENTS

In terms of the above different combinations, the equations can be expressed in simplified matrix forms.

- Two sets of measurements made from a vertical section and an inclined section

$$\{u_{3Dcon}\}_{I+II} = [M_{3Dcon}]_{I+II} \{\sigma_o\} + C \quad (8.41)$$

- Two sets of measurements made from two different inclined sections

$$\{u_{3Dcon}\}_{II+III} = [M_{3Dcon}]_{II+III} \{\sigma_o\} + C \quad (8.42)$$

- Three sets of measurements made from a vertical section and two different inclined sections

$$\{u_{3Dcon}\}_{I+II+III} = [M_{3Dcon}]_{I+II+III} \{\sigma_o\} + C \quad (8.43)$$

- Three sets of measurements made from three different inclined sections

$$\{u_{3Dcon}\}_{II+III+IV} = [M_{3Dcon}]_{II+III+IV} \{\sigma_o\} + C \quad (8.44)$$

All formulae above for the combination analysis can be written in a unified general matrix form:

$$\{u_{3Dcon}\}_{com} = [M_{3Dcon}]_{com} \{\sigma_o\} + C \quad (8.45)$$

The coefficient matrix  $[M_{3Dcon}]$  and  $C$  in the model vary with the conditions of well wall and rock formation. Eqn. (8.45) is a set of linear equations with six unknown parameters. If the number of measurements is more than six, it becomes a set of redundant equations. If the least square method is adopted in Eqn. (8.45), the unknown parameters can be solved, such that the in-situ stresses appear as outputs and the measured convergence as inputs as follows:

$$\{\sigma_o\} = \left( [M_{3Dcon}]_{com}^T [M_{3Dcon}]_{com} \right)^{-1} [M_{3Dcon}]_{com}^T \cdot (\{u_{3Dd}\}_{com} - C) \quad (8.46)$$

This chapter explored several back analysis methods to estimate the 3D in-situ stresses from combined diametrical convergence. Next chapter will focus on testing the developed potential methods and assessing the influencing factors.

# CHAPTER 9 TEST OF 3D BACK ANALYSIS AND ASSESSMENT OF INFLUENCING FACTORS

## 9.1 MODEL TEST CONDITIONS

Like in 2D back analysis, examples are introduced to test the 3D back-analysis methods, the mathematical models and the calculation program. In this test, analysis is performed for each of the scenarios described in Chapter 8.

The following factors as indicated in Figure 9.1 are also investigated and discussed:

- Combination number of well sections / boreholes to search for a valid solution;
- Minimum difference of orientation between well sections (or the angle between the measurement planes) for a valid solution;
- Number of measurements in each well section / borehole to check the effect on solution.

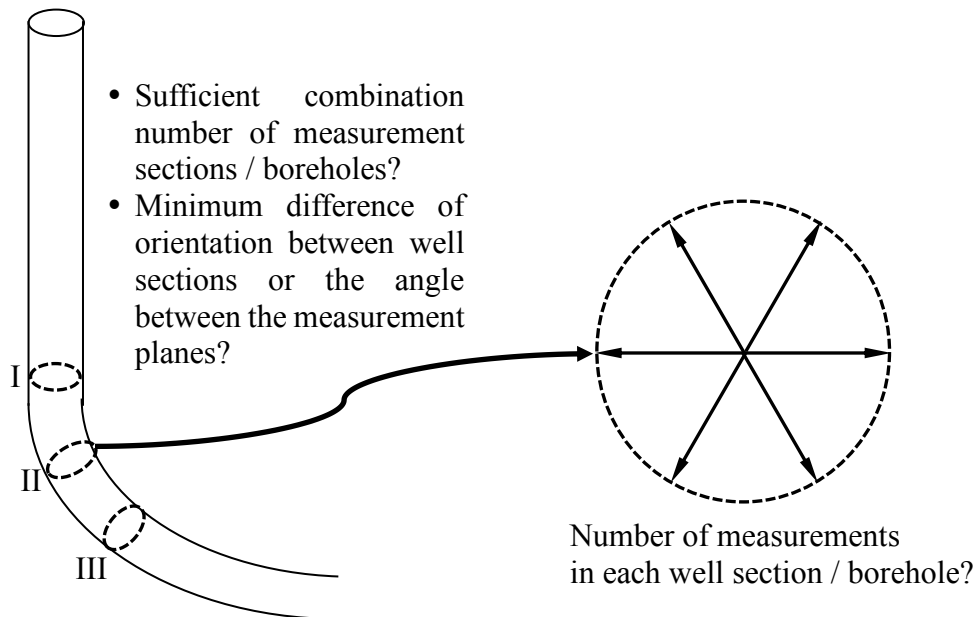


**Figure 9.1** Factors that may influence 3D back analysis of diametrical convergence

## 9.2 CALCULATION OF IN-SITU STRESSES FROM 3D BACK-ANALYSIS

All calculations are performed in excel sheets. Five analysis packages have been developed for 3D calculation. They correspond to the following five scenarios respectively:

- Package 1: rock formation with no pore pressure effect;
- Package 2: high permeability rock formation and permeable well wall;
- Package 3: high permeability rock formation and impermeable well wall;
- Package 4: low permeability rock formation and permeable well wall;
- Package 5: low permeability rock formation and impermeable well wall.

The interface is displayed in Figures 9.2 and 9.3 showing typical relevant input information and output data.

<b>3D stress determination from well deformation</b>				Model 3: high permeability rock formation and impermeable well wall						
x, y are horizontal; z is vertically up (x//E, y//N and z//V)										
by Cui Lin, September 2018										
<b>Input data</b>				1	2	3	4	5	6	
Young's modulus	E [MPa]	20000	Well 1	$\theta$ [°]	0	30	60	90	120	150
Poisson's ratio	$\nu$	0.20	Well 2	$\theta'$ [°]	0	30	60	90	120	150
Skempton's coefficient	s	0.92	Well 3	$\theta''$ [°]	0	30	60	90	120	150
Biot's coefficient	$\alpha$	0.80	Well 1	I [°]	0					
Porosity	$\phi$	0.3	Well 1	$\beta$ [°]	0					
Mud pressure	$p_m$ [MPa]	25	Well 2	I' [°]	25					
Pore pressure	$p_p$ [MPa]	20	Well 2	$\beta'$ [°]	45					
Well 1 radius	$r_o$ [m]	0.1	Well 3	I'' [°]	50					
Well 2 radius	$r_o'$ [m]	0.1	Well 3	$\beta''$ [°]	45					
Well 3 radius	$r_o''$ [m]	0.1								
Measurement ID (1- $u_r$ , 2- $u_d$ )		2								

**Figure 9.2** Interface information for the 3D in-situ stress automated analysis

The analysis procedure for 3D in-situ stresses is similar to that in the 2D in-situ stress automated analysis explained in Section 7.2 of Chapter 7. The major difference is that the information from two or more well sections or boreholes are combined in calculations.

## 1) Input Data

The common input data include the following parameters (Figure 9.2):

- Rock properties,  $E$  and  $\nu$
- Porosity  $\phi$ , Biot's coefficient  $\alpha$  and Skempton's coefficient  $s$
- Mud pressure  $p_m$  and pore pressure  $p_p$ .

For each section or borehole, there is a separate set of data to enter:

- Well section or borehole defined by inclination angle  $I$  and bearing angle  $\beta$
- Borehole geometry (radius)  $r_o$
- Measurement location defined by its angle,  $\theta$  and the measured radial displacement  $u_r$  or diametrical convergence  $u_d$

## 2) Analysis and output

As described in the previous chapter, all calculations and matrix manipulations are done automatically with final results showing:

- the estimated stresses  $\{\sigma_o\} = \{\sigma_x, \sigma_y, \sigma_z, \tau_{xy}, \tau_{yz}, \tau_{zx}\}$  and
- the principal stresses  $\{\sigma_1, \sigma_2, \sigma_3\}$  with their orientations.

The conversion from  $\{\sigma_x, \sigma_y, \sigma_z, \tau_{xy}, \tau_{yz}, \tau_{zx}\}$  to the magnitudes and orientations of the principal stresses is given in Appendices G and H. Figure 9.3 shows typical output.

	Output	Applied [MPa]	Back-analyzed [MPa]	
	$\sigma_x$	45.04	45.57	
	$\sigma_y$	48.38	48.68	
	$\sigma_z$	60.9	59.08	
	$\tau_{xy}$	-3.38	-3.68	
	$\tau_{yz}$	-15.9	-15.81	
	$\tau_{xz}$	-6.7	-7.53	
	$\sigma_1$	$\sigma_2$	$\sigma_3$	
mag [MPa]	72.24	48.43	33.65	Applied
plunge [°]	56.4	10.3	31.6	
trend [°]	14.5	120.4	216.8	
mag [MPa]	71.17	49.36	32.81	calculated
plunge [°]	55.0	10.1	33.1	
trend [°]	16.4	121.1	217.8	
mag [%]	-1.5%	1.9%	-2.5%	differences
plunge [°]	-1.4	-0.2	1.5	
trend [°]	1.9	0.7	1.0	

**Figure 9.3** Typical output (with up to 15% errors in input data)

### 9.3 INPUT PARAMETERS OF TEST EXAMPLES

The assumed in-situ principal stresses in a three-dimensional stress field are given in Table 9.1 as demonstration. In the chosen coordinate system where  $z$  is vertical up,  $x$  horizontal parallel to East and  $y$  to North, the in-situ stress components are then to be  $\sigma_x = 45.04$  MPa,  $\sigma_y = 48.43$  MPa,  $\sigma_z = 60.9$  MPa,  $\tau_{xy} = -3.38$  MPa,  $\tau_{yz} = -15.9$  MPa, and  $\tau_{zx} = -6.7$  MPa.

**Table 9.1** Assumed 3D in-situ principal stresses

In-situ principal stresses	$\sigma_1$	$\sigma_2$	$\sigma_3$
Magnitude [MPa]	72.24	48.43	33.65
Plunge [°]	56.4	10.3	31.6
Trend [°]	14.5	120.4	216.8

The rock formation properties, pore pressure and mud pressure used in this test are the same as those in the test of 2D stress back analysis, listed in Table 7.2. The depth of the measurement planes is in the range of 2000 m to 3000 m.

### 9.4 ANALYSIS AND RESULTS

#### 9.4.1 Results from Two Well Sections / Boreholes

As discussed in Chapter 8, all convergence is measured within a well / borehole, effectively within the plane perpendicular to the well / borehole. We also noticed that measurements in two perpendicular boreholes are not sufficient and that measurements in two non-perpendicular boreholes may be able to provide a solution. The first step here is to test the combination of well sections (non-perpendicular to each other). A vertical section and an inclined section are considered:

- 1<sup>st</sup> combination:  $I = 0$ ,  $\beta = 0$  and  $I = 25^\circ$ ,  $\beta = 45^\circ$ ;
- 2<sup>nd</sup> combination:  $I = 0$ ,  $\beta = 0$  and  $I = 50^\circ$ ,  $\beta = 45^\circ$ ;
- 3<sup>rd</sup> combination:  $I = 0$ ,  $\beta = 0$  and  $I = 75^\circ$ ,  $\beta = 45^\circ$ .

For each section, there is a total of 9 measurements. The measurement angles are 0, 20°, 40°, 60°, 80°, 100°, 120°, 140° and 160°.

Data of exact diametrical convergence caused by drilling at the specific measurement locations for the two well sections are generated using Eqn. (8.37) with the specified 3D in-situ stresses in Table 9.1. These exact convergence were used as input data in the test. The applied and back-analyzed in-situ principal stress results for the 1<sup>st</sup> combination are displayed in Table 9.2. The results from the 2<sup>nd</sup> and the 3<sup>rd</sup> combinations are given in Table I.1 and I.2 in Appendix I, respectively for reference.

As can be seen from these tables, the results for scenarios 1, 2 and 3 are the same, and the results for scenarios 4 and 5 are the same. In the 1st combination and 3rd combination, there are no solutions for scenarios 4 and 5, and for others, even the solutions exist, the results of the magnitudes and orientations of back-analyzed in-situ principal stresses are very different from the applied stresses. Apparently the results are not acceptable at all.

The in-situ stresses in 3D have six components, therefore Eqn. (8.41) needs to provide at least six linearly independent equations to obtain the complete and unique solution for all six components. Otherwise, no solution. In order to check the independence of columns of matrix  $[M_{3Dcon}]_{com}$ ,  $([M_{3Dcon}]_{com}^T[M_{3Dcon}]_{com})^{-1}$  is multiplied by  $([M_{3Dcon}]_{com}^T[M_{3Dcon}]_{com})$  as an alternative way. If  $[M_{3Dcon}]_{com}$  has six independent columns, when a matrix is multiplied by its inverse, the result should be a unit matrix with 1.0 on diagonal elements and zero for the rest. The results of the matrices multiplication for all scenarios in the 1<sup>st</sup>, 2<sup>nd</sup> and 3<sup>rd</sup> combination are shown in Table I.3, I.4 and I.5 in Appendix I, respectively.

As can be seen in the results of the three tables, the resultant matrix is however not a unit matrix, which means that some columns of matrix  $[M_{3Dcon}]_{com}$  may not be linearly independent. This test indicates that convergence measurements in a pair of non-perpendicular well sections did not provide six independent conditions for solutions of the 3D in-situ stresses. It further implies that convergence measurements in two well sections



/ two planes (parallel, perpendicular or non-perpendicular) cannot provide the required number of independent equations for a complete and unique solution to the 3D in-situ stresses.

**Table 9.2** Results of back-analyzed 3D in-situ principal stresses from two well sections or boreholes (the 1<sup>st</sup> combination)

In-situ principal stresses		$\sigma_1$	$\sigma_2$	$\sigma_3$
Scenario 1: NP; scenario 2: HPR and PW; scenario 3: HPR and IPW				
Back-analyzed	Magnitude [MPa]	138.88	-303.10	-317.78
	Plunge [°]	6.6	24.8	27.2
	Trend [°]	270.1	271.9	272.1
Differences with the applied stresses	Magnitude [%]	92.3	-725.8	-1044.4
	Plunge [°]	-49.8	14.5	-4.4
	Trend [°]	255.6	151.5	55.3
Scenario 4: LPR and PW; scenario 5: LPR and IPW				
Back-analyzed	Magnitude [MPa]	No solution		
	Plunge [°]			
	Trend [°]			
Differences with the applied stresses	Magnitude [MPa]			
	Plunge [°]			
	Trend [°]			

## 9.4.2 Results from Three Well Sections or Boreholes

Since combining convergence measurements from the two sections / boreholes does not provide a converging solution to the 3D in-situ stresses, combination from three sections / boreholes are considered in the next step. These three sections as indicated in the previous chapter should be non-parallel to each other (i.e., all measurements should not be within parallel planes).

### 9.4.2.1 Input Data with Exact Diametrical Convergence

In this test, a vertical well section / borehole ( $I = 0, \beta = 0$ ) and two inclined sections / boreholes ( $I = 25^\circ, \beta = 45^\circ; I = 50^\circ, \beta = 45^\circ$ ) are combined. The measurements are made in six directions in each section, 0, 30°, 60°, 90°, 120°, and 150°. Eqn. (8.39) was used to generate the exact diametrical convergences induced by drilling at the measurement locations with the specified 3D in-situ stresses. These exact data were used as input without any error. The back-analyzed results of the in-situ stresses are displayed in Table 9.3.

**Table 9.3** Results of back-analyzed 3D in-situ principal stresses from three well sections / boreholes

In-situ principal stresses	$\sigma_1$	$\sigma_2$	$\sigma_3$
Combination of three well sections / boreholes: $I = 0, \beta = 0$ ; $I = 25^\circ, \beta = 45^\circ$ and $I = 50^\circ, \beta = 45^\circ$ . Same results for all five scenarios (models) analysed.			
Magnitude [MPa]	72.24	48.43	33.65
Plunge [ $^\circ$ ]	56.4	10.3	31.6
Trend [ $^\circ$ ]	14.5	120.4	216.8

As can be seen, the solutions to the 3D in-situ principal stresses in all scenarios are exactly the same as the actual ones (Table 9.1) when the measured diametrical convergence is exact. There are no differences between these two sets of stresses (applied and back-analyzed in-situ principal stresses). This suggests that the developed method and the analysis procedure are valid and all calculations are correct. Furthermore the idea of combining three well sections / boreholes (non-parallel) is a valid approach to determine the 3D in-situ stresses.

#### 9.4.2.2 Effects of Errors in Input of Diametrical Convergence

In order to further test the viability of this method, random errors of up to 10%, 15%, 20%, 25%, 30%, 40%, 50% are introduced respectively to the exact diametrical convergence data to simulate real measurements. The random errors were generated in the same way as 2D test. They are given in Table I.6 in Appendix I. The orientation of three sections or boreholes is  $(I = 0, \beta = 0)$ ,  $(I = 25^\circ, \beta = 45^\circ)$  and  $(I = 50^\circ, \beta = 45^\circ)$ , respectively. There are 6 measurements in each section.

The magnitudes of the back-analyzed and applied principal stresses are shown in Figure 9.4. Graphs of the output errors of the principal stress magnitudes versus the maximum random input errors are presented in Figure 9.5. The orientations of back-analyzed and applied principal stresses are plotted on stereonet, as demonstrated in Figure 9.6.

When the maximum random input errors are greater than 40%, the magnitudes of back-analyzed in-situ principal stresses show a relatively larger difference with the applied in-

situ principal stresses. All output errors are however less than the introduced maximum random input errors.

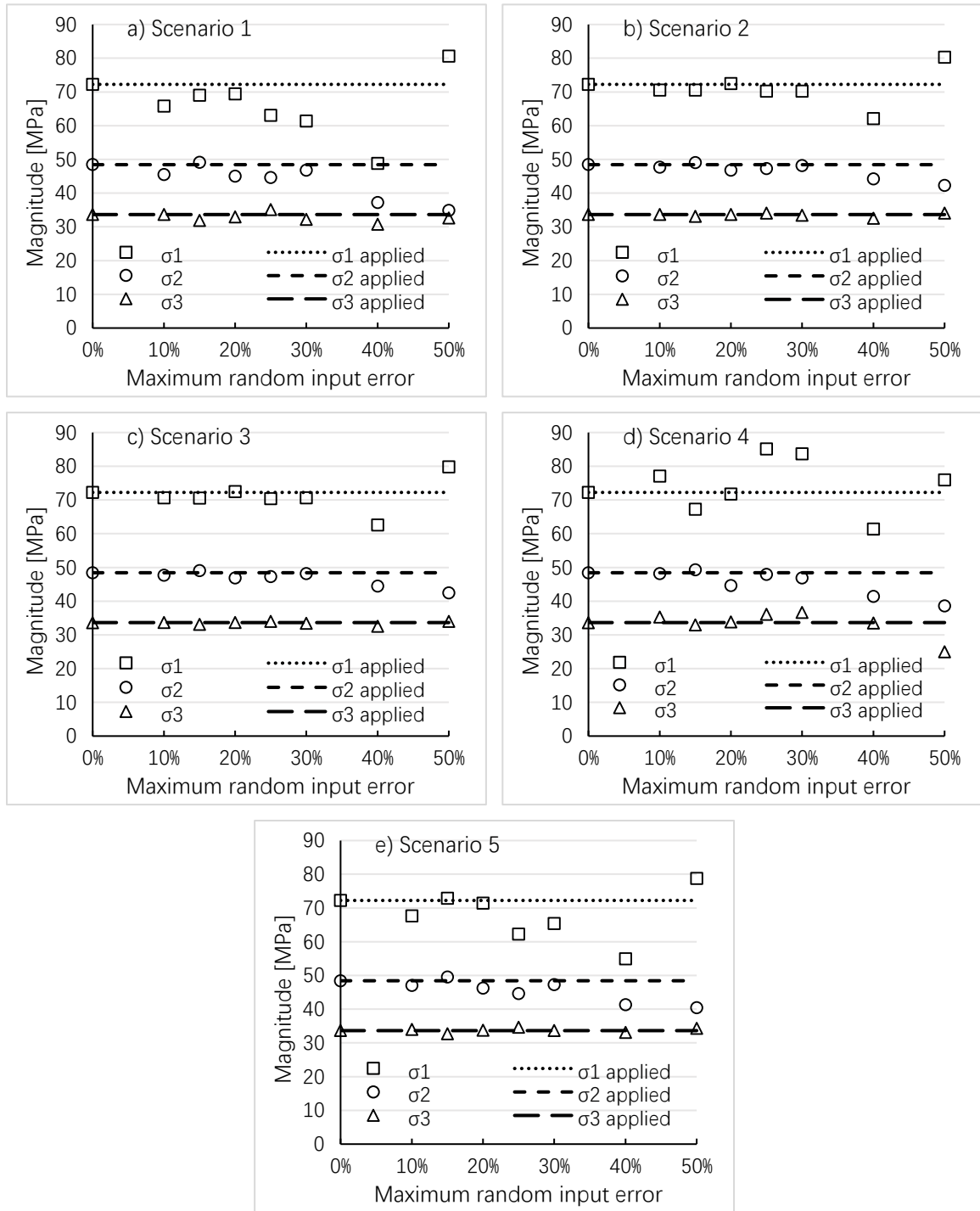


**Figure 9.4** Magnitudes of the back-analyzed and applied principal stresses with various random errors in input data for all 5 scenarios (Inclination angle interval 50°. 6 measurements per section).

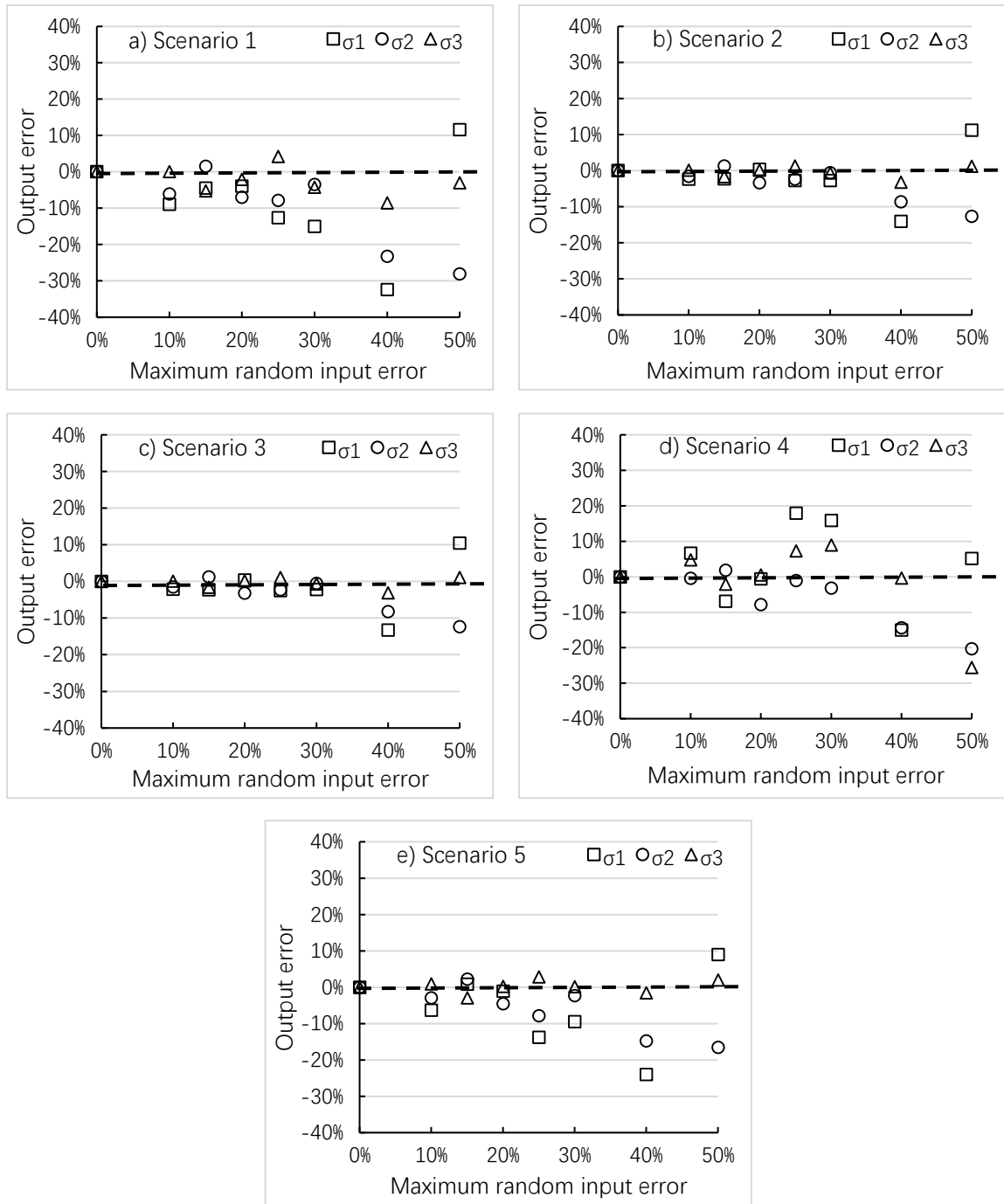


**Figure 9.5** Output errors of the back-analyzed principal stress magnitudes in comparison with the actual principal stresses versus the introduced maximum random input errors for all 5 scenarios (Inclination angle interval  $50^\circ$ . 6 measurements per section).

In terms of the orientations of principal stresses, they have a larger deviation from those of the applied stresses when the introduced maximum random errors are greater than 30%.

The points in Figure 9.6 representing the orientations of the back-analyzed principal

stresses distribute closely around those for the orientations of the applied stresses with the introduced maximum random errors that are  $\leq 30\%$ .

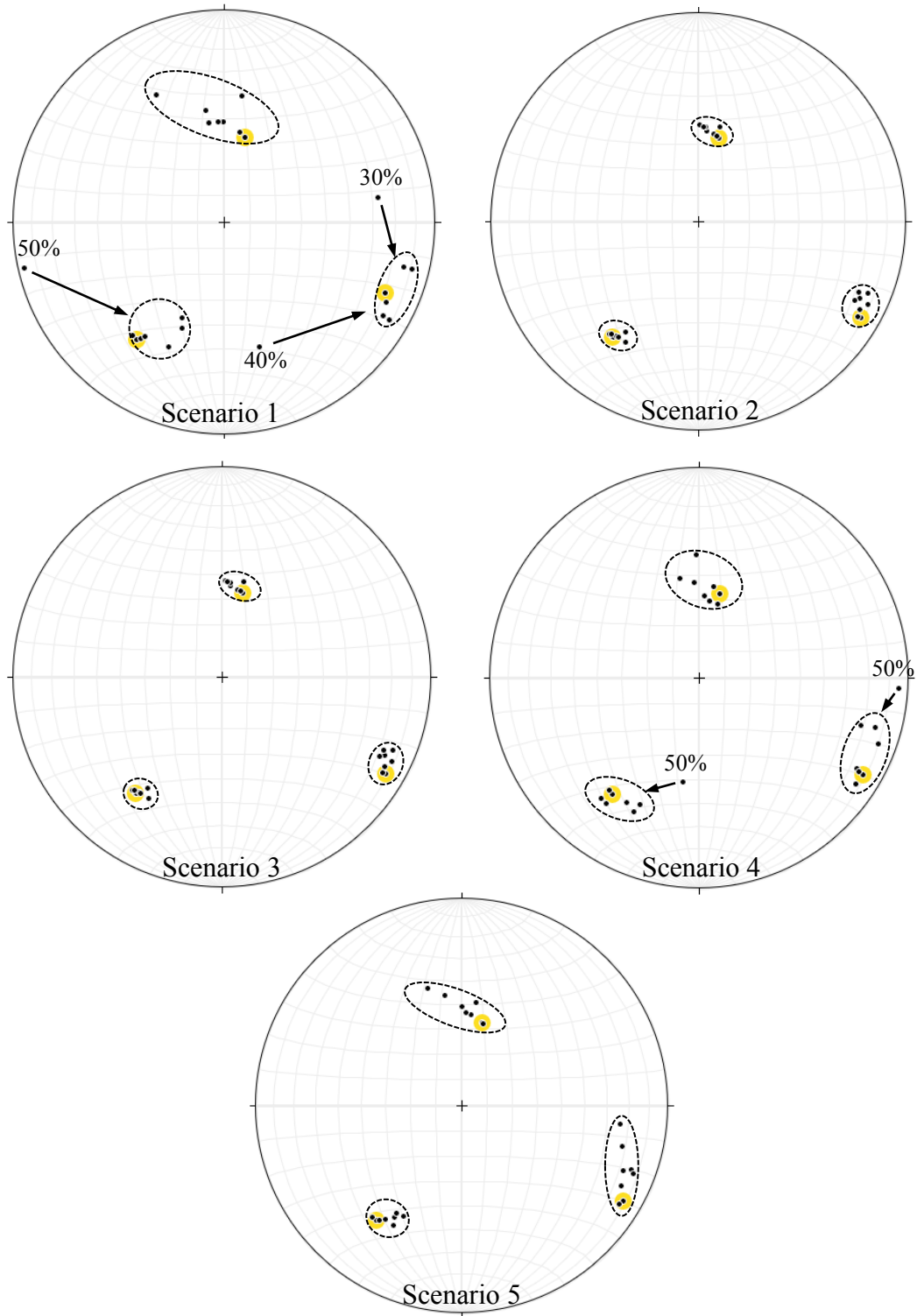


**Figure 9.6** Orientations of the back-analyzed and applied principal stresses with various random errors in input data for all 5 scenarios (Inclination angle interval  $50^\circ$ . 6 measurements per section).

Results of these tests clearly demonstrated that diametrical convergence measured in three well sections (within three non-parallel planes) are adequate to provide a unique solution to the 3D in-situ stresses and the accuracy of the results is acceptable provided the input errors are under 30%.

#### **9.4.3 Effect of Inclination Angle Interval between Measurement Sections / Planes**

When diametrical convergence is measured in three non-parallel well sections (or measurement planes), it was proven earlier that a unique solution can be found for the in-situ 3D stresses. This is possible in practice in a directionally drilled well in petroleum industry. For mining application, three non-parallel boreholes can be drilled in any directions in an area. The question is how much apart the three measurement sections should be (or how far the measurement planes should deviate from each other). In the following, the effect of the inclination angle of each measurement section (the deviation of the measurement planes) will be assessed.

For simplicity, the inclination angle interval between two adjacent measurement sections (or planes) is assumed to be the same. The inclination angle interval between the first and the third sections is considered as a variable. The maximum deviation from a vertical measurement plane to a horizontal measurement plane is  $90^\circ$ , which is the maximum deviation to be considered. The first section is vertical ( $I = 0, \beta = 0$ ). The bearing angle  $\beta$  of the second and the third sections are  $45^\circ$ . The selected inclination angle intervals between the first and the third measurement sections (planes) in this test is  $20^\circ, 35^\circ, 50^\circ, 75^\circ$  and  $90^\circ$ , respectively. Furthermore, each section is assumed to have 6 measurements and random errors of up to 20% are introduced in the input data of diametrical convergence.

Figure 9.7 shows the magnitudes of the back-analyzed principal stresses as a function of inclination angle interval between the measurement sections (planes). Figure 9.8 shows output errors (in comparison with the actual principal stresses) of the back-analyzed principal stress magnitudes at different inclination angle intervals.

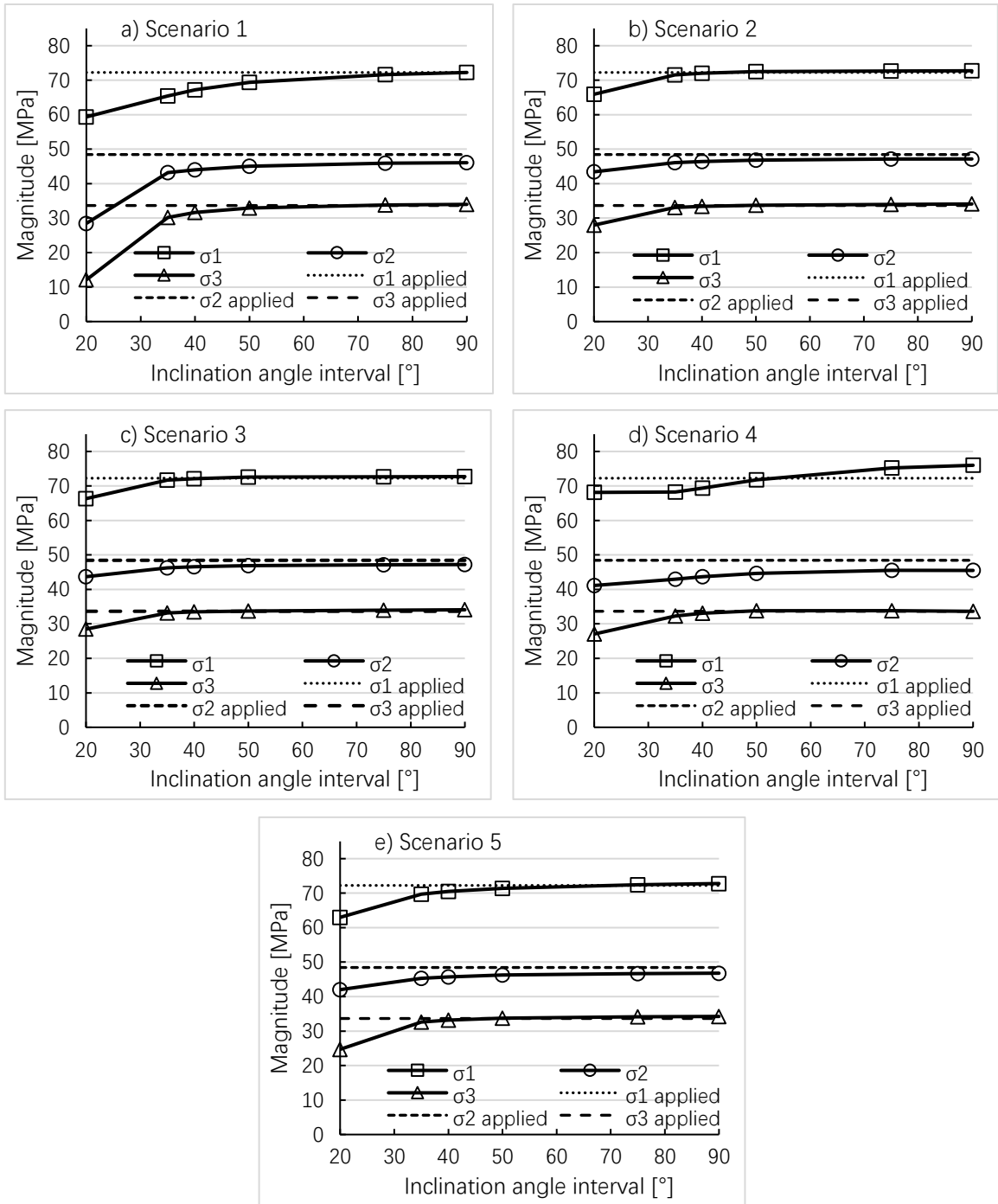


**Figure 9.7** Magnitudes of the back-analyzed and applied principal stresses with different inclination angle interval for all 5 scenarios (6 measurements in each section. Max. error in input data 20%).

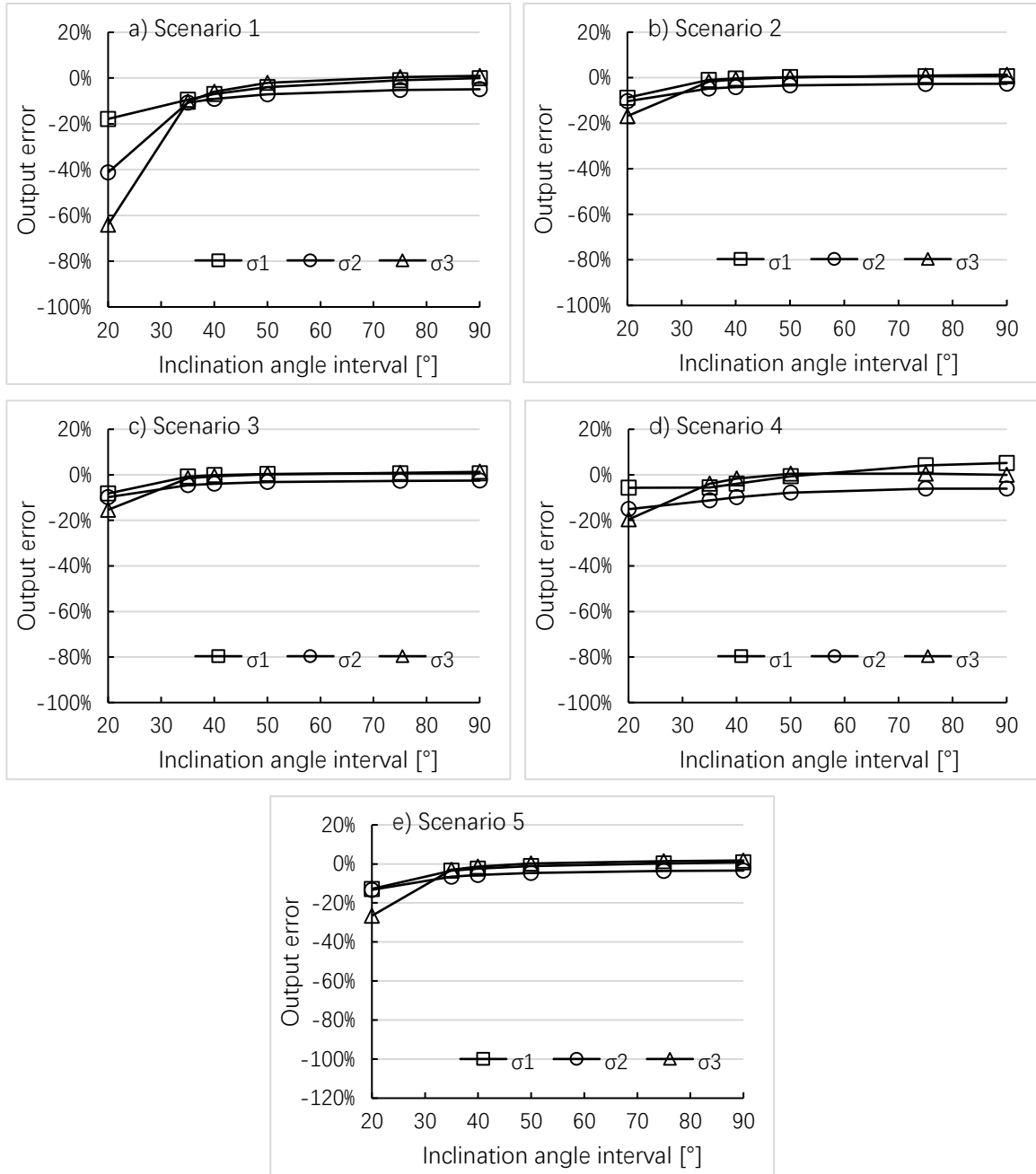


**Figure 9.8** Output errors of the back-analyzed principal stress magnitudes in comparison with the actual principal stresses versus inclination angle interval for all 5 scenarios (6 measurements in each section. Max. error in input data 20%).

Similarly, the orientations of the back-analyzed and applied principal stresses are exhibited on stereonet in Figure 9.9.



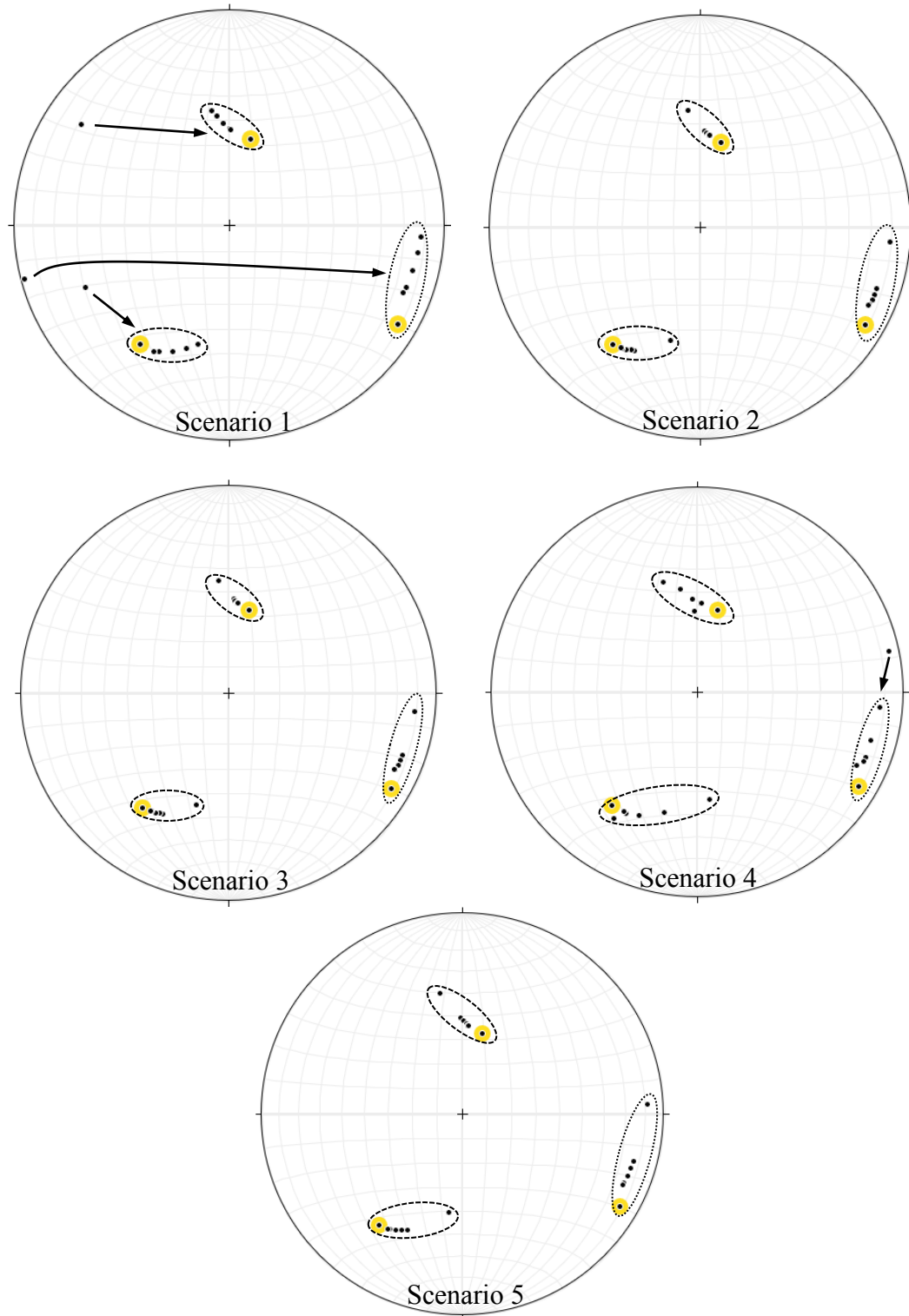


**Figure 9.9** Orientations of the back-analyzed principals stresses with different inclination angle intervals for all 5 scenarios. (“Runaway” point at  $20^\circ$  interval or less. 6 measurements in each section. Max. error in input data 20%).

As can be seen from Figures 9.7 to 9.9, the inclination angle interval between the measurement planes exerts some influence on the results of the back-analyzed in-situ principal stresses for all scenarios. In general, at 90° of inclination interval, there is a true 3D representation and the results are closest to the actual stresses. The small differences in magnitudes and orientations of the back-analyzed in-situ principal stresses from the applied in-situ principal stresses are considered to be the result of the random input data errors of up to 20%.

As the inclination angle interval decreases, variation in both magnitude and orientation from the actual stresses tends to increase. However the appearance of the decreasing trend in scenario 4 (total inclination angle interval 50°-90°) is believed to be caused by the specific random errors in the input data. When the inclination angle interval is 20°, the differences in both magnitudes and orientations between the back-analyzed and the applied in-situ principal stresses become very large and the results are unacceptable. Analysis revealed that in this condition, the three measurement planes are so close to each other, near parallel, and do not have a good 3D representation.

The implication of the analysis of inclination angle interval is that in order to achieve reasonably good results,

- the inclination angle interval between the first and the third well sections should be  $\geq 35^\circ$ ,
- the second section should be approximately in the middle between the other two sections,
- the same principle applies to mining applications when three boreholes may be drilled in any direction.

#### **9.4.4 Effects of Number of Measurement in a Section / Plane**

To solve for the 6 in-situ stress components, a minimum of 6 independent measurements must be made. That is minimum 2 measurements in each section / borehole. Considering practical issues and field instruments, three, six, nine and twelve measurements in each

section / borehole are selected for analysis and comparison. The same measurement number is assumed in all three sections in a directionally-drilled well or in three boreholes. The measurement angle  $\theta$  corresponding to a measurement number is listed in Table 9.4.

**Table 9.4** Measurement angles  $\theta$  [°] with different number of measurement

Measurement No.	1	2	3	4	5	6	7	8	9	10	11	12
3	0	60	120									
6	0	30	60	90	120	150						
9	0	20	40	60	80	100	120	140	160			
12	0	15	30	45	60	75	90	105	120	135	150	165

In this test, the random errors of up to 20% are introduced in the input measurement data. The orientations of the three measurement sections are  $I = 0, \beta = 0$ ;  $I = 25^\circ, \beta = 45^\circ$  and  $I = 50^\circ, \beta = 45^\circ$ , respectively. The magnitudes of the back-analyzed principal stresses and the output errors for all scenarios are depicted in Figure 9.10 and 9.11, respectively. The orientations of the back-analyzed and applied principal stresses are illustrated in Figure 9.12.

It is found that the measurement number seems to have some impact on the results. However, compared with the input data error and the inclination angle interval between measurement planes, the effect of measurement number is much smaller. The magnitude differences between the back-analyzed and applied in-situ principal stresses are less than the introduced maximum random errors of 20% in all scenarios and for all measurement numbers. In general, larger number of measurements corresponds to more accurate results. With three measurements, a mathematical solution exists. However the measurements may not be truly representative to the real stress field. In practical application, more measurement directions on the well wall in the plane perpendicular to the well axis have more coverage around the wellbore wall and will provide a better sampling of the well deformation. Therefore, equally-spaced measurement directions with more measurement number is suggested for better results in solving for the 3D in-situ stresses.

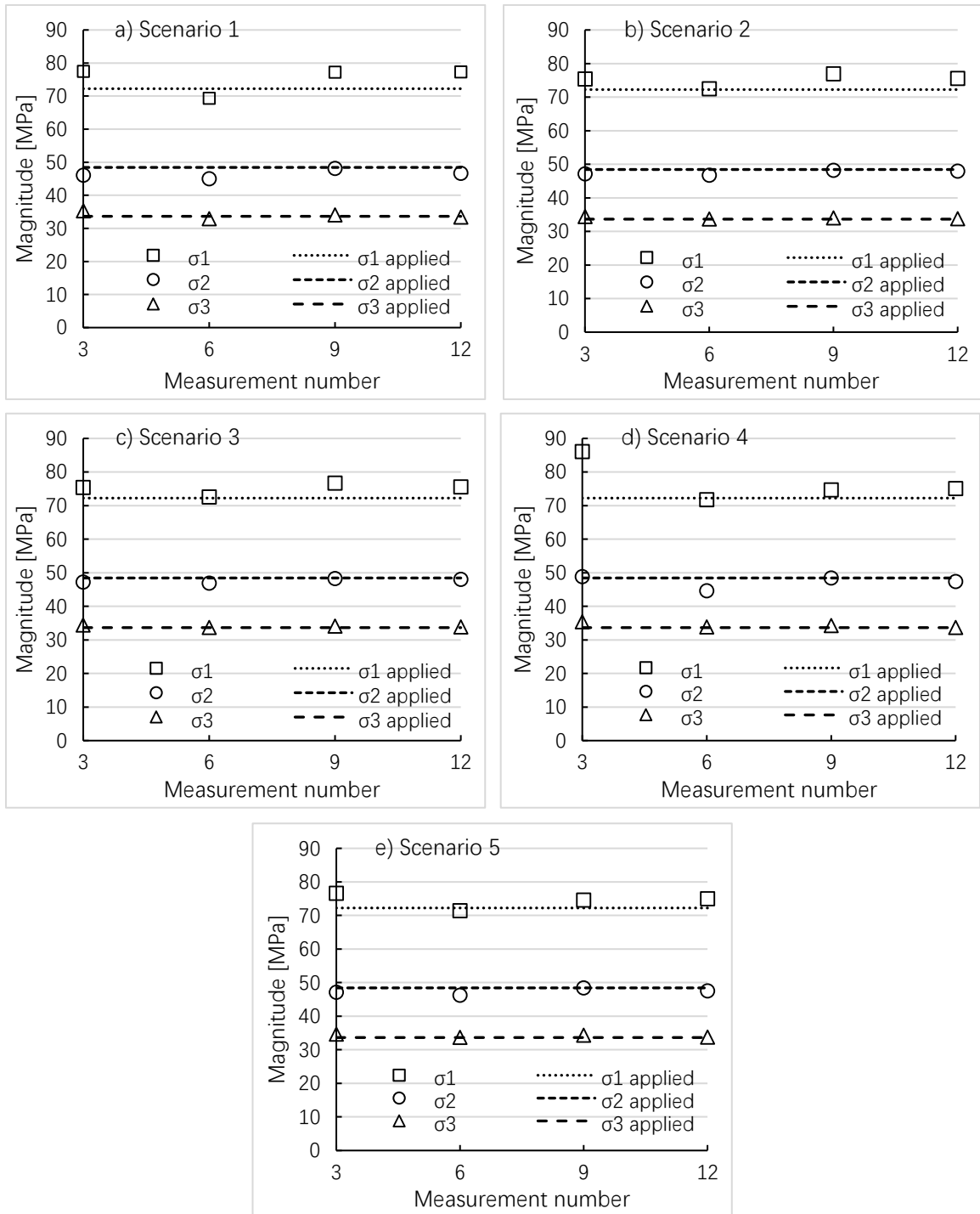


**Figure 9.10** Magnitudes of the back-analyzed principal stresses using different number of measurements for all 5 scenarios (Inclination angle interval 50°. Max. error in input data 20%).

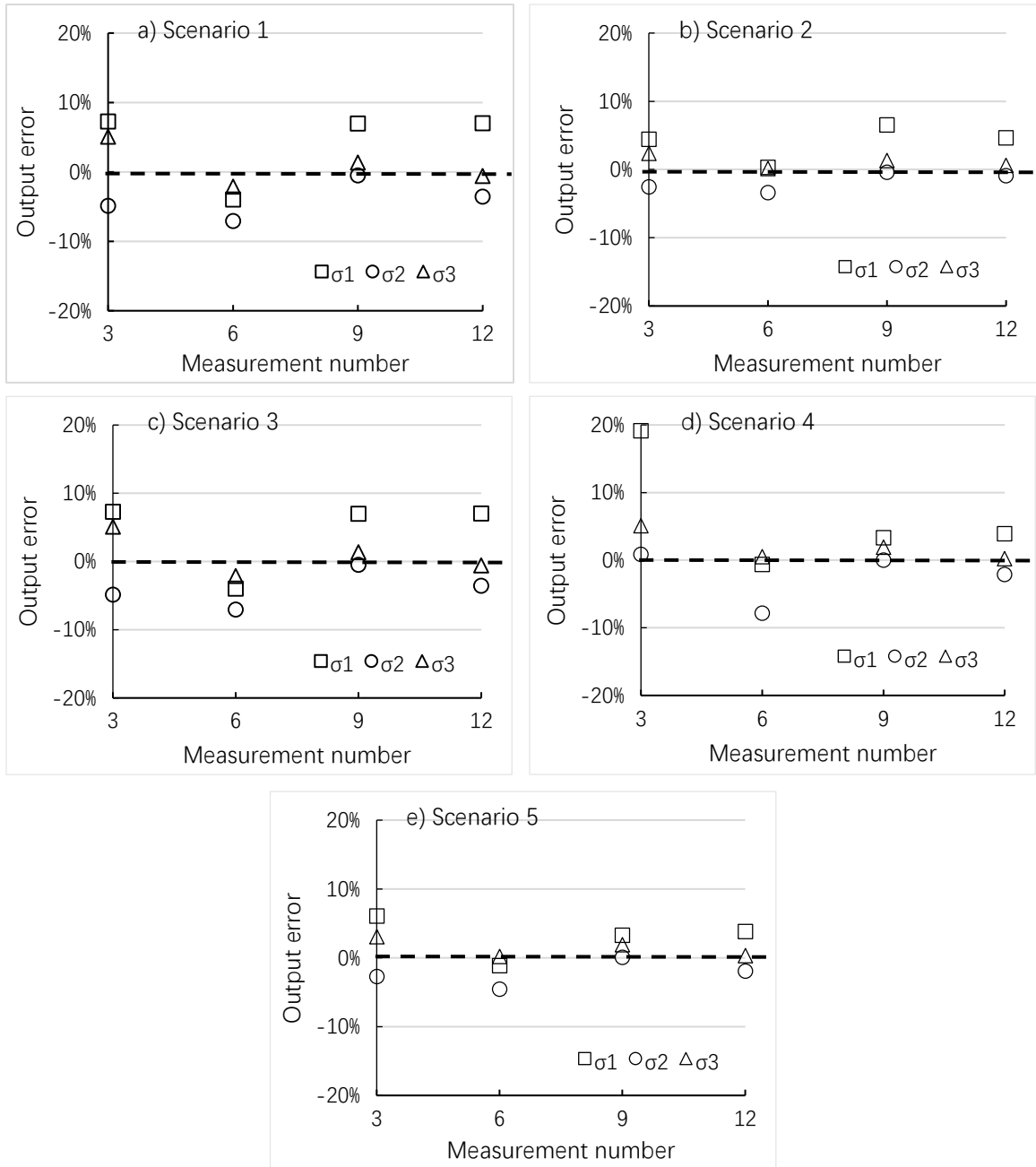


**Figure 9.11** Output errors of the principal stress magnitudes versus number of measurements for all 5 scenarios (Inclination angle interval  $50^\circ$ . Max. error in input data 20%).

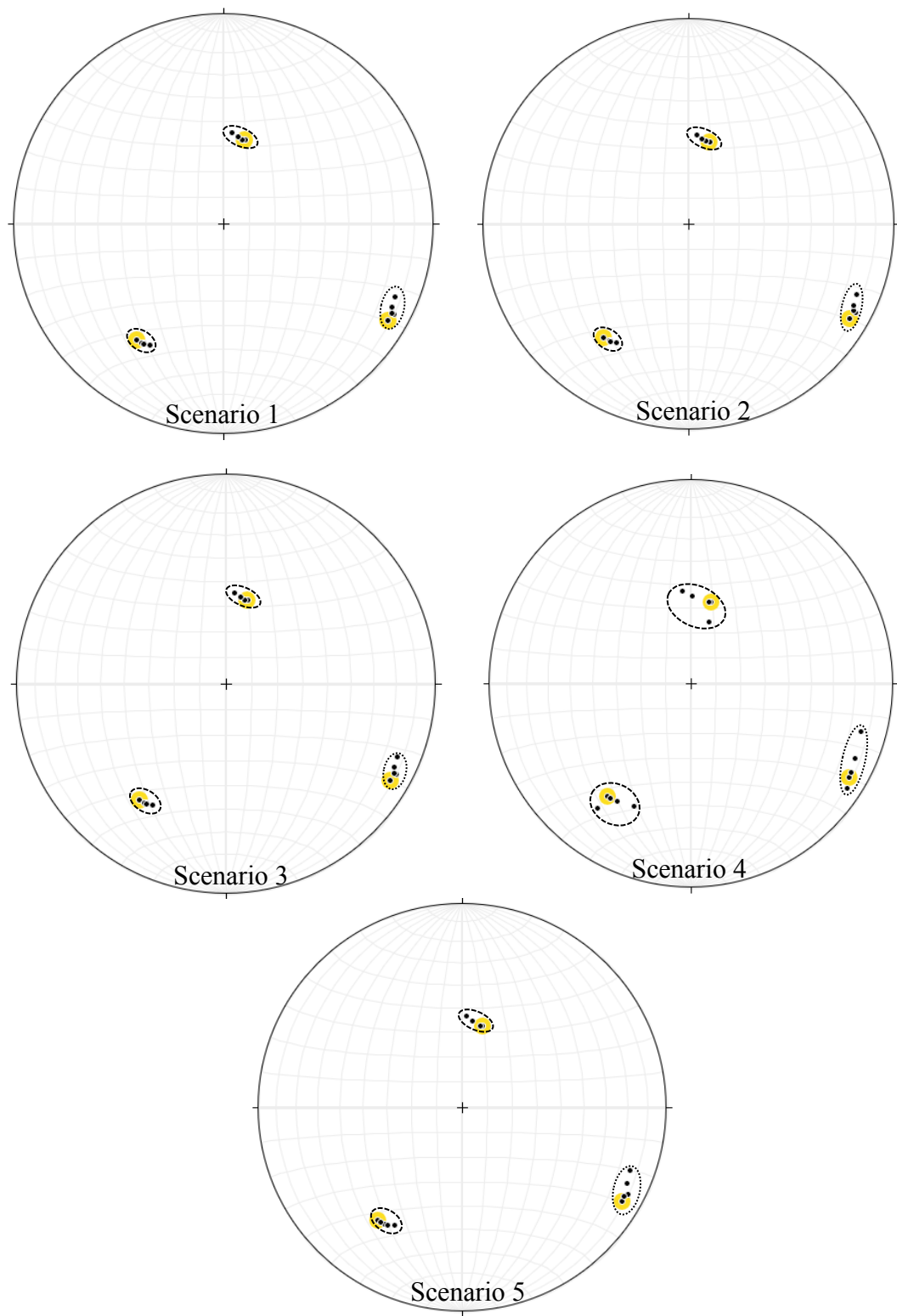


**Figure 9.12** Orientations of the back-analyzed principal stresses using different number of measurements for all 5 scenarios (Inclination angle interval  $50^\circ$ . Max. error in input data 20%).

All results in the above tests are given in Appendix I. These results have demonstrated that the method for estimation of 3D in-situ stresses is valid and reliable. In the following section, statistical method WLS is applied further to optimize the results.

## 9.5 OPTIMIZATION BY STATISTICAL ANALYSIS

In practice, there are various factors which will affect the accuracy of measurements and some may be erroneous, not representing the actual condition. If these erroneous data are treated equally as other “good data”, the results from back-analysis will not be able to represent the real condition. It is therefore necessary to identify those erroneous data points and remove them from the input data set when justified.

In the following, scenario 3 is used to demonstrate the procedure for result optimization through regression analysis. The orientations of the three measurement sections are  $I = 0, \beta = 0; I = 25^\circ, \beta = 45^\circ; I = 50^\circ, \beta = 45^\circ$ . The measurement number per section is 9 and the random error up to 20% given to diametrical convergence for individual measurement points is listed in Table 9.5.

**Table 9.5** Introduced random errors [%] for statistical analysis

Section	1	2	3	4	5	6	7	8	9
1st	-6	-8	3	15	16	-6	-10	1	-6
2 <sup>nd</sup>	12	18	13	5	-11	7	6	-10	9
3 <sup>rd</sup>	2	-11	16	13	20	-19	-3	-18	4

The same procedure as used in Section 7.4.3.2 of Chapter 7 to perform analysis. Two parameters to detect the erroneous data points,  $t$  and  $d$ , during each iteration are calculated and shown in Table 9.6. 90% confidence level is considered in this analysis. Two iterations were performed. The results of the back-analyzed 3D principal stresses and some important statistical parameters are given in Table 9.7. Identified points with  $t_{max}$  and  $d_{max}$  and some important statistical parameters are listed in Table 9.8.

As shown in Tables 9.6 and 9.7, during the first iteration, the measurement point 2 of section 2 yielded the maximum absolute value of the standardized residual  $t$  (2.21), labeled as  $t_{max}$  in Table 9.8. It is however less than  $t_o$  at the 90% confidence level (2.72). Meanwhile it was not the most influential data point either since its  $d$  value of  $0.108 < d_{max}$  (0.137). Accordingly it was not considered as an outlier. No high leverage point was observed because  $h_{iimax}$  (0.33) is smaller than  $2m/n$  (0.44).

**Table 9.6**  $t$  and  $d$  values for model 3 in regression analysis in 3D in-situ stress determination

Section	Iteration	1		2	
	Data point	$t$	$d$	$t$	$d$
1 <sup>st</sup> section	1	-0.44	0.011	-0.22	0.003
	2	-0.86	0.055	-0.82	0.050
	3	-0.35	0.010	-0.39	0.013
	4	0.61	0.029	0.59	0.028
	5	1.16	0.088	1.22	0.098
	6	-1.18	0.062	-1.28	0.073
	7	-1.42	0.056	-1.41	0.057
	8	0.37	0.003	0.69	0.013
	9	-0.36	0.005	-0.08	0.000
2 <sup>nd</sup> section	1	-1.62	0.062	-1.54	0.061
	2	<b>2.21</b>	0.108		
	3	0.98	0.026	1.37	0.054
	4	-0.14	0.001	-0.03	0.000
	5	-0.47	0.017	-0.58	0.026
	6	0.04	0.000	-0.13	0.001
	7	0.41	0.008	0.30	0.004
	8	-0.47	0.006	-0.56	0.008
	9	1.37	0.041	1.66	0.062
3 <sup>rd</sup> section	1	0.43	0.004	0.74	0.014
	2	-2.10	<b>0.137</b>	<b>-2.04</b>	<b>0.143</b>
	3	1.04	0.054	1.46	0.113
	4	0.04	0.000	0.23	0.004
	5	0.21	0.004	0.27	0.006
	6	-0.73	0.043	-0.89	0.064
	7	0.41	0.012	0.38	0.010
	8	-0.36	0.007	-0.40	0.008
	9	1.13	0.039	1.39	0.061

Note: Bold numbers in this table have the maximum absolute value of  $t$  ( $t_{max}$ ) and  $d$  ( $d_{max}$ ).



**Table 9.7** Results of 3D in-situ principal stresses from WLS analysis

Iteration	3D in-situ principal stresses		$\sigma_1$	$\sigma_2$	$\sigma_3$
1 (all data)	Back-analyzed	Magnitude [MPa]	76.66	48.29	34.08
		Plunge [°]	56.4	10.0	31.7
		Trend [°]	12.6	118.0	214.3
	Differences with the applied stresses	Magnitude [%]	6.1%	-0.3%	1.3%
		Plunge [°]	0.0	-0.3	0.1
		Trend [°]	-1.9	-2.4	-2.6
2 (data point 2 of section 2 deleted)	Back-analyzed	Magnitude [MPa]	76.04	47.80	34.08
		Plunge [°]	56.2	10.2	31.8
		Trend [°]	12.5	118.2	214.6
	Differences with the applied stresses	Magnitude [%]	5.3%	-1.3%	1.3%
		Plunge [°]	-0.2	-0.1	0.2
		Trend [°]	-2.0	-2.2	-2.2

**Table 9.8** Identified points with  $t_{max}$  and  $d_{max}$  and some important statistical parameters

Iteration	$t_{max}$	$t_o$ @ 90%	Point @ $t_{max}$	$d$	$d_{max}$	$h_{iimax}$	$2m/n$	$r_c$	$F_o$ @ 95%	$F/F_o$
1	2.21	2.72	2 <sup>nd</sup> section-2	0.109	0.137	0.33	0.44	0.975	2.00	32.69
2	2.04	2.70	3 <sup>rd</sup> section-2	0.349	0.349	0.33	0.46	0.979	2.01	36.40

To check the possible masking effect due to multiple outliers, data point 2 of section 2 was deleted and the analysis was repeated. This time, the data point 2 of section 3 produced the maximum standardized residual  $t$  (2.04 in Table 9.8), which is however less than  $t_o$  at the 90% confidence level (2.70). This point was the most influential data point with the largest value of  $d$  (0.349), designated as  $d_{max}$  in Table 9.8. However, since  $t_{max}$  is smaller than  $t_o$  (1.90) ( $t_{max} < t_o$ ), it was not declared as an outlier. At the same time,  $h_{iimax}$  (0.33) is smaller than  $2m/n$  (0.42), so there was no high leverage point.

The two consecutive iterations have not identified any erroneous data points, the test was stopped. Subsequently, the reliability of the regression results was checked. The tests of  $r_c$  and  $F$  indicate that the set of measurement data point in each iteration is statistically meaningful. The results from iteration 1 with full data set are accepted as the best fit solution. The variation of results for the in-situ stresses in is small (Table 9.7). It has little

problem in choosing a best solution. If the measurements are poor, the solution is expected to vary widely. Hence it is not easy to decide which solution is more representative of the unknown reality.

In addition, it can be seen from the results in Table 9.9a, despite of the up to 20% errors introduced in the input data (Table 9.6), the magnitude differences of the back-analyzed principal stresses are very small, all  $< 6.5\%$  and their orientation differed with less than  $2.6^\circ$  from the actual stresses. This further indicates the robust and reliability of this back-analysis method.

## **9.6 DISCUSSION ON PRACTICAL APPLICATION**

To obtain the complete solution of 3D in-situ stresses, diametrical convergence needs to be measured in three sections with a total inclination angle interval at least  $35^\circ$  in a directionally-drilled, and in each section, the recommended number of measurement is at least six in different directions and the data combined in analysis. Test analysis showed that when the measured diametrical convergence is exact, the back-analyzed in-situ stresses with this method are the same as the actual stresses. If random errors exist in the measured diametrical convergence, the results of the back-analyzed in-situ stresses will differ from the actual stresses. However the errors in the results are smaller than the error in the input data.

### **1) Advantages of the developed method**

As noted in Chapter 2, in mining and geotechnical engineering, the only method to determine the 3D stresses underground is the overcoring method with strain gages attached onto borehole wall and strains are measured during overcoring. This method requires physical access to the measurement location and a process of complete stress relief at the measurement point. This method provides the stress information at a single point involving a very small volume of rock. In addition, overcoring is very expensive in the field.

In petroleum engineering, no method is available to determine the complete 3D stress magnitudes and orientations at present. The overcoring method cannot be directly applied to petroleum industry because physical access is impossible in a small deep.

The back-analysis method developed in this research does not require overcoring and involves a large volume of rock mass. It has a potential of practical applications. It is expected to have the following advantages:

- a) it is the only potential method capable of measuring the complete 3D stresses in a small deep well in petroleum industry at present,
- b) it only needs drilling and convergence measurements in drilled wells / boreholes,
- c) it gives more meaningful results of the in-situ stress state than overcoring because it involves a large volume of rock rather than at a point,
- d) it is less expensive than the overcoring method because there is no need for overcoring, making it more versatile in application.
- e) In mining and other rock engineering, three holes can be drilled in different directions in a drift, which would give better representation of a 3D in-situ stresses.

## 2) Practical application considerations and limitations of the developed method

At current stage, this method is developed with the assumption of ideal rock behavior: continuous, homogeneous, isotropic and linear elastic. If the rock behavior is not ideal, the accuracy of results may be affected. Further research is required to consider other field conditions.

In this method, the diametrical convergence is calculated from the difference between the diameter of wellbore wall measured after drilling at different directions around a wellbore wall and the designed borehole size. In petroleum field, when using caliper tool to measure well deformation, there is a time delay from drilling. Therefore a number of factors need to be considered.

- The actual size of a borehole drilled with a designated bit immediately after drilling before deformation takes place needs to be studied.

- Mechanical multi-arm tool is usually used 2-10 days after drilling and ultrasonic caliper tool is used normally minutes to hours after drilling. with time delay, wellbore wall conditions may be changed, affecting the accuracy of measurements.
- The roughness of wellbore wall may also have some influence on the caliper measurement.
- The thick and hard mud cake is also another factor which may have an impact on the caliper measurement.

The further research needs to study appropriateness of the present caliper tools for measuring borehole deformation in open wellbore for use in the back analysis.

- a) assess whether the accuracy and resolution of caliper instrumentation are sensitive enough to measure small displacements as required.
- b) identify approaches and methods, if necessary, to improve existing caliper log system, and/or to explore other potential measurement methods.
- c) evaluate the appropriate time window after drilling and the location for measurement to ensure the rock mass around a drill hole is in the linear elastic stage, taking into consideration of field conditions and industrial operations.
- d) assess the suitability of well-logging calipers for use in drill-hole in mine environment. Modification of these devices may be considered.
- e) alternatively a new device may need to designed for use in wells and/or in boreholes.

# CHAPTER 10 SOFTWARE DEVELOPMENT IN 2D ANALYSIS

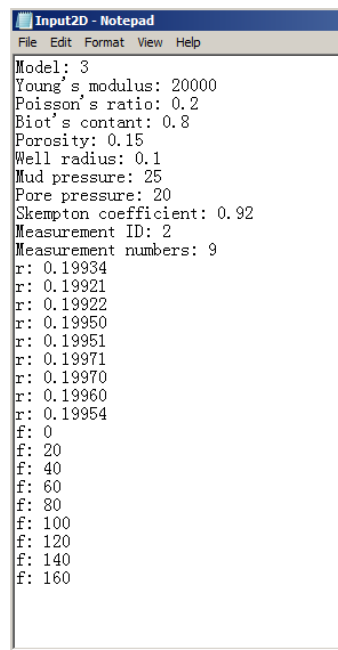
A stand-alone automated analysis software – 2D In-situ Stress Calculation is developed for field personnel use. The basic program structure and outcome of the software are briefly described below.

## 10.1 SOFTWARE STRUCTURE

The source codes are written in C++ computer programming language and compiled with compiler Dev C++.

The current software developed for 2D in-situ stress automated back analysis consists of:

- program core for computation, and
- the following user interfaces:
  - Input data file (Figure 10.1)
  - Output data file (Figure 10.2)
  - Graphical interface (Figure 10.3)



```
Input2D - Notepad
File Edit Format View Help
Model: 3
Young's modulus: 20000
Poisson's ratio: 0.2
Biot's contant: 0.8
Porosity: 0.15
Well radius: 0.1
Mud pressure: 25
Pore pressure: 20
Skempton coefficient: 0.92
Measurement ID: 2
Measurement numbers: 9
r: 0.19934
r: 0.19921
r: 0.19922
r: 0.19950
r: 0.19951
r: 0.19971
r: 0.19970
r: 0.19960
r: 0.19954
f: 0
f: 20
f: 40
f: 60
f: 80
f: 100
f: 120
f: 140
f: 160
```

Figure 10.1 Input data file

```

Output2D - Notepad
File Edit Format View Help
---This is the result of in-situ stress field---
The value of Sigma X is 52.51194 MPa
The value of Sigma Y is 42.70908 MPa
The value of Shear stress XY is 5.86288 MPa
The value of Sigma Maximum is 55.25232 MPa
The value of Sigma Minimum is 39.96869 MPa
The value of the angle between Sigma Maximum and X axis is 25.05200°

```

Figure 10.2 Output data file

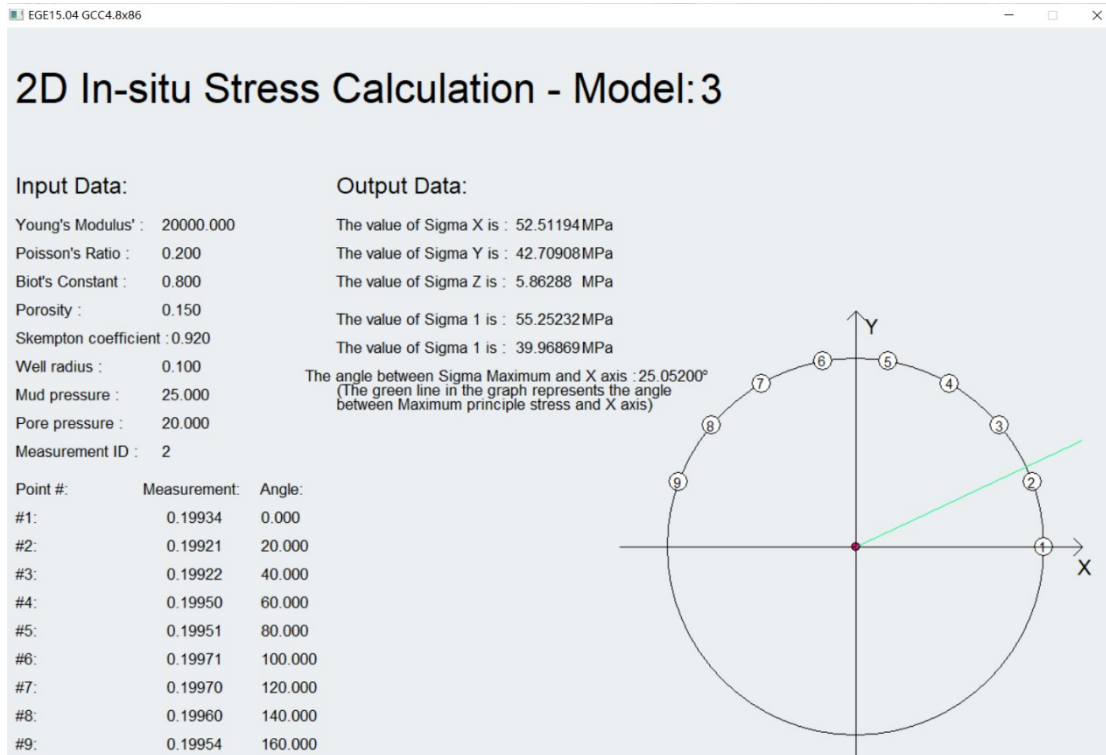


Figure 10.3 Graphical interface

## 10.2 PROCESS FLOW DESIGN

Figure 10.4 depicts screenshot of some source codes in Dev C++ compiler. The basic parts in programming for 2D in-situ stress back analysis consist of the following modules:

- Definition of calculation function for different models/scenarios.  
This is linked to the back-analysis calculation part in the main routine.
- Data input and results output for users.  
They are linked to the input and output text files, respectively.
- Definition of all variables and matrices.

- Pre-assessment of input data.  
Before input data are assigned to the corresponding variables and matrices, a built-in function checks errors of parameters entered by users, whether these data are in reasonable range and if a model number matches with other input data. If not, a warning message will be shown to user.
- Back-analysis calculation.  
This contains different calculation parts for the five models. According to the case number entered by user, the specific calculations for the case will be performed.
- Determination of magnitudes and orientations of in-situ principal stresses.  
In this part, the results of stresses in the global coordinate system ( $xy$ ) will be converted to the principal stresses with their magnitudes and orientations.
- Output.  
This part displays and results of the in-situ stresses in  $xy$  system and in-situ principal stresses and saves them in an output file.

```

1 //input E
2 cout << "Please input Young's modulus" << endl;
3
4 while (fscanf(fp, "Young's modulus: %lf", &E))
5 {
6     if (E > 0) break;
7     cout << "Not in reasonable range (E>0), please input again!" << endl;
8     fprintf(fpw, "Not in reasonable range (E>0), please input again! Thank you!");
9     return 0;
10 }
11 getc(fp);
12
13
14 cout << "The Youngs modulus: " << E << " MPa" << endl;
15 cout << "-----" << endl;
16
17 //input v
18 cout << "Please input Poissons ratio" << endl;
19
20 while (fscanf(fp, "Poissons ratio: %lf", &v))
21 {
22     if (v > 0 && v <= 0.5) break;
23     cout << "Not in reasonable range (0<<=0.5), please input again!" << endl;
24     fprintf(fpw, "Not in reasonable range (0<<=0.5), please input again! Thank you!");
25     return 0;
26 }
27
28 getc(fp);
29
30
31 cout << "The Poisson's ratio: " << v << " No unit" << endl;
32 cout << "-----" << endl;
33
34 //input a
35
36 cout << "Please input Biot's contant" << endl;
37 while (fscanf(fp, "Biots contant: %lf", &a))
38 {
39     if (a >= 0 && a <= 1) break;
40     cout << "Not in reasonable range (0=<a<=1), please input again!" << endl;

```

Figure 10.4 Screenshot of some source codes written in Dev C++ compiler

Figure 10.5 illustrates the basic design of flow chart in programming.

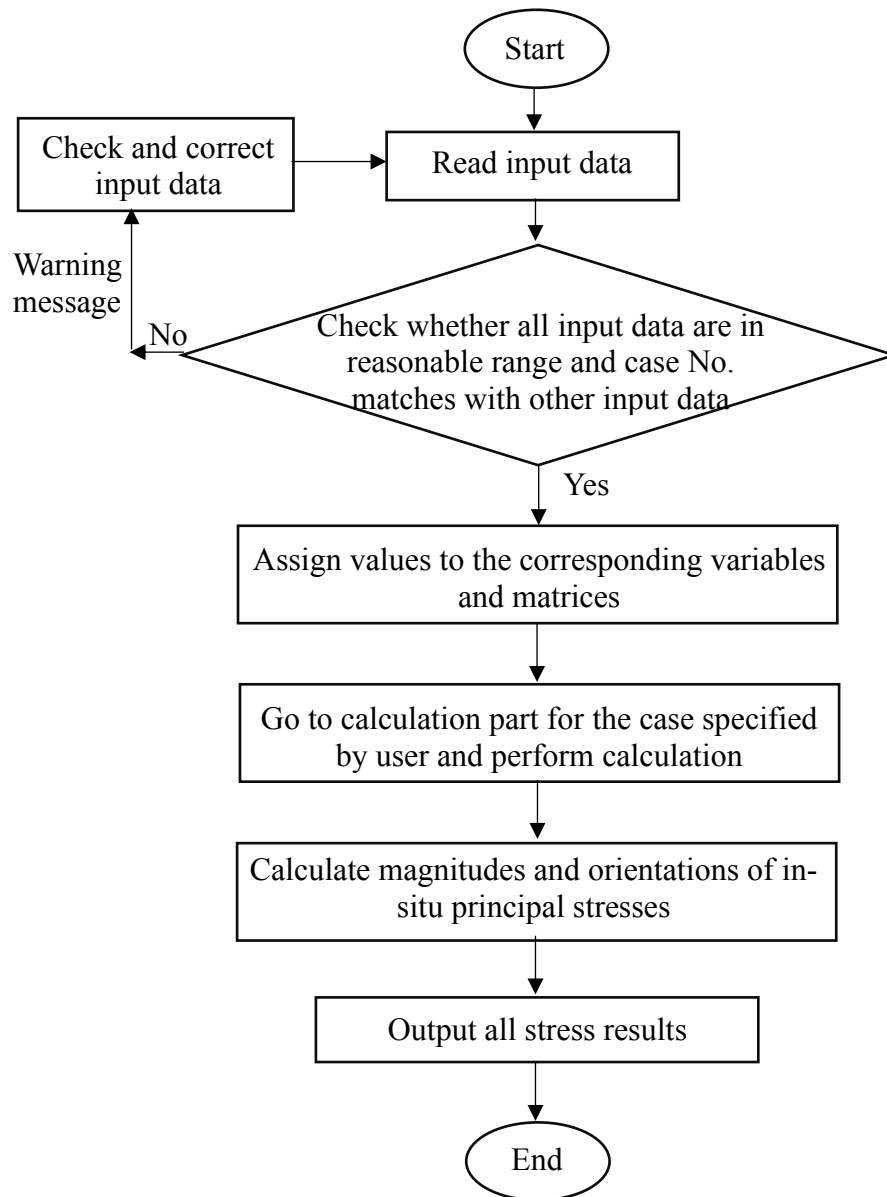


**Figure 10.5** Basic flow chart in programming

### 10.3 SOFTWARE TESTING

The developed software for 2D in-situ stress back analysis has gone through a vigorous process of debugging to ensure it function properly. The examples used in Chapter 7 are applied here to test. The diametrical convergence measurements without and with errors are considered.



- 1)  $u_d$  with no errors, exact convergence values calculated from the applied stresses.
- 2)  $u_d$  with hypothetical errors of up to 15% randomly assigned to each data point, with the same set of random errors for all 5 scenarios (Table 10.1).

**Table 10.1** Same set of random errors set for different scenarios (up to 15%)

Measurement point	1	2	3	4	5	6	7	8	9
Hypothetic error [%]	-1	8	10	-14	15	-8	4	7	-11

The results from the automated analysis packages developed in Excel and those from the software developed using C++ for all 5 scenarios are compared in Table 10.2 to 10.6, respectively .

**Table 10.2** Comparison of calculated stresses from the automated analysis sheets developed in Excel and the software developed using C++ for scenario 1

Model 1	Applied	Results from automated analysis in Excel		Results from software developed in C++	
		No errors	With errors	No errors	With Errors
Stresses					
$\sigma_x$ [MPa]	52.09	52.09	52.73	52.09	52.73
$\sigma_y$ [MPa]	42.42	42.42	42.99	42.42	42.99
$\tau_{xy}$ [MPa]	5.40	5.40	5.98	5.40	5.98
$\sigma_{Hmax}$ [MPa]	54.50	54.50	55.57	54.50	55.57
$\sigma_{Hmin}$ [MPa]	40.00	40.00	40.15	40.00	40.15
$\theta_{Hmax}$ [°]	24.00	24.00	25.41	24.00	25.41

**Table 10.3** Comparison of calculated stresses from the automated analysis sheets developed in Excel and the software developed using C++ for scenario 2

Model 2	Applied	Results from automated analysis in Excel		Results from software developed in C++	
		No errors	With errors	No errors	With Errors
Stresses					
$\sigma_x$ [MPa]	52.09	52.09	52.54	52.09	52.54
$\sigma_y$ [MPa]	42.42	42.42	42.72	42.42	42.72
$\tau_{xy}$ [MPa]	5.40	5.40	5.82	5.40	5.82
$\sigma_{Hmax}$ [MPa]	54.50	54.50	55.25	54.50	55.25
$\sigma_{Hmin}$ [MPa]	40.00	40.00	40.01	40.00	40.01
$\theta_{Hmax}$ [°]	24.00	24.00	24.92	24.00	24.92

**Table 10.4** Comparison of calculated stresses from the automated analysis sheets developed in Excel and the software developed using C++ for scenario 3

Model 3	Applied	Results from automated analysis in Excel		Results from software developed in C++	
		No errors	With errors	No errors	With Errors
Stresses					
$\sigma_x$ [MPa]	52.09	52.09	52.54	52.09	52.54
$\sigma_y$ [MPa]	42.42	42.42	42.71	42.42	42.71
$\tau_{xy}$ [MPa]	5.40	5.40	5.82	5.40	5.82
$\sigma_{Hmax}$ [MPa]	54.50	54.50	55.24	54.50	55.24
$\sigma_{Hmin}$ [MPa]	40.00	40.00	40.01	40.00	40.01
$\theta_{Hmax}$ [°]	24.00	24.00	24.90	24.00	24.90

**Table 10.5** Comparison of calculated stresses from the automated analysis sheets developed in Excel and the software developed using C++ for scenario 4

Model 4	Applied	Results from automated analysis in Excel		Results from software developed in C++	
		No errors	With errors	No errors	With Errors
Stresses					
$\sigma_x$ [MPa]	52.09	52.09	52.52	52.09	52.52
$\sigma_y$ [MPa]	42.42	42.42	42.72	42.42	42.72
$\tau_{xy}$ [MPa]	5.40	5.40	5.87	5.40	5.87
$\sigma_{Hmax}$ [MPa]	54.50	54.50	55.27	54.50	55.27
$\sigma_{Hmin}$ [MPa]	40.00	40.00	39.98	40.00	39.98
$\theta_{Hmax}$ [°]	24.00	24.00	25.08	24.00	25.08

**Table 10.6** Comparison of calculated stresses from the automated analysis sheets developed in Excel and the software developed using C++ for scenario 5

Model 5	Applied	Results from automated analysis in Excel		Results from software developed in C++	
		No errors	With errors	No errors	With Errors
Stresses					
$\sigma_x$ [MPa]	52.09	52.09	52.51	52.09	52.51
$\sigma_y$ [MPa]	42.42	42.42	42.71	42.42	42.71
$\tau_{xy}$ [MPa]	5.40	5.40	5.86	5.40	5.86
$\sigma_{Hmax}$ [MPa]	54.50	54.50	55.25	54.50	55.25
$\sigma_{Hmin}$ [MPa]	40.00	40.00	39.97	40.00	39.97
$\theta_{Hmax}$ [°]	24.00	24.00	25.05	24.00	25.05

For measurement data with no errors and the same set of random errors for all 5 scenarios, the solutions of the 2D in-situ stresses back-calculated from the software developed in C++ are exactly the same as those obtained from the automated analysis in Excel. This proves that the software developed in C++ works properly.

By comparison of all results, it can be found that

- When the measured input data has no errors, the solutions of magnitudes and orientations of the 2D in-situ stresses are the same as the applied stresses;
- When the random errors up to 15% are introduced, there a little difference between the solutions of the 2D in-situ stresses obtained from the set of input data with errors and the applied stresses. The output errors are less than the introduced errors of 15%.

# CHAPTER 11 CONCLUSIONS AND RECOMMENDATIONS

## 11.1 CONCLUSIONS

In this research work, a practical back analysis method based on borehole / well diametrical convergence has been developed for estimating the 2D and 3D in-situ stresses underground for applications in mining, geotechnical and petroleum engineering. The following summarizes the major works and the relevant conclusions.

- 1) The elastic behaviour of the rock formation, the permeability of rock formation and well wall, and mud pressure all play a role and affect the displacements in the vicinity of a well induced by drilling. The effects of the in-situ stresses, the pore pressure and mud pressure are superimposed surrounding the well and are all considered in analysis.
- 2) To consider different field conditions, five scenarios are studied, each having a mathematical model developed to correlate the well deformation and the in-situ stresses: one linear elastic model (rock formation without pore pressure effect) and four linear poroelastic models (with impermeable and permeable well wall in high and low permeability rock formations). The linear elastic model corresponds to the condition in mining and geotechnical engineering when mud pressure is zero. The linear poroelastic models are for the specific conditions in petroleum field.
- 3) In 2D analysis, plane strain condition is assumed in the plane perpendicular to a well. Measurements of diametrical convergence are made in that plane and the back-analyzed results of the in-situ stresses correspond to that plane as well. This method provides an alternative method for estimating the 2D in-situ stresses.
- 4) It is discovered during the research that diametrical convergence measured in a plane perpendicular to a well can only provide a maximum of four independent correlations between deformation and stress components. No matter how many measurements are made in the same plane or parallel planes, they are not sufficient for a complete solution

of the six stress components in three dimensions. Further analysis indicated that measurements made in two wells are not sufficient either. To solve for the complete six in-situ stress components in 3D, diametrical convergence must be made in at least three non-parallel planes (or three boreholes / wells) and within each plane a minimum of six measurements suggest to be made at independent directions.

- 5) With measurements in three non-parallel planes, the data need to be combined in a global system through coordinate transformation for use in back analysis. The comprehensive back analysis mathematical models have been formulated to combine the three sets of measured convergence properly.
- 6) To obtain the complete solution of 3D in-situ stresses in petroleum application, one solution is typically to make another two sets of measurements in inclined directions, in addition to the vertical section, in a directional well. The three sets of measurements can also be made in three inclined sections. The back-analyzed results of the 3D in-situ stresses are found to be acceptable when the three sets of measurements are made in three strategical sections (the total inclination angle interval between the first and the third section at least  $35^\circ$ ).
- 7) The effects of permeability of rock formation, permeability of well wall and change in mud pressure on the diametrical convergence are evaluated. In low permeability rock formation, as a consequence of unequal pore pressure around the well, the difference of diametrical convergence between the direction of  $\sigma_{Hmax}$  and  $\sigma_{Hmin}$  is decreased. For a permeable mud cake in the well wall, mud penetrates the wall and loses some pressure, causing an increase of the diametrical convergence. Change in mud pressure seems to have similar impact on the convergence amount in both types of rock formation. Relative to permeable well wall, an increase in mud pressure results in the smaller diametrical convergence for impermeable well wall without mud loss.
- 8) In the process of back analysis and handling surplus data sets, statistical principles have been applied in order to detect erroneous data (outliers and high leverage points) on the

basis of standardized residuals, to check the reliability of the results and to optimize the final results. Correlation coefficient is used to measure how closely the regression model fits the data. The quality of the regression results is measured by the regression significance ratio. This procedure can help one see whether the measured data are reliable and whether the obtained results are meaningful.

- 9) Automated analysis packages based on excel for 2D and 3D analyses have been developed for the five different scenarios. The interface sheet includes Input Data, Analysis and Results. For 2D analysis, a standalone software is also developed for each model. They allow users to input data and view the results conveniently.
- 10) The back analysis mathematical models and statistical process for result optimization have been tested using simulated measurement input data with 0% to 50% maximum random errors. At 0% input error, exact solution is found. With up to 30% input errors, there are small differences between the back-analyzed stresses and applied stresses. These test results have demonstrated the accuracy and reliability of the solutions and shown the validity of the developed methods and the calculations.

## **11.2 RECOMMENDATIONS**

- 1) To verify the developed method, real convergence data from the field are to be used,
- 2) To use the developed method to application in mining and geotechnical engineering, boreholes drilled in different directions should be tested.

Furthermore, the complex field conditions and practical factors need to be considered to further improve the method:

- 3) The actual size of a borehole drilled with a designated bit before deformation,
- 4) The effect of time delay on wellbore measurement,
- 5) The influence of roughness of wellbore wall on the measurement,
- 6) The effect of thick and hard mud cake on the measurement,
- 7) The suitability of well-logging calipers as field tools,
- 8) Alternatively a new device for use in wells and/or in boreholes.

For analysis convenience,

9) A stand-alone automated analysis software is to be developed in 3D analysis with ease of use for field personnel. It should include the following features:

- A user interface
- Visual images for wellbore and cross-section planes with locations of measurement points be displayed to allow users to visualize and assess the measurement locations underground.

## REFERENCES

Aadnøy, B.S. and Looyeh, R., 2011. Petroleum Rock Mechanics: Drilling Operations and Well Design. Gulf Professional Publishing, Oxford, UK, 350p.

Afsari, M., Amani, M., Razmgir, S.M., Karimi, H. and Yousefi, S., 2010. Using drilling and logging data for developing 1D mechanical earth model for a mature oil field to predict and mitigate wellbore stability challenges. Paper SPE 132187 presented at the CPS/SPE International Oil & Gas Conference and Exhibition in China held in Beijing, China, 8-10 June.

Amadei, B. and Stephansson, O., 1997. Rock Stress and its Measurement. Chapman and Hall, UK, 490p.

Barnet, V and Lewis, T., 1978. Outlier in Statistic Data. Wiley, New York, 584p.

Bock, H. and Foruria, V., 1983. A recoverable borehole slotting instrument for in-situ stress measurements in rocks? not requiring overcoring. International Symposium on Field Measurements in Geomechanics, Zurich, September 5 - 8, 15 - 29.

Boonen, P., McElhinney, G., 2002. Rock mechanics and wellbore stability analysis while drilling using LWD sonic, density and caliper measurements. Paper SPE/ISRM 78208 presented at the SPE/ISRM Rock Mechanics Conference held in Irving, Texas, USA, 20-23 October.

Borehole imaging, 2015. [https://petrowiki.org/Borehole\\_imaging](https://petrowiki.org/Borehole_imaging).

Bourgoyne, A.T., Millheim, K.K., Chenevert, M.E. and Young, F.S., 2003. Applied Drilling Engineering. Society of Petroleum Engineers, Richardson, TX, US, 502p.

Brady, B.H.G. and Brown, E.T., 1993. Rock Mechanics for Underground Mining (2<sup>nd</sup> edition). Chapman and Hall, London, 571p.

Brady, B.H.G. and Brown, E.T., 2004. Rock Mechanics for Underground Mining (3<sup>rd</sup> edition). Springer Netherlands, 626p.

Caliper log (Schlumberger), 2019. [https://www.glossary.oilfield.slb.com/en/Terms/c/caliper\\_log.aspx](https://www.glossary.oilfield.slb.com/en/Terms/c/caliper_log.aspx).



Charlez, Ph. A., 1997. Rock Mechanics-volume 2 Petroleum Applications. Paris: Éditions Technip, 661p.

Chen, G.Z., Chenevert, M.E., Sharma M.M. and Yu, M.J., 2003. A study of wellbore stability in shales including poroelastic, chemical, and thermal effects. *Journal of Petroleum Science and Engineering*, 38: 167 – 176.

Cheng, H.D., 2016. Poroelasticity. Springer International Publishing, Switzerland, 877p.

Cornet, F.H. and Valette, B., 1984. In-situ stress determination from hydraulic injection test data. *Journal of Geophysical Research*, 89: 11527 - 11537.

Cornet, F.H., 1986. Stress Determination from Hydraulic Tests on Pre-Existing Fractures - the H.T.P.F. Method. *Proceedings of the International Symposium on Rock Stress and Rock Stress Measurements*, 301 - 312.

Dehghan, A.N., Shafiee, S.M., Rezaei, F., 2012. 3-D stability analysis and design of the primary support of Karaj metro Tunnel: Based on convergence data and back analysis algorithm. *Engineering Geology*, 141-142: 141 - 149.

Deng, X.H., Xu, W.S. and Cao, J.Y., 2010. Inversion analysis of mechanical parameters of surrounding rocks in buried-deep tunnel. *Journal of Computational Information Systems*, 6(6): 1877 - 1886.

Duncan-Fama, M.E. and Pender, M.J., 1980. Analysis of the hollow inclusion technique for measuring in-situ rock stress. *International Journal of Rock Mechanics and Mining Sciences & Geomechanics Abstracts*, 17(3): 113-146.

Fairhurst, C., 2003. Stress estimation in rock: a brief history and review. *International Journal of Rock Mechanics and Mining Sciences*, 40: 957 - 973.

Feng, X.T., Zhang, Z.Q. and Sheng, Q., 2000. Estimating mechanical rock mass parameters relating to the Three Gorges Project permanent shiplock using an intelligent displacement back analysis method. *International Journal of Rock Mechanics and Mining Sciences*, 37(7): 1039 - 1054.

Fjar, E., Holt, R.M., Horsrud, P., Raaen, A.M. and Risnes, R., 2008. *Petroleum Related Rock Mechanics*. Elsevier Science, Oxford, UK, 491p.

Ghassemi, G., Tao, Q. and Diek, A., 2009. Influence of coupled chemo-poro-thermoelastic processes on pore pressure and stress distributions around a wellbore in swelling shale. *Journal of Petroleum Science and Engineering*, 67: 57 – 64.

Ghorbani, M. and Sharifzadeh, M., 2009. Long term stability assessment of Siah Bisheh powerhouse cavern based on displacement back analysis method. *Tunnelling and Underground Space Technology*, 24(5), 574 - 583.

Gioda, G., 1980. Indirect identification of the average elastic characteristics of rock masses. *Proceedings of International Conference on Structural Foundations on Rock*, 7-9 May, Sydney, Rotterdam, A.A. Balkema, 65 - 73.

Goodman, R.E., 1989. *Introduction to Rock Mechanics*. John Wiley & Sons, New York, US, 562p.

Gray, W.M. and Toew, N.A., 1967. Analysis of accuracy in the determination of the ground stress tensor by means of borehole devices, in *Proc. 9th US Symposium on Rock Mechanics (USRMS)*, 17-19 April, Golden, Colorado, SME/AIME, 45 - 72.

Hearst, J.R., Nelson, P.H. and Paillet, F.L., 2000. *Well Logging for Physical Properties*. John Wiley & Sons, Ltd, England. 483p.

Heidbach, O., Reinecker, J., Tingay, M., Müller, B., Sperner, B., Fuchs, K. and Wenzel, F., 2007. Plate boundary forces are not enough: Second- and third-order stress patterns highlighted in the World Stress Map database. *Tectonics*, 26: 1 - 19.

Herget, G., 1988. *Stresses in Rock*. A.A. Balkema, Rotterdam, Netherlands, 179p.

Hines, W.W. and Montgomery, D.C., 1990. *Probability and Statistics in Engineering and Management Science*. John Wiley & Sons, Canada, 732p.

Hoek, E. and Brown, E.T., 1990. *Underground Excavations in Rock*. Institution of Mining and Metallurgy, CRC Press, London, UK, 527p.

Holzhausen, G.R. and Johnson, A.M., 1979. The concept of residual stress in rock. *Tectonophysics*, 58(3): 237 - 267.

Jaeger, J.C. and Cook, N.G.W., 1976. *Fundamentals of Rock Mechanics*. Chapman and Hall, London, 593p.

Jeon, Y.S. and Yang, H.S., 2004. Development of a back analysis algorithm using flac. *International Journal of Rock Mechanics and Mining Sciences*, 41(3): 441 - 442.

Jin, Y. and Chen, M., 2012. *Mechanics of Wellbore Stability*. Science Press, Beijing, 215. (in Chinese)

Jin, Y., Chen, M., Liu, G.H. and Chen, Z.X., 1999. Wellbore stability analysis of extended reach wells. *Journal of Geomechanics*, 5(1): 4-11. (in Chinese)

Jin, Y.J. and Cao, S.J., 2016. Calculate the in-situ stress using logging data. *IOSR Journal of Engineering*, 6(3): 20 - 22.

Julian, J.Y., Cismoski, D.A., Younger, R.O., Burton, J.P. and Lawrence, M.W., 2007. Use of 3D visualization software for multifinger caliper analysis at Prudhoe Bay, Alaska. Paper SPE 106625 presented at the 2007 SPE/ICoTA Coiled Tubing and Well Intervention Conference and Exhibition held in the Woodlands, Texas, USA, 20-21 March.

Kaiser, P.K., Zou, D.H. and Lang, P.A., 1990. Stress determination by back-analysis of excavation-induced stress changes – a case study. *Rock Mechanics and Rock Engineering*, 23: 185 - 200.

Kirsten, H.A.D., 1976. Determination Rock Mass Elastic Moduli by Back Analysis of Deformation Measurements. *Proceeding of Symposium on Exploration for Rock Engineering*, November 1 - 5, Johannesburg, South Africa, Cape Town: A.A. Balkema. 165 - 172.

Landsea, 2018. Four-arm Caliper Logging Tool (ECAL70). <http://www.lsea.com.sg/oilandgas/slim-hole-open-hole-logging-tool/four-arm-caliper-logging-tool-ecal70/>.

Ledesma, A., Gens, A. and Alonso, E.E., 1996. Estimation of parameters in geotechnical back analysis - I. Maximum likelihood approach. *Computers and Geotechnics*, 18(1): 1 - 27.

Leeman, E.R., 1967. The borehole deformation type of rock stress measuring instrument. *International Journal of Rock Mechanics and Mining Sciences*, 4: 23 - 44.

Lin, C. and Zou, D.H., 2016. In-Situ stress estimation by back analysis based on wellbore deformation with consideration of pore pressure. *International Journal of Geohazards and Environment*, 2(1): 2 - 16.

Lin, C., Zou, D.H. and Sun, H.R., 2019. Exploration of measurement methods of 3D in-situ stresses in rock masses. *International Journal of Georesources and Environment*, 2019, 5(1): 1 - 13.

Lin, H.S., Oh, J., Masoumi, H., Canbulat, I. and Zhang, C.G., 2018. A Review of In-Situ Stress Measurement Techniques. *Proceedings of the 18th Coal Operator's Conference*, Mining Engineering University of Wollongong, February 7 - 9, 95 - 102.

Ljunggren, C., Chang, Y. T., Jansonb, T. and Christianssonc, R., 2003. An overview of rock stress measurement methods. *International Journal of Rock Mechanics & Mining Sciences*, 40: 975 - 989.

Lund, R.E., 1975. Tables for an approximate test for outliers in linear models. *Technometrics*, 17(4): 473 - 476.

Maxted, I. and Hazel, P., 1995. Advances in multi-finger caliper technology and data acquisition. Paper OTC 7871 presented at the 27th Annual Offshore Technology Conference held in Houston, Texas, USA, 1-4 May.

Mello Franco, J.A., Armelin, J.L., Santiago, J.A.F., Telles, J.C.F. and Mansur, W.J., 2002. Determination of the natural stress state in a Brazilian rock mass by back analysis excavation measurements: a case study. *International Journal of Rock Mechanics & Mining Sciences*, 39(8): 1005 - 1032.

MFC, 2017. Multi-finger caliper. [https://www.bonnettsenergy.com/images/pdf\\_files/2018/mfc\\_56\\_arm.pdf](https://www.bonnettsenergy.com/images/pdf_files/2018/mfc_56_arm.pdf).

Moreira, N., Miranda, T., Pinheiro, M., Fernandes, P., Dias, D., Costa, L. and Sean-Cruz, J., 2013. Back analysis of geomechanical parameters in underground works using an evolution strategy algorithm. *Tunnelling and Underground Space Technology*, 33: 143 - 158.

MSC, 2014. High resolution 40- and 60- arm multi-sensor caliper tool guide. Weatherford.

Nauroy, J.F., 2011. *Geomechanics Applied to the Petroleum Industry*. Editions Technip, Paris, 198p.

Openhole caliper logs, 2015. [https://petrowiki.org/Openhole\\_caliper\\_logs](https://petrowiki.org/Openhole_caliper_logs).

Oreste, P., 2005. Back-analysis techniques for the improvement of the understanding of rock in underground constructions. *Tunnelling and Underground Space Technology*, 20(1): 7 – 21.

Panek, I.A., 1966. Calculation of the average ground-stress components from measurements of the diametral deformation of a drill hole. *Testing Techniques for Rock Mechanics*, ASTM STP 402.

Pfaffenberger, R.C. and Patterson, J.H., 1977. *Statistical methods for business and economics*. Richard D. Irwin, Inc., Illinois, 750p.

Reinecker, J., Tingay, M. and Müller, B., 2003. Borehole breakout analysis from four-arm caliper logs. *World Stress Map Project – Four-arm Caliper Logs*.

Sakurai, S., 1997. Lessons learned from field measurements in tunnelling. *Tunnelling and Underground Space Technology*, 12(4): 453 - 460.

Sakurai, S. and Takeuchi, K., 1983. Back analysis of measured displacement of tunnels. *Rock Mechanics and Rock Engineering*, 16: 173 - 180.

Sakurai, S., 2017. *Back Analysis in Rock Engineering*. CRC press, London, UK, 223p.

Sarwade, D.V., Mishra, K.K., Kapoor, V.K. and Kumar, N., 2009. Stress measurement in rock mass. *IGC, Guntur, India*, 233 - 237.

Schlumberger, 2002. Borehole properties analysis. [www.connent.slb.com](http://www.connent.slb.com).

Schön, J.H., 2011. *Physical Properties of Rocks- A Workbook*, Elsevier, 494p.

Serra, O. and Serra, L., 2004. *Well Logging Data Acquisition and Applications*. Editions Technip, Paris, France, 688p.

Shang, Y.J., Cai, J.G., Hao, W.D., Wu, X.Y., Li, S.H., 2002. Intelligent back analysis of displacements using precedent type analysis for tunneling. *Tunnelling and Underground Space Technology*, 17(4): 381 - 389.

Special Open Hole Tools-Caliper Logs, 2009. <http://petroleumcrudeoil.blogspot.com/2008/11/well-logging-tools-techniques-special.html>.

Stacey, T. R. and Wesseloo, J., 2002. Application of indirect stress measurement techniques (non strain gauge based technology) to quantify stress environments in mines. Project report, Safety in Mines Research Advisory Committee.

Suzuki, K., 1966. Fundamental study on the rock stress measurement by borehole deformation method. 1st ISRM Congress, 25 September-1 October, Lisbon, Portugal, International Society for Rock Mechanics.

Tang, X.M. and Cheng, A., 2004. Quantitative Borehole Acoustic Methods. Elsevier, 255p.

Tingay, M., Reinecker, J. and Müller, B., 2008. Borehole Breakout and Drilling-Induced Fracture Analysis from Image Logs. World Stress Map Project-Image Logs.

Vreede, F.A., 1981. Critical study of the method of calculating virgin rock stresses from measurement results of the CSIR triaxial strain cell. Research report, Pretoria, South Africa.

Wang, C.H., 2014. Brief review and outlook of main estimate and measurement methods for in-situ stresses in rock mass. Geological Review, 60(5): 971 - 996. (in Chinese)

Wang, W.X., 2009. Rock Mass Mechanics. Central South University Press, Changsha, China, 350p.

Warrior logging software, 2014. Multi-finger caliper and pipe tally guide. Scientific Data Systems, Inc.

Wiles, T.D. and Kaiser, P.K., 1994a. In-situ stress determination using the under-excavation technique - I: theory. International Journal of Rock Mechanics and Mining Sciences, 31: 439 - 446.

Wiles, T.D. and Kaiser, P.K., 1994b. In-situ stress determination using the under-excavation technique – II: applications. International Journal of Rock Mechanics and Mining Sciences, 31: 447 - 456.

Yazdani, M., Sharifzadeh, M. and Ghorbani, M., 2012. Displacement-based numerical back analysis for estimation of rock mass parameters in Siah Bisheh powerhouse cavern using continuum and discontinuum approach. Tunnelling and Underground Space Technology, 28: 41 - 48.

Yin, X.Y., Ma, N., Ma, Z.Q. and Zong, Z.Y., 2018. Review of in-situ stress prediction technology. Geophysical Prospecting for Petroleum, 57(4): 488 - 504. (in Chinese)

Zang, A. and Stephansson, O., 2010. Stress Field of the Earth's Crust. Springer, Netherlands, 324p.

Zhang, J., Standifird, W.B., Adesina, K., Keaney, G., 2006a. Wellbore stability with consideration of pore pressure and drilling fluid interactions. Paper ARMA/USRMS 06-922 presented at the 41st U.S. Symposium on Rock Mechanics (USRMS): "50 Years of Rock Mechanics-Landmarks and Future Challenges." , Golden, Colorado, 17-21 June.

Zhang, L.Q., Yue, Z.Q., Yang, Z.F., Qi, J.X. and Liu, F.C., 2006b. A displacement-based back-analysis method for rock mass modulus and horizontal in situ stress in tunneling – Illustrated with a case study. Tunnelling and Underground Space Technology, 21(6): 636 - 649.

Zhao, X.L., 2007. Study on borehole stability in sidewall rock of petroleum drilling. Master thesis, Chongqing University, College of Resources and Environmental Science. (in Chinese)

Zou, D.H. and Kaiser, P.K., 1990a. In situ stress determination by stress change monitoring. Proceedings of 31st US Symposium of Rock Mechanics, Golder, Balkema, Rotterdam, 27 - 34.

Zou, D.H. and Kaiser, P.K., 1990b. Determination of in situ stresses from excavation-induced stress changes. Rock Mechanics and Rock Engineering, 23: 167 - 184.

Zou, D.H., 1995a. Evaluation of field properties and stress condition by displacement back-analysis using boundary element principle. CAMI' 95 3rd Canadian Conference on Computer Application in the Mineral Industry. Montreal, Canada, 22 - 25 October.

Zou, D.H., 1995b. Statistical regression applied to borehole strain measurements data analysis. Geotechnical and Geological Engineering, 13: 17-27.

Zou, D.H., 2015. Applied Rock Mechanics and Ground Stability. Canamaple Academia Services, Halifax, Canada, 284p.

## APPENDIX A Governing Equations in Linear Elastic Theory

### Equilibrium Equations

In order to remain at rest for a stressed rock body, it is required that all forces acting on the body cancel. This produces a set of equations for the stress gradients, which are called the “equilibrium equations”. These equations, crudely, relates the stresses developed in the body to the forces and moment applied on it.

$$\frac{\partial \sigma_x}{\partial x} + \frac{\partial \tau_{yx}}{\partial y} + \frac{\partial \tau_{zx}}{\partial z} + \rho f_x = 0 \quad (\text{A.1a})$$

$$\frac{\partial \sigma_y}{\partial y} + \frac{\partial \tau_{xy}}{\partial x} + \frac{\partial \tau_{zy}}{\partial z} + \rho f_y = 0 \quad (\text{A.1b})$$

$$\frac{\partial \sigma_z}{\partial z} + \frac{\partial \tau_{xz}}{\partial x} + \frac{\partial \tau_{yz}}{\partial y} + \rho f_z = 0 \quad (\text{A.1c})$$

where  $\rho$  is the density and  $\rho f_x, \rho f_y, \rho f_z$  are the components of the body force per unit volume of the continuum in the  $x, y$  and  $z$  directions, respectively.

The equilibrium equations (A.1a) - (A.1c) may also be expressed in cylindrical coordinates:

$$\frac{\partial \sigma_r}{\partial r} + \frac{1}{r} \frac{\partial \tau_{r\theta}}{\partial \theta} + \frac{\partial \tau_{zr}}{\partial z} + \frac{\sigma_r - \sigma_\theta}{r} + \rho f_r = 0 \quad (\text{A.2a})$$

$$\frac{1}{r} \frac{\partial \sigma_\theta}{\partial \theta} + \frac{\partial \tau_{r\theta}}{\partial r} + \frac{\partial \tau_{z\theta}}{\partial z} + \frac{2\tau_{r\theta}}{r} + \rho f_\theta = 0 \quad (\text{A.2b})$$

$$\frac{\partial \sigma_z}{\partial z} + \frac{\partial \tau_{rz}}{\partial r} + \frac{1}{r} \frac{\partial \tau_{\theta z}}{\partial \theta} + \frac{\tau_{rz}}{r} + \rho f_z = 0 \quad (\text{A.2c})$$

where  $\sigma_r, \sigma_\theta, \sigma_{zz}, \tau_{r\theta}, \tau_{\theta z},$  and  $\tau_{rz}$  are the components of stresses in terms of the system of cylindrical coordinates  $r, \theta, z$ .  $\rho f_r, \rho f_\theta$  and  $\rho f_z$  are the components of the body force per unit volume of the continuum in the  $r, \theta, z$  directions, respectively.

### Constitutive Relations (Hooke's Law)

Constitutive relation gives the value of stress for a known value of the strain or vice versa. By the general Hooke's law, the strain-stress relationship in Cartesian coordinates can be



given by Eqn. (A.3).

$$\varepsilon_x = \frac{1}{E} [\sigma_x - \nu(\sigma_y + \sigma_z)] \quad (\text{A.3a})$$

$$\varepsilon_y = \frac{1}{E} [\sigma_y - \nu(\sigma_x + \sigma_z)] \quad (\text{A.3b})$$

$$\varepsilon_z = \frac{1}{E} [\sigma_z - \nu(\sigma_x + \sigma_y)] \quad (\text{A.3c})$$

$$\gamma_{xy} = \frac{1}{G} \tau_{xy} \quad (\text{A.3d})$$

$$\gamma_{yz} = \frac{1}{G} \tau_{yz} \quad (\text{A.3e})$$

$$\gamma_{zx} = \frac{1}{G} \tau_{zx} \quad (\text{A.3f})$$

where  $E$  is the Young's modulus,  $\nu$  is the Poisson's ratio, and  $G$  is the modulus of rigidity, or the shear modulus.

$$G = \frac{E}{2(1+\nu)} \quad (\text{A.4})$$

Hooke's law has the same form in cylindrical as in Cartesian coordinates.

$$\varepsilon_r = \frac{1}{E} [\sigma_r - \nu(\sigma_\theta + \sigma_{zz})] \quad (\text{A.5a})$$

$$\varepsilon_\theta = \frac{1}{E} [\sigma_\theta - \nu(\sigma_r + \sigma_{zz})] \quad (\text{A.5b})$$

$$\varepsilon_{zz} = \frac{1}{E} [\sigma_{zz} - \nu(\sigma_r + \sigma_\theta)] \quad (\text{A.5c})$$

$$\gamma_{r\theta} = \frac{1}{G} \tau_{r\theta} \quad (\text{A.5d})$$

$$\gamma_{\theta z} = \frac{1}{G} \tau_{\theta z} \quad (\text{A.5e})$$

$$\gamma_{rz} = \frac{1}{G} \tau_{rz} \quad (\text{A.5f})$$

where  $\sigma_r$  is the radial stress component acting along the radius of the well,  $\sigma_\theta$  is the tangential stress (hoop stress) acting around the circumference of well borehole,  $\sigma_{zz}$  is the axial stress acting parallel to the well orientation, and  $\tau_{r\theta}$ ,  $\tau_{\theta z}$ ,  $\tau_{rz}$  are the shear stress components.  $\varepsilon_r$  is the radial strain,  $\varepsilon_\theta$  is the tangential strain and  $\varepsilon_{zz}$  is the axial strain.  $\gamma_{r\theta}$ ,  $\gamma_{\theta z}$

and  $\gamma_{rz}$  are the shear strains.

### Compatibility Equations

The relations between strains and displacements in cylindrical coordinates by physical and geometrical law are

$$\varepsilon_r = \frac{\partial u_r}{\partial r} \quad (\text{A.6a})$$

$$\varepsilon_\theta = \frac{u_r}{r} + \frac{1}{r} \frac{\partial u_\theta}{\partial \theta} \quad (\text{A.6b})$$

$$\varepsilon_{zz} = \frac{\partial u_z}{\partial z} \quad (\text{A.6c})$$

$$\gamma_{r\theta} = \frac{\partial u_\theta}{\partial r} + \frac{1}{r} \frac{\partial u_r}{\partial \theta} - \frac{u_\theta}{r} \quad (\text{A.6d})$$

$$\gamma_{\theta z} = \frac{1}{r} \frac{\partial u_z}{\partial \theta} + \frac{\partial u_\theta}{\partial z} \quad (\text{A.6e})$$

$$\gamma_{zr} = \frac{\partial u_r}{\partial z} + \frac{\partial u_z}{\partial r} \quad (\text{A.6f})$$

where  $u_r$ ,  $u_\theta$  and  $u_z$  are the displacements in the radial, tangential and axial directions, respectively.

## APPENDIX B Typical Values of Mechanical Properties for Some Rock Types

**Table B.1** Some mechanical properties for some common rock types (after Fjar et al 2008)

Rock type	Density $\rho$ $10^3$ [kg/m <sup>3</sup> ]	Young's modulus $E$ [GPa]	Poisson's ratio $\nu$
Unconsolidated sands	1.5-1.7	0.01-0.1	~0.45
Sandstone	2.0-2.65	0.1-30	0-0.45
Clay	1.9-2.1	0.06-0.15	~0.40
Shale	2.3-2.8	0.4-70	0-0.30
High porosity chalk	1.4-1.7	0.5-5	0.05-0.35
Low porosity chalk	1.7-2.0	5-30	0.05-0.30
Basalt	2.7-2.9	50-100	0.2-0.3
Granite	2.6-2.8	5-85	0.1-0.34
Dolomite	2.4-3.2	10-100	0-0.5
Limestone	1.4-2.9	2-100	0-0.3
Gnesis	2.7-3.1	40-100	0.1-0.3
Marble	2.7-3.2	5-90	0-0.3

## APPENDIX C Isotropic Linear Poroelastic and Thermoelastic Stress Strain Law

### C.1 Isotropic linear poroelastic stress strain law

Solved for strain

$$\left\{ \begin{array}{l} \varepsilon_r = \frac{1}{E} [\sigma_r - \nu(\sigma_\theta + \sigma_{zz})] - \frac{1-2\nu}{E} \alpha P_p \\ \varepsilon_\theta = \frac{1}{E} [\sigma_\theta - \nu(\sigma_r + \sigma_{zz})] - \frac{1-2\nu}{E} \alpha P_p \\ \varepsilon_{zz} = \frac{1}{E} [\sigma_{zz} - \nu(\sigma_r + \sigma_\theta)] - \frac{1-2\nu}{E} \alpha P_p \\ \gamma_{r\theta} = \frac{2(1-\nu)}{E} \tau_{r\theta} \\ \gamma_{\theta z} = \frac{2(1-\nu)}{E} \tau_{\theta z} \\ \gamma_{rz} = \frac{2(1-\nu)}{E} \tau_{rz} \end{array} \right. \quad (C.1)$$

Solved for stress

$$\left\{ \begin{array}{l} \sigma_r = \frac{E}{(1+\nu)(1-2\nu)} [(1-\nu)\varepsilon_r + \nu\varepsilon_\theta + \nu\varepsilon_{zz}] + \alpha p_p \\ \sigma_\theta = \frac{E}{(1+\nu)(1-2\nu)} [\nu\varepsilon_r + (1-\nu)\varepsilon_\theta + \nu\varepsilon_{zz}] + \alpha p_p \\ \varepsilon_{zz} = \frac{E}{(1+\nu)(1-2\nu)} [\nu\varepsilon_r + \nu\varepsilon_\theta + (1-\nu)\varepsilon_{zz}] + \alpha p_p \\ \tau_{r\theta} = \frac{E}{2(1+\nu)} \gamma_{r\theta} \\ \tau_{\theta z} = \frac{E}{2(1+\nu)} \gamma_{\theta z} \\ \tau_{rz} = \frac{E}{2(1+\nu)} \gamma_{rz} \end{array} \right. \quad (C.2)$$

Eqn. (C.2) is written on a more compact form.

$$\sigma_{ij} = \frac{E}{(1+\nu)(1-2\nu)} \varepsilon_{vol} \delta_{ij} + \frac{E}{1+\nu} \varepsilon_{ij} + \alpha p_p \delta_{ij} \quad (C.3)$$

where  $\varepsilon_{vol}$  is volumetric strain, the sum of  $\varepsilon_r$ ,  $\varepsilon_\theta$  and  $\varepsilon_{zz}$ . The subscripts  $i$  and  $j$  are any of the numbers 1, 2, 3, representing the  $r$ ,  $\theta$ , and  $z$  in cylindrical coordinate system.  $\delta_{ij}$  is Kronecker's symbol. It is defined by

$$\delta_{ij} = \begin{cases} 1 & \text{if } i = j \\ 0 & \text{if } i \neq j \end{cases} \quad (\text{C.4})$$

## C.2 Isotropic linear thermoelastic stress strain law

Solved for strain

$$\left\{ \begin{array}{l} \varepsilon_r = \frac{1}{E} [\sigma_r - \nu(\sigma_\theta + \sigma_{zz})] - \alpha_T(T - T_o) \\ \varepsilon_\theta = \frac{1}{E} [\sigma_\theta - \nu(\sigma_r + \sigma_{zz})] - \alpha_T(T - T_o) \\ \varepsilon_{zz} = \frac{1}{E} [\sigma_{zz} - \nu(\sigma_r + \sigma_\theta)] - \alpha_T(T - T_o) \\ \gamma_{r\theta} = \frac{2(1-\nu)}{E} \tau_{r\theta} \\ \gamma_{\theta z} = \frac{2(1-\nu)}{E} \tau_{\theta z} \\ \gamma_{rz} = \frac{2(1-\nu)}{E} \tau_{rz} \end{array} \right. \quad (\text{C.5})$$

where  $\alpha_T$  is the coefficient of linear thermal expansion.

Solved for stress

$$\left\{ \begin{array}{l} \sigma_r = \frac{E}{(1+\nu)(1-2\nu)} [(1-\nu)\varepsilon_r + \nu\varepsilon_\theta + \nu\varepsilon_{zz}] + \frac{E}{1-2\nu} \alpha_T(T - T_o) \\ \sigma_\theta = \frac{E}{(1+\nu)(1-2\nu)} [\nu\varepsilon_r + (1-\nu)\varepsilon_\theta + \nu\varepsilon_{zz}] + \frac{E}{1-2\nu} \alpha_T(T - T_o) \\ \varepsilon_{zz} = \frac{E}{(1+\nu)(1-2\nu)} [\nu\varepsilon_r + \nu\varepsilon_\theta + (1-\nu)\varepsilon_{zz}] + \frac{E}{1-2\nu} \alpha_T(T - T_o) \\ \tau_{r\theta} = \frac{E}{2(1+\nu)} \gamma_{r\theta} \\ \tau_{\theta z} = \frac{E}{2(1+\nu)} \gamma_{\theta z} \\ \tau_{rz} = \frac{E}{2(1+\nu)} \gamma_{rz} \end{array} \right. \quad (\text{C.6})$$

Eqn. (C.6) is written on a compact notation:

$$\sigma_{ij} = \frac{E}{(1+\nu)(1-2\nu)} \varepsilon_{vol} \delta_{ij} + \frac{E}{1+\nu} \varepsilon_{ij} + \frac{E}{1-2\nu} \alpha_T(T - T_o) \delta_{ij} \quad (\text{C.7})$$

## APPENDIX D Fundamentals of Multiple Linear Regression

For a set of variables  $x_j$  ( $j=1, \dots, m$ ), if there is a response variable  $y$ , then  $y$  can be written as

$$y = f(x_j, a_j), \quad j=1, \dots, m \quad (\text{D.1})$$

where  $f$  can be any function of  $x_j$ .  $a_j$  are the parameters, which may be simple constants or functions of other parameters.

If  $f$  is a polynomial function, then

$$y = c \cdot 1 + \sum_{j=1}^k a_j^p z_j \quad (\text{D.2})$$

where  $p$  is a real number,  $z_j$  is some function of all  $x_j$ ,  $c$  is a constant term.

When a series of tests are conducted on  $x_j$  and the corresponding values of  $y$  are measured, the parameters  $a_j$  can be estimated by regression analysis. If  $y$  is linear in the unknown parameters  $a_j$  (i.e.,  $p=1$ ), linear regression analysis is applicable. Otherwise non-linear regression analysis is required. In a linear case, each term  $a_j z_j$  in Eqn. (D.2) can have a simple  $x_j$  ( $y$  is called linear in the variable  $x_j$ ) or any kind of function of  $x_j$  ( $y$  is called non-linear in  $x_j$ ). If the number of variables is more than one, the analysis involves multiple regression.

A general model for multiple linear regression can be written as

$$\begin{cases} E(\{y\}) = [X]\{A\} \\ V(\{y\}) = [I]s_v^2 \end{cases} \quad (\text{D.3})$$

where  $E(\ )$  is the expectation,  $V(\ )$  is the co-variance matrix,  $\{y\}$  is an  $(n \times 1)$  vector, representing the response variables,  $[X]$  is an  $(n \times m)$  vector, representing the explanatory variables, the  $(m \times 1)$  vector  $\{A\}$  is the unknown parameters,  $s_v^2$  is the variance of errors, and  $[I]$  is identity.

With the compact notation, the linear regression model can be written in the form

$$\{y\} = [X]\{A\} + \{R\} \quad (D.4)$$

Using least square method leads to the solution to  $\{A\}$

$$\{\hat{A}\} = ([X]^T [X])^{-1} [X]^T \{y\} \quad (D.5)$$

and the corresponding response variable

$$\{\hat{y}\} = [X]\{\hat{A}\} = [X]([X]^T [X])^{-1} [X]^T \{y\} = [H]\{y\} \quad (D.6)$$

where  $[H] = [X]([X]^T [X])^{-1} [X]^T$  is the projection matrix, or called hat matrix.

The residual  $R_i$  is equal to  $y_i - \hat{y}_i$ , the difference between the observed and fitted values.

$$\{R\} = \{y\} - \{\hat{y}\} = ([I] - [H])\{y\} \quad (D.7)$$

The covariance matrix for the estimated parameters  $\{\hat{A}\}$  is

$$V(\{\hat{A}\}) = ([X]^T [X])^{-1} s_v^2 \quad (D.8)$$

For the fitted response variables  $\{\hat{y}\}$  is

$$V(\{\hat{y}\}) = [H] s_v^2 \quad (D.9)$$

and for the residual  $\{R\}$  is

$$V(\{R\}) = ([I] - [H]) s_v^2 \quad (D.10)$$

This gives the minimum sum of squares

$$S_{\min} = \{R\}^T \{R\} \quad (D.11)$$

and the standard deviation of residual

$$std = \sqrt{S_{\min} / (n - m)} \quad (D.12)$$

where the rank of matrix  $[X]$  is  $m \leq n$ .

For a general model of Eqn. (D.2), there may be more than one minimum sum of squares. However, if the model is linear in the unknown parameters  $\{A\}$ , there can only be one minimum and a unique solution can be achieved.

## APPENDIX E Some Tables for Statistical Analysis

**Table E.1** Upper bound for critical values for standardized residual (after Lund 1975, Barnett and Lewis 1978)

10% critical values

$n \backslash m$	1	2	3	4	5	6	8	10	15	25
5	1.87									
6	2.00	1.89								
7	2.10	2.02	1.90							
8	2.18	2.12	2.03	1.91						
9	2.24	2.20	2.13	2.05	1.92					
10	2.30	2.26	2.21	2.15	2.06	1.92				
12	2.39	2.37	2.33	2.29	2.24	2.17	1.93			
14	2.47	2.45	2.42	2.39	2.36	2.32	2.19	1.94		
16	2.53	2.51	2.50	2.47	2.45	2.42	2.34	2.20		
18	2.58	2.57	2.56	2.54	2.52	2.50	2.44	2.35		
20	2.63	2.62	2.61	2.59	2.58	2.56	2.52	2.46	2.11	
25	2.72	2.72	2.71	2.70	2.69	2.68	2.66	2.63	2.50	
30	2.80	2.79	2.79	2.78	2.77	2.77	2.75	2.73	2.66	2.13
35	2.86	2.85	2.85	2.85	2.84	2.84	2.82	2.81	2.77	2.55
40	2.91	2.91	2.90	2.90	2.90	2.89	2.88	2.87	2.84	2.72
45	2.95	2.95	2.95	2.95	2.94	2.94	2.93	2.93	2.90	2.82
50	2.99	2.99	2.99	2.99	2.98	2.98	2.98	2.97	2.95	2.89
60	3.06	3.06	3.05	3.05	3.05	3.05	3.05	3.04	3.03	3.00
70	3.11	3.11	3.11	3.11	3.11	3.11	3.10	3.10	3.09	3.07
80	3.16	3.16	3.16	3.15	3.15	3.15	3.15	3.15	3.14	3.12
90	3.20	3.20	3.19	3.19	3.19	3.19	3.19	3.19	3.18	3.17
100	3.23	3.23	3.23	3.23	3.23	3.23	3.23	3.22	3.22	3.21

5% critical values

$n \backslash m$	1	2	3	4	5	6	8	10	15	25
5	1.92									
6	2.07	1.93								
7	2.19	2.08	1.94							
8	2.28	2.20	2.10	1.94						
9	2.35	2.29	2.21	2.10	1.95					
10	2.42	2.37	2.31	2.22	2.11	1.95				
12	2.52	2.49	2.45	2.39	2.33	2.24	1.96			
14	2.61	2.58	2.55	2.51	2.47	2.41	2.25	1.96		
16	2.68	2.66	2.63	2.60	2.57	2.53	2.43	2.26		
18	2.73	2.72	2.70	2.68	2.65	2.62	2.55	2.44		
20	2.78	2.77	2.76	2.74	2.72	2.70	2.64	2.57	2.15	
25	2.89	2.88	2.87	2.86	2.84	2.83	2.80	2.76	2.60	
30	2.96	2.96	2.95	2.94	2.93	2.93	2.90	2.88	2.79	2.17
35	3.03	3.02	3.02	3.01	3.00	3.00	2.98	2.97	2.91	2.64
40	3.08	3.08	3.07	3.07	3.06	3.06	3.05	3.03	3.00	2.84



**Table E.1** 5% critical values continued:

$\begin{matrix} m \\ n \end{matrix}$	1	2	3	4	5	6	8	10	15	25
45	3.13	3.12	3.12	3.12	3.11	3.11	3.10	3.09	3.06	2.96
50	3.17	3.16	3.16	3.16	3.15	3.15	3.14	3.14	3.11	3.04
60	3.23	3.23	3.23	3.23	3.22	3.22	3.22	3.21	3.20	3.15
70	3.29	3.29	3.28	3.28	3.28	3.28	3.27	3.27	3.26	3.23
80	3.33	3.33	3.33	3.33	3.33	3.33	3.32	3.32	3.31	3.29
90	3.37	3.37	3.37	3.37	3.37	3.37	3.36	3.36	3.36	3.34
100	3.41	3.41	3.40	3.40	3.40	3.40	3.40	3.40	3.39	3.38

1% critical values

$\begin{matrix} m \\ n \end{matrix}$	1	2	3	4	5	6	8	10	15	25
5	1.98									
6	2.17	1.98								
7	2.32	2.17	1.98							
8	2.44	2.32	2.18	1.98						
9	2.54	2.44	2.33	2.18	1.99					
10	2.62	2.55	2.45	2.33	2.18	1.99				
12	2.76	2.70	2.64	2.56	2.46	2.34	1.99			
14	2.86	2.82	2.78	2.72	2.65	2.57	2.35	1.99		
16	2.95	2.92	2.88	2.84	2.79	2.73	2.58	2.35		
18	3.02	3.00	2.97	2.94	2.90	2.85	2.75	2.59		
20	3.08	3.06	3.04	3.01	2.98	2.95	2.87	2.76	2.20	
25	3.21	3.19	3.18	3.16	3.14	3.12	3.07	3.01	2.75	
30	3.30	3.29	3.28	3.26	3.25	3.24	3.21	3.17	3.04	2.21
35	3.37	3.36	3.35	3.34	3.34	3.33	3.30	3.28	3.19	2.81
40	3.43	3.42	3.42	3.41	3.40	3.40	3.38	3.36	3.30	3.05
45	3.48	3.47	3.47	3.46	3.46	3.45	3.44	3.43	3.38	3.23
50	3.52	3.52	3.51	3.51	3.51	3.50	3.49	3.48	3.45	3.34
60	3.60	3.59	3.59	3.59	3.58	3.58	3.57	3.56	3.54	3.48
70	3.65	3.65	3.65	3.65	3.64	3.64	3.64	3.63	3.61	3.57
80	3.70	3.70	3.70	3.70	3.69	3.69	3.69	3.68	3.67	3.64
90	3.74	3.74	3.74	3.74	3.74	3.74	3.73	3.73	3.72	3.70
100	3.78	3.78	3.78	3.77	3.77	3.77	3.77	3.77	3.76	3.74

**Table E.2 *F* critical values**

<i>p</i> 0.10		Degrees of freedom for the numerator					
		1	2	3	4	5	6
Degrees of freedom for the denominator	1	39.86	49.50	53.59	55.83	57.24	58.20
	2	8.53	9.00	9.16	9.24	9.29	9.33
	3	5.54	5.46	5.39	5.34	5.31	5.28
	4	4.54	4.32	4.19	4.11	4.05	4.01
	5	4.06	3.78	3.62	3.52	3.45	3.40
	6	3.78	3.46	3.29	3.18	3.11	3.05
	7	3.59	3.26	3.07	2.96	2.88	2.83
	8	3.46	3.11	2.92	2.81	2.73	2.67
	9	3.36	3.01	2.81	2.69	2.61	2.55
	10	3.29	2.92	2.73	2.61	2.52	2.46
	11	3.23	2.86	2.66	2.54	2.45	2.39
	12	3.18	2.81	2.61	2.48	2.39	2.33
	13	3.14	2.76	2.56	2.43	2.35	2.28
	14	3.10	2.73	2.52	2.39	2.31	2.24
	15	3.07	2.70	2.49	2.36	2.27	2.21
	16	3.05	2.67	2.46	2.33	2.24	2.18
	17	3.03	2.64	2.44	2.31	2.22	2.15
	18	3.01	2.62	2.42	2.29	2.20	2.13
	19	2.99	2.61	2.40	2.27	2.18	2.11
	20	2.97	2.59	2.38	2.25	2.16	2.09
	21	2.96	2.57	2.36	2.23	2.14	2.08
	22	2.95	2.56	2.35	2.22	2.13	2.06
	23	2.94	2.55	2.34	2.21	2.11	2.05
	24	2.93	2.54	2.33	2.19	2.10	2.04
	25	2.92	2.53	2.32	2.18	2.09	2.02
	26	2.91	2.52	2.31	2.17	2.08	2.01
	27	2.90	2.51	2.30	2.17	2.07	2.00
	28	2.89	2.50	2.29	2.16	2.06	2.00
	29	2.89	2.50	2.28	2.15	2.06	1.99
	30	2.88	2.49	2.28	2.14	2.03	1.98
40	2.84	2.44	2.23	2.09	2.00	1.93	
60	2.79	2.39	2.18	2.04	1.95	1.87	

Table E.2 continued:

$p$ 0.05		Degrees of freedom for the numerator					
		1	2	3	4	5	6
Degrees of freedom for the denominator	1	161.4	199.50	215.7	224.6	230.2	234.0
	2	18.51	19.00	19.16	19.25	19.30	19.33
	3	10.13	9.55	9.28	9.12	9.01	8.94
	4	7.71	6.94	6.59	6.39	6.26	6.16
	5	6.61	5.79	5.41	5.19	5.05	4.95
	6	5.99	5.14	4.76	4.53	4.39	4.28
	7	5.59	4.74	4.35	4.12	3.97	3.87
	8	5.32	4.46	4.07	3.84	3.69	3.58
	9	5.12	4.26	3.86	3.63	3.48	3.37
	10	4.96	4.10	3.71	3.48	3.33	3.22
	11	4.84	3.98	3.59	3.36	3.20	3.09
	12	4.75	3.89	3.49	3.26	3.11	3.00
	13	4.67	3.81	3.41	3.18	3.03	2.92
	14	4.60	3.74	3.34	3.11	2.96	2.85
	15	4.54	3.68	3.29	3.06	2.90	2.79
	16	4.49	3.63	3.24	3.01	2.85	2.74
	17	4.45	3.59	3.20	2.96	2.81	2.70
	18	4.41	3.55	3.16	2.93	2.77	2.66
	19	4.38	3.52	3.13	2.90	2.74	2.63
	20	4.35	3.49	3.10	2.87	2.71	2.60
	21	4.32	3.47	3.07	2.84	2.68	2.57
	22	4.30	3.44	3.05	2.82	2.66	2.55
	23	4.28	3.42	3.03	2.80	2.64	2.53
	24	4.26	3.40	3.01	2.78	2.62	2.51
	25	4.24	3.39	2.99	2.76	2.60	2.49
	26	4.23	3.37	2.98	2.74	2.59	2.47
	27	4.21	3.35	2.96	2.73	2.57	2.46
	28	4.20	3.34	2.95	2.71	2.56	2.45
	29	4.18	3.33	2.93	2.70	2.55	2.43
	30	4.17	3.32	2.92	2.69	2.53	2.42
40	4.08	3.23	2.84	2.61	2.45	2.34	
60	4.00	3.15	2.76	2.53	2.37	2.25	

## APPENDIX F Stresses in 2D

For the stress components  $(\sigma_x, \sigma_y)$  in the  $xy$  plane as in Figure F.1, the stress components in  $x'$  direction (rotated  $\theta$  angle from  $x$ ),  $\sigma$  and  $\tau$  are given (Zou 2015)

$$\begin{cases} \sigma = \sigma_x \cos^2 \theta + \sigma_y \sin^2 \theta + \tau_{xy} \sin 2\theta \\ \tau = -\frac{1}{2}(\sigma_x - \sigma_y) \sin 2\theta + \tau_{xy} \cos 2\theta \end{cases} \quad (\text{F.1})$$

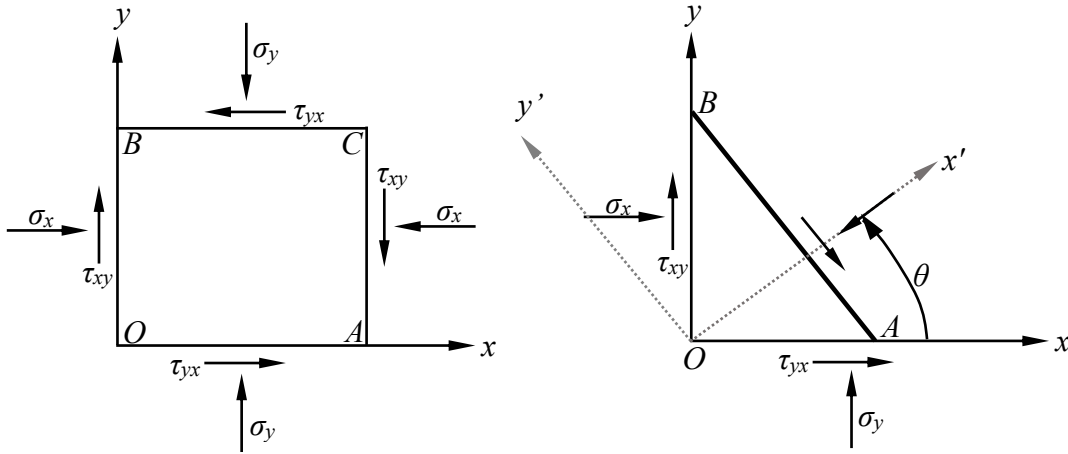


Figure F.1 2D stress definition and stress in an arbitrary direction

The principal stresses  $\sigma_{Hmax}$ ,  $\sigma_{Hmin}$  are given as

$$\sigma_{Hmax, Hmin} = \frac{\sigma_x + \sigma_y}{2} \pm \sqrt{\left(\frac{\sigma_x - \sigma_y}{2}\right)^2 + \tau_{xy}^2} \quad (\text{F.2})$$

And the orientation of  $\sigma_{Hmax}$

$$\theta^* = \frac{1}{2} \cdot \text{tg}^{-1}\left(\frac{2\tau_{xy}}{\sigma_x - \sigma_y}\right) \quad (\text{F.3})$$

$\theta^*$  is measured from  $x$  counter clockwise. If  $x'$  is rotated  $\theta$  angle from  $x$ , (counter clockwise positive), the stress rotation from  $(\sigma_x, \sigma_y, \tau_{xy})$  to  $(\sigma_{x'}, \sigma_{y'}, \tau_{x'y'})$  is carried out

$$\begin{cases} \sigma_{x'} = \sigma_x \cos^2 \theta + \sigma_y \sin^2 \theta + \tau_{xy} \sin 2\theta \\ \sigma_{y'} = \sigma_x \sin^2 \theta + \sigma_y \cos^2 \theta - \tau_{xy} \sin 2\theta \\ \tau_{x'y'} = -\frac{1}{2}(\sigma_x - \sigma_y) \sin 2\theta + \tau_{xy} \cos 2\theta \end{cases} \quad (\text{F.4})$$

## APPENDIX G Principal Stresses and Orientations in 3D

### Magnitudes of principal stresses in 3D

For the stress components in the  $xyz$  coordinate system ( $\sigma_x, \sigma_y, \sigma_z, \tau_{xy}, \tau_{yz}, \tau_{zx}$ ) in Figure G.1a, the stress components across a plane ABC (the  $\vec{n}$  direction is defined in Figure H.1b),  $p_x$ ,  $p_y$  and  $p_z$  are given as

$$\begin{Bmatrix} p_x \\ p_y \\ p_z \end{Bmatrix} = \begin{bmatrix} \sigma_x & \tau_{xy} & \tau_{xz} \\ \tau_{yx} & \sigma_y & \tau_{yz} \\ \tau_{zx} & \tau_{zy} & \sigma_z \end{bmatrix} \begin{Bmatrix} l \\ m \\ n \end{Bmatrix} \quad (\text{G.1})$$

where  $(l, m, n)$  are the direction cosine of  $\vec{n}$  with respect to axes  $(x, y, z)$  respectively.

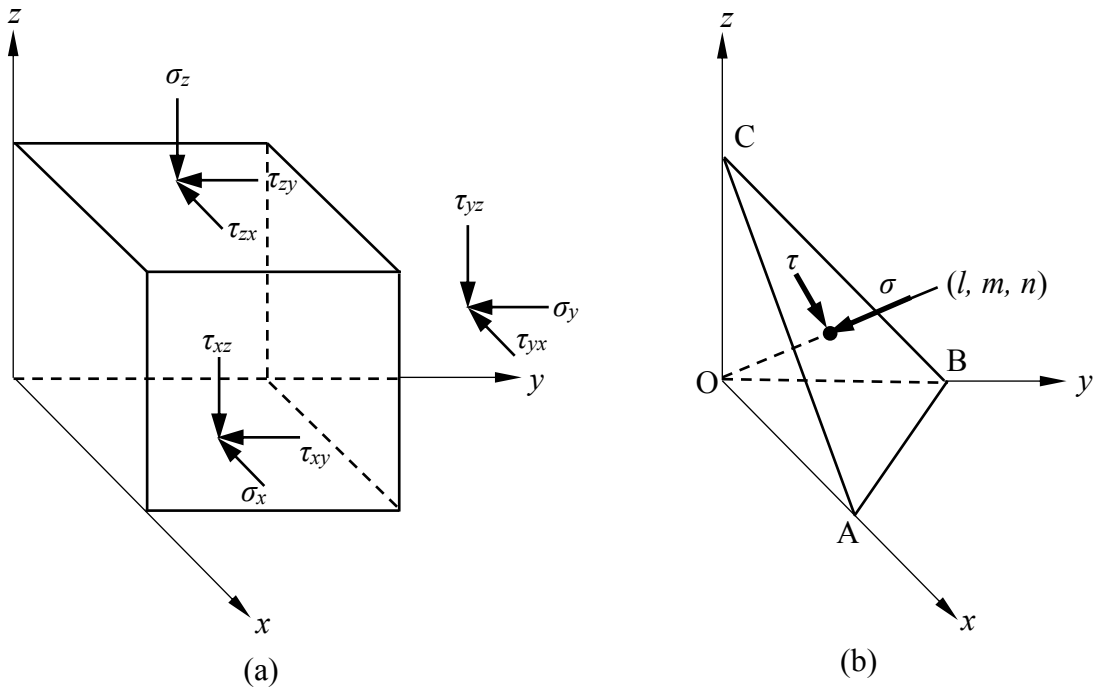


Figure G.1 3D stress definition and stress in an arbitrary plane

The magnitude of the resultant stress on this plane is

$$p = \sqrt{p_x^2 + p_y^2 + p_z^2} \quad (\text{G.2})$$

The principal stress components of the stress tensor can be obtained by solving this equation

$$\begin{bmatrix} (\sigma_x - \sigma) & \tau_{xy} & \tau_{xz} \\ \tau_{yx} & (\sigma_y - \sigma) & \tau_{yz} \\ \tau_{zx} & \tau_{zy} & (\sigma_z - \sigma) \end{bmatrix} \begin{Bmatrix} l \\ m \\ n \end{Bmatrix} = \begin{Bmatrix} 0 \\ 0 \\ 0 \end{Bmatrix} \quad (\text{G.3})$$

Eq. (G.3) has a non-zero solution only if  $\sigma$  is a root of

$$\begin{vmatrix} (\sigma_x - \sigma) & \tau_{xy} & \tau_{xz} \\ \tau_{yx} & (\sigma_y - \sigma) & \tau_{yz} \\ \tau_{zx} & \tau_{zy} & (\sigma_z - \sigma) \end{vmatrix} = 0 \quad (\text{G.4})$$

This leads to

$$\sigma^3 + I_1\sigma^2 + I_2\sigma + I_3 = 0 \quad (\text{G.5})$$

where  $I_1$ ,  $I_2$ ,  $I_3$  are the stress invariants:

$$\begin{cases} I_1 = -(\sigma_x + \sigma_y + \sigma_z) \\ I_2 = \sigma_x\sigma_y + \sigma_x\sigma_z + \sigma_y\sigma_z - \tau_{xy}^2 - \tau_{yz}^2 - \tau_{zx}^2 \\ I_3 = -(\sigma_x\sigma_y\sigma_z - \sigma_x\tau_{yz}^2 - \sigma_y\tau_{xz}^2 - \sigma_z\tau_{xy}^2 + 2\tau_{xy}\tau_{yz}\tau_{xz}) \end{cases} \quad (\text{G.6})$$

and the three roots  $\sigma_1$ ,  $\sigma_2$ ,  $\sigma_3$  are the principal stress components.

The analytical solution of Eqn. (G.5) is given in Appendix H. It should be noted that since the values of  $I_1$ ,  $I_2$ ,  $I_3$  are very large, it can cause unexpected computational errors during the calculation of the cubic root. It is advised to scale the six stress components before solving Eqn. (G.5). Scaling can be done by dividing the six components ( $\sigma_x$ ,  $\sigma_y$ ,  $\sigma_z$ ,  $\tau_{xy}$ ,  $\tau_{yz}$ ,  $\tau_{zx}$ ) by a large constant  $c$ , which can be

$$c = \sqrt{\sigma_x^2 + \sigma_y^2 + \sigma_z^2 + \tau_{xy}^2 + \tau_{yz}^2 + \tau_{zx}^2} \quad (\text{G.7a})$$

$$\text{or } c = |\sigma_x| + |\sigma_y| + |\sigma_z| + |\tau_{xy}| + |\tau_{yz}| + |\tau_{zx}| \quad (\text{G.7b})$$

If  $(\sigma_1^*, \sigma_2^*, \sigma_3^*)$  are the cubic roots after scaling, the real roots will be

$$\sigma_i = c\sigma_i^* \quad i=1,2,3 \quad (\text{G.8})$$

## Orientations of principal stresses in 3D

If a stress tensor is given as principal components

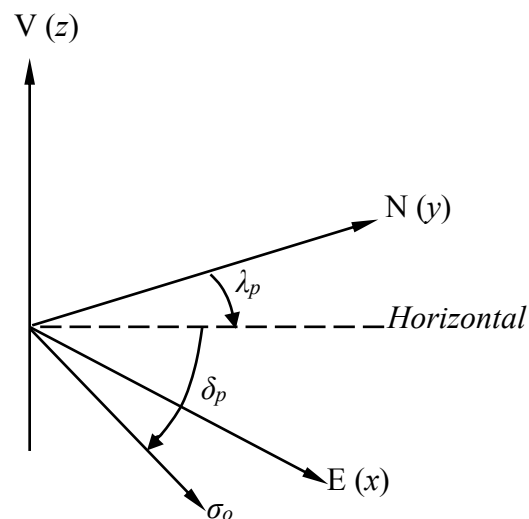
$$[\sigma_o] = \begin{bmatrix} \sigma_1 & 0 & 0 \\ 0 & \sigma_2 & 0 \\ 0 & 0 & \sigma_3 \end{bmatrix} \quad (\text{G.9})$$

With the orientation  $(\lambda_{pi}, \delta_{pi})$  of  $\sigma_i$ , ( $i=1,2,3$ ), it can be transformed to the  $xyz$  system. In this work, a coordinate system  $x, y, z$  is set to coincide with the global coordinates E, N, V.

The orientation of this stress tensor  $[\sigma_o]$  is defined by its trend  $\lambda_p$  (measured in the horizontal plane, positive clockwise from North when looking down) and plunge  $\delta_p$  (measured positive downwards from the horizontal plane) as in Figure G.2, the direction cosines can be related to  $\lambda_p$  and  $\delta_p$ .

$$\begin{cases} l = \cos \delta_p \sin \lambda_p \\ m = \cos \delta_p \cos \lambda_p \\ n = -\sin \delta_p \end{cases} \quad (\text{G.10})$$

The negative sign of  $n$  means positive  $\sigma$  points downwards.



$\lambda_p$  is the trend from North and  $\delta_p$  is the plunge positive down

**Figure G.2** Principal stress orientation

$[\sigma_o]$  is transformed into ENV system by

$$[\sigma]_{ENV} = [L_s]^T [\sigma_o] [L_s] \quad (G.11)$$

where  $[L_s]$  is the direction cosine matrix of  $(\sigma_1, \sigma_2, \sigma_3)$  with respect to the East, North and Vertical\_up axes from Eqn. (G.12).

$$[L_s] = \begin{matrix} & \begin{matrix} E & N & V \end{matrix} \\ \begin{matrix} \sigma_1 \\ \sigma_2 \\ \sigma_3 \end{matrix} & \begin{bmatrix} \cos \delta_{p1} \sin \lambda_{p1} & \cos \delta_{p1} \cos \lambda_{p1} & -\sin \delta_{p1} \\ \cos \delta_{p2} \sin \lambda_{p2} & \cos \delta_{p2} \cos \lambda_{p2} & -\sin \delta_{p2} \\ \cos \delta_{p3} \sin \lambda_{p3} & \cos \delta_{p3} \cos \lambda_{p3} & -\sin \delta_{p3} \end{bmatrix} \end{matrix} \quad (G.12)$$

The direction cosines  $(l_i, m_i, n_i)$  of the principal axis corresponding to the principal stress  $\sigma_i$  is obtained by any two equations of Eqn. (G.3) replacing  $\sigma$  by  $\sigma_i$ .

e.g., using the 1st and the 2nd equations:

$$l_i = \pm C_1 / C, \quad m_i = \pm C_2 / C, \quad n_i = \pm C_3 / C \quad (G.13)$$

$$\text{where } C_1 = \begin{vmatrix} \tau_{xy} & \tau_{xz} \\ (\sigma_y - \sigma_i) & \tau_{yz} \end{vmatrix} \quad (G.14a)$$

$$C_2 = \begin{vmatrix} (\sigma_x - \sigma_i) & \tau_{xz} \\ \tau_{yx} & \tau_{yz} \end{vmatrix} \quad (G.14b)$$

$$C_3 = \begin{vmatrix} (\sigma_x - \sigma_i) & \tau_{xy} \\ \tau_{yx} & (\sigma_y - \sigma_i) \end{vmatrix} \quad (G.14c)$$

Either one of the two pairs of solutions is valid.

Then  $\lambda$  and  $\delta$  can be determined from  $(l, m, n)$

$$\left\{ \begin{array}{l} \delta = \sin^{-1}(-n) \frac{180}{\pi} \quad \delta \in [-90^\circ, 90^\circ] \\ \lambda = \begin{cases} \cos^{-1}\left(\frac{m}{\cos \delta}\right) \frac{180}{\pi} & \text{if } l > 0, \lambda \in [0, 180^\circ] \\ -\cos^{-1}\left(\frac{m}{\cos \delta}\right) \frac{180}{\pi} & \text{if } l < 0, \lambda \in [-180^\circ, 0] \end{cases} \end{array} \right. \quad (G.15)$$



Since  $\lambda$  and  $\delta$  from Eqn. (G.15) can be both positive and negative, it is necessary to adjust their values so that  $\delta > 0$  always holds and  $\lambda$  is changed accordingly

$$\begin{cases} \delta = |\delta| \\ \lambda = \begin{cases} \lambda & \text{if } \delta \geq 0 \text{ and } \lambda \geq 0, \\ \lambda + 360^\circ & \text{if } \delta \geq 0 \text{ and } \lambda < 0, \\ \lambda + 180^\circ & \text{if } \delta < 0 \end{cases} \end{cases} \quad (\text{G.16})$$

## APPENDIX H Analytical Solution to a Cubic Equation

From mathematics manual, it is known that

$$\text{if } x^3 - 1 = 0 \quad (\text{H.1})$$

$$\text{then } \begin{cases} x_1 = 1 \\ x_2 = \omega_1 = \frac{-1 + \sqrt{3}i}{2} \\ x_3 = \omega_2 = \frac{-1 - \sqrt{3}i}{2} \end{cases} \quad (\text{H.2})$$

$$\text{if } x^3 + ax^2 + bx + c = 0 \quad (\text{H.3})$$

a variable transformation is needed.

$$\text{let } x = y - a/3 \quad (\text{H.4})$$

$$\text{Eqn. (H.3) becomes } y^3 + py + q = 0 \quad (\text{H.5})$$

$$\text{where } \begin{cases} p = b - \frac{a^2}{3} \\ q = \frac{2}{27}a^3 - \frac{ab}{3} + c \end{cases} \quad (\text{H.6})$$

$$\text{If } \begin{cases} f = \left(\frac{q}{2}\right)^2 + \left(\frac{p}{3}\right)^3 \\ A = \sqrt[3]{-\frac{q}{2} + \sqrt{f}} \\ B = \sqrt[3]{-\frac{q}{2} - \sqrt{f}} \end{cases} \quad (\text{H.7})$$

The standard solution to Eqn. (H.5) is

$$\begin{cases} y_1 = A + B \\ y_2 = -\frac{A+B}{2} + \frac{A-B}{2}\sqrt{3}i \\ y_3 = -\frac{A+B}{2} - \frac{A-B}{2}\sqrt{3}i \end{cases} \quad (\text{H.8})$$

and the solution to Eqn. (H.3) is obtained by Eqn. (H.4). It can be seen from Eqn. (H.8) that:

if  $f > 0$ , there are one real root and two complex roots;

if  $f = 0$ , then  $A = B = \sqrt[3]{-q/2}$  and there are three real roots with two equal:

$$\begin{cases} y_1 = 2A \\ y_2 = -A \\ y_3 = -A \end{cases} \quad (\text{H.9})$$

(if  $p=q=0$ , all roots are zero);

if  $f < 0$ , there are three unequal real roots. By Eqn. (H.7) we define a complex variable  $z$

$$z = -q/2 + \sqrt{|f|}i = r(\cos \theta_z + i \sin \theta_z) \quad (\text{H.10})$$

$$\text{where } r = \sqrt{\left(-\frac{q}{2}\right)^2 + |f|} \quad \text{and} \quad \theta = \text{tg}^{-1}\left(-\frac{\sqrt{|f|}}{q/2}\right) \quad (\text{H.11})$$

$$\text{then } \begin{cases} A = \sqrt[3]{z} = \sqrt[3]{r} \left( \cos \frac{\theta_z + 2k\pi}{3} + i \sin \frac{\theta_z + 2k\pi}{3} \right) \\ B = \sqrt[3]{\bar{z}} = \sqrt[3]{r} \left( \cos \frac{-\theta_z + 2k\pi}{3} + i \sin \frac{-\theta_z + 2k\pi}{3} \right) \end{cases} \quad (\text{H.12})$$

$$\begin{aligned}
A + B &= \sqrt[3]{z} + \sqrt[3]{\bar{z}} \\
&= \sqrt[3]{r} \left[ \cos \frac{\theta_z + 2k\pi}{3} + \cos \frac{-\theta_z + 2k\pi}{3} + i \left( \sin \frac{\theta_z + 2k\pi}{3} + \sin \frac{-\theta_z + 2k\pi}{3} \right) \right]
\end{aligned}$$

Since  $A + B$  is one of the roots and must be real,  $k$  must be zero.

$$A + B = \sqrt[3]{r} \left( \cos \frac{\theta_z}{3} + \cos \frac{-\theta_z}{3} \right) = 2\sqrt[3]{r} \cos \frac{\theta_z}{3} \quad (\text{H.13})$$

Similarly,

$$\begin{aligned}
A - B &= \sqrt[3]{z} - \sqrt[3]{\bar{z}} \\
&= \sqrt[3]{r} \left( \cos \frac{\theta_z}{3} + i \sin \frac{\theta_z}{3} - \cos \frac{-\theta_z}{3} - i \sin \frac{-\theta_z}{3} \right) \\
&= 2\sqrt[3]{r} i \sin \frac{\theta_z}{3}
\end{aligned} \quad (\text{H.14})$$

By Eqn. (H.8)

$$\begin{cases}
y_1 = 2\sqrt[3]{r} \cos \frac{\theta_z}{3} \\
y_2 = -\sqrt[3]{r} \left( \cos \frac{\theta_z}{3} + \sqrt{3} \sin \frac{\theta_z}{3} \right) \\
y_3 = \sqrt[3]{r} \left( -\cos \frac{\theta_z}{3} + \sqrt{3} \sin \frac{\theta_z}{3} \right)
\end{cases} \quad (\text{H.15})$$

where  $r$  and  $\theta_z$  are given by Eqn. (H.11). Eqn. (H.15) is applicable to the case of  $f < 0$  or  $f = 0$ . If  $f > 0$ , Eqn. (H.8) has to be used.

## APPENDIX I Results of Back-analyzed 3D In-situ Principal Stresses

**Table I.1** Results of 3D back-analyzed in-situ principal stresses from two well sections or boreholes (the 2<sup>nd</sup> combination)

In-situ principal stresses		$\sigma_1$	$\sigma_2$	$\sigma_3$
Combination: $I = 0, \beta = 0; I = 50^\circ, \beta = 45^\circ$				
Scenario 1: NP; scenario 2: HPR and PW; scenario 3: HPR and IPW				
Back-analyzed	Magnitude [MPa]	60.19	32.44	25.38
	Plunge [°]	28.2	88.4	67.2
	Trend [°]	288.8	255.0	79.6
Differences with the applied stresses	Magnitude [%]	-16.7%	-33.0%	-24.6%
	Plunge [°]	-28.2	78.1	35.6
	Trend [°]	274.3	134.6	-137.2
Scenario 4: LPR and PW; scenario 5: LPR and IPW				
Back-analyzed	Magnitude [MPa]	62.81	2.29	-3.10
	Plunge [°]	11.1	39.6	48.7
	Trend [°]	273.6	275.6	278.4
Differences with the applied stresses	Magnitude [%]	-13.1%	-95.3%	-109.2%
	Plunge [°]	-45.3	29.3	17.1
	Trend [°]	259.1	155.2	61.6

**Table I.2** Results of 3D back-analyzed in-situ principal stresses from two well sections or boreholes (the 3<sup>rd</sup> combination)

In-situ principal stresses		$\sigma_1$	$\sigma_2$	$\sigma_3$
Combination: $I = 0, \beta = 0; I = 75^\circ, \beta = 45^\circ$				
Scenario 1: NP; scenario 2: HPR and PW; scenario 3: HPR and IPW				
Back-analyzed	Magnitude [MPa]	126.44	9.63	-58.06
	Plunge [°]	34.4	19.9	54.8
	Trend [°]	241.8	312.8	20.4
Differences with the applied stresses	Magnitude [%]	75.0%	-80.1%	-272.6%
	Plunge [°]	-22.0	9.6	23.2
	Trend [°]	227.3	192.4	-196.4
Scenario 4: LPR and PW; scenario 5: LPR and IPW				
Back-analyzed	Magnitude [MPa]	No solution		
	Plunge [°]			
	Trend [°]			
Differences with the applied stresses	Magnitude [%]			
	Plunge [°]			
	Trend [°]			

**Table I.3** Results of  $([M_{3Dcon}]_{com}^T [M_{3Dcon}]_{com})^{-1} ([M_{3Dcon}]_{com}^T [M_{3Dcon}]_{com})$  from two well sections or boreholes (the 1<sup>st</sup> combination)

Scenarios 1, 2 and 3					
0.25	0.59	-0.02	0.38	0.22	0.00
-1.00	1.47	0.02	0.50	0.19	-0.25
-4.00	2.50	0.88	3.00	0.75	0.00
-0.05	0.05	0.00	1.01	0.02	-0.01
0.38	-0.81	0.02	-0.75	0.72	0.00
0.38	-0.50	0.02	-0.75	-0.25	0.88
Scenarios 4 and 5					
No solution					

**Table I.4** Results of  $([M_{3Dcon}]_{com}^T [M_{3Dcon}]_{com})^{-1} ([M_{3Dcon}]_{com}^T [M_{3Dcon}]_{com})$  from two well sections or boreholes (the 2<sup>nd</sup> combination)

Scenarios 1, 2 and 3					
1.06	-0.19	0.00	-0.03	-0.41	0.00
0.13	0.94	-0.06	-0.22	-0.55	0.13
-0.50	-0.50	0.00	-2.50	-4.25	0.00
0.03	-0.03	-0.03	0.96	-0.08	-0.01
0.00	0.25	0.00	0.38	1.69	-0.50
0.00	0.38	-0.13	0.25	0.94	0.50
Scenarios 4 and 5					
1.00	-0.13	0.03	-0.03	-0.07	0.06
-0.09	0.94	0	-0.02	0.04	-0.13
-0.5	-0.25	0.5	-0.125	0.3125	0
0	0	0.01	1.01	0.03	0
0.25	0.13	0.13	-0.13	0.77	0.25
0.13	0.19	0.13	-0.13	-0.30	1

**Table I.5** Results of  $([M_{3Dcon}]_{com}^T [M_{3Dcon}]_{com})^{-1} ([M_{3Dcon}]_{com}^T [M_{3Dcon}]_{com})$  from two well sections or boreholes (the 3<sup>rd</sup> combination)

Scenarios 1, 2 and 3					
1.03	0.03	-0.09	0.00	-0.06	0.00
0.02	1.00	-0.13	-0.02	-0.25	0.13
0.00	-0.25	0.50	0.19	0.00	1.00
0.00	0.00	0.00	1.00	0.00	0.00
0.00	0.00	0.75	0.00	1.00	0.00
0.00	0.00	0.50	-0.06	0.00	1.00
Scenarios 4 and 5					
No solution					

**Table I.6** Random errors with 6 measurements for different maximum error

Section	Measurement angles	Maximum errors in %						
	$\theta$ [°]	10%	15%	20%	25%	30%	40%	50%
1	0	-8.9%	-2.6%	-6.0%	11.8%	13.6%	-17.6%	-46.1%
	30	0.7%	-6.8%	-16.8%	-4.8%	24.0%	-36.0%	-11.7%
	60	-0.6%	-9.9%	15.1%	-14.4%	4.1%	-7.5%	31.2%
	90	-6.4%	8.2%	3.0%	22.6%	9.0%	2.0%	42.1%
	120	-0.2%	7.3%	-10.3%	23.6%	-1.1%	-7.1%	49.5%
	150	-5.3%	5.1%	-0.1%	-24.3%	-21.7%	-7.0%	-29.5%
2	0	-7.7%	14.3%	-11.7%	-19.5%	-3.0%	-15.1%	-16.0%
	30	-3.6%	9.5%	15.2%	14.9%	-10.8%	-7.2%	-18.5%
	60	-2.2%	-7.3%	4.7%	1.4%	28.6%	27.1%	25.6%
	90	5.3%	-4.0%	-4.3%	12.1%	18.8%	17.8%	-0.9%
	120	5.4%	-7.5%	6.0%	11.7%	8.0%	-31.9%	-28.0%
	150	7.3%	-5.5%	-0.9%	-14.9%	7.7%	-22.1%	-24.4%
3	0	9.6%	4.7%	2.1%	12.8%	25.6%	-1.6%	-35.3%
	30	4.6%	-8.3%	18.6%	12.4%	12.6%	-2.1%	5.7%
	60	7.7%	-10.4%	12.9%	-4.7%	-22.3%	-12.5%	-15.1%
	90	-6.8%	-7.4%	-14.2%	-4.2%	-25.3%	-28.2%	36.0%
	120	-1.8%	-6.4%	-2.5%	24.0%	21.9%	16.8%	2.4%
	150	0.7%	1.6%	-19.9%	7.5%	-22.9%	-2.6%	-26.8%

**Table I.7** Random errors with different number of measurements (maximum error in input data 20%)

No. of measurement			No. of measurement			No. of measurement			No. of measurement		
Sec.	3		Sec.	6		Sec.	9		Sec.	12	
1	0	-6.0%	1	0	-6.0%	1	0	-6.0%	1	0	-6.0%
	60	15.1%		30	-16.8%		20	-7.9%		15	-7.9%
	120	-10.3%		60	15.1%		40	3.3%		30	-16.8%
2	0	-11.7%		90	3.0%		60	15.1%		45	3.3%
	60	4.7%		120	-10.3%		80	16.4%		60	15.1%
	120	6.0%		150	-0.1%		100	-6.0%		75	16.4%
3	0	2.1%	2	0	-11.7%		120	-10.3%		90	3.0%
	60	12.9%		30	15.2%		140	1.2%		105	-6.0%
	120	-2.5%		60	4.7%		160	-5.8%		120	-10.3%
				90	-4.3%	2	0	-11.7%		135	1.2%
				120	6.0%		20	17.8%		150	-0.1%
				150	-0.9%		40	13.4%		165	-5.8%
			3	0	2.1%		60	4.7%	2	0	-11.7%
				30	18.6%		80	-11.3%		15	17.8%
				60	12.9%		100	7.1%		30	15.2%
				90	-14.2%		120	6.0%		45	13.4%
				120	-2.5%		140	-9.9%		60	4.7%
				150	-19.9%		160	9.4%		75	-11.3%
						3	0	2.1%		90	-4.3%
							20	-10.6%		105	7.1%
							40	15.5%		120	6.0%
							60	12.9%		135	-9.9%
							80	20.0%		150	-0.9%
							100	-19.3%		165	9.4%
							120	-2.5%	3	0	2.1%
							140	-18.0%		15	-10.6%
							160	4.4%		30	18.6%
										45	15.5%
										60	12.9%
										75	20.0%
										90	-14.2%
										105	-19.3%
										120	-2.5%
										135	-18.0%
										150	-19.9%
										165	4.4%



**Table I.8** Back-analyzed 3D in-situ principal stresses with various random errors in input data for scenario 1 (Inclination angle interval 50°. 6 measurements per section)

3D in-situ principal stresses		$\sigma_1$	$\sigma_2$	$\sigma_3$
10%				
Back-analyzed	Magnitude [MPa]	65.8	45.5	33.7
	Plunge [°]	51.3	17.8	33.1
	Trend [°]	360.0	113.6	215.6
Differences with the applied stresses	Magnitude [%]	-8.9%	-6.1%	0.1%
	Plunge [°]	-5.1	7.5	1.5
	Trend [°]	345.5	-6.8	-1.2
15%				
Back-analyzed	Magnitude [MPa]	68.98	49.15	31.87
	Plunge [°]	54.6	13.7	31.9
	Trend [°]	10.3	120.3	219.0
Differences with the applied stresses	Magnitude [%]	-4.5%	1.5%	-5.3%
	Plunge [°]	-1.8	3.4	0.4
	Trend [°]	-4.2	-0.1	2.2
20%				
Back-analyzed	Magnitude [MPa]	69.36	45.01	32.93
	Plunge [°]	51.1	13.3	35.8
	Trend [°]	357.0	104.0	203.9
Differences with the applied stresses	Magnitude [%]	-4.0%	-7.1%	-2.1%
	Plunge [°]	-5.4	3.0	4.2
	Trend [°]	342.5	-16.4	-12.9
25%				
Back-analyzed	Magnitude [MPa]	63.08	44.60	35.06
	Plunge [°]	45.9	23.5	34.9
	Trend [°]	350.5	107.0	214.6
Differences with the applied stresses	Magnitude [%]	-12.7%	-7.9%	4.2%
	Plunge [°]	-10.6	13.2	3.3
	Trend [°]	335.9	-13.4	-2.2
30%				
Back-analyzed	Magnitude [MPa]	61.38	46.74	32.20
	Plunge [°]	39.8	9.0	49.0
	Trend [°]	8.3	104.1	203.8
Differences with the applied stresses	Magnitude [%]	-15.0%	-3.5%	-4.3%
	Plunge [°]	-16.6	-1.3	17.4
	Trend [°]	-6.3	-16.3	-13.0
40%				
Back-analyzed	Magnitude [MPa]	48.80	37.16	30.75
	Plunge [°]	32.7	27.0	45.1
	Trend [°]	331.8	81.0	201.7
Differences with the applied stresses	Magnitude [%]	-32.4%	-23.3%	-8.6%
	Plunge [°]	-23.7	16.7	13.5
	Trend [°]	317.3	-39.4	-15.1
50%				
Back-analyzed	Magnitude [MPa]	80.60	34.83	32.62
	Plunge [°]	51.0	38.7	3.6
	Trend [°]	351.4	164.0	256.9
Differences with the applied stresses	Magnitude [%]	11.6%	-28.1%	-3.1%
	Plunge [°]	-5.4	28.5	-27.9
	Trend [°]	336.9	43.6	40.1

**Table I.9** Back-analyzed 3D in-situ principal stresses with various random errors in input data for scenario 2 (Inclination angle interval 50°. 6 measurements per section)

3D in-situ principal stresses		$\sigma_1$	$\sigma_2$	$\sigma_3$
10%				
Back-analyzed	Magnitude [MPa]	70.54	47.64	33.68
	Plunge [°]	55.3	12.4	31.9
	Trend [°]	10.2	118.6	216.4
Differences with the applied stresses	Magnitude [%]	-2.4%	-1.6%	0.1%
	Plunge [°]	-1.1	2.1	0.3
	Trend [°]	-4.4	-1.8	-0.4
15%				
Back-analyzed	Magnitude [MPa]	70.54	49.06	33.08
	Plunge [°]	55.6	11.9	31.7
	Trend [°]	12.8	120.7	218.2
Differences with the applied stresses	Magnitude [%]	-2.3%	1.3%	-1.7%
	Plunge [°]	-0.8	1.6	0.1
	Trend [°]	-1.8	0.3	1.4
20%				
Back-analyzed	Magnitude [MPa]	72.48	46.79	33.69
	Plunge [°]	54.1	12.3	33.1
	Trend [°]	5.3	112.9	211.1
Differences with the applied stresses	Magnitude [%]	0.3%	-3.4%	0.1%
	Plunge [°]	-2.3	2.0	1.6
	Trend [°]	-9.2	-7.5	-5.7
25%				
Back-analyzed	Magnitude [MPa]	70.23	47.27	34.07
	Plunge [°]	52.8	14.9	33.1
	Trend [°]	4.8	115.4	215.4
Differences with the applied stresses	Magnitude [%]	-2.8%	-2.4%	1.3%
	Plunge [°]	-3.6	4.6	1.6
	Trend [°]	-9.7	-5.0	-1.4
30%				
Back-analyzed	Magnitude [MPa]	70.23	48.16	33.42
	Plunge [°]	51.6	10.0	36.7
	Trend [°]	13.2	116.1	213.6
Differences with the applied stresses	Magnitude [%]	-2.8%	-0.6%	-0.7%
	Plunge [°]	-4.9	-0.3	5.1
	Trend [°]	-1.3	-4.3	-3.2
40%				
Back-analyzed	Magnitude [MPa]	62.04	44.23	32.56
	Plunge [°]	52.0	16.6	33.1
	Trend [°]	1.2	113.6	214.8
Differences with the applied stresses	Magnitude [%]	-14.1%	-8.7%	-3.2%
	Plunge [°]	-4.4	6.3	1.5
	Trend [°]	-13.3	-6.8	-2.0
50%				
Back-analyzed	Magnitude [MPa]	80.30	42.28	34.05
	Plunge [°]	52.7	16.8	32.2
	Trend [°]	3.4	116.8	217.8
Differences with the applied stresses	Magnitude [%]	11.2%	-12.7%	1.2%
	Plunge [°]	-3.7	6.5	0.6
	Trend [°]	-11.1	-3.6	1.0

**Table I.10** Back-analyzed 3D in-situ principal stresses with various random errors in input data for scenario 3 (Inclination angle interval 50°. 6 measurements per section)

3D in-situ principal stresses		$\sigma_1$	$\sigma_2$	$\sigma_3$
10%				
Back-analyzed	Magnitude [MPa]	70.69	47.69	33.68
	Plunge [°]	55.4	12.2	31.8
	Trend [°]	10.4	118.7	216.5
Differences with the applied stresses	Magnitude [%]	-2.1%	-1.5%	0.1%
	Plunge [°]	-1.0	1.9	0.2
	Trend [°]	-4.1	-1.7	-0.3
15%				
Back-analyzed	Magnitude [MPa]	70.59	49.05	33.12
	Plunge [°]	55.7	11.9	31.7
	Trend [°]	12.8	120.7	218.2
Differences with the applied stresses	Magnitude [%]	-2.3%	1.3%	-1.6%
	Plunge [°]	-0.7	1.6	0.1
	Trend [°]	-1.7	0.3	1.4
20%				
Back-analyzed	Magnitude [MPa]	72.53	46.88	33.71
	Plunge [°]	54.2	12.3	33.0
	Trend [°]	5.7	113.2	211.3
Differences with the applied stresses	Magnitude [%]	0.4%	-3.2%	0.2%
	Plunge [°]	-2.2	2.0	1.4
	Trend [°]	-8.8	-7.2	-5.5
25%				
Back-analyzed	Magnitude [MPa]	70.45	47.32	34.03
	Plunge [°]	53.0	14.7	33.1
	Trend [°]	5.1	115.5	215.4
Differences with the applied stresses	Magnitude [%]	-2.5%	-2.3%	1.1%
	Plunge [°]	-3.5	4.4	1.5
	Trend [°]	-9.4	-4.9	-1.4
30%				
Back-analyzed	Magnitude [MPa]	70.63	48.20	33.42
	Plunge [°]	51.9	10.0	36.3
	Trend [°]	13.4	116.4	213.8
Differences with the applied stresses	Magnitude [%]	-2.2%	-0.5%	-0.7%
	Plunge [°]	-4.5	-0.3	4.7
	Trend [°]	-1.1	-4.0	-3.0
40%				
Back-analyzed	Magnitude [MPa]	62.64	44.45	32.61
	Plunge [°]	52.4	16.1	32.9
	Trend [°]	2.1	114.2	215.0
Differences with the applied stresses	Magnitude [%]	-13.3%	-8.2%	-3.1%
	Plunge [°]	-4.0	5.8	1.3
	Trend [°]	-12.4	-6.2	-1.8
50%				
Back-analyzed	Magnitude [MPa]	79.83	42.44	34.02
	Plunge [°]	52.6	16.7	32.3
	Trend [°]	3.6	116.7	217.7
Differences with the applied stresses	Magnitude [%]	10.5%	-12.4%	1.1%
	Plunge [°]	-3.8	6.4	0.7
	Trend [°]	-11.0	-3.7	0.9

**Table I.11** Back-analyzed 3D in-situ principal stresses with various random errors in input data for scenario 4 (Inclination angle interval 50°. 6 measurements per section)

3D in-situ principal stresses		$\sigma_1$	$\sigma_2$	$\sigma_3$
10%				
Back-analyzed	Magnitude [MPa]	77.08	48.22	35.27
	Plunge [°]	60.6	10.6	27.0
	Trend [°]	14.4	123.8	219.3
Differences with the applied stresses	Magnitude [%]	6.7%	-0.4%	4.8%
	Plunge [°]	4.2	0.3	-4.5
	Trend [°]	-0.2	3.4	2.5
15%				
Back-analyzed	Magnitude [MPa]	67.26	49.32	32.94
	Plunge [°]	54.1	14.3	32.2
	Trend [°]	9.1	119.7	218.9
Differences with the applied stresses	Magnitude [%]	-6.9%	1.8%	-2.1%
	Plunge [°]	-2.4	4.0	0.6
	Trend [°]	-5.5	-0.7	2.1
20%				
Back-analyzed	Magnitude [MPa]	71.79	44.64	33.82
	Plunge [°]	52.6	13.6	34.0
	Trend [°]	357.4	105.8	205.2
Differences with the applied stresses	Magnitude [%]	-0.6%	-7.8%	0.5%
	Plunge [°]	-3.8	3.3	2.5
	Trend [°]	342.8	-14.6	-11.6
25%				
Back-analyzed	Magnitude [MPa]	85.17	47.92	36.11
	Plunge [°]	60.1	12.5	26.7
	Trend [°]	7.7	120.2	216.6
Differences with the applied stresses	Magnitude [%]	17.9%	-1.1%	7.3%
	Plunge [°]	3.7	2.2	-4.8
	Trend [°]	-6.9	-0.2	-0.2
30%				
Back-analyzed	Magnitude [MPa]	83.70	46.87	36.66
	Plunge [°]	58.0	9.8	30.1
	Trend [°]	4.2	110.2	205.9
Differences with the applied stresses	Magnitude [%]	15.9%	-3.2%	9.0%
	Plunge [°]	1.6	-0.5	-1.4
	Trend [°]	-10.3	-10.2	-10.9
40%				
Back-analyzed	Magnitude [MPa]	61.42	41.47	33.52
	Plunge [°]	50.5	20.7	31.9
	Trend [°]	349.1	106.4	210.0
Differences with the applied stresses	Magnitude [%]	-15.0%	-14.4%	-0.4%
	Plunge [°]	-5.9	10.4	0.3
	Trend [°]	334.5	-14.0	-6.8
50%				
Back-analyzed	Magnitude [MPa]	75.95	38.60	25.04
	Plunge [°]	41.2	4.9	48.4
	Trend [°]	358.8	93.0	188.6
Differences with the applied stresses	Magnitude [%]	5.1%	-20.3%	-25.6%
	Plunge [°]	-15.2	-5.4	16.8
	Trend [°]	344.2	-27.3	-28.2

**Table I.12** Back-analyzed 3D in-situ principal stresses with various random errors in input data for scenario 5 (Inclination angle interval 50°. 6 measurements per section)

3D in-situ principal stresses		$\sigma_1$	$\sigma_2$	$\sigma_3$
10%				
Back-analyzed	Magnitude [MPa]	67.66	47.02	33.96
	Plunge [°]	53.7	14.5	32.5
	Trend [°]	5.9	116.5	215.9
Differences with the applied stresses	Magnitude [%]	-6.3%	-2.9%	0.9%
	Plunge [°]	-2.7	4.2	0.9
	Trend [°]	-8.6	-3.9	-0.9
15%				
Back-analyzed	Magnitude [MPa]	72.85	49.51	32.66
	Plunge [°]	56.4	10.8	31.4
	Trend [°]	15.2	121.9	218.6
Differences with the applied stresses	Magnitude [%]	0.8%	2.2%	-2.9%
	Plunge [°]	0.0	0.5	-0.2
	Trend [°]	0.6	1.5	1.8
20%				
Back-analyzed	Magnitude [MPa]	71.42	46.22	33.72
	Plunge [°]	53.1	13.1	33.8
	Trend [°]	2.5	110.7	209.6
Differences with the applied stresses	Magnitude [%]	-1.1%	-4.6%	0.2%
	Plunge [°]	-3.3	2.8	2.2
	Trend [°]	-12.0	-9.7	-7.2
25%				
Back-analyzed	Magnitude [MPa]	62.28	44.63	34.61
	Plunge [°]	45.4	20.9	37.2
	Trend [°]	351.6	104.4	211.3
Differences with the applied stresses	Magnitude [%]	-13.8%	-7.8%	2.9%
	Plunge [°]	-11.0	10.6	5.6
	Trend [°]	337.1	-16.0	-5.5
30%				
Back-analyzed	Magnitude [MPa]	65.40	47.30	33.70
	Plunge [°]	48.4	11.7	39.2
	Trend [°]	8.1	111.6	211.3
Differences with the applied stresses	Magnitude [%]	-9.5%	-2.3%	0.1%
	Plunge [°]	-8.0	1.4	7.6
	Trend [°]	-6.4	-8.8	-5.5
40%				
Back-analyzed	Magnitude [MPa]	54.88	41.27	33.11
	Plunge [°]	41.2	23.9	39.4
	Trend [°]	343.8	96.6	207.9
Differences with the applied stresses	Magnitude [%]	-24.0%	-14.8%	-1.6%
	Plunge [°]	-15.2	13.6	7.8
	Trend [°]	329.3	-23.8	-8.9
50%				
Back-analyzed	Magnitude [MPa]	78.71	40.40	34.32
	Plunge [°]	50.7	16.7	34.3
	Trend [°]	0.4	111.9	213.7
Differences with the applied stresses	Magnitude [%]	9.0%	-16.6%	2.0%
	Plunge [°]	-5.7	6.4	2.8
	Trend [°]	-14.2	-8.5	-3.1

**Table I.13** Back-analyzed 3D in-situ principal stresses with different inclination angle interval for scenario 1 (6 measurements in each section. Max. error in input data 20%)

In-situ principal stresses		$\sigma_1$	$\sigma_2$	$\sigma_3$
20°				
Back-analyzed	Magnitude [MPa]	59.35	28.46	12.10
	Plunge [°]	18.4	2.3	28.2
	Trend [°]	304.1	255.1	246.6
Differences with the applied stresses	Magnitude [%]	-17.8%	-41.2%	-64.1%
	Plunge [°]	-38.1	-8.0	-3.3
	Trend [°]	289.5	134.7	29.8
35°				
Back-analyzed	Magnitude [MPa]	65.42	43.23	30.18
	Plunge [°]	45.4	11.8	42.1
	Trend [°]	351.2	93.5	194.4
Differences with the applied stresses	Magnitude [%]	-9.4%	-10.7%	-10.3%
	Plunge [°]	-11.0	1.5	10.6
	Trend [°]	336.7	-26.9	-22.4
40°				
Back-analyzed	Magnitude [MPa]	67.19	44.03	31.62
	Plunge [°]	48.1	12.7	39.1
	Trend [°]	353.7	98.3	198.8
Differences with the applied stresses	Magnitude [%]	-7.0%	-9.1%	-6.0%
	Plunge [°]	-8.3	2.4	7.5
	Trend [°]	339.2	-22.1	-18.0
50°				
Back-analyzed	Magnitude [MPa]	69.36	45.01	32.93
	Plunge [°]	51.1	13.3	35.8
	Trend [°]	357.0	104.0	203.9
Differences with the applied stresses	Magnitude [%]	-4.0%	-7.1%	-2.1%
	Plunge [°]	-5.4	3.0	4.2
	Trend [°]	342.5	-16.4	-12.9
75°				
Back-analyzed	Magnitude [MPa]	71.59	45.91	33.81
	Plunge [°]	53.4	13.9	33.1
	Trend [°]	0.1	109.6	208.9
Differences with the applied stresses	Magnitude [%]	-0.9%	-5.2%	0.5%
	Plunge [°]	-3.0	3.6	1.5
	Trend [°]	-14.4	-10.8	-7.9
90°				
Back-analyzed	Magnitude [MPa]	72.23	46.07	33.98
	Plunge [°]	53.8	14.4	32.4
	Trend [°]	0.7	111.2	210.6
Differences with the applied stresses	Magnitude [%]	0.0%	-4.9%	1.0%
	Plunge [°]	-2.6	4.1	0.8
	Trend [°]	-13.9	-9.2	-6.3

**Table I.14** Back-analyzed 3D in-situ principal stresses with different inclination angle interval for scenario 2 (6 measurements in each section. Max. error in input data 20%)

In-situ principal stresses		$\sigma_1$	$\sigma_2$	$\sigma_3$
20°				
Back-analyzed	Magnitude [MPa]	65.91	43.43	27.98
	Plunge [°]	44.1	10.5	43.9
	Trend [°]	354.1	94.5	194.8
Differences with the applied stresses	Magnitude [%]	-8.8%	-10.3%	-16.9%
	Plunge [°]	-12.3	0.3	12.4
	Trend [°]	339.6	-25.9	-22.0
35°				
Back-analyzed	Magnitude [MPa]	71.51	46.10	33.07
	Plunge [°]	52.6	12.3	34.6
	Trend [°]	2.7	109.2	207.9
Differences with the applied stresses	Magnitude [%]	-1.0%	-4.8%	-1.7%
	Plunge [°]	-3.8	2.0	3.1
	Trend [°]	-11.8	-11.2	-8.9
40°				
Back-analyzed	Magnitude [MPa]	72.02	46.42	33.40
	Plunge [°]	53.4	12.3	33.9
	Trend [°]	3.9	111.0	209.4
Differences with the applied stresses	Magnitude [%]	-0.3%	-4.2%	-0.8%
	Plunge [°]	-3.0	2.0	2.3
	Trend [°]	-10.6	-9.4	-7.4
50°				
Back-analyzed	Magnitude [MPa]	72.48	46.79	33.69
	Plunge [°]	54.1	12.3	33.1
	Trend [°]	5.3	112.9	211.1
Differences with the applied stresses	Magnitude [%]	0.3%	-3.4%	0.1%
	Plunge [°]	-2.3	2.0	1.6
	Trend [°]	-9.2	-7.5	-5.7
75°				
Back-analyzed	Magnitude [MPa]	72.68	47.10	33.95
	Plunge [°]	54.4	12.7	32.6
	Trend [°]	6.1	114.4	212.7
Differences with the applied stresses	Magnitude [%]	0.6%	-2.7%	0.9%
	Plunge [°]	-2.1	2.4	1.1
	Trend [°]	-8.4	-6.0	-4.1
90°				
Back-analyzed	Magnitude [MPa]	72.72	47.15	34.10
	Plunge [°]	54.3	13.1	32.5
	Trend [°]	5.9	114.8	213.3
Differences with the applied stresses	Magnitude [%]	0.7%	-2.6%	1.3%
	Plunge [°]	-2.1	2.8	0.9
	Trend [°]	-8.6	-5.6	-3.5

**Table I.15** Back-analyzed 3D in-situ principal stresses with different inclination angle interval for scenario 3 (6 measurements in each section. Max. error in input data 20%)

In-situ principal stresses		$\sigma_1$	$\sigma_2$	$\sigma_3$
20°				
Back-analyzed	Magnitude [MPa]	66.31	43.68	28.48
	Plunge [°]	44.9	10.8	43.1
	Trend [°]	354.9	95.8	196.1
Differences with the applied stresses	Magnitude [%]	-8.2%	-9.8%	-15.4%
	Plunge [°]	-11.5	0.5	11.5
	Trend [°]	340.3	-24.6	-20.7
35°				
Back-analyzed	Magnitude [MPa]	71.66	46.23	33.15
	Plunge [°]	52.9	12.2	34.4
	Trend [°]	3.2	109.8	208.3
Differences with the applied stresses	Magnitude [%]	-0.8%	-4.5%	-1.5%
	Plunge [°]	-3.5	1.9	2.8
	Trend [°]	-11.3	-10.6	-8.5
40°				
Back-analyzed	Magnitude [MPa]	72.13	46.53	33.45
	Plunge [°]	53.6	12.2	33.7
	Trend [°]	4.4	111.4	209.7
Differences with the applied stresses	Magnitude [%]	-0.1%	-3.9%	-0.6%
	Plunge [°]	-2.8	1.9	2.1
	Trend [°]	-10.2	-9.0	-7.1
50°				
Back-analyzed	Magnitude [MPa]	72.53	46.88	33.71
	Plunge [°]	54.2	12.3	33.0
	Trend [°]	5.7	113.2	211.3
Differences with the applied stresses	Magnitude [%]	0.4%	-3.2%	0.2%
	Plunge [°]	-2.2	2.0	1.4
	Trend [°]	-8.8	-7.2	-5.5
75°				
Back-analyzed	Magnitude [MPa]	72.69	47.16	33.95
	Plunge [°]	54.4	12.6	32.6
	Trend [°]	6.3	114.6	212.9
Differences with the applied stresses	Magnitude [%]	0.6%	-2.6%	0.9%
	Plunge [°]	-2.0	2.3	1.0
	Trend [°]	-8.2	-5.8	-3.9
90°				
Back-analyzed	Magnitude [MPa]	72.71	47.20	34.09
	Plunge [°]	54.4	13.0	32.5
	Trend [°]	6.1	114.9	213.4
Differences with the applied stresses	Magnitude [%]	0.7%	-2.5%	1.3%
	Plunge [°]	-2.0	2.7	0.9
	Trend [°]	-8.4	-5.4	-3.4



**Table I.16** Back-analyzed 3D in-situ principal stresses with different inclination angle interval for scenario 4 (6 measurements in each section. Max. error in input data 20%)

In-situ principal stresses		$\sigma_1$	$\sigma_2$	$\sigma_3$
20°				
Back-analyzed	Magnitude [MPa]	68.12	41.13	27.05
	Plunge [°]	43.5	5.4	46.0
	Trend [°]	342.8	78.0	173.6
Differences with the applied stresses	Magnitude [%]	-5.7%	-15.1%	-19.6%
	Plunge [°]	-12.9	-4.9	14.4
	Trend [°]	328.3	-42.4	-43.2
35°				
Back-analyzed	Magnitude [MPa]	68.25	42.99	32.32
	Plunge [°]	48.2	12.2	39.2
	Trend [°]	351.0	94.9	195.1
Differences with the applied stresses	Magnitude [%]	-5.5%	-11.2%	-4.0%
	Plunge [°]	-8.2	1.9	7.6
	Trend [°]	336.5	-25.4	-21.8
40°				
Back-analyzed	Magnitude [MPa]	69.40	43.64	33.10
	Plunge [°]	50.0	13.1	37.0
	Trend [°]	353.4	99.5	199.6
Differences with the applied stresses	Magnitude [%]	-3.9%	-9.9%	-1.6%
	Plunge [°]	-6.4	2.8	5.4
	Trend [°]	338.8	-20.9	-17.2
50°				
Back-analyzed	Magnitude [MPa]	71.79	44.64	33.82
	Plunge [°]	52.6	13.6	34.0
	Trend [°]	357.4	105.8	205.2
Differences with the applied stresses	Magnitude [%]	-0.6%	-7.8%	0.5%
	Plunge [°]	-3.8	3.3	2.5
	Trend [°]	342.8	-14.6	-11.6
75°				
Back-analyzed	Magnitude [MPa]	75.21	45.49	33.83
	Plunge [°]	54.5	13.3	32.2
	Trend [°]	2.2	111.5	210.0
Differences with the applied stresses	Magnitude [%]	4.1%	-6.1%	0.5%
	Plunge [°]	-1.9	3.0	0.7
	Trend [°]	-12.3	-8.9	-6.8
90°				
Back-analyzed	Magnitude [MPa]	75.99	45.49	33.64
	Plunge [°]	54.4	13.4	32.2
	Trend [°]	3.2	112.7	211.4
Differences with the applied stresses	Magnitude [%]	5.2%	-6.1%	0.0%
	Plunge [°]	-2.0	3.1	0.6
	Trend [°]	-11.4	-7.7	-5.4

**Table I.17** Back-analyzed 3D in-situ principal stresses with different inclination angle interval for scenario 5 (6 measurements in each section. Max. error in input data 20%)

In-situ principal stresses		$\sigma_1$	$\sigma_2$	$\sigma_3$
20°				
Back-analyzed	Magnitude [MPa]	62.98	42.01	24.71
	Plunge [°]	39.3	9.0	49.2
	Trend [°]	349.6	87.1	187.7
Differences with the applied stresses	Magnitude [%]	-12.8%	-13.3%	-26.6%
	Plunge [°]	-17.1	-1.3	17.7
	Trend [°]	335.1	-33.3	-29.1
35°				
Back-analyzed	Magnitude [MPa]	69.69	45.27	32.65
	Plunge [°]	50.6	12.8	36.5
	Trend [°]	359.3	105.4	205.0
Differences with the applied stresses	Magnitude [%]	-3.5%	-6.5%	-3.0%
	Plunge [°]	-5.8	2.5	4.9
	Trend [°]	344.8	-15.0	-11.8
40°				
Back-analyzed	Magnitude [MPa]	70.49	45.71	33.20
	Plunge [°]	51.8	13.0	35.1
	Trend [°]	0.8	107.8	207.2
Differences with the applied stresses	Magnitude [%]	-2.4%	-5.6%	-1.3%
	Plunge [°]	-4.6	2.7	3.6
	Trend [°]	-13.7	-12.6	-9.6
50°				
Back-analyzed	Magnitude [MPa]	71.42	46.22	33.72
	Plunge [°]	53.1	13.1	33.8
	Trend [°]	2.5	110.7	209.6
Differences with the applied stresses	Magnitude [%]	-1.1%	-4.6%	0.2%
	Plunge [°]	-3.3	2.8	2.2
	Trend [°]	-12.0	-9.7	-7.2
75°				
Back-analyzed	Magnitude [MPa]	72.44	46.70	34.12
	Plunge [°]	54.0	13.5	32.6
	Trend [°]	3.8	113.2	212.1
Differences with the applied stresses	Magnitude [%]	0.3%	-3.6%	1.4%
	Plunge [°]	-2.4	3.3	1.0
	Trend [°]	-10.7	-7.2	-4.7
90°				
Back-analyzed	Magnitude [MPa]	72.78	46.78	34.24
	Plunge [°]	54.1	13.9	32.3
	Trend [°]	3.9	113.9	212.9
Differences with the applied stresses	Magnitude [%]	0.8%	-3.4%	1.8%
	Plunge [°]	-2.3	3.6	0.8
	Trend [°]	-10.6	-6.5	-3.9

**Table I.18** Back-analyzed 3D in-situ principal stresses using different number of measurements for scenario 1 (Inclination angle interval 50°. Max. error in input data 20%)

In-situ principal stresses		$\sigma_1$	$\sigma_2$	$\sigma_3$
3 measurements				
Back-analyzed	Magnitude [MPa]	77.48	46.08	35.36
	Plunge [°]	55.0	7.7	33.9
	Trend [°]	12.4	113.5	208.8
Differences with the applied stresses	Magnitude [%]	7.3%	-4.9%	5.1%
	Plunge [°]	-1.4	-2.6	2.3
	Trend [°]	-2.2	-6.8	-8.0
6 measurements				
Back-analyzed	Magnitude [MPa]	69.36	45.01	32.93
	Plunge [°]	51.1	13.3	35.8
	Trend [°]	357.0	104.0	203.9
Differences with the applied stresses	Magnitude [%]	-4.0%	-7.1%	-2.1%
	Plunge [°]	-5.4	3.0	4.2
	Trend [°]	342.5	-16.4	-12.9
9 measurements				
Back-analyzed	Magnitude [MPa]	77.27	48.19	34.11
	Plunge [°]	56.2	10.0	31.8
	Trend [°]	12.0	117.4	213.7
Differences with the applied stresses	Magnitude [%]	7.0%	-0.5%	1.4%
	Plunge [°]	-0.2	-0.3	0.3
	Trend [°]	-2.5	-3.0	-3.1
12 measurements				
Back-analyzed	Magnitude [MPa]	77.31	46.71	33.46
	Plunge [°]	53.86	12.08	33.47
	Trend [°]	3.53	110.56	208.69
Differences with the applied stresses	Magnitude [%]	7.0%	-3.6%	-0.6%
	Plunge [°]	-2.6	1.8	1.9
	Trend [°]	-11.0	-9.8	-8.1

**Table I.19** Back-analyzed 3D in-situ principal stresses using different number of measurements for scenario 2 (Inclination angle interval 50°. Max. error in input data 20%)

In-situ principal stresses		$\sigma_1$	$\sigma_2$	$\sigma_3$
3 measurements				
Back-analyzed	Magnitude [MPa]	75.44	47.20	34.44
	Plunge [°]	56.1	8.9	32.4
	Trend [°]	14.5	118.0	213.6
Differences with the applied stresses	Magnitude [%]	4.4%	-2.5%	2.4%
	Plunge [°]	-0.3	-1.4	0.8
	Trend [°]	0.0	-2.4	-3.2
6 measurements				
Back-analyzed	Magnitude [MPa]	72.48	46.79	33.69
	Plunge [°]	54.1	12.3	33.1
	Trend [°]	5.3	112.9	211.1
Differences with the applied stresses	Magnitude [%]	0.3%	-3.4%	0.1%
	Plunge [°]	-2.3	2.0	1.6
	Trend [°]	-9.2	-7.5	-5.7
9 measurements				
Back-analyzed	Magnitude [MPa]	76.96	48.24	34.09
	Plunge [°]	56.3	10.0	31.8
	Trend [°]	12.3	117.7	214.0
Differences with the applied stresses	Magnitude [%]	6.5%	-0.4%	1.3%
	Plunge [°]	-0.1	-0.3	0.2
	Trend [°]	-2.2	-2.7	-2.8
12 measurements				
Back-analyzed	Magnitude [MPa]	75.60	47.98	33.85
	Plunge [°]	55.7	11.3	31.9
	Trend [°]	9.2	116.2	213.3
Differences with the applied stresses	Magnitude [%]	4.6%	-0.9%	0.6%
	Plunge [°]	-0.7	1.0	0.3
	Trend [°]	-5.3	-4.2	-3.5

**Table I.20** Back-analyzed 3D in-situ principal stresses using different number of measurements for scenario 3 (Inclination angle interval 50°. Max. error in input data 20%)

In-situ principal stresses		$\sigma_1$	$\sigma_2$	$\sigma_3$
3 measurements				
Back-analyzed	Magnitude [MPa]	75.36	47.25	34.40
	Plunge [°]	56.2	8.9	32.3
	Trend [°]	14.6	118.1	213.8
Differences with the applied stresses	Magnitude [%]	4.3%	-2.5%	2.2%
	Plunge [°]	-0.2	-1.4	0.7
	Trend [°]	0.1	-2.3	-3.0
6 measurements				
Back-analyzed	Magnitude [MPa]	72.53	46.88	33.71
	Plunge [°]	54.2	12.3	33.0
	Trend [°]	5.7	113.2	211.3
Differences with the applied stresses	Magnitude [%]	0.4%	-3.2%	0.2%
	Plunge [°]	-2.2	2.0	1.4
	Trend [°]	-8.8	-7.2	-5.5
9 measurements				
Back-analyzed	Magnitude [MPa]	76.66	48.29	34.08
	Plunge [°]	56.4	10.0	31.7
	Trend [°]	12.6	118.0	214.3
Differences with the applied stresses	Magnitude [%]	6.1%	-0.3%	1.3%
	Plunge [°]	0.0	-0.3	0.1
	Trend [°]	-1.9	-2.4	-2.6
12 measurements				
Back-analyzed	Magnitude [MPa]	75.53	48.03	33.86
	Plunge [°]	55.8	11.2	31.8
	Trend [°]	9.5	116.4	213.5
Differences with the applied stresses	Magnitude [%]	4.6%	-0.8%	0.6%
	Plunge [°]	-0.6	0.9	0.3
	Trend [°]	-5.1	-4.0	-3.3

**Table I.21** Back-analyzed 3D in-situ principal stresses using different number of measurements for scenario 4 (Inclination angle interval 50°. Max. error in input data 20%)

In-situ principal stresses		$\sigma_1$	$\sigma_2$	$\sigma_3$
3 measurements				
Back-analyzed	Magnitude [MPa]	86.08	48.86	35.37
	Plunge [°]	64.2	7.8	24.4
	Trend [°]	17.0	123.5	217.0
Differences with the applied stresses	Magnitude [%]	19.2%	0.9%	5.1%
	Plunge [°]	7.8	-2.5	-7.1
	Trend [°]	2.5	3.1	0.2
6 measurements				
Back-analyzed	Magnitude [MPa]	71.79	44.64	33.82
	Plunge [°]	52.6	13.6	34.0
	Trend [°]	357.4	105.8	205.2
Differences with the applied stresses	Magnitude [%]	-0.6%	-7.8%	0.5%
	Plunge [°]	-3.8	3.3	2.5
	Trend [°]	342.8	-14.6	-11.6
9 measurements				
Back-analyzed	Magnitude [MPa]	74.64	48.45	34.30
	Plunge [°]	56.3	10.4	31.6
	Trend [°]	12.7	118.7	215.2
Differences with the applied stresses	Magnitude [%]	3.3%	0.0%	1.9%
	Plunge [°]	-0.1	0.1	0.0
	Trend [°]	-1.8	-1.7	-1.6
12 measurements				
Back-analyzed	Magnitude [MPa]	75.08	47.41	33.73
	Plunge [°]	55.0	12.0	32.4
	Trend [°]	6.8	114.4	212.2
Differences with the applied stresses	Magnitude [%]	3.9%	-2.1%	0.2%
	Plunge [°]	-1.5	1.7	0.8
	Trend [°]	-7.7	-6.0	-4.6

**Table I.22** Back-analyzed 3D in-situ principal stresses using different number of measurements for scenario 5 (Inclination angle interval 50°. Max. error in input data 20%)

In-situ principal stresses		$\sigma_1$	$\sigma_2$	$\sigma_3$
3 measurements				
Back-analyzed	Magnitude [MPa]	76.61	47.11	34.68
	Plunge [°]	56.4	8.8	32.1
	Trend [°]	14.4	117.8	213.4
Differences with the applied stresses	Magnitude [%]	6.1%	-2.7%	3.1%
	Plunge [°]	0.0	-1.5	0.6
	Trend [°]	-0.1	-2.6	-3.4
6 measurements				
Back-analyzed	Magnitude [MPa]	71.42	46.22	33.72
	Plunge [°]	53.1	13.1	33.8
	Trend [°]	2.5	110.7	209.6
Differences with the applied stresses	Magnitude [%]	-1.1%	-4.6%	0.2%
	Plunge [°]	-3.3	2.8	2.2
	Trend [°]	-12.0	-9.7	-7.2
9 measurements				
Back-analyzed	Magnitude [MPa]	74.61	48.46	34.30
	Plunge [°]	56.4	10.4	31.6
	Trend [°]	12.7	118.7	215.2
Differences with the applied stresses	Magnitude [%]	3.3%	0.1%	1.9%
	Plunge [°]	-0.1	0.1	0.0
	Trend [°]	-1.8	-1.7	-1.6
12 measurements				
Back-analyzed	Magnitude [MPa]	75.00	47.50	33.75
	Plunge [°]	55.1	11.9	32.3
	Trend [°]	7.2	114.8	212.4
Differences with the applied stresses	Magnitude [%]	3.8%	-1.9%	0.3%
	Plunge [°]	-1.3	1.6	0.7
	Trend [°]	-7.3	-5.6	-4.4